University of Cyprus

DEPARTMENT OF BIOLOGICAL SCIENCES

FUNCTIONAL CHARACTERIZATION OF THE ENDOPLASMIC RETICULUM AND NUCLEAR ENVELOPE TRANSMEMBRANE PROTEIN TMEM147 IN HeLa CELLS

GIANNIS MAIMARIS

A dissertation submitted to the University of Cyprus in partial fulfillment of the requirements for the degree of Doctor of Philosophy

November 2021

VALIDATION PAGE

Doctoral Candidate: Giannis Maimaris

Doctoral Dissertation Title: Functional characterization of the endoplasmic reticulum and nuclear envelope transmembrane protein TMEM147 in HeLa cells.

The present Doctoral Dissertation was submitted in partial fulfillment of the requirements for the Degree of Doctor of Philosophy at the ***Department of Biological Sciences*** *and was approved on the ………………… by the members of the* ***Examination Committee****.*

Examination Committee:

Research Supervisor:

Niovi Santama	Professor, Department of Biological Sciences, University of Cyprus

----

Committee Member:

Paris A. Skourides	Associate Professor, Department of Biological Sciences, University of Cyprus

----

Committee Member:

Pantelis Georgiades	Associate Professor, Department of Biological Sciences, University of Cyprus

----

Committee Member:

Panagiotis Papageorgis,	Associate Professor, Department of Life Sciences, European University of Cyprus

----

Committee Member:

Dimitrios J. Stravopodis,	Associate Professor, Department of Biology, National and Kapodistrian University Athens, Greece

----

DECLARATION OF DOCTORAL CANDIDATE

The present doctoral dissertation was submitted in partial fulfillment of the requirements for the degree of Doctor of Philosophy of the University of Cyprus. It is a product of original work of my own, unless otherwise mentioned through references, notes, or any other statements.

Giannis Maimaris

……………………………………..

Abstract

The Endoplasmic Reticulum (ER) is the largest membrane-bound cytoplasmic compartment with diverse functionality, including protein synthesis and processing, calcium storage, and lipid and cholesterol biosynthesis. It comprises the nuclear envelope (NE) and the peripheral ER, further divided to the distinct subdomains of flat cisternae sheets and the tubular network. Transmembrane protein TMEM147 has been implicated in muscarinic receptor 3 (M3R) trafficking, in the stabilization of the Nicalin-NOMO protein complex in nodal signaling, and in the activation of NF-κB transcription factors.

In this work, we report TMEM147 as a resident protein of the ER and NE membrane in HeLa cells and describe its physical and functional association with the NE protein lamin B receptor (LBR). We find that downregulation of TMEM147 negatively regulates both gene expression and protein levels of LBR and disrupts its proper inner nuclear membrane (INM) localization, causing its dispersion to the peripheral ER membranes. Silencing of TMEM147 is accompanied by further changes in ER membrane domain organization and changes in nuclear shape and loss of chromatin compaction as well as decreased cell viability. LBR is structurally and functionally a modular protein. Its N-terminus protrudes to the nucleoplasm and is known to be involved in anchoring and organizing heterochromatin, while its C-terminus in the INM extends towards the cytoplasm and hosts a cholesterol reductase activity that we document as essential for the interaction with TMEM147. We determined that DHCR7, another key sterol reductase, catalyzing cholesterol synthesis, also interacts with TMEM147 and, similar to LBR, is downregulated upon TMEM147 depletion at both protein and gene expression levels. Our proteomic analysis of the TMEM147 interactome also revealed an interaction of TMEM147 with sterol reductase TM7SF2, whose gene expression however we found not to be co-ordinated with that of TMEM147. Here we also report that silencing of TMEM147 alters the lipidomic profile of the cells, including total cholesterol levels and cholesteryl ester species and its depletion also modulates the receptor-mediated uptake of cholesterol by cells. Addition of exogenous cholesterol in TMEM147-silenced and lipid starved cells rescued cell viability and growth while it had a modest ameliorating effect on control cells. Taken together, our findings illuminate TMEM147 as a new likely regulator of cholesterol homeostasis in human cells.

Complementary to this work, we conducted a protein network and pathway analysis of a manually curated list of TMEM147 interactors, co-factors and modulators. Pathway analysis identified four major pathways including G protein-coupled receptor activity, ribosome binding, oxidoreductase activity, and transmembrane transport activity, while protein network analysis identified hub proteins of these corresponding pathways. Association of identified pathways and network hub proteins can be regarded as future research pointers to further TMEM147 functional studies.

Work from this thesis has been included in two publications [J. Cell Science 2020 (doi: 10.1242/jcs.245357) and Int J Molecular Science 2021 (doi: 10.3390/ijms221910231)].

Περίληψη

Το Ενδοπλασματικό Δίκτυο (ER) είναι το μεγαλύτερο μεμβρανικό κυτταροπλασματικό διαμέρισμα με ποικιλία λειτουργιών που περιλαμβάνουν τη σύνθεση και επεξεργασία πρωτεϊνών, αποθήκευση ασβεστίου και τη βιοσύνθεση χοληστερόλης και λιπιδίων. Αποτελείται από τον πυρηνικό φάκελο (NE) και το περιφερειακό ER, που διακρίνεται περαιτέρω σε δύο περιοχές αποτελούμενες από επίπεδους σακοειδείς σχηματισμούς (cisternae) και το σωληνοειδές δίκτυο (tubules). Η διαμεμβρανική πρωτεΐνη TMEM147 εμπλέκεται στη μεταφορά του μουσκαρινικού υποδοχέα 3 της ακετυλχολίνης, στη σταθεροποίηση του πρωτεϊνικού συμπλόκου Nicalin-NOMO στο μονοπάτι μεταγωγής σήματος nodal και την ενεργοποίηση των μεταφραστικών παραγόντων τύπου NF-κB.

Σε αυτή την εργασία καθορίσαμε ότι σε κύτταρα HeLa, η TMEM147 βρίσκεται στις μεμβράνες του ER και του NE και περιγράφουμε τη φυσική αλληλεπίδραση και λειτουργική της σχέση με τον υποδοχέα της λαμίνης B (LBR), πρωτεΐνης του NE. Βρήκαμε ότι η μειορύθμιση της TMEM147 ρυθμίζει αρνητικά τόσο τη γονιδιακή έκφραση όσο και τα πρωτεϊνικά επίπεδα του LBR, διαταράσσοντας επίσης το σωστό εντοπισμό του στην εσωτερική μεμβράνη του NE (INM) και προκαλώντας την διασπορά του στις μεμβράνες του περιφερειακού ER. Η αποσιώπηση της TMEM147 ακολουθείται από περαιτέρω αλλαγές στην οργάνωση των μεμβρανών του ER, αλλαγές στο σχήμα του πυρήνα και τη συσπείρωση της χρωματίνης, όπως επίσης μείωση στη βιωσιμότητα των κυττάρων. Ο LBR είναι δομικά και λειτουργικά μια αρθρωτή πρωτεΐνη. Η αμινοτελική του περιοχή προβάλει στο νουκλεόπλασμα και εμπλέκεται στην αγκυροβόληση και την οργάνωση της ετεροχρωματίνης, ενώ η καρβοξυτελική του περιοχή εκτείνεται προς το κυτταρόπλασμα και εμπεριέχει ενζυμική ενεργότητα αναγωγάσης της χοληστερόλης που καταγράφουμε ως ουσιώδη για την φυσική του αλληλεπίδραση με την TMEM147. Διαπιστώσαμε ότι η DHCR7, μια άλλη αναγωγάση-κλειδί των στερολών, που καταλύει την σύνθεση της χοληστερόλης, επίσης αλληλεπιδρά με την TMEM147 και, όμοια με τον LBR, μειορυθμίζεται παράλληλα με τη μείωση των επιπέδων της TMEM147, τόσο σε πρωτεϊνικό επίπεδο όσο και σε επίπεδο γονιδιακής έκφρασης. Πρωτεομική ανάλυση των αλληλεπιδράσεων της TMEM147 κατέδειξε την αλληλεπίδραση της με μια άλλη αναγωγάση των στερολών, την TM7SF2, της οποίας η γονιδιακή έκφραση δεν εναρμονίζεται με αυτήν της TMEM147. Ακόμα, στην εργασία αυτή αναδεικνύεται ότι η αποσιώπηση της TMEM147 μεταβάλλει το λιπιδικό προφίλ των κυττάρων συμπεριλαμβανομένων αλλαγών των επιπέδων της ολικής χοληστερόλης και ειδών των εστέρων της χοληστερόλης, όπως επίσης ότι η μείωση των επιπέδων της TMEM147 τροποποιεί τη

διαμεσολαβούμενη από υποδοχέα πρόσληψη της χοληστερόλης από τα κύτταρα. Προσθήκη εξωγενούς χοληστερόλης σε αποσιωποιημένα για την TMEM147 κύτταρα κάτω από συνθήκες λιπιδικής πενίας, επανέφερε την κυτταρική βιωσιμότητα και ανάπτυξη ενώ προκάλεσε μόνο μικρή βελτίωση στα κύτταρα σε πειράματα ελέγχου. Τα πιο πάνω ευρήματα σκιαγραφούν την TMEM147 ως ένα νέο πιθανό ρυθμιστή της ομοιόστασης της χοληστερόλης στα ανθρώπινα κύτταρα.

Συμπληρωματικά, σε αυτήν την εργασία διενεργήσαμε ανάλυση των πρωτεινικών δικτύων και μονοπατιών ενός δια χειρός επιμελημένου μη αυτοματοποιημένου (manually curated) καταλόγου από αλληλεπιδρώσες πρωτεΐνες, συμπαράγοντες και τροποποιητές της TMEM147. Η ανάλυση των μονοπατιών ταυτοποίησε τέσσερα κύρια μονοπάτια στα οποία συμπεριλαμβάνονται η ενεργότητα υποδοχέα συζευγμένη με πρωτεΐνη G, η σύνδεση με ριβοσώματα, η ενεργότητα οξειδοαναγωγάσης και η ενεργότητα διαμεμβρανικής μεταφοράς, ενώ η ανάλυση των πρωτεϊνικών δικτύων αναγνώρισε πρωτεΐνες-κόμβους σε αυτά τα μονοπάτια. Συσχέτιση των ταυτοποιημένων μονοπατιών και των πρωτεϊνών-κόμβων μπορούν να θεωρηθούν ως μελλοντικοί ερευνητικοί στόχοι για περαιτέρω λειτουργική διερεύνηση της TMEM147.

Μέρος από αυτή τη διδακτορική διατριβή συμπεριλαμβάνεται σε δύο δημοσιεύσεις [J. Cell Science 2020 (doi: 10.1242/jcs.245357) και Int J Molecular Science 2021 (doi: 10.3390/ijms221910231)].

Acknowledgements

I would like to thank,

my research supervisor Professor Niovi Santama, for the opportunity and her trust to work in her lab elaborating on an interesting and intriguing topic in molecular and cellular biology, her continued support and guidance in every step of this journey even when things were heading south, qualifying me to step up and complete this doctoral dissertation.

the post-doctoral researcher Dr. Andri Christodoulou for letting me continue the research work she had initiated, her constant guidance, support, help and talks regarding experimental and theoretical aspects, so this work can come to a completion,

Associate Professor Carsten Werner Lederer, for his support, guidance, cooperation and great contribution in achieving my first authorship in a scientific publication,

Dr. Antonis Ververis for his support, advising and great collaboration during my studies,

the undergraduate student Andri Makrigiorgi for her help and contribution to this work, and the lab associate Renos Georgiou for his help and cooperation.

the doctoral candidate Andria Theofanous, the graduate students Rafaela Michailidou and Anastasia Raouka for the harmonious cooperation in the lab.

Last but not least, I would like to thank my father for his constant support but, more importantly,

I would like to thank my wife Andria, for her endless love and patience, moral support, and continuous understanding through all these years, letting me neglect my fatherhood obligations for whatever was needed to achieve my goal for this Doctoral degree.

My motivation to this scientific journey

My Wife

Andria

My daughters

Anna, Nayia and Rania

Thank you for your support and patience!

Table of Contents

I. List of Figures

II. List of Tables

III. Abbreviations

7DHC	7-dehydrocholesterol
ABC	ATP-binding cassette
ACAT	Acyl-CoA:cholesterol acyltransferace
AMPK	AMP-activated protein kinase
APH	Amphipathic helix
Atl	Atlastin
CDK	Cycle dependent kinase
CE	Cholesteryl esters
CEs	CE species
CLIMP63	Cytoskeleton Linking Membrane Protein 63
Co-A	Co-enzyme-A
DHCR7	7-dehydrocholesterol reductase transmembrane protein
ER	Endoplasmic Reticulum (Ενδοπλασματικό Δίκτυο)
ERAD	ER-associated degradation
GFP	Green fluorescence protein
H4K20me2	Lys 20 residue of histone 4
HDL	High-density lipoprotein
HL	Hydrophilic loop
hLBR	Human LBR
HMG-CoA	3-hydroxy-3-methylglutaryl-CoA
HMGCR	HMGC-reductase
hTM7SF2	Human TM7SF2
HTR	Hydrophobic transmembrane regions
IF	Immunofluorescence
INM	Inner nuclear membrane (Εσωτερική πυρηνική μεμβράνη)
INSIG	Insulin induced gene
IP	Immunoprecipitation
Lam	Lipid transfer proteins anchored at a membrane contact site
LBR	Lamin B receptor (Υποδοχέας της λαμίνης Β)
LD	Lipid Droplet
LDL	Low-density lipoprotein
LDLR	LDL receptor
LE/LY	Late endosome fused with lysosome
LNP	Lunapark
M1R	Muscarinic Receptor 1
M3R	Muscarinic Receptor 3 (Μουσκαρινικός υποδοχέας 3)
MCS	Membrane contact site
NE	Nuclear Envelope (Πυρηνικός φάκελος)
NPC	Nuclear pore complex
NPC1	Niemann-Pick type C1
NPC2	Niemann-Pick type C2
ONM	Outer nuclear membrane
ORP	Oxysterol-related protein
OSBP	Oxysterol-binding protein
PCA	Principal component analysis
PKA	Protein kinase A
rER	Rough endoplasmic reticulum
RHD	Reticulon Homology Domain

RS-rich	Arginine/serine rich
RTN	Reticulon
SCAP	SREBP cleavage-activating protein
sER	Smooth endoplasmic reticulum
SHH	Sonic hedgehog signal pathway
siRNA	Small interfering RNA
SLOS	Smith-Lemli-Opitz-syndrome
SMO	Smoothened receptor
SQS	Squalene synthase
SR-B	Scavenger receptor class-B
SRE	Sterol regulatory element
SREBP	Sterol regulatory element binding protein
SRP	Signal recognition particle
SSD	Sterol sensing domain
StAR	Steroidogenic acute regulatory protein
STARD	Steroidogenic acute related domain protein
START	Steroidogenic acute related lipid transfer protein
STP	Sterol transfer protein
TEM	Transmission electron microscopy
TM	Transmembrane
TM7SF2	Transmembrane protein 7 Superfamily Member 2
TMEM147	Transmembrane protein 147
UPR	Unfolded protein response
WB	Western Blot
wt.	Wild-type

1

Introduction

Chapter 1: Introduction

This PhD thesis investigates the function of a transmembrane protein, present in both Endoplasmic Reticulum and Nuclear Envelope membranes, termed TMEM147, that has not been extensively characterized before (Dettmer et al., 2010, Rosemond et al., 2011). Due to the interest of our lab in ER membrane morphogenesis (Christodoulou et al., 2016, Santama et al., 2004), we focused on fully functionally characterizing TMEM147. In the course of the study, we found that it affected the composition and density of the ER, interacted with a well-known and extensively studied NE protein LBR, and affected cellular cholesterol homeostasis, along with reductases DHCR7 and TM7SF2. The following introductory section attempts to give a detailed overview of these topics in order to give the relevant background to our study.

1.1 The Endoplasmic Reticulum

1.1.1 Introduction

Emilio Veratti first described the endoplasmic reticulum (ER) in 1902 as a unique membrane network within the cell (Veratti, 1902). Despite the early discovery, research on the ER advanced only upon the advent of electron microscope technology and the work of Palade and Porter (Palade, 1955, Palade and Porter, 1954, Porter and Palade, 1957) revealing the complex structure of this important membranous network system.

The ER is a single bilayer, a continuous and interconnected membrane network system, extending from the nuclear membrane throughout the cytoplasm to the far end of the cell boundaries. It comprises the nuclear envelope (NE) and the peripheral ER. The latter can be further discriminated based on membrane morphological characteristics in two distinct domains. In the perinuclear region, the ER is characterized mostly by flat cisternal sheet structures, while further outwards in the cell periphery it is characterized, instead, by reticular cylindrical structures of ER tubules, interconnected by three-way junctions. This polygonal connection array of ER tubules allows the organelle to expand all over the cytoplasm of the cell to form an extended and intricate network (Westrate et al., 2015), without excluding other organelles from being present in the same cell regions, as they can traffic freely around it (Friedman and Voeltz, 2011).

Sheets are characterized by two opposing single lipid bilayers with little curvature up to the edges of the flat cisternae in an open-arc shape, which enclose the inner volume of the

ER, the ER lumen, and which have a height of 30 nm in yeast and 50 nm in mammals (Bernales et al., 2006). Overall, ER sheets form stacks and are interconnected by regions of twisted membranes with helical edges (Terasaki et al., 2013a). In contrast to cisternae, tubules are characterized by high curvature of the lipid bilayer along one axis and by a resulting long cylindrical shape with a cross sectional diameter of 50 nm in eukaryotes, similar to that of ER sheets (West et al., 2011b). ER is a dynamic structure continuously shifting its shape, with the ratio of sheets to tubules being altered as well. Different cell types present disparities in ER shape and domain ratio, according to external or internal stimuli and the corresponding physiological cell responses, such as differentiation, cell cues, cell cycle, protein interactions and cell developmental stage (Schwarz and Blower, 2016).

The morphologically different regions of the ER present a different surface-to-volume ratio, which is higher in tubules than in sheets. This suggests a functional difference of the two domains, with ER tubules being more suitable for surface-dependent functions, whereas sheets are more suitable for luminal processes (Westrate et al., 2015). This difference in functionality is additionally indicated by the presence of membrane-bound ribosomes, mainly on the sheets and rarely on the tubules, thus distinguishing the ER into rough ER (rER) and smooth ER (sER), respectively (Shibata et al., 2006). All of the above imply that the ER has multiple functionalities, and research revealed that protein synthesis, post-translational modifications, folding and transporting are functions typically associated with sheets, while lipid metabolism, carbohydrate metabolism and calcium storage/release are functions associated with tubules (Shibata et al., 2006, Voeltz et al., 2002).

1.1.2 Endoplasmic Reticulum Dynamics

The presence of these distinct morphological regions of the ER raised questions concerning their regulation, formation and maintenance, which cell biologists have been trying to address and fully characterize over the last few decades, with great advances only recently due to technological advances such as electron microscopy, three-dimensional electron tomography and confocal fluorescence microscopy, as will be detailed later (Shibata et al., 2006, Voeltz et al., 2002, Baumann and Walz, 2001, West et al., 2011a, Terasaki et al., 2013b). Towards this characterization, several proteins have been identified as implicated in the mechanisms of ER morphogenesis, with reticulons and REEPs/DP1/Yop1 families playing a fundamental role in tubule formation. Correspondingly, CLIMP63, Kinectin and p180 are thought important in sheet formation. The latter proteins are supplemented by Atlastins and Sey1/RHD3, which are implicated in three-way junctions, and Lunapark, Protrudin and Rab GTPases, which are required for further maintenance.

1.1.3 ER Tubules

A century after the discovery of the ER, evidence of a crucial membrane-associated protein family involved in ER formation (Voeltz et al., 2006), along with other diverse functions (Di Scala et al., 2005), emerged in higher vertebrates and was named as the Reticulon family. It is a highly conserved family of integral ER-membrane proteins encompassing a characteristic wedge-shape topological domain and typically 200-1200 amino acid- long (van de Velde et al., 1994). They localize throughout the ER membranes, excluding the NE and the flat regions of ER sheets. Reticulon labeling exclusively marks regions of high membrane curvature, such as ER tubules and the highly-bent membrane edges of ER sheets (Shibata et al., 2010, Westrate et al., 2015).

Orthologs of the Reticulon protein family can be found from *Saccharomyces cerevisiae and Caenorhabditis elegans* to lower vertebrates and mammals, including human. Analysis of the *C. elegans* genome found only one Reticulon family gene (ret-1), which encodes three different isoforms (nRTN-A, nRTN-B, nRTN-C) (Iwahashi et al., 2002), while the *S. cerevisiae* genome contains two single-transcript genes (RTN1: Rtn1p, RTN2: Rtn2p) (Oertle et al., 2003b). In mammals, there are four Reticulon orthologs (RTN1, RTN2, RTN3, RTN4/Nogo), and through alternative splicing or control by different tissue specific promoters, each gene encodes two or three isoforms (RTN1A-C, RTN2A-C, RTN3A and B, RTN4/NogoA-C) (Roebroek et al., 1998, Oertle et al., 2003b, Oertle et al., 2003a, Moreira et al., 1999, GrandPre et al., 2000).

A series of experiments have shown the importance of Reticulons in tubule formation. First, experiments with purified Reticulon variants revealed their contribution to membrane tubule generation upon reconstitution into proteoliposomes *in vitro* (Hu et al., 2008). Following experimental overexpression of Reticulons, analyses revealed an increase in tubule length at the expense of sheets, which were disrupted (Shibata et al., 2008). Conversely, depletion of Reticulons resulted in the expansion of peripheral sheets and the reduction of tubules (Voeltz et al., 2006). These results suggest the importance of Reticulons in controlling the levels of ER tubules and moreover imply that Reticulons are not only necessary but sufficient to regulate the ratio of sheets to tubules (Shibata et al., 2010, Westrate et al., 2015). Despite the general role of the Reticulons in tubule shaping and their high level of mutual C-terminal sequence similarity, their N-terminal region shows variability (Yang and

Strittmatter, 2007), implying slightly different specialized functions for each transcript, yet to be found and characterized.

Along with Reticulons, another membrane protein family has been identified as implicated in tubule formation. Members of this six-member family called REEPs are ubiquitous among eukaryotes, with identification of Yop1p in yeast and its DP1 ortholog in mammals as the fifth family member that is of particular interest here. The tubule-inducing REEPs colocalize with Reticulons in ER regions of high membrane curvature, such as sheet edges and tubules (Voeltz et al., 2006). Experiments with purified members of this protein family have shown *in vitro* membrane tubule generation induction, comparable to that prompted by purified Reticulons (Hu et al., 2008). Furthermore, experiments in yeast, where both Reticulons and Yop1p were depleted, resulted in cells where the highly curved ER periphery was replaced by enormous sheets. When either Reticulons or Yop1p proteins were depleted, the Yeast ER structure was relatively normal, suggesting that both protein families may have functional redundancy. Taken together, these observations suggest that Reticulons and the REEPs/Yop1p family members interact in order to regulate and maintain the high-curvature domains of the ER (Voeltz et al., 2006).

Sequence comparison of these ubiquitous tubule-shaping protein families did not reveal any homology. Interestingly though, the two families contain a topologically conserved domain independent of amino acid sequence, termed core Reticulon Homology Domain (RHD) (Voeltz et al., 2006). It is located at the C-terminus of the protein and consists of two sequential hydrophobic transmembrane regions (HTRs). Notably, the mammalian REEP1–6 isoforms can be divided into two subgroups. Isoforms 5 and 6, share similar HTR with Reticulons, but isoforms 1–4 share a distinct topology, suggesting subtle functional differences in ER shaping properties between the two mammalian REEP groups [Park et al., 2010].

Each HTR contains 30–35 amino acids, joined together by a hydrophilic loop (HL), 60-70 residue-long (Yang and Strittmatter, 2007). N-terminal, intervening hydrophilic loop and C-terminal regions of these proteins all face the cytosol, leading to an unusual topology (Voeltz et al., 2006). Each one of these two HTR regions forms a wedge-shaped hairpin, embedded in the membrane bilayer perpendicularly but short enough, so as not to span the entire lipid bilayer of the ER membrane. In this orientation, each HTR occupies more space in the outer leaflet than in the inner leaflet of the lipid bilayer, consequently resulting in greater outer-leaflet lipid displacement compared with the inner leaflet, which causes the ER membrane to bend. In this manner, high curvature regions are generated, shaping the tubules and the sheet edges of the ER (Lin et al., 2012, Shibata et al., 2009, Voeltz et al., 2006) thus serving as the first mechanism of tubular membrane generation. Moreover, the significance of the wedge-shaped HTR length in membrane bending has been proven in experiments with mutant RTN4. In these experiments, either both or one of the tandem transmembrane (TM) domains of the protein were extended to a length spanning both lipid bilayers, resulting in loss of membrane-shaping properties compared with the wild-type (wt.) protein (Zurek et al., 2011).

Following the work by Voeltz et al., Shibata et al. suggested a second mechanism of tubular membrane generation in 2008. They found that the conserved RHD region, aside from targeting the ER tubules, lead mammalian RTNs and REEP5/DP1 to either homo- or hetero- oligomerization, proposing that these oligomers acquire an arc-like shape. The oligomers serve as scaffolds stabilizing the structure of tubules by surrounding the curved ER-membrane and complement the wedge-like RHD proteins in the induction of high-curvature regions in both tubules and sheet edges (Shibata et al., 2008).

In addition to the RHD and the tubule-generating mechanisms, a complementary curvature-inducing and stabilizing motif was initially identified in Yop1p. Studies of this yeast REEP5/DP1 ortholog showed an amphipathic helix (APH) motif located downstream of RHD and interacting with membranes but, more importantly, regulating tubule formation, by acting as an additional wedge inserted in the outer lipid leaflet and causing the membrane to bend. This crucial role is suggested by *in vitro* experiments, where C-terminally truncated mutants were unable to generate membrane tubules, implying a loss of bending properties. Furthermore, sequence analysis of the APH motif among most ER curvature-inducing proteins has revealed that it is conserved in most of them, whereas in some members it is also found upstream of RHD (Brady et al., 2015).

1.1.4 ER Sheets

As previously mentioned, the flat cisternae structures of ER sheets extend directly from the NE to the perinuclear ER and can be divided in two distinct morphological regions: their flat central region and the semi-tubular curved edges. Curved edge-formation is based on the oligomerization and scaffolding properties of RHD, the embedded hydrophobic HRT wedge membrane-insertion, and the amphipathic helices of both Reticulons and REEPs/Yop1p families. Rather than on the mere absence of those factors, shaping, maintaining and stabilizing the flat central ER sheet membrane region relies on additional factors sharing a characteristic common cytosolic coiled-coil domain with rod-like scaffolding properties, localized exclusively at these regions of sheets (Zhang and Hu, 2016).

Early electron microscopy studies showed that the ER regions do not only differ in their curvature but revealed that the two distinct areas additionally appear different in terms of “rough” and “smooth” membrane surface area. The rough compartment appeared to be the ER sections proximal to the NE, and comprised ER sheets studded with ribosomes, whereas the smooth compartment was that of the distal tubular ER periphery, where ribosomes were virtually absent (Shibata et al., 2006, Voeltz et al., 2002). The presence of ribosomes and the organization of polyribosomes (polysomes) suggest that ER sheets are the primary location for protein synthesis, translocation, post-translational modifications, and folding of integral membrane- and secreted proteins. The translation of these proteins starts in the cytosol where mRNA and ribosome subunits associate. The nascent polypeptide contains a signal sequence within its amino terminus, which is recognized and bound by the signal recognition particle (SRP) (Walter and Blobel, 1981, Walter et al., 1981). This ribonucleoprotein co-translationally targets the four-member complex (mRNA:ribosome:nascent polypeptide:SRP) to the ER membrane, where it docks on the SRP receptor (Gilmore et al., 1982, Meyer et al., 1982). The translation continues and the polypeptide at the same time enters the ER via the translocon, a protein channel which contains Sec proteins and spans the lipid bilayer (Rapoport, 2007, Deshaies et al., 1991). Integral proteins contain either a hydrophobic leader sequence or a stop-transfer membrane anchor signal, which pause their translocation, followed by lateral shifting and anchoring in the ER membrane (Blobel, 1980). Integral proteins may span the phospholipid bilayer once or multiple times, classified as single-pass transmembrane proteins or multi-pass transmembrane proteins, respectively (Braakman and Hebert, 2013). In the case of secreted or ER lumen proteins, the sequence bound to the SRP is cleaved by a signal peptidase and the protein is released in the lumen (Evans et al., 1986), where chaperones and folding proteins aid proper folding and modification of these proteins, including N-linked glycosylation, disulfide bond formation and oligomerization (Braakman and Hebert, 2013). ER lumen-resident proteins are destined to function in the ER, e.g. as chaperons, whereas proteins destined for other organelles or for secretion are enclosed in specific protein-coated lipid vesicles, depending on their destination. For instance, COPII-coated vesicles are targeted to the Golgi and represent the first membrane-trafficking step in the secretory pathway, whereas clathrin-coated vesicles chiefly target the endo/lysosomes and, in turn, COPI-coated vesicles help recycle vesicle material back from the Golgi to the ER (Barlowe et al., 1994, Bonifacino and Glick, 2004, Schekman and Orci, 1996).

In reference back to the mechanisms underlying ER curvature, application of antibiotic drugs, reveals that ribosomes organized in polysomes might not only correlate with but might have a determining role in ER shape and the regulation of cisternal and tubular compartments (West et al., 2011b, Shibata et al., 2010). Puromycin and cycloheximide are two drugs both inducing translational inhibition but doing so with distinct mechanisms. While puromycin releases the nascent polypeptide chain from the ribosomes and disassembles polysomes from translocons and the ER membrane, cycloheximide inhibits translation without affecting the ribosomes/polysomes. Cell incubation with puromycin resulted in elevated ER tubules and disrupted ER sheets, compared with untreated cells whereas, incubation with cycloheximide did not result in the same phenotype. This indicates that polysomes might regulate ER shape by stabilizing ER sheet construction (Shibata et al., 2010, Puhka et al., 2007).

Cytoskeleton Linking Membrane Protein 63 (CLIMP63 former known as p63), is a 63-kDa type II integral ER membrane protein belonging to the superfamily of coiled-coil (CC) proteins (Schweizer et al., 1993). It localizes exclusively to ER sheets (Foster et al., 2006), embedded in the ER membrane with a single transmembrane-spanning domain. Its cytoplasmic N-terminal region contains a microtubule binding domain (Klopfenstein et al., 1998), while the C-terminus, protruding into the lumen, contains a CC motif. This motif interacts with the CC domains of opposing CLIMP63 proteins to form oligomers and consequently restricts protein mobility. In the process, it assumes a role as luminal spacer and generates, stabilizes and maintains an optimal luminal distance of ≈50 nm by bridging close together the opposing sections of ER membrane (Shibata et al., 2010).

Experiments where CLIMP63 is overexpressed showed a massive proliferation of sheets at the expense of tubules, whereas transcriptional inhibition and thus depletion of CLIMP63 unexpectedly does not affect the number of ER sheets *per se*, but, instead, decreases the luminal distance to ≈30nm, comparable to that observed in lower organisms that lack CLIMP63. Furthermore, overexpression diffuses sheets throughout the cytoplasm, reminiscent of the phenomenon of disorganized translocons, upon puromycin-induced translational inhibition (Shibata et al., 2010). However, the phenotype observed in CLIMP63 depletion experiments does not involve any disorganization of translocons, which were still abundant on ER sheets (Nikonov et al., 2007). Observations for both experimental up- and down-regulation of CLIMP63, therefore indicate that CLIMP63 has a positive role in sheet generation and is critical for the regulation of luminal distance, but that the ratio of sheets to tubules is regulated by a protein network involving additional factors (Schwarz and Blower, 2016).

Along with CLIMP63, two additional membrane proteins are involved in ER sheet formation (Shibata et al., 2010); ribosome-interacting protein p180 and Kinectin. Both proteins are abundant in proliferated ER sheets, and their reciprocal N- and C-terminus orientation in the membrane, compared with CLIMP63, classifies them as type I integral proteins. Moreover, similar to CLIMP63, both proteins include a CC motif at their cytosolic C-terminal region, which enables oligomerization and therefore grants them rod-like scaffolding properties, with a likely role in stabilizing and maintaining the flat surface of the ER sheets. Overexpression experiments of p180 in yeast result in sheet induction, whereas depletion of both p180 and Kinectin does not abolish ER sheets (Shibata et al., 2010). These findings, combined with the observation that all three factors, CLIMP63, p180 and Kinectin, are absent in lower organisms, in contrast to the ubiquitous reticulons and REEPs/Yop1p, imply that the main mechanism for sheet and tubule generation does not rely on both families but only on the latter, while the former merely complements the formation by stabilization and maintenance.

1.1.5 Homotypic fusion

The ER is rearranged dynamically, so that the ratio of tubules to sheets keeps changing in response to developmental and cellular processes, but nonetheless always remains continuous as the result of a phenomenon called homotypic fusion. Homotypic fusion governs the merging of ER membranes whenever they come in contact and maintains ER network continuity, by a mechanism facilitated by several ER-localized GTPases.

ER tubules interconnect throughout the cytoplasm to form a branched network with characteristic three-way junctions. Atlastins (Atls), a conserved dynamin-related GTPase protein family, are specifically localized at these three-way junctions, absent from NE and perinuclear ER as can be seen and confirmed by overexpression experiments (English and Voeltz, 2013). The GTPase activity region is located at the N-terminus of the amino acid sequence, while the C-terminus contains two transmembrane domains in a hairpin shape. There are three paralogs in mammalian cells (ATL1-3), which exhibit tissue-specific expression and regulate ER membrane fusion (Orso et al., 2009). Along with ATLs, their yeast and plant orthologs, Sey1p and DH3, respectively, showed *in vitro* membrane fusion activity indicating their ER role as fusogens (Anwar et al., 2012, Zhang et al., 2013). Furthermore, DH3 depletion experiments in plants resulted in cable-like ER tubules with decreased mobility (Zheng et al., 2004). In yeast, Sey1p depletion decreased the reticulated cortical ER and in turn increased ER sheets (Anwar et al., 2012). Moreover, depletion of ATLs in mammalian cells resulted in unbranched ER (Hu et al., 2009), while in *Drosophila* the phenotype was more severe, as ER appeared fragmented (Orso et al., 2009). Taken together, the phenotypes observed for all four lines of GTPase depletion experiments show an ER tubular network devoid of interconnections and indicates a regulatory role of the ATLs family in three-way junction formation (Westrate et al., 2015, Zhang and Hu, 2016).

Another protein family with members concentrated at three-way junctions is the Lunapark (Lnps) family (Chen et al., 2012). This family is highly conserved among species and localizes to the ER, where it has a role in shape regulation of peripheral ER. Experiments in *S. cerevisiae* have shown that while Atls induce reticulation of cortical ER, Lnps disrupt the shape of the cortical ER network. Moreover, cells not expressing Lnps show a massively increased cortical ER network, resembling the phenotype observed in Atls depletion experiments (Chen et al., 2012). Therefore, these findings suggest that Lnps and Atls act antagonistically with opposing roles in regulating reticulation of the peripheral ER network (Chen et al., 2013, Westrate et al., 2015).

1.2 Transmembrane Protein 147

The Human Transmembrane Protein 147 (TMEM147), also known as NIFIE14, is a small protein that localizes at the endoplasmic reticulum (Dettmer et al., 2010, Rosemond et al., 2011). Its gene locus resides on the large arm of chromosome 19 (19q13.12) in *Homo sapiens,* consisting of seven exons which, through alternative splicing, give rise to multiple isoforms (NCBI-AceView, 2021, February 10), three of which have been validated in the Gene database of NCBI (Gene ID: 10430) (NCBI, 2021, November 9). The most abundant of the latter three in-frame isoforms, is also the largest and translates to a 224 amino acid (aa) protein of 26.2 kDa (see Table 1.1 and Fig. 1.1-3).

H. sapiens	**mRNA**	**Protein**	**Accession number**	**Info**
Isoform-1	868 nt	224 aa	NP_116024.1 NM_032635.4	
Isoform-2	939 nt	175 aa (aa 50-224)	NP_001229526.4 NM_001242597.2	Compared with isoform-1, has truncated N terminus and identical C terminus by inclusion of an additional exon in its extended 5′UTR initiating translation at a downstream, in-frame start codon
Isoform-3	646 nt	150 aa (aa 1-70/144-224)	NP_001229527.1 NM_001242598.2	Compared with isoform-1, has identical N and C terminus but lacks two consecutive exons in the coding region; shortest isoform

Table 1.1: TMEM147 isoforms in H. sapiens
Sequence comparison of the most abundant TMEM147 isoforms in H. sapiens; nt – nucleotides; aa – amino acids.

TMEM147 has 7 transmembrane domains that each fully span the ER membrane, with its N-terminus facing the ER lumen and the C-terminus facing the cytosol (Fig. 1.4) (McGilvray et al., 2020). The *TMEM147* gene is highly conserved among mammals and its expression in many tissues (Ensembl, 2021) suggests an important role in organism's physiology, whereas the sequence similarity of TMEM147 in human, mouse, rat, and bovine species is up to 99% (Rosemond et al., 2011, Dettmer et al., 2010).

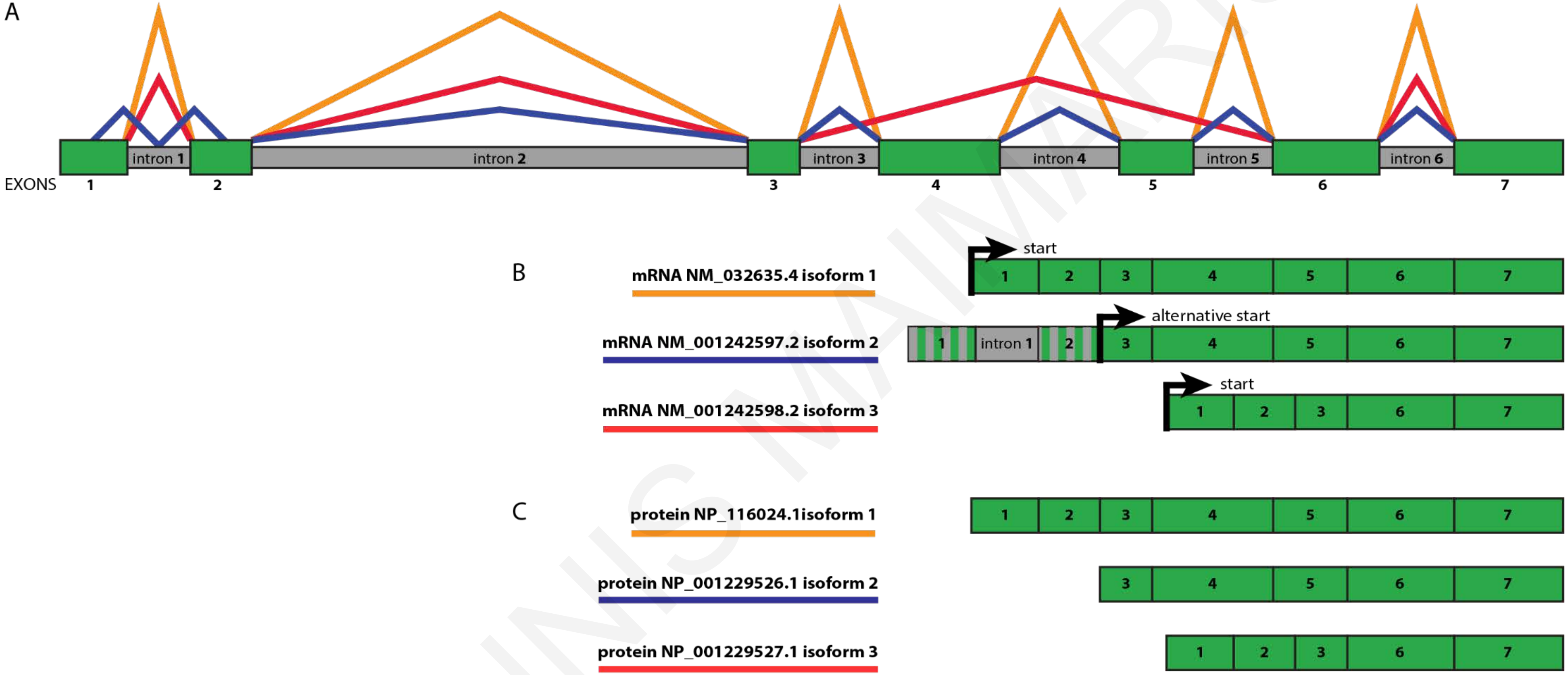

Figure 1.1: The three main alternative splicing isoforms of TMEM147 gene.

(A) Diagram of the three main alternative splicing isoforms of TMEM147 gene. (B) The corresponding three main transcript isoforms of TMEM147. (C) The three main protein isoforms corresponding to the mRNA isoforms. Color codes: green: exons; gray: introns; orange, blue and red lines: indicate the corresponding three alternative splice events transcripts and protein isoforms of TMEM147.

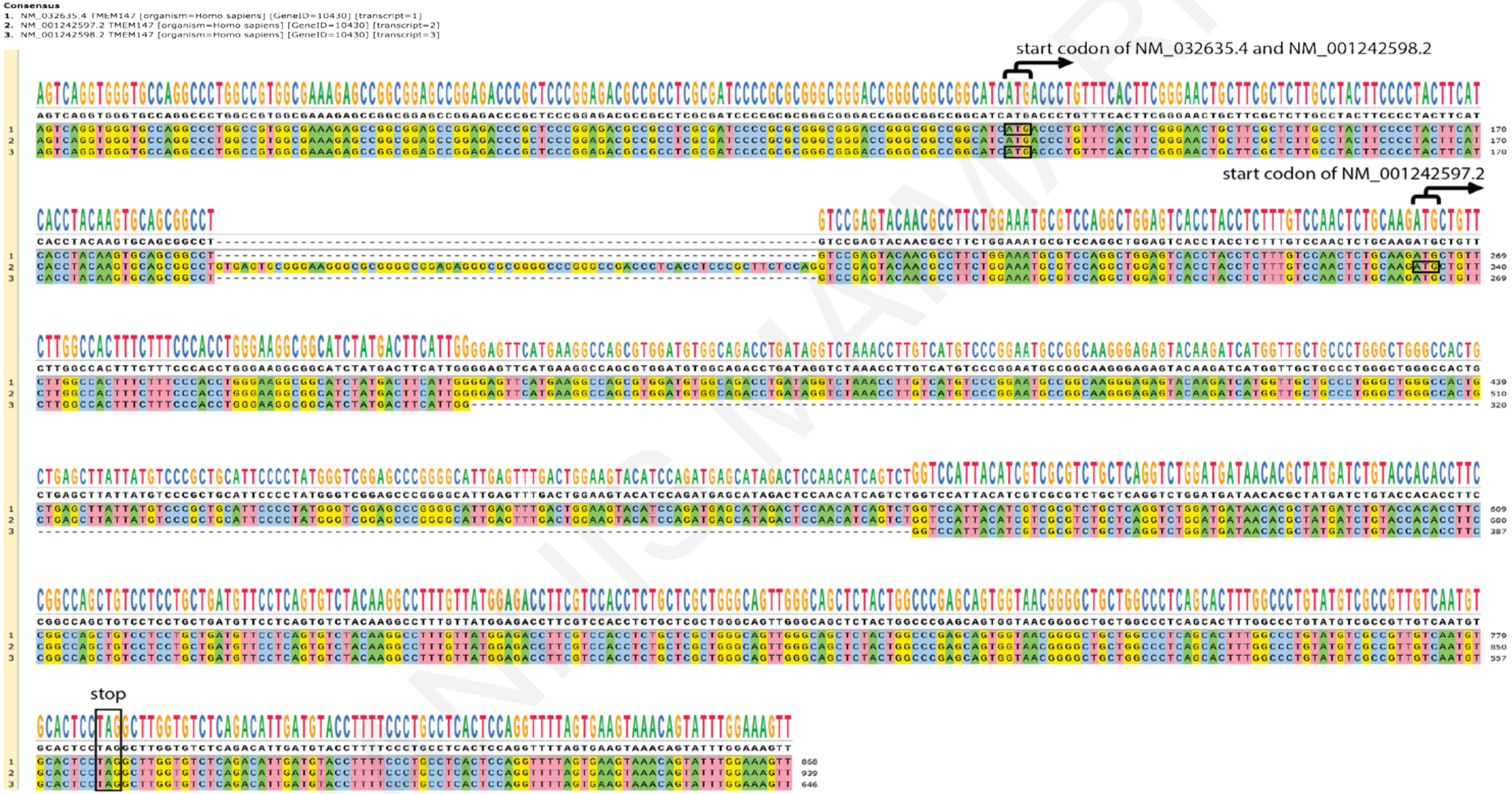

Figure 1.2: Alignment of RefSeq cDNA sequences for the three main TMEM147 splice variants

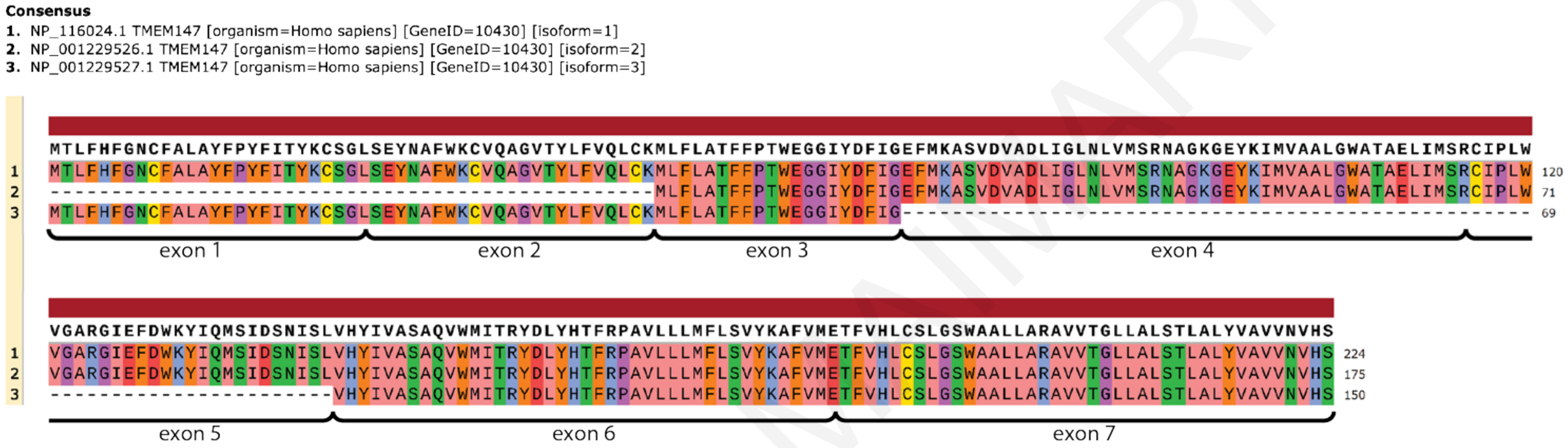

Consensus

1. NP_116024.1 TMEM147 [organism=Homo sapiens] [GeneID=10430] [isoform=1]
2. NP_001229526.1 TMEM147 [organism=Homo sapiens] [GeneID=10430] [isoform=2]
3. NP_001229527.1 TMEM147 [organism=Homo sapiens] [GeneID=10430] [isoform=3]

```
  MTLFHFGNCFALAYFPYFITYKCSGLSEYNAFWKCVQAGVTYLFVQLCKMLFLATFFPTWEGGIYDFIGEFMKASVDVADLIGLNLVMSRNAGKGEYKIMVAALGWATAELIMSRCIPLW
1 MTLFHFGNCFALAYFPYFITYKCSGLSEYNAFWKCVQAGVTYLFVQLCKMLFLATFFPTWEGGIYDFIGEFMKASVDVADLIGLNLVMSRNAGKGEYKIMVAALGWATAELIMSRCIPLW 120
2 -------------------------------------------------MLFLATFFPTWEGGIYDFIGEFMKASVDVADLIGLNLVMSRNAGKGEYKIMVAALGWATAELIMSRCIPLW 71
3 MTLFHFGNCFALAYFPYFITYKCSGLSEYNAFWKCVQAGVTYLFVQLCKMLFLATFFPTWEGGIYDFIG--------------------------------------------------- 69

  VGARGIEFDWKYIQMSIDSNISLVHYIVASAQVWMITRYDLYHTFRPAVLLLMFLSVYKAFVMETFVHLCSLGSWAALLARAVVTGLLALSTLALYVAVVNVHS
1 VGARGIEFDWKYIQMSIDSNISLVHYIVASAQVWMITRYDLYHTFRPAVLLLMFLSVYKAFVMETFVHLCSLGSWAALLARAVVTGLLALSTLALYVAVVNVHS 224
2 VGARGIEFDWKYIQMSIDSNISLVHYIVASAQVWMITRYDLYHTFRPAVLLLMFLSVYKAFVMETFVHLCSLGSWAALLARAVVTGLLALSTLALYVAVVNVHS 175
3 -----------------------VHYIVASAQVWMITRYDLYHTFRPAVLLLMFLSVYKAFVMETFVHLCSLGSWAALLARAVVTGLLALSTLALYVAVVNVHS 150
```

Figure 1.3: Alignment of RefSeq protein sequences for the three main TMEM147 protein isoforms

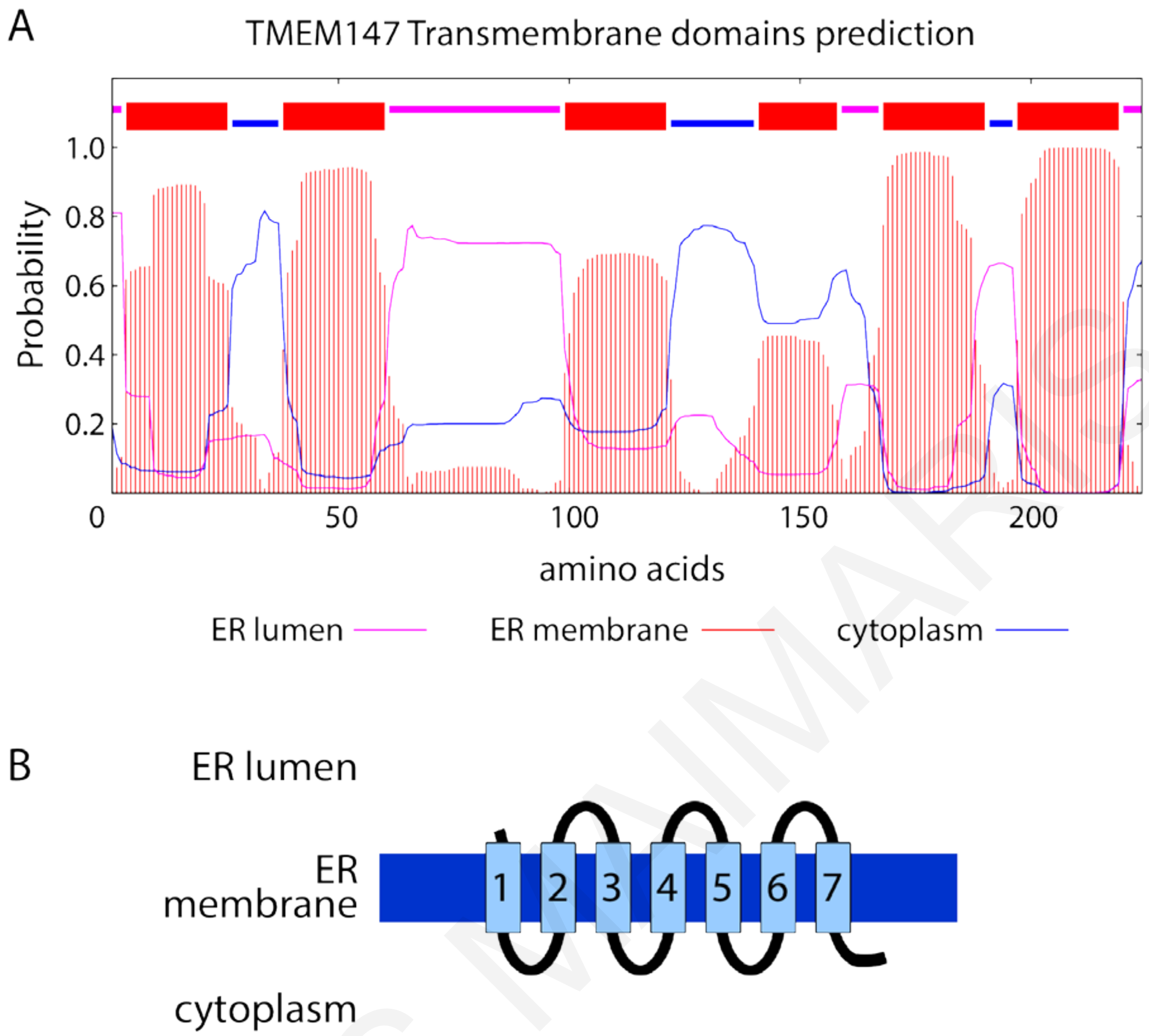

Figure 1.4: Prediction of TMEM147 transmembrane domains.
(A) TMEM147 transmembrane domains as predicted by the TMHMM program (TransMembrane prediction using Hidden Markov Model). (B) Topology model of TMEM147 (Krogh et al., 2001)

TMEM147 interacts with the M3 muscarinic acetylcholine receptor (M3R) as well as with other class-I GPCRs, like Vasopressin-2 receptor and M1 muscarinic acetylcholine receptor (M1R). Expression of TMEM147 in COS-7 cells not only inhibits trafficking of the receptor to the cell surface, but impairs its function as well, resulting in reduced levels of Ca^{2+}, upon induction with the muscarinic agonist carbachol, compared with control cells. Silencing of TMEM147 in colon cancer cells H508, where TMEM147 and the M3R are co-expressed normally, causes an increase of the receptors on the cell surface along with an increase of the overall properly folded receptors. Therefore, TMEM147 is implicated not only in trafficking but also in proper folding of M3R (Rosemond et al., 2011).

In parallel to the Rosemond et al., 2011 research, TMEM147 was shown to be a core component of the Nicalin-NOMO complex (Dettmer et al., 2010). The Nicalin-NOMO complex modulates the NODAL signal transduction pathway, which controls the early embryonic development in *Zebrafish* (Haffner et al., 2007). The purified protein complex has a molecular mass (200-220 kDa) that exceeded the calculated addition of the individual molecular masses of the already known complex components, Nicalin (60 kDa) and NOMO (130 kDa). This discrepancy was explained when the team successfully purified from the complex a small 26 kDa protein that was co-selected with Nicalin. MS analysis identified this protein as TMEM147 which was co-selected upon immunoprecipitation of both NOMO and Nicalin. Further analysis of TMEM147 and its interacting partners showed that all three are localized to the ER and in contrast to Nicalin and NOMO, TMEM147 is not a glycoprotein in agreement with the absence of any N-glycosylation motifs present in its sequence. Furthermore, depletion of either of the three complex components using RNA interference, showed that the other two were also downregulated destabilizing the complex formation. Additionally, this complex instability is restricted at the protein level as further analysis using quantitative real-time PCR revealed that the mRNA levels of the proteins were not affected. This observation was confirmed for any of the three complex component proteins, indicating that the expression level modifications occur at the posttranslational level. Moreover, overexpression experiments of these proteins revealed that, the protein levels of NOMO and TMEM147 are regulated by the expression of the Nicalin and stabilized upon complex formation indicative of a posttranslational regulatory mechanism as each protein mRNA levels remained unaffected (Dettmer et al., 2010).

1.3 Lamin B Receptor

1.3.1 Introduction

As mentioned above, the ER membrane network system encompasses the outer NE, which separates the nuclear content from the rest of the cytoplasm. This compartmentalization, along with organization of nuclear functions such as gene regulation and chromosomal replication, define the NE not only as a spatial separation structure distinguishing the nucleoplasm from cytoplasm but also as an essential nuclear function structure. Specifically, NE comprises of the outer nuclear membrane, decorated with ribosomes as it is an extension of the ER cisternae membrane, and the inner nuclear membrane making the perinuclear space a continuity with the ER lumen. Furthermore, INM and ONM fuse together at the nuclear pores, through which nuclear localization signal harboring proteins can traffic between the nucleoplasm and the cytoplasm.

The NE has been studied extensively and integral membrane proteins spanning the INM have been identified to play a crucial role in the stabilization of the meshwork of intermediate filament lamin layers inside the NE, referred to as the nuclear lamina, where heterochromatin is anchored and regulated. Such an integral membrane protein, is the receptor of lamin B, LBR, a protein interacting specifically with lamin-B protein (in contrast to lamin-A), the chromatin and the heterochromatin associated proteins HP1 and MeCP2 (Makatsori et al., 2004, Pyrpasopoulou et al., 1996, Worman et al., 1988).

LBR is widely expressed in all vertebrates, including some deuterostomes (Olins et al., 2010) and the human homologue is 68% identical to chicken LBR. Human LBR is a polytopic integral protein that comprises of 615 aa residues as a translational product of 13 exons. Furthermore, these exons can be divided in two groups consisting of exons 1-4, termed as the N-terminal region, and 5-13 termed as the C-terminal region. An interesting aspect is that LBR is considered a chimeric protein because exons 4 and 5 are separated by an abnormally long intron. This implies that the LBR gene might be an evolutionary fusion result of two primordial genes. Moreover, evidence of the functional divergence between N-terminal (1-4 exons) and C-terminal (5-13 exons) regions hosting two discreet activities are in agreement with the fusion evolutionary event theory (Schuler et al., 1994, Ye and Worman, 1994).

1.3.2 N-terminal region of LBR

The N-terminal region, derived from exons 1-4, translates to 208 aa, allocating basic and hydrophilic attributes to the region, and can be divided into three segments: a hinge of 40 highly charged residues linking two globular conformations; the first spanning the first 60 aa and the second the 1ast 108 aa (Schuler et al., 1994). Furthermore, hinge-containing serine and threonine residues were proven to be substrates for two protein kinases regulating the binding affinity for lamin B, hence the stability of the lamina and therefore, the integrity of the NE. Experiments discerning the phosphorylation state of the N-terminal LBR region during interphase or mitosis, showed that PKA was found to phosphorylate serine residues during interphase stabilizing the interaction, whereas dephosphorylation of these sites resulted in destabilization (Appelbaum et al., 1990). Additionally, during interphase, hence stable LBR-lamin B interaction, a member of the cycle dependent kinase family (CDK1), p34^{cdc2} phosphorylates specific serine residues whereas different phosphorylation profiles including both serine (different than the previous sites) and threonine residues in particular thr^{188}, were present in mitosis, reducing the interaction and promoting the disassembly of NE (Courvalin et al., 1992).

Moreover, although the phosphorylation state of thr^{188} is a marker of the LBR binding affinity for lamin-B, along with other specific sites particularly in the 61-89 aa segment (RS domain, see later), the integrity of the N-terminal domain is crucial for this interaction. This has been demonstrated by Ye and Worman when, in an attempt to map the Lamin-B binding site on LBR N-terminus, they constructed three GST-fused truncated versions of its N-terminal domain comprising 2-71, 2-100, and 72-216 aa residues. These constructs, when immobilized on glutathione-sepharose resin, under non-denaturing conditions, failed to co-select lamin-B, in contrast to a full length N-terminal construct (Ye and Worman, 1994). This clearly suggests that inherent conformational properties of the N-terminal region are necessary for lamin-B interaction and binding.

Whereas the presence of the entire N-terminal region is essential for lamin B binding, chromatin tethering is constrained to specific regions of the LBR. The first and most important region is the Tudor domain (Lu and Wang, 2013, Maurer-Stroh et al., 2003) comprised of the first 60 aa residues forming a β-barrel-like structure (Yoneyama, 2006, Liokatis et al., 2012). This methyl-lysine binding domain in LBR resembles the one found in the mammalian DNA repair factor 53BP1 (Olins et al., 2010) which binds to the dimethylated

Lys 20 residue of histone 4 (H4K20me2) shown to induce transcriptional silencing by chromatin compaction (heterochromatin) (Hirano et al., 2012).

In addition to the Tudor domain, the hinge domain is equally crucial for the chromatin binding. This 40 aa-region, without any obvious structural organization, encompasses an arginine/serine rich (RS-rich) domain, and its phosphorylation state regulates the interaction between LBR and lamin B. In general, RS-rich motifs are present in proteins with a role in RNA polymerase II transcription, pre-mRNA splicing and nuclear translocation and export (Long and Caceres, 2009, Boucher et al., 2001). Experiments employing truncated LBR constructs, lacking either the Tudor or RS-rich domain, have shown that both domains are required for chromatin tethering and immobilization on the NE as a reduced chromatin binding and an elevated diffusional mobility at the NE has been observed related to these LBR constructs (Hirano et al., 2012, Liokatis et al., 2012).

Regarding the functional status of the chromatin in gene expression, as previously mentioned, Hirano et al., have shown that Tudor interacts with H4K20me2 promoting the repression of the transcription by chromatin compaction. Furthermore, chromatin retainment at the periphery of nucleus also induces transcriptional repression (a localization that is consequently driven by LBR interaction) (Andrulis et al., 1998). Additionally, this repression is contributed also by other transcriptional modulators and repressors, such as the aforementioned HP1 and MeCP2 that have been found to interact with LBR. The latter interacts specifically with both Tudor and RS-rich domains (Guarda et al., 2009) while the strong transcriptional repressor HP1 binds to the last segment of the N-terminal domain (last 108 aa) forming the second globular domain (Lechner et al., 2005).

In conclusion, the N-terminal domain of LBR not only serves as a platform for the organization of the lamina meshwork but also anchors chromatin to the periphery inducing compaction and transcriptional silencing by recruiting transcriptional modulators and blocking the binding of transcriptional factors.

1.3.3 C-terminal region of LBR

The C-terminal region derived from exons 5-13, translates to 407 aa with interesting and unexpected attributes for an INM protein. It has been proposed that this sequence, spanning from residue 209 to 615 integrates the protein to the INM with 8 to 10 transmembrane segments, hence its tail either protrudes the nucleoplasm (8 and 10 transmembrane domain versions) or the lumen i.e. the perinuclear space between INM and ONM (9 transmembrane domain version) (Fig. 1.5) (Olins et al., 2010, Tsai et al., 2016). The topological differences concern the middle section and the terminal part of the C-terminal domain. The various TM prediction tools consent only for the first four domains whereas the fifth domain of the 8 TM model appears as two domains for both 9 and 10 TM models. Furthermore, all three predicted models agree for the next two TM domains while the last domain of both 8 and 9 TM models appears as two domains in the 10 TM model (Fig. 1.5).

Despite this disagreement in conformation, the findings of Schuler and Worman in their first LBR sequence analysis back in 1994 is what makes the C-terminal of LBR interesting. They found that this INM protein has 42% sequence similarity with ERG24, a C-14 sterol reductase protein from yeast, implicated in the synthesis of ergosterol, the predominate cholesterol analog in fungi and protozoa, a cellular function compartmentalized specifically to ER membranes (Schuler et al., 1994). The same group in other work analyzing the human genome, found two paralogs of LBR regarding its C-terminal domain, TM7SF2 and DHCR7 (Holmer et al., 1998). Both paralogs are also sterol reductases present in the late, post-squalene, steps of the cholesterol biosynthesis which are localized at the ER. The C-terminus of LBR shares 58% sequence similarity with TM7SF2 while 75% of the residues are conserved, whereas compared with DHCR7, it shows a sequence similarity up to 37% and 62% conservation.

A more detailed sequence similarity analysis of this region with specific motifs, revealed that it comprises two short characteristic motifs that are common between many sterol reductases. These motifs termed, “sterol reductase family signatures 1 and 2” are both present in ERG24 and ERG4 in yeast and the human TM7SF2 and DHCR7. The first signature spans from 362 to 377 aa and the second from 573 to 602, positions that either reside in the nucleoplasm in the 8 and 10 TM-segment conformation, or the first in the nucleoplasm and the second in the lumen in the 9-TM version (Olins et al., 2010). Due to this sequence similarity, LBR has been proposed to have sterol reductase activity and has been shown to rescue ergosterol deficiency in *S. cerevisiae* strains lacking the sterol reductase ERG24 (Silve et al., 1998). Additionally, C-terminal mutant LBR constructs when transfected in cholesterol deficient HeLa cells did not succeed to restore cholesterol auxotrophy, proving the sterol reductase activity of the LBR (Tsai et al., 2016). A more detailed reference on how LBR and its reductase paralogues, TM7SF2 and DHCR7 are implicated in cholesterol metabolism, follows in the next section.

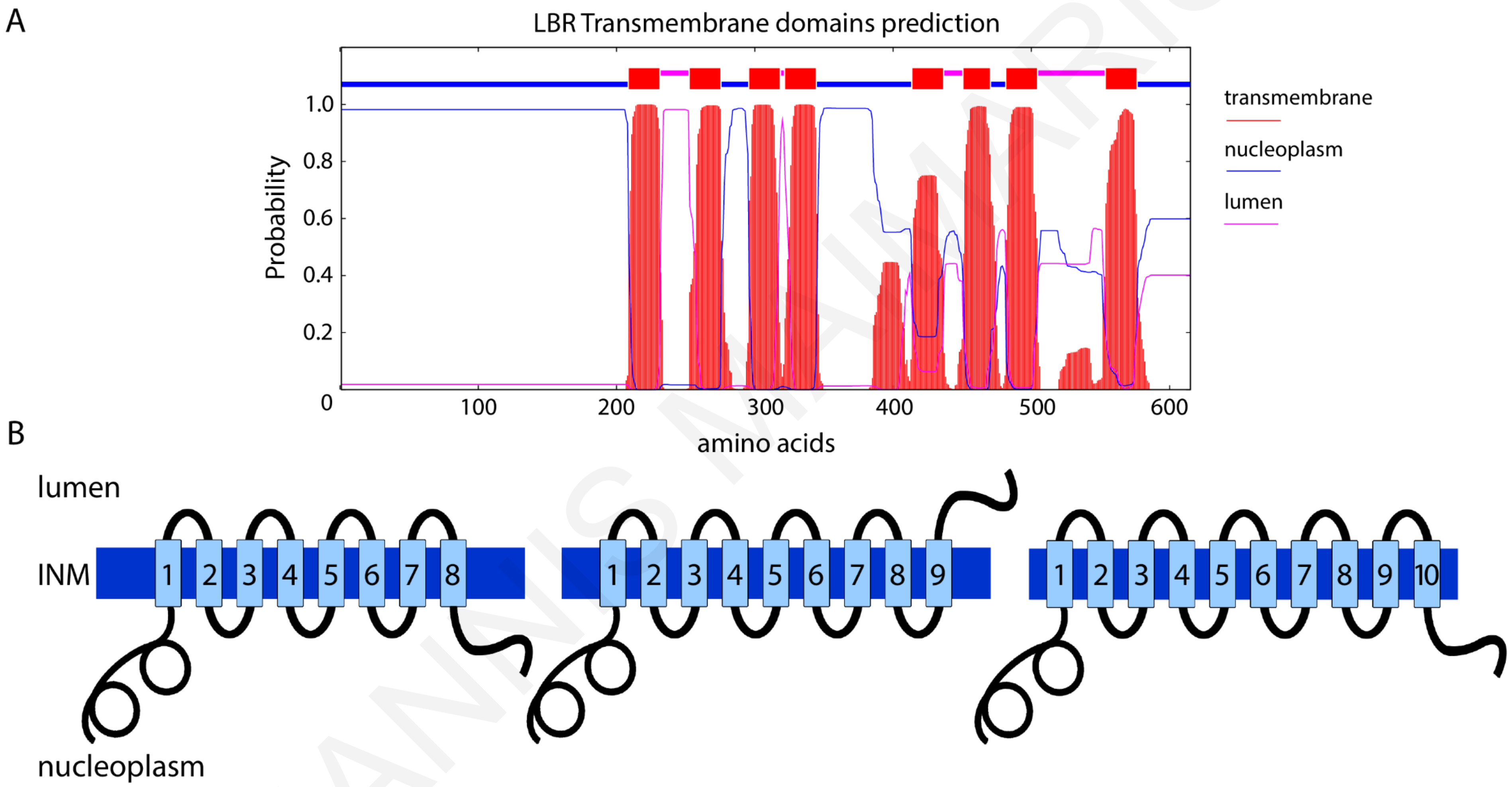

***Figure 1.5*: Prediction of TMEM147 transmembrane domains.**
(A) LBR transmembrane domains as predicted from TMHMM program (TransMembrane prediction using Hidden Markov Model). (B) Topology of the three LBR predicted models (Krogh et al., 2001).

1.4 Cholesterol Homeostasis

1.4.1 Introduction

The discovery of cholesterol dates back to 1769; François Poulletier de la Salle first isolated solid cholesterol from gallstones and in early 18th century it was named as “cholesterine” by Michel Eugène Chevreul (1815) who rediscovered this important lipid. Since, an enormous amount of literature has been published and more than 11 Nobel Prizes have been awarded to cholesterol researchers like Konrad Emil Bloch and Feodor Lynen in 1964 for their work on cholesterol biosynthesis and fatty acids metabolism, or Michael S. Brown and Joseph L. Goldstein in 1985 for their work on the regulation of cholesterol metabolism (Brown and Goldstein, 1984, Endo, 2010).

Cholesterol is a major structural component of cell plasma membrane and interacting with adjacent lipids, regulates fluidity, rigidity and permeability of the lipid bilayer. Additionally, it interacts with transmembrane proteins contributing to their conformational maintenance and activity. Furthermore, interacting with sterol transport proteins, it mediates its own trafficking and regulates its subcellular distribution (Luo et al., 2019b). Cholesterol is also required for the formation of the myelin sheath insulating neuronal axons and allowing a faster electrical signal transport (Jurevics and Morell, 1995). Finally, it serves as a precursor molecule for the synthesis of bile acids and bile salts, Vitamin D and several steroid hormones in adrenal and sex glands in both male and female (Cerqueira et al., 2016).

1.4.2 Cholesterol Biosynthesis

As a chemical compound, it consists of 27 carbons, organized in four fused non-aromatic rings comprising the “steroid nucleus”, a polar hydroxyl group at C3, oriented towards the polar heads of membrane phospholipids and an aliphatic side-chain at C17, oriented towards the membrane’s phospholipid fatty acid chains. Biosynthesis of cholesterol relies on a series of more than 20 reactions, employing numerous ER transmembrane enzymes and a multi-level regulation machinery. In summary, three activated acetic-acid (acetyl-CoA) molecules are fused to the 3-hydroxy-3-methylglutaryl-CoA (HMG-CoA) and this is reduced to mevalonic acid catalyzed by the HMGC-reductase (HMGCR). Downstream the pathway, farnesyl diphosphate is produced and converted to the linear 30-carbon unit compound of squalene. Squalene is then cyclized and forms lanosterol which ultimately converts to cholesterol. Starting from lanosterol, formation of cholesterol can follow two pathways. It either follows the Bloch pathway, via desmosterol production, and then reduced to cholesterol or it follows the Kandutsch-Russel pathway, producing the 7-dehydrocholesterol which is also reduced to cholesterol (Cerqueira et al., 2016).

The enzymes participating in cholesterol biosynthesis are transmembrane proteins localized to the ER, therefore, the initial notion was that cholesterol biosynthesis was held in the ER (Reinhart et al., 1987). This is in contrast to the localization of acetyl-CoA, the initiative synthesis molecule found in the cytoplasm after exiting mitochondria. More recent detailed topological and structural studies on these enzymes have revealed that biosynthesis of cholesterol occurs both in the cytoplasm and the membranes of the ER. Namely, cytoplasmic reactions are performed in close proximity to the membranes of ER as enzymes are embedded in it and particularly those participating in steps leading to farnesyl pyrophosphate formation. The production of squalene from two molecules of farnesyl pyrophosphate is the key step of this membranous internalization, which is catalyzed by the squalene synthase (SQS). SQS binds the two farnesyl molecules from the cytoplasm on its cytoplasmic domain and releases them as squalene within the membrane (Cerqueira et al., 2016). From this step onwards, all reactions are held in the ER membrane where cholesterol is intertwined with other lipids in the bilayer. This stepwise transition of the biosynthetic reaction site is consistent with the gradually increased hydrophobicity of the molecules produced during cholesterol synthesis. Specifically, the long carbohydrate chain of squalene and the four-ring carbohydrate-core of lanosterol sharply raise the hydrophobicity of these molecules compared with their predecessors in the pathway.

Interestingly, among the enzymes catalyzing the cholesterol biosynthesis are two reductases that exhibit, as already mentioned, extensive sequence similarity and identity with the C-terminal region of LBR (see section 1.3.3). These reductases are TM7SF2 and DHCR7; LBR can compensate for the depletion of TM7SF2 in cholesterol biosynthesis. More details on these two reductases are discussed later in this section.

1.4.3 Regulation of the pathway

Regulation of this biosynthetic pathway is very strict as this process consumes large amounts of acetyl-CoA, NADPH and energy, all vital for cell living. This regulation includes both transcriptional and post-translational regulators. The expression of almost all the participating enzymes (LBR is excluded) is under the regulation of the sterol regulatory element binding protein 2 (SREBP2), which binds on the respective domain of their gene promoter upregulating their transcription keeping the pathway active. SREBP2 is a transmembrane protein, resident of ER membranes and when, membrane cholesterol levels are limited, it interacts with SREBP cleavage-activating protein (SCAP), another ER protein. The complex is further transported from the ER to Golgi via COPII-coated vesicles where SREBP2 is cleaved by proteases S1P and S2P to the activated transcription factor. The cleavage-activated SREBP2 is then transferred to the nucleus where it binds to the SRE promoter sequence and upregulates the transcription of the targeted enzyme gene. In contrast, when membrane cholesterol levels are substantial, cholesterol interacts with the sterol sensing domain (SSD) of SCAP which is embedded in the transmembrane domains, inducing such conformational changes that SCAP interacts with an insulin induced gene (INSIG) protein which further blocks the COPII binding to SCAP. Thus, the transport of SREBP2-containing vesicles to Golgi for proteolysis and transcription factor activation is impaired.

Another important enzyme that is tightly regulated in cholesterol biosynthesis is the rate-limiting enzyme HMGCR. Regulation of this reductase is at the post-translational level and facilitated via mediated degradation or phosphorylation. When cholesterol is in excess, accumulation of intermediate metabolites, like oxysterols and lanosterol, induces the interaction between HMGCR transmembrane domain and INSIG (Sever et al., 2003b). This interaction triggers the ubiquitylation and its extraction from the ER membrane, which is then degraded by the proteasomal as a response to the ER-associated degradation (ERAD) pathway (Sever et al., 2003a). Although HMGCR transmembrane domains host an SSD, sensitivity to cholesterol levels does not promote impaired activity (Song et al., 2005). The same enzyme is also regulated via phosphorylation. When ATP levels are low, AMP-activated protein kinase (AMPK), is activated and phosphorylates the catalytic domain of HMGCR which resides at the C-terminal region and particularly it phosphorylates the last serine residue resulting in disruption of its activity (Istvan et al., 2000). In contrast, when ATP levels are restored and cholesterol synthesis can proceed, then AMPK is deactivated and the HMGCR activity is once again restored, enabling cholesterol synthesis to proceed (Soto-Acosta et al., 2017).

1.4.4 Cholesterol uptake

Although cells can synthesize cholesterol *de novo*, when the “demand exceeds production”, a different mechanism is employed resulting in a rapid increase of intracellular cholesterol levels. This mechanism exploits uptake of cholesterol from the extracellular repository. Esterified cholesterol is accumulated in low-density lipoprotein (LDL) particles surrounded by a spherical monolayer of phospholipids and an embedded protein named apolipoprotein-B. This LDL particle is recognized by a dedicated glycoprotein receptor termed LDLR which is under the transcriptional regulation of SREBP2. When bound together, they diffuse over the plasma membrane recruiting the adapters ARH and DAB2, before a specific four-residue cytoplasmic sequence of the receptor is associated with AP2 and clathrin, residing at particular regions of the plasma membrane. Thus, ligands and receptors are accumulated at these regions and therefore are internalized in increased amounts. Internalization occurs via a mechanism well described by Goldstein and Brown in the 80s, termed receptor-mediated endocytosis, whereby clathrin-coated pits are rapidly pinched-off forming clathrin-coated vesicles inside the plasma membrane. For this work both researches were awarded the Nobel prize in 1985 (Goldstein and Brown, 1985, Goldstein et al., 1982, Goldstein and Brown, 2009). Intracellularly, these vesicles abolish their clathrin coat and then fuse with early endosomes residing under the plasma membrane. The low pH of the endosomes dissociates the bound LDL particles from their receptors and the latter are then recycled to the plasma membrane. These late endosomes containing free LDLs fuse with lysosomes (LE/LY) where cholesteryl esters are hydrolyzed by acid lipase releasing free cholesterol. Furthermore, membrane proteins of the LE/LY Niemann-Pick type C1 (NPC1), NPC2 and the lysosome-associated membrane glycoprotein 2, absorb the free cholesterol in the membrane bilayer. From this repository, the free cholesterol is subsequently delivered to other membranes that are in need of cholesterol (Luo et al., 2017, Kwon et al., 2009, Luo et al., 2020).

1.4.5 Cholesterol transport

Cholesterol, as mentioned earlier, is a common membrane structural component of all intracellular organelles and must be transported there from its accumulation sites; the ER membranes or the fused LE/LY. Transportation mainly occurs in a non-vesicular way. This means, that upon cholesterol formation, either employing *de novo* synthesis or after LDL cholesterol esters hydrolysis, no vesicles are utilized for sterol transport. Transportation is mediated directly through the membranes under the condition that the organelles are very close to each other. These specialized at close proximity membrane regions are kept at 30 nm apart and they are termed membrane contact sites (MCSs). Such MCSs are observed between fused LE/LY and the membranes of the ER, peroxisomes, mitochondria and the Golgi, and between the membranes of ER and endosomes, the Golgi and mitochondria. Furthermore, MCSs are dynamically regulated and some of them appear to be stable over time, whereas others are transient (Helle et al., 2013, Prinz, 2014).

Allocated to these sites are specialized proteins called sterol transfer proteins (STPs) that mediate cholesterol transportation directly from one membrane to the other. STPs can mainly be divided in three families. The first is oxysterol-binding protein and -related protein family (OSBP, ORP), the second is steroidogenic acute regulatory protein, -related lipid transfer and -related domain protein family (StAR, START, STARD), and the third is the lipid transfer proteins anchored at a membrane contact site family (Lam). The interaction of the cholesterol molecule and these STPs occurs in a hydrophobic pocket of their structure (Wong et al., 2017) and the transportation passively follows the cholesterol concentration gradient. If cholesterol needs to be transported from low concentration to high, then a coupled-transfer of a second molecule provide the driving force for the counter-gradient cholesterol transportation. Such an auxiliary coupled-transfer is the transportation of PI4P when OSBP or Osh4p deliver cholesterol from ER to the Golgi (Maxfield and Menon, 2006, Chung et al., 2015). Furthermore, STPs not only mediate the transportation but also contribute to the maintenance of the MCSs. Additionally to the hydrophobic pocket and the transportation activity, some STPs comprise domains that mediate the tethering of the two membranes and some of them have membrane-targeting domains that anchor to specific organelle-membranes, suggesting that there is specificity among STPs and organelle MCSs (Luo et al., 2019a, Eisenberg-Bord et al., 2016, Helle et al., 2013, Prinz, 2014).

1.4.6 Cholesterol efflux

Despite the mechanism driving the cholesterol accumulation in ER membranes (*de novo* biosynthesis or extracellular uptake), excess of free cholesterol is toxic to the cells. Excessive cholesterol, depletes the calcium stores in the ER lumen and, as a consequence, programmed cell death is mediated via the unfolded protein response (UPR) (Zhang and Kaufman, 2003). In the absence of a catabolic cholesterol pathway, the answer to this toxicity is the complete removal of excessive cholesterol from within the cell, termed as cholesterol efflux or the esterification of cholesterol to cholesteryl esters which are non-toxic and can be stored intracellularly.

Cholesterol efflux is facilitated via the plasma membrane and cholesterol must first be transported to this external cell barrier before being released. It has been found that four mechanisms facilitate this exchange of cholesterol with the extracellular medium and all implicate high-density lipoprotein (HDL) particles as the cholesterol acceptor (Bates and Rothblat, 1974). Two pathways use the concentration gradient of cholesterol while the other two are ATP-dependent. The first mechanisms, exploit the limited water solubility of cholesterol molecules to desorb-off the plasma membrane. This activated-cholesterol (partially protruding) is afterwards released and absorbed by the HDL particles (Phillips et al., 1987). While this is the principle on which the mechanism of simple diffusion (aqueous diffusion) works, the second mechanism has some differences. This facilitated diffusion, is mediated by a bidirectional channel, the scavenger receptor class-B, type-I (SR-BI) protein and thus cholesterol efflux direction is determined by the ratio of cholesterol to phospholipids of the implicated plasma membrane and HDL particle. Additionally the size of the HDL particles bound on SR-BI and their extracellularly concentration is a second parameter accounting for this mechanism (de la Llera-Moya et al., 1999, Thuahnai et al., 2004). The two active mechanisms employ two members of the ATP-binding cassette (ABC) protein family, ABCA1 and ABCG1. ABCA1 transporter, upon ATP binding on its cytoplasmic domain, changes its transmembrane domain conformation creating an opening in the membrane to the extracellular region leading to cholesterol efflux, which is then absorbed by HDL. Additionally, along with cholesterol efflux, ABCA1 facilitates the translocation of phospholipids as well; therefore, along with cholesterol, phospholipids can also be transferred to lipid-free apolipoprotein-A1 (Smith et al., 2004, Gillotte et al., 1998). The second transporter, ABCG1, facilitates cholesterol efflux by mediating increased simple diffusion. While the ATP-activated transporter leads to cholesterol accumulation in the plasma membrane, at the same time the increased concentration gradient of cholesterol leads to increased passive diffusion and, hence, absorption from the HDL increases accordingly (Phillips, 2014, Sankaranarayanan et al., 2009).

1.4.7 Storage of cholesterol

The esterification of free cholesterol is facilitated by acyl-CoA:cholesterol acyltransferaces (ACATs) and esters are initially stored in the membranes of ER. While cholesterol esters accumulate in the lipid bilayer of the ER, the outer leaflet starts to protrude to the cytoplasm. This increasing protrusion event gradually leads to the biogenesis of a distinct organelle termed Lipid Droplets (LDs) (Cohen, 2018, Farese and Walther, 2009). LDs have been found in all cell types and comprise an extremely hydrophobic core where cholesterol esters are stored along with triglycerides while they are surrounded by a monolayer of phospholipids with their hydrophilic heads oriented to the surface of the droplet (like LDL particles). These organelles are characterized by a lifecycle that includes biogenesis, maturation and turnover when cholesterol is needed, whereas events of fusion or fission are also present (Thiam et al., 2013, Hashemi and Goodman, 2015). Biogenesis of LDs starts from ER and follows a budding like mechanism where, in mammalian cells, leads to complete separation from the ER membranes in contrast to yeast (Wilfling et al., 2013, Soni et al., 2009). Cells contain different types of LDs that can be discerned in populations, depending on their lipid and associated protein content. Furthermore, protein content has been associated with the size of LDs. Particularly, perilipin protein family members are present in all LDs but Plin3, Plin2 and Plin1 members are constrained between small, medium and large LDs respectively (Wolins et al., 2005). These differences make the idea of maturation process during their lifecycle more attractive. During cell life, and specially under stress conditions, the need of extra energy or fast supply of structural materials in not uncommon and LDs can provide both, either by turnover or breakdown. Depending on the cell type, LDs content can be hydrolyzed by cytoplasmic lipases or can be degraded by a specialized autophagy mechanism termed lipophagy (Singh et al., 2009, Zechner et al., 2017).

1.4.8 TM7SF2 in cholesterol homeostasis

TM7SF2 is a 3 β-hydroxysterol Δ-14 reductase, catalyzing the C-14 unsaturated bond of lanosterol in the pathway of cholesterol biosynthesis (Lemmens et al., 1998). It is a transmembrane protein and resides at the ER membranes as the majority of enzymes involved in cholesterol biosynthesis. Its expression is regulated by cellular cholesterol levels via a sterol regulatory element, SRE. The SRE consensus sequence is absent from the LBR, hence cellular cholesterol levels do not regulate its expression levels rendering the protein as constitutively expressed (Tsai et al., 2016, Bennati et al., 2006a).

To pursue the function of TM7SF2 and LBR, a C-14 reductase from *Neurospora crassa* was employed. ERG3 is involved in ergosterol biosynthesis and exhibits 40% sequence similarity with both TM7SF2 and C-terminal region of LBR. When ERG3 is mutant, ergosterol synthesis is impaired in this fungus but when part of ERG3 sequence was replaced by TM segments of either human LBR (hLBR) or human TM7SF2 (hTM7SF2) ergosterol synthesis was restored (Prakash et al., 1999). In addition, ectopic expression of hLBR in several sterol reductase-defective strains of *S. cerevisiae* showed that whereas the disruption of the C-24 reductase ERG4 (32% sequence similarity to the LBR C-terminal region) did not complement ergosterol synthesis, hLBR expression compensated the deficiency in mutant ERG24 strains (Silve et al., 1998),

Functional comparison of LBR and TM7SF2 in mice, showed that in homozygous Tm7sf2 knockout, where Lbr is constitutively expressed, cholesterol synthesis was normal (Bennati et al., 2006a), whereas in Ichthyosis mice where both Lbr alleles are deficient, the presence of Tm7sf2 did not compensate the cholesterol impairment (Shultz et al., 2003). This suggests that while Lbr can complement cholesterol synthesis for Tm7sf2 deficiency, the opposite is not applicable.

Furthermore, experiments in three human cell lines (HeLa, 293T, HFF) showed that under lipid restrictive conditions, there is a dependency on LBR for cholesterol synthesis. Specifically, LBR knockout HeLa cells cultured in cholesterol-depleted medium, expressing either only the C-terminal LBR domain or the C-terminal LBR domain fused to another truncated INM protein (SUN2: containing only a nuclear targeting signal) rescued the observed decrease in cell viability. Additionally, mutant C-terminal shorter LBR proteins have been related to two congenital disorders depending on whether one or both alleles are deficient. Pelger-Huët anomaly with hypolobulated nuclei in granulocytes is manifested in the heterozygous state, whereas the homozygous state results in more severe phenotype with abnormal bone development, fetal hydrops and nonviable fetus termed Greenberg skeletal dysplasia. Such LBR mutants, when introduced in LBR knockout cell lines under cholesterol restrictive conditions, failed to rescue the decreased viability raise questions if these congenital disorders are related to cholesterol metabolism deficiencies (Tsai et al., 2016). Moreover, the same group demonstrated that TM7SF2 is upregulated under cholesterol-restrictive growth conditions, but this increase did not compensate for LBR cholesterol deficiency. These findings indicate LBR as essential for cholesterol synthesis and its C-terminal domain both necessary and sufficient in this pathway, with TM7SF2 regulation and interaction requiring further investigation.

1.4.9 DHCR7 in cholesterol homeostasis

DHCR7 is a 7-dehydrocholesterol reductase transmembrane protein, ubiquitously expressed and localized at the ER membranes and the ONM. It catalyzes the last step in cholesterol biosynthesis pathway, reducing the C7-C8 double bond and converting 7-dehydrocholesterol (7DHC) to cholesterol. Mutations in this gene disrupt cholesterol synthesis at the conversion step, consequently accumulating cholesterol precursor 7DHC (Moebius et al., 1998). Both cholesterol deficit and 7DHC accumulation have been observed in an autosomal-recessive disorder, the Smith-Lemli-Opitz syndrome (SLOS) and both findings are used as diagnostic biochemical hallmarks by physicians. Furthermore, the serum concentration levels of both cholesterol and 7DHC associate with the severity and the outcome of the disease. In more than 80% of cases, SLOS manifested with 2nd and 3rd toe syndactyly, mental retardation, microcephaly and postnatal growth retardation (Waterham et al., 1998, Wassif et al., 1998, Fitzky et al., 1998, Jira et al., 2003).

These morphological abnormalities in SLOS, were early noted by Kelley et al., for their resemblance with those observed in congenital Hedgehog (SHH) deficient conditions, suggesting a functional correlation between the two syndromes (Kelley et al., 1996). Sterol molecules derived from cholesterol biosynthesis regulate either positively or negatively the activation of Smoothened receptor (SMO) and the appropriate localization at the primary cilium during SHH signaling. Therefore, a deficit in cholesterol, impairs this signal transduction, rendering not only the absence of cholesterol but also the abnormally accumulated 7DHC metabolite as a potent cause of the aberrant signaling.

Interestingly, recent work has found that, in contrast to cholesterol shortage, the accumulation of 7DHC *per se*, does not affect SHH signaling by repressing SMO activation or translocation through the receptor Patched (PTC is the SHH receptor and negative repressor of SMO). Experiments have shown that upon inhibition of cholesterol synthesis at the early pathway stages, the disruption of the SHH signaling is not altered, indicating that the impaired SMO activation resulting from the loss of DHCR7 activity is due to reduced levels of cholesterol rather than an accumulation of 7DHC (Blassberg et al., 2016). Nevertheless, DHCR7 deficiency is essential in cholesterol synthesis affecting both SHH signaling, SLOS and the manifested phenotypes and needs to be further investigated.

1.5 Scientific motivation and specific objectives

Early findings of the post-doctoral researcher Dr. Andri Christodoulou in our laboratory revealed that upon depletion of TMEM147, LBR was also downregulated. This finding was unexpected and also of great importance as LBR and its role in organizing and tethering heterochromatin to the NE, the involvement of LBR mutants in early developmental syndromes and its modular structure, comprising a second activity as a sterol reductase implicating LBR in cholesterol biosynthesis, made this study even more intriguing and the necessity of elucidating all these aspects our target.

In particular, we sought to pursue the following specific objectives:

1. Characterize the physical and functional interaction between TMEM147 and LBR.
2. Given the modular structure of LBR and its dual activity, determine which domain mediates this interaction.
3. Considering the interaction of LBR with intermediate filaments of the nuclear lamina and TMEM147 presence in NE, investigate whether downregulation of both proteins may result in any nuclear morphological alterations.
4. Considering that TMEM147 resides in both NE and ER, examine whether depletion of TMEM147 affects the morphology of the ER and LBR topology.
5. Apart from LBR, identify whether there any other proteins residing in the ER or NE that are regulated by the expression levels of TMEM147 and determine at what level these newly identified proteins may be regulated by depletion of TMEM147.
6. Knowing that LBR is associated with cholesterol biosynthesis due to its reductase activity, characterize how downregulation of TMEM147 may impact on cholesterol homeostasis and the full lipidic profile of the cell.
7. Perform datamining to reveal new research directions for TMEM147.

2

Materials and Methods

Chapter 2: Materials & Methods

2.1 Molecular Biology Methods

2.1.1 Bacterial strains of *E. coli*

The *E. coli* strains used in this work are included in Table 2.1

Bacterial Strain	Genotype	Antibiotic Resistance
DH5a	F^- Φ80*lac*ZΔM15 Δ(*lac*ZYA-*arg*F) U169 *rec*A1 *end*A1 *hsd*R17(r_K^-, m_K^+) *pho*A *sup*E44 *thi*-1 *gyr*A96 *rel*A1 λ^-	Ampicillin
TOP10 F	F^- mcrA Δ(mrr-hsdRMS-mcrBC) φ80lacZΔM15 ΔlacX74 nupG recA1 araD139 Δ(ara-leu)7697 galE15 galK16 rpsL(Str^R) endA1 λ^-	Streptomycin

Table 2.1: Bacterial strains of E. coli used.

2.1.2 Plasmid Vectors

The plasmid vectors used for cloning and expression are included in Table 2.2.

Plasmid Vectors	Description	Antibiotic Resistance	Size	Source
Cloning Plasmid Vectors				
pCR 2.1-TOPO	lacZa fragment (selectable marker)	Kanamycin, Ampicillin	3.9 kb	Invitrogen
Eukaryotic Expression Plasmid Vectors				
pEGFP-N1	EGFP is a red shifted variant of wild-type GFP, excitation max: 488 nm, insert construct fuses at the N-terminus of EGFP protein.	Kanamycin, Neomycin	4.7 kb	Clonetech
pFLAG-CMV2	insert construct fuses at the C-terminus of the FLAG epitope.	Ampicillin	4.7 kb	Clonetech

Table 2.2: Plasmid Vectors used.

2.1.3 Antibiotics used for bacterial cultures

The antibiotics that were used for the growth of bacterial cultures and the appropriate concentrations are listed in the following table.

Antibiotic	Final Concentration	Description
Ampicillin	100 μg/μl	Sigma A9518
Streptomycin	50 μg/μl	Sigma S9137
Kanamycin	50 μg/μl	Sigma 60615

Table 2.3: Antibiotics and their concentrations used

2.1.4 Preparation of liquid bacterial culture medium.

Materials

- ddH_2O
- LB Broth Base (86.2 mM NaCl, 10000 mg/L peptone, 5000 mg/L Yeast Extract) (Invitrogen 12780-052)
- Antibiotic(s)

Methodology

1. Dissolve 20g of LB Broth in 1 L of ddH_2O.
2. Confirm that pH of the mixture is 7
3. Autoclave the liquid medium
4. Store at room temperature
5. The appropriate antibiotic(s) is always added just before the use of the medium at concentrations according to Table 2.3.

2.1.5 Preparation of solid bacterial culture medium.

Materials

- ddH_2O
- LB Agar (86.2 mM NaCl, 10000 mg/L peptone, 5000 mg/L Yeast Extract, 12000 mg/L Agar) (Invitrogen 22700-025)
- Bacterial culture petri dishes 90 mm (Sterilin 101VR20, Thermo Fisher Scientific)
- Antibiotic(s)

Methodology

1. Dissolve 32 g of LB Agar in 1 L ddH_2O
2. Confirm that the pH of the mixture is 7
3. Autoclave the liquid medium
4. Let the medium on bench at room temperature until its temperature is lower than 50°C
5. If antibiotics are needed, they are added at this point at a final concentration according to Table 2.3.
6. 15 ml of the mixture is then poured in the plates the lid is placed and they are let on the bench to solidify.
7. The plates can then be stored in the fridge at 4°C until they are used.

2.1.6 Frozen Storage of bacterial strains

Bacterial strains are stored in glycerol 50% v/v, at -80°C.

Materials

- Bacterial liquid culture in high density.
- Sterilized 50% v/v glycerol (Sigma G5516)
- Plastic tubes 1.5ml (Eppendorf 0030120086)

Methodology

1. Add 500 μl of 50% v/v glycerol in several plastic tubes of 1.5 ml
2. Put the plastic tubes in a storage glass bottle and sterilize by autoclave.
3. Shake well the flask containing the bacterial culture to homogenized
4. Transfer 500 μl of homogenized bacterial liquid culture in one autoclaved plastic tube containing glycerol 50% v/v under aseptic conditions.
5. Mix well the mixture and store at -80°C.
6. Document the storage at the appropriate lab list for future reference.

2.1.7 Preparation of chemically competent cells using calcium chloride method

When the plastic tubes of competent cells frozen stock are reduced to 10 or transformation efficiency is abnormally lower than expected new fresh frozen competent bacterial stock is prepared.

For the following steps aseptic techniques must be practiced to ensure contamination is minimized

Materials

- DH5a competent cells
- Sterile plastic loops
- Bacterial petri dish with LB agar (without antibiotic)
- Sterile toothpicks
- Sterile LB liquid bacterial culture medium (without antibiotic)
- Plastic tube of 15 ml (Corning CLS430052)
- Plastic tubes of 50 ml (Corning CLS430829)
- Sterile plastic tubes 1.5 ml (Eppendorf 0030120086)
- Bucket with ice
- Bath with ice cold water
- Solution mix of 80 mM $MgCl_2$ and 20 mM $CaCl_2$
- 0.1 M $CaCl_2$
- ice-cold DMSO
- Liquid nitrogen

Methodology

1. Dip the plastic loop into the frozen competent cell stock and spread it over an LB agar plate without any antibiotics.
2. Let the plate to incubate for at 37°C for 16-20 h.
3. The following day pick one single colony and inoculate a liquid culture of 3 ml and incubate the tube at 37°C for 16-20 h at 200 rpm.
4. Inoculate 100 ml LB liquid medium with 1 ml of the incubated bacterial culture and incubate the bacterial culture until OD reaches 0.4
5. Split the culture in 2x50 ml ice-cold plastic tubes and leave on ice for 10 min
6. While waiting pre-cool the centrifuge at 4°C.
7. Centrifuge at 2700 g for 10 min at 4°C and discard the supernatant letting the tube to dry for 1 min.
8. Resuspend each bacterial pellet by gently swirling in 30 ml ice-cold solution mix of 80 mM $MgCl_2$ and 20 mM $CaCl_2$.
9. Incubate on ice for 30 min

10. Centrifuge again, at 2700 g for 10 min at 4°C and discard the supernatant letting the tube to dry for 1 min.
11. Resuspend each pellet by gently swirling in 2 ml ice-cold $CaCl_2$ 0.1 M and incubate the tubes on ice for 10 min.
12. In each 50 ml tube add 100 μl of ice-cold DMSO and incubate again on ice for 15 min.
13. In each 50 ml tube add 100 μl of ice-cold DMSO and incubate in ice bath.
14. Transfer and store the chemically competent bacterial cells in aliquots of 100 μl in sterile 1.5 mL plastic tubes.
15. Each aliquot is abruptly frozen by submerging it in liquid nitrogen.
16. The tubes are then stored at -80°C.
17. Document the storage at the appropriate lab list for future reference.

2.1.8 Transformation of competent bacterial cells

Materials

- Plasmid of interest
- Competent bacterial cells
- LB sterile liquid medium
- Petri dishes with LB agar and antibiotics

Methodology

1. Defrost fast on palm one aliquot of competent cells and let on ice for 10 min
2. Add 100ng plasmid DNA or 2 μl of the ligation product and mix gently.
3. Incubate on ice for 30 min
4. Thermal shock at 42°C for 45 sec
5. Let on ice for 2 min
6. Add 400 ml LB liquid medium and incubate at 37°C for 1h and rotating at 200 rpm
7. Transfer on a petri dish 200 μl of transformed bacteria containing the LB agar and incubate at 37°C for 16-18 h with dish upside down. (only successfully transformed bacteria can grow on the LB agar because of the plasmid antibiotic resistance they have incorporated).
8. Further analysis of the transformed bacteria is applied. Restriction digest are used to confirm the plasmid.

2.1.9 Purification of plasmid DNA small scale (mini) QIAprep Spin Column.

Qiagen plasmid DNA purification QIAprep Spin Miniprep Kit (#27104)

Materials

- Buffer P1: 50 mM Tris-Cl, pH 8.0, 10 mM EDTA, 100 μg/mL RNase A
- Buffer P2: 200 mM NaOH, 1% SDS
- Buffer N3: 4.2 M Gu-HCl, 0.9 M potassium acetate, pH 4.8
- QIAprep Spin Column
- Buffer P3: 3.0 M potassium acetate, pH 5.5
- Buffer PB: 5 M Gu-HCl, 30% isopropanol
- Buffer PE: 10 mM Tris-HCl pH 7.5, 80% ethanol
- Buffer TE: 10 mM Tris-Cl, 1 mM EDTA, pH 8.0.
- Plastic tubes 1.5 ml (Eppendorf 0030120086)

Methodology

1. In a consecutive manner, transfer and centrifuge a 3-5 ml liquid bacterial culture to small plastic tubes 1.5 ml, at 6000 g for 15 min at 4°C.
2. Decant the supernatant and resuspend the bacterial pellet in 0.250 ml buffer P1 by pipetting and/or vortexing until no cell clumps are visible.
3. Add 0.250 ml buffer P2, mix thoroughly by vigorously inverting the tubes 4-6 times and incubate at room temperature for no more than 5 min.
4. Add 0.350 ml pre-chilled buffer N3 immediately and thoroughly mixing by vigorously inverting the tube 4-6 times.
5. Centrifuge at 13000 rpm (~18000 g) for 10 min. The plasmid DNA remains in the liquid phase.
6. Assemble the QIAprep Spin Column and Collection Tube and decant the supernatant to the QIAprep spin column. Centrifuge at 13000 rpm (~18000 g) for 1 min and discard the flow through.
7. Assemble the QIAprep Spin Column and Collection Tube again and wash the column by adding 500 μl buffer PB and centrifuge at 13000 rpm (~18000 g) for 1 min. Discard the flow through.
8. Assemble the QIAprep Spin Column and Collection Tube and wash the column by adding 750 μl buffer PE and centrifuge at 13000 rpm (~18000 g) for 1 min. Discard the flow through.

9. Centrifuge one last time for residual wash buffer removal.
10. Place the QIAprep Spin Column in a new clean plastic tube 1.5 ml.
11. Add 50 μl buffer EB and let it stand for 1 min. Elute the plasmid DNA from the column by centrifugation at 13000 rpm (~18000 g) for 1 min.
12. Determine the plasmid DNA concentration using Thermo Scientific™ NanoDrop 2000, label the tube and store at -20°C.

2.1.10 Purification of plasmid DNA small scale (mini) Ethanol precipitation for diagnostic purposes.

Materials

- Buffer P1: 50 mM Tris-Cl, pH 8.0, 10 mM EDTA, 100 μg/mL RNase A
- Buffer P2: 200 mM NaOH, 1% SDS
- Buffer P3: 3.0 M potassium acetate, pH 5.5
- 100% (v/v) Ethanol ice-cold
- 70% (v/v) Ethanol
- Buffer EB: 10 mM Tris-Cl, pH 8.5.
- Plastic tubes 1.5 ml (Eppendorf EP0030120086)

Methodology

1. Centrifuge a 1.5 ml liquid bacterial culture to small plastic tubes 1.5 ml, at 6000 g for 5 min at 4°C.
2. Decant the supernatant and resuspend the bacterial pellet in 0.150 ml buffer P1 by pipetting and/or vortexing until no cell clumps are visible.
3. Add 0.150 ml buffer P2, mix thoroughly by vigorously inverting the tubes 4-6 times and incubate at room temperature for no more than 5 min.
4. Add 0.150 ml pre-chilled buffer P3 immediately and thoroughly mixing by vigorously inverting the tube 4-6 times.
5. Centrifuge at 13000 rpm (~18000 g) for 10 min. The plasmid DNA remains in the liquid phase. The plasmid DNA is pelleted at the bottom of the tube.
6. Transfer the supernatant to a new 1.5 ml plastic tube and add ~1.0 ml ice-cold Ethanol 100% (2.5xVolumes) mixing and incubate at -20°C for more than 30 min.
7. Centrifuge at 13000 rpm (~18000 g) for 15 min at 4°C.
8. Carefully discard the supernatant and add 300 μl 70% Ethanol without disturbing the plasmid DNA pellet.

9. Discard the 70% Ethanol and let the lid open to air dry the pellet.
10. Resuspend the pellet in 40 μl buffer EB.
11. Determine the plasmid DNA concentration using Thermo Scientific™ NanoDrop 2000, label the tube and store at -20°C for further diagnostic analysis.

2.1.11 Purification of Plasmid DNA big scale (midi).

Plasmid DNA purification midi kit of Qiagen (#12143)

Materials

- Buffer P1: 50 mM Tris-Cl, pH 8.0, 10 mM EDTA, 100 μg/mL RNase A
- Buffer P2: 200 mM NaOH, 1% SDS
- Buffer P3: 3.0 M potassium acetate, pH 5.5
- Buffer QBT: 750 mM NaCl, 50 mM MOPS, pH 7.0, 15% (v/v) isopropanol, 0.15% (v/v) Triton X-100
- Buffer QC: 1.0 M NaCl, 50 mM MOPS, pH 7.0, 15% (v/v) isopropanol
- Buffer QF: 1.25 M NaCl, 50 mM Tris-Cl, pH 8.5, 15% (v/v) isopropanol
- Buffer TE: 10 mM Tris-Cl,1 mM EDTA, pH 8.0.
- Qiagen-tip 100 anion-exchange column
- 100% (v/v) Isopropanol
- 70% (v/v) Ethanol
- Plastic tubes 50 ml (Corning CLS430829)
- Plastic tubes 2.0 ml (Eppendorf EP0030120094)

Methodology

1. Separate the total liquid bacterial culture to 50 ml plastic tubes and centrifuge at 6000 rpm for 15 min at 4°C
2. Decant the supernatant and resuspend the entire bacterial pellet in 4 ml P1 buffer until no bacterial accumulations or clumps are visible. (add 4 ml P1 in the first tube, dissolve well and transfer it to the second tube. Do the same until all pellets are dissolved in a total 4 ml P1 buffer)
3. Add 4 ml of P2 buffer and mix thoroughly by inverting vigorously the tube 4-6 times and incubate at room temperature for 5 min.
4. Add 4 ml of chilled P3 and mix thoroughly by inverting vigorously the tube 4-6 times
5. Incubate on ice for 15 min.

6. Centrifuge at 20000 g for 30 min at 4°C and transfer the supernatant containing the plasmid to a new tube.
7. Repeat centrifuge at 20000 g for 15 min at 4°C.
8. During the centrifugation equilibrate a Qiagen -tip 100, by applying 4ml buffer QBT and let the column empty by gravity flow.
9. When the centrifugation ends, decant the supernatant to the Qiagen-tip and allow it to enter the resin by gravity flow. (Plasmid DNA is trapped on the tip)
10. Wash the Qiagen-tip twice, with 10 ml buffer QC and allow until the tip is empty.
11. Elute plasmid DNA with 5 ml buffer QF collecting the eluate in a clean 50 ml plastic tube.
12. Add 3.5 ml room temperature isopropanol to the eluate, mix and centrifuge at 15000 g for 30 min at 4°C.
13. Decant the supernatant as DNA is pelleted at the bottom of the tube.
14. Add 2 ml 70% ethanol to the pellet and carefully transfer it to a small 2 ml tube.
15. Centrifuge the tube at 15000 g for 10 min at 4°C
16. Remove the supernatant and let the tube-lid open to air dry the pellet
17. Re-dissolve the pellet with 50 μl TE buffer overnight on rocker.
18. Determine the plasmid DNA concentration using Thermo Scientific™ NanoDrop 2000, label the tube and store at -20°C.

2.1.12 RNA isolation and genomic DNA removal.

Materials

- RNA RNeasy mini kit (Qiagen 74104)
- Cell culture plate up to 80% confluency
- DPBS (Dulbecco’s phosphate-buffered saline) w/o Calcium or Magnesium (Gibco 14190-144).
- Buffer RLT
- 14.3 M β-mercaptoethanol (Sigma 63689)
- 70% ethanol
- Buffer RW1
- DNase-I 2 units/μl (NEB M0303S)
- 10x DNase buffer
- Buffer RDD

- Buffer RPE
- ddH2O DNase free water
- RNeasy Spin Column
- 2.0 ml plastic tube (Eppendorf EP0030120094)
- 1.5 ml plastic tube (Eppendorf EP0030120086)

Methodology

1. Discard the cell culture medium from the cell culture plate.
2. Add 5ml DPBS to wash the remaining medium from the plate
3. Completely remove and discard DPBS.
4. Add buffer RLT and β-mercaptoethanol (10 cm plate: 600 μl RLT + 6 μl β-mercaptoethanol, 60 mm plate: 350 μl RLT + 3,5 μl β-mercaptoethanol) to lyse the cells. Use the tip of pipette to collect the cells in 1.5 ml plastic tube.
5. With a pipette measure the volume of the lysate and add equal volume of 70% ethanol and mix well by pipetting.
6. Place the RNeasy spin column in a 2 ml collection tube, transfer up to 700 μl of sample into the column and centrifuge at 8000 g (~10000rpm) for 15 sec.
7. Discard the flow through and place the spin column back in the 2 ml collection tube.
8. If there is more sample, transfer it in successive aliquots and repeat the previous centrifuge step.
9. Add 350 μl buffer RW1 to the RNeasy spin column and centrifuge at 8000 g (~10000 rpm) for 15 sec to wash the column. Discard the flow through and place the spin column back in the 2ml collection tube.
10. Prepare the DNase mix by gently mixing for each tube 10 μl DNase I stock solution and 70 μl buffer RDD.
11. Add the DNase-I mix directly to the spin column membrane and incubate at room temperature for 15 min.
12. Add 350 μl buffer RW1 to the RNeasy spin column and centrifuge at 8000 g (~10000 rpm) for 15 sec to wash the column.
13. Add 500 μl buffer RPE to the spin column and centrifuge at 8000 g (~10000 rpm) for 15 sec.
14. Add 500 μl buffer RPE to the spin column and centrifuge at 8000 g (~10000 rpm) for 2 min.

15. Discard the flow through, place the column in a new 2 ml collection tube and centrifuge the column once more.
16. Place the column in a new 1.5 ml collection tube.
17. Add 50 μl RNase free water and centrifuge at 8000 g (~10000 rpm) for 1 min to elute the RNA.
18. Determine the RNA concentration using Thermo Scientific™ NanoDrop 2000, label the tube and store at -80°C until use.

2.1.13 Reverse Transcriptase cDNA synthesis.

<u>Materials</u>

- iScript cDNA Synthesis Kit (BIO-RAD 170-8890)
- 5x iScript reaction mix
- Nuclease free water
- iScript Reverse Transcriptase
- RNA template
- Sterile PCR tubes (Corning CLS6571-960EA)

<u>Methodology</u>

1. Prepare the reaction according to the following table mix gently and spin down:

Components	Volume per Reaction
5x iScript reaction mix	4 μl
iScript Reverse Transcriptase	1 μl
Nuclease-free water	Volume up to 20 μl
RNA template (100 fg - 1 μg)	Volume equivalent to 1 μl

Table 2.4: Reagents and their final concentrations used in cDNA synthesis

2. The complete reaction mix is incubated in a PCR machine (MJ Research PTC 200 Thermal Cycler) according to the following conditions:
    a. 5 min at 25°C
    b. 30 min at 42°C
    c. 5 min at 85°C
    d. Hold at 4°C
3. Determine the cDNA concentration using Thermo Scientific™ NanoDrop 2000 and label the tube.

4. Dilute the sample to a final concentration of 50 ng/μl with nuclease-free water
5. Store samples in -20°C until use.

2.1.14 Expand High Fidelity DNA PCR System

If the product of PCR needs to be highly accurate without any point mutations or any changes in reading frame, then High Fidelity PCR System is used.

Expand High Fidelity PCR System (Roche 11732641001)

Materials

- Expand High Fidelity DNA polymerase mixture, (3.5 units/μl)
- 10x Expand Polymerase buffer containing 15 mM $MgCl_2$
- dNTPs, mixture of four dNTPs, 10 mM each
- RNase-free water, ddH2O
- Sterile PCR tubes (Corning CLS6571-960EA)
- cDNA template
- Forward and Reverse oligonucleotide primers

Methodology

1. Prepare the mixtures 1 and 2 according to the following table and the number of reactions.

Mixture 1 (25μl per reaction)		**Mixture 1 (25μl per reaction)**	
Components	**Conc./Reaction**	**Components**	**Vol./Reaction**
RNase-free water	up to 25 μl	RNase-free water	19.25 μl
dNTPs	200 μM each dNTP	Expand buffer	5 μl
FW primer	300 nM	Expand enzyme mix	0.75 μl
RV primer	300 nM		
cDNA template	0.1-250 ng		

Table 2.5: Reagents and their final concentration/volume used in Expand High Fidelity PCR System

2. Transfer mixture 1 in mixture 2 and mix gently.
3. Spin down the mixture.
4. Place the tube in the PCR machine (MJ Research PTC 200 Thermal Cycler) and incubate under the following conditions:

LBR cloning conditions		
a.	Initial denaturation	94°C for 2 min
b.	Denaturation	94°C for 15 sec
c.	Annealing	55°C for 30 sec
d.	Elongation	72°C for 2 min
e.	Repeat	Repeat b to d 34 more times
f.	Final elongation	72°C for 7 min
g.	Cooling	Hold at 4°C

Table 2.6: Cloning conditions of Expand High Fidelity PCR System

5. 10 μl of this reaction are used to validate the reaction products via agarose gel electrophoresis

2.1.15 Polymerase chain reaction (PCR)

Taq DNA Polymerase Kit (Qiagen 201205)

Materials

- Taq DNA Polymerase, 5 units/μl
- 10x PCR buffer
- 5x Solution Q
- dNTPs, mixture of four dNTPs, 10 mM each
- RNase-free water, ddH2O
- PCR tubes
- cDNA template
- Forward and Reverse oligonucleotide primers

Methodology

1. Prepare the reaction according to the following table:

Component	Final Concentration	Component	Final Concentration
dNTPs	200 μM	5x solution Q	1x
Forward primer	400 nM	Taq DNA Polymerase	2.5 units
Reverse primer	400 nM	cDNA	1 μg

10x PCR buffer	1x	ddH_2O	Up to 50µl volume

Table 2.7: Reagents and their final concentrations used for Taq PCR

2. Gently mix the components by pipetting.
3. Spin down the mixture and place the tube in the PCR machine and incubate under these conditions:

LBR cloning conditions		
a.	Initial denaturation	94°C for 3 min
b.	Denaturation	94°C for 30 sec
c.	Annealing	55°C for 30 sec
d.	Elongation	72°C for 1 min
e.	Repeat	Repeat b to d 29 more times
f.	Final elongation	72°C for 10 min
g.	Cooling	Hold at 4°C

Table 2.8: Cloning conditions of Taq PCR

4. 10 µl of this reaction are used to validate the reaction products via agarose gel electrophoresis.

2.1.16 Quantification of mRNA using real-time PCR

To quantify the mRNA levels of the proteins of interest Comparative Ct real-time PCR analysis was employed. For comparison reasons mRNA levels of a housekeeping gene were also quantified and used for normalization. Statistical analysis was performed using REST-384$^{©}$ software, which applies a Pair Wise Fixed Reallocation Randomization Test$^{©}$ to compare the relative levels of the protein-mRNAs of interest expressed in the different investigated conditions and test the statistical significance of the results (Pfaffl et al., 2002).

Materials

- cDNA samples
- Forward and Reverse oligonucleotide primers
- 2x Reaction mixture for PCR (Fast SYBR Green Master Mix, ABI 4385612)
- PCR 96 well plates (ABI 4346907)
- Optical Adhesive film (ABI 4311971)
- RNase free water, ddH_2O

Methodology

1. Each reaction is triplicate to minimize the standard error.
2. In each well of the plate the reaction mixture is indicated in the following table.

Reagent	Final Concentration/Volume
ddH_2O	up to 10 μl
FW primer	400 nM
RV primer	400 nM
2x reaction mixture	1x
cDNA	100 ng

Table 2.9: Final concentration/volume of the reagents for RT-qPCR

3. The plate is covered by the specific adhesive film.
4. The plate is centrifuged for 1 min at 4°C at 1000 rpm
5. The plate is placed in Real-Time PCR machine (CFX96 Real-Time PCR system Bio-Rad), which is set for Comparative Ct analysis employing the following protocol.

real-time PCR conditions		
a.	Polymerase activation	95°C for 20 sec
b.	Denaturing	95°C for 1 sec
c.	Annealing/extension	60°C for 30 sec
d.	Repeat	Repeat b and c, 39 more times
e.	Denaturing	95°C for 15 sec
f.	Final annealing/extension	60°C for 1 min
g.	Final denaturing	95°C for 15 sec
a.	Cooling	Hold at 4°C

Table 2.10: Conditions for RT-qPCR

6. The results are analyzed using the REST-384© software

2.1.17 Restriction enzyme reactions

Materials

- Appropriate Restriction enzyme (New England Biolabs)
- 10x buffer relative to the endonuclease used (New England Biolabs)
- 100x BSA (New England Biolabs)
- Isolated plasmid DNA

- Nuclease free ddH2O
- 1.5ml plastic tube (Eppendorf EP0030120086)

Methodology

1. Preparation of the reaction in a 1.5 ml tube according to the following table

Reagent	Final Concentration/Volume
ddH_2O	up to 20 μl
Endonuclease	1 unit/μg DNA
10x buffer	1x
plasmid	25 ng

Table 2.11: Final concentration/volume of the restriction enzyme reaction

2. Mix gently until homogenization and the tube is incubated at 37°C for 2 h.
3. 5 μl from each reaction are used in agarose electrophoresis to confirm the correct transformation along with undigested plasmid for comparative reasons

2.1.18 DNA agarose gel electrophoresis.

Materials

- Agarose (Nippon genetics AG02)
- 1x TBE electrophoresis buffer (89 mM Tris-Borate, 2mM EDTA)
- Ethidium Bromide (EtBr) at a final concentration of 0.5μg/ml (Sigma, E1510 10 mg/ml)
- 5x loading sample
- DNA marker (1 kb plus Invitrogen 10787-018)

Methodology

1. Preparation of agarose gel:
    a. Weigh out the appropriate agarose mass according to the desired w/v (g/ml) percentage of gel thickness depending on the size of the separated DNA fragments.
    b. Add the agarose in the appropriate volume of 1x TBE and apply heat in intervals until the mixture is homogenized.
    c. Wait until cool down just before clotting and add Ethidium bromide at a final concentration 0.5 μg/ml
    d. Pour the mixture in the casting apparatus with the appropriate comb to create wells.

   e. Wait until the agarose is set, remove the comb carefully, place the gel in the gel box if not casted in it and cover the gel with 1x TBE running buffer.
2. Prepare the loading samples by adding the appropriate 5x loading buffer to a final concentration of 1x.
3. Load the samples and the marker on the gel and apply voltage at 90 V.
4. Wait until the samples run almost the full length of the gel
5. Take the gel out of the running apparatus check and image the separation under UV lamp (Syngene G:BOX).

2.1.19 DNA extraction from agarose gel

To purify PCR products or plasmids from agarose gel after electrophoresis, was used the QiAquick Gel Extraction Kit of Qiagen (Qiagen 28704).

Materials

- Gel sample containing the DNA fraction.
- QiAquick Gel Extraction Kit containing
    - QIAquick spin column
    - QG solubilizing/binding buffer
    - PE wash buffer containing ethanol
    - EB elution buffer
    - 2.0 ml plastic tube (provided in the kit)
- Isopropanol 100% (v/v)
- Sterilized scalpel
- 1.5 ml plastic tube (Eppendorf EP0030120086)

Methodology

1. Observe the agarose gel with the desired DNA product for extraction under a UV lamp and identify the desired DNA band.
2. Excise the DNA fragment from the agarose gel by cutting the gel with a sterilized scalpel minimizing the extra agarose gel as possible.
3. Transfer the gel fragment in 1.5 ml plastic tube and weigh out the containing DNA/gel fragment.
4. Add 3 volumes of buffer QG in the plastic tube for every 1 volume of gel according to the w:v gel equivalence 100 mg : 100 μl.
5. Incubate the tube at 50°C for 10 min until the gel is dissolved completely.

6. Place a QIAquick spin column in the provided 2 ml collection tube.
7. Transfer the dissolved gel in the column and centrifuge at 13000 rpm for 1 min.
8. Remove the column, discard the flow-through and add 0.75 ml of wash buffer PE.
9. Centrifuge again for 1 min at 13000 rpm and discard the flow-through.
10. Place the column in a new clean 1.5 ml plastic tube and add 50 ml of elution buffer EB.
11. Centrifuge at 13000 rpm for 1 min.
12. The flow-through contains the DNA fragment and can be quantified by Thermo Scientific™ NanoDrop 2000.
13. The DNA fragment is ready for use or can be stored for future use.

2.1.20 DNA ethanol precipitation method

Materials

- DNA fragment sample
- 3 M Sodium Acetate buffer
- 100% (v/v) ice cold ethanol (-20°C)
- 70% (v/v) ice cold ethanol (-20°C)
- EB elution buffer (10 mM Tris-HCl, pH 8.5) or TE buffer (10 mM Tris-HCl, pH 8.5, 1 mM EDTA)

Methodology

1. Add 1/10 of the DNA fragment sample 3 M Sodium Acetate and mix well.
2. Add 2.5 volumes of the mixture in the previous step, of 100% ice cold ethanol and mix well.
3. Incubate the tube in -20°C for at least 30 min.
4. Set the centrifuge at 4°C.
5. Centrifuge the tube at 13000 rpm for 15 min at 4°C marking the tube orientation.
6. Discard the supernatant.
7. Cautiously add 1 ml 70% ice cold ethanol without disturbing the DNA pellet precipitated at the bottom of the tube.
8. Discard the supernatant and let the pellet to dry at room temperature on the bench. If necessary, repeat centrifuge.
9. Dissolve the DNA pellet in the appropriate volume of EB or TE buffer.

2.1.21 DNA ligation

Materials

- Plasmid vector and cDNA construct digested with the same endonucleases.
- T4 DNA ligase (400000 units/ml, NEB M0202S)
- 10x ligase buffer solution
- ddH$_2$O, nuclease free
- Sterile PCR tubes (Corning CLS6571-960EA)

Methodology

1. Prepare the ligation reaction tube according the following table.

Reagent	**Final Concentration**
ddH$_2$O	up to 10 μl volume
10x ligation solution buffer	1x
plasmid vector	50 ng
cDNA construct	50-150 ng
T4 DNA ligase	400 units

Table 2.12: Final concentration of T4 DNA ligation reaction components

2. Gently mix the reaction by pipetting up and down and incubate at 16°C for 12 h.
3. The ligation product is labeled and either used for immediate transformation or stored in -20°C for future use.

2.1.22 Oligonucleotides.

2.1.22.1 PCR cloning

The following table shows the oligonucleotides used for the cloning of the LBR cDNA and the subsequent cloning of the truncated variants of the LBR.

Primer	**Sequence (5′→ 3′)**	**Restriction Enzyme**
LBR_full_FW	5′- CGCGCTCGAGATGCCAAGTAGGAAATTTG -3′ (29)	XhoI
LBR_full_RV	5′- CGCGGAATTCGGTAGATGTATGGAAATA -3′ (28)	EcoRI

LBR_ 209-615_FW	5′- CGCGCTCGAGTTTGGAGGAGTACCTGGTG -3′ (29)	XhoI
LBR_ 1-372_RV	5′- CGCGGAATTCGACGGCCAATGAAGAAATCATA -3′ (32)	EcoRI

Table 2.13: The oligonucleotides used in pcr cloning reactions for LBR DNA constructs

For the cloning of the full length LBR cDNA, LBR_full_FW and LBR_full_RV primers were used initially in pCR 2.1-TOPO vector and then in pEGFP-N1. Both the truncated LBR constructs were cloned from pEGFP-N1_LBR full length using for the construction of the LBR C-terminal domain cDNA comprising of 209-615 residues, the LBR_209-615_FW and LBR_full_RV whereas for the construction of the LBR N-terminal domain cDNA, comprising of 1-372 residues, the LBR_full_FW and LBR_1-372_RV. The table also indicates the restriction sites of each oligonucleotide used to clone the LBR constructs in pEGFP-N1. For the cloning of the three cDNAs in the pFLAG-CMV2 vector, BglII and KpnI restriction sites and the relevant endonucleases were used.

2.1.22.2 Quantitative real-time PCR

The following table shows the oligonucleotides used for the quantification of the mRNA levels of proteins of interest using quantitative real-time PCR.

Primer	Sequence
TMEM147_FW	5′- GTACAACGCCTTCTGGAAATG -3′
TMEM147_RV	5′- ATGCTGTTCTTGGCCACTTT -3′
LBR_FW	5′- GGTCGACCACCTAAAAGTGC -3′
LBR_RV	5′- CCCCATTATATCTGCTGATGC -3′
DHCR7_FW	5′- CCCAGCTCTATACCTTGTGG -3′
DHCR7_RV	5′- CCAGAGCAGGTGCGTGAGGAG -3′
TM7SF2_FW	5′- AACTCAGGCAATCCGATTTACG -3′
TM7SF2_RV	5′- GGGTCGCAGTTCACAGAAATA -3′
PUMI_UP	5′- TGAGGTGTGCACCATGAAC -3′
PUMI_DO	5′- CAGAATGTGCTTGCCATAGG -3′

Table 2.14: The oligonucleotides used for quantitative real-time PCR

2.2 Cell culture

2.2.1 Cell lines

HeLa (Kyoto; K; EMBL) is the main cell line used for experimental purposes in this thesis Moreover, they were used for the development of specific stably transfected cell lines as tools for further experimental investigation.

1. HeLa TMEM147-GFP stable cell line (expressing pEGFPN1-TMEM147).
2. HeLa GFP only (expressing pEGFP only)
3. HeLa LBR$_{238}$-GFP stable cell line (expressing the first N-terminal 238 amino acids including first TM of Human LBR fused in frame with GFP, kindly gifted from Jan Ellenberg, EMBL Heidelberg).

2.2.1.1 HeLa TMEM147-GFP and HeLa GFP only

Both stable cell lines were derived from wt. HeLa (Kyoto; K; EMBL) in our lab at an earlier time. HeLa TMEM147-GFP were generated by transient transfection of the recombinant plasmid construct pEGFP-N1-TMEM147, and HeLa-GFP-only by an empty pEGFP-N1 vector. Expressing cells were then selected until stable expression was established by means of antibiotic selection.

2.2.1.2 Generation of HeLa TMEM147-GFP stable cell line

Materials

- Geneticin Selective Antibiotic (G418 Sulfate) 50 mg/ml. (Gibco 10131-035).

Methodology

1. HeLa K are transient transfected using lipofectamine methodology (2.2.9) with pEGFP-N1-TMEM147 (TMEM147 fused to the N-terminal side of GFP)
2. Cells expressing TMEM147-GFP were cultured in Complete medium supplemented with 0.5 mg/ml G418 (Invitrogen).
3. For further enrichment purposes transfected cells were sorted out based on the fluorescence scattering using Fluorescence-activated cell sorting (FACS).

2.2.1.3 HeLa-LBR$_{238}$-GFP

Jan Ellenberg (EMBL Heidelberg, Germany) (Ellenberg et al., 1997), produced a Hela cell line stably expressing an N-terminal truncated version of LBR, tagged with GFP, HeLa-LBR$_{238}$-GFP. This construct of LBR contained the first 238 amino acids, including the N-terminal region and the first transmembrane domain. Protein extracts from this cell line, analyzed by WB with an anti-LBR antibody, show two distinct bands around 63 kDa; the higher band corresponds to the endogenous LBR and the lower to the truncated GFP-tagged version, LBR$_{238}$-GFP. The latter is also detected with anti-GFP antibody. This cell line was a kind gift. (Fig. 3.18).

2.2.2 Cell culture medium

Materials

- DMEM-GlutaMAX (Dulbecco's Modified Eagle Medium) containing 25 mM Glucose, 3.97 mM Glutamine, without Sodium Pyruvate, (Gibco 61965-026).
- FBS (Fetal Bovine Serum) qualified, heat inactivated, (Gibco 10500-064).
- Antibiotics Mixture: Penicillin, 10000 units/mL and Streptomycin, 10000 μg/mL (Gibco 15140-122)
- Sodium Pyruvate, 100 mM, (Gibco 11360-039)

Methodology

Cell culture medium (Complete medium) was prepared by mixing DMEM-GlutaMAX (440 ml), and FBS at 10% v/v (50 ml), Penicillin/Streptomycin at 100 U/mL (5 ml) and Sodium Pyruvate at 1mM (5 ml).

2.2.3 Recovery of cultured cells from liquid nitrogen

Materials

- Frozen cells in cryovials (Nalgene Cryogenic Tubes 5000-0012)
- Complete Cell Culture medium at 37°C
- Cell culture plates, 100 mm (Corning BD Falcon, 353003).

Methodology

1. 7 ml of Complete cell culture medium are added in the 100 mm cell culture plate.
2. Quick defreeze/resuspend the frozen cells of a cryovial by rubbing the vial in hand.
3. Pour the cells in the cell culture plate by inverting the cryovial cautiously.

4. Incubate the cells until 80% confluency maintaining 37°C and 5% CO_2 environmental conditions.

2.2.4 Subculturing cells

Materials

- Cell culture plate with the appropriate cell line to be subcultured (split/recultured).
- Cell culture plates (100 mm or 60 mm depending the experiment) (Corning CLS353003 or CLS430166)
- Complete cell culture medium at 37°C
- DPBS (Dulbecco's phosphate-buffered saline) w/o Calcium or Magnesium (Gibco 14190-169).
- 0.25% Trypsine-EDTA (1x) (Gibco 25200-072).
- Sterile coverslips (Deckglaser cover glasses 12x12 mm)

Methodology

1. Remove and Discard the cell culture medium from the cell culture plate.
2. Add 5 ml DPBS to wash the remaining medium from the plate.
3. Completely remove and discard DPBS.
4. Add 1ml Trypsine-EDTA (1x) agitate the plate until the surface is covered and incubate at 37°C, 5% CO_2 for 2 min.
5. Observe under microscope for cell detachment.
6. Add 7 ml of prewarmed Complete medium and disperse by pipetting over the cell layer surface several times to detach the cells and break down the cell aggregations.
7. If cells intend to be used for Immunofluorescence staining experiments, sterile coverslips (cvs) are placed on the bottom of the plate.
8. Prepare new culture plate(s) by adding 7 ml prewarmed complete medium.
9. Add 1 ml of detached cells to the new plate(s) and disperse the medium by gently pipetting.
10. Incubate the new culture plates at 37°C, 5% CO_2.

2.2.5 Freezing of cell lines for storage

Materials

- Cell culture plate with the appropriate cell line to be frozen stored.
- 0.25% Trypsine-EDTA (1x) (Gibco 25200-072).

- Complete cell culture medium at 37°C
- DPBS (Dulbecco’s phosphate-buffered saline) w/o Calcium or Magnesium (Gibco 14190-169).
- DMEM-GlutaMAX (Dulbecco's Modified Eagle Medium) containing 25 mM Glucose, 3.97 mM Glutamine, without Sodium Pyruvate, (Gibco 61965-026).
- 100% (v/v) DMSO (Sigma D2650)
- Sterile plastic tubes 15 ml (Corning CLS430052)
- Freezing Container at RT (Nalgene Mr. Frosty 5100-0001)
- Cryovials (Nalgene Cryogenic Tubes 5000-0012)
- Ice.

Methodology

1. Prepare the cell freezing medium containing 95% Complete Cell Culture medium and 5% DMSO and put on ice.
2. Remove and discard the cell culture medium from the cell culture plate.
3. Add 5 ml DPBS to wash the remaining medium from the plate.
4. Completely remove and discard DPBS.
5. Add 1ml Trypsin-EDTA (1x) and agitate the plate until the surface is covered and incubate at 37°C, 5% CO2 for 2 min.
6. Observe under microscope for cell detachment.
7. Add 7 ml of prewarmed Complete medium and disperse by pipetting over the cell layer surface several times to detach the cells and brake down the cell aggregations.
8. Transfer the mixture to a sterile 15 ml plastic tube and centrifuge at 950 rpm at 4°C for 5 min.
9. Remove and discard the supernatant medium.
10. Wash the cells by gently resuspend the pellet in 4ml DPBS and centrifuge again at the same conditions.
11. Remove and discard the supernatant DPBS and gently resuspend the cell pellet in 1ml of ice-cold freezing medium.
12. Transfer the cell-freezing medium mixture in a sterile cryovial and label it.
13. Place the cryovial in the freezing container and place the container at -80°C freezer for 24 h.
14. After 24 h, transfer the cryovial in liquid nitrogen for long term storage.
15. Document the storage at the appropriate lab list for future reference.

2.2.6 siRNA mediated protein expression silencing using INTERFERin

Materials

- Cell culture plate 80% confluent
- DPBS (Dulbecco’s phosphate-buffered saline) w/o Calcium or Magnesium (Gibco 14190-144)
- 0.25% Trypsine-EDTA (1x) (Gibco 25200-072)
- Complete cell culture medium.
- 60 mm cell culture plates (Corning CLS430166)
- Sterile coverslips (Deckglaser cover glasses 12x12 mm)
- 1.5 ml plastic tube (Eppendorf EP0030120086)
- INTERFERin (Polyplus Transfection 409-10)
- siRNA oligonucleotides (see Table 2.15)
- Opti-MEM cell culture medium (Gibco 51985-026)

Methodology

1. 24 h prior the silencing (t=-24 h) experiment pour off the medium from the plate and sub-culture the cells to the appropriate dilution in 50 mm cell culture plates so that after 24 h cell coverage is up to 50-60% adapting the previous protocol 2.2.4.
2. If needed, sterile cvs are placed at the bottom of the plate(s) for cells to grow on them for Immunofluorescence experiments.
3. The new cell plates are incubated at 37°C, 5% CO_2.
4. On silencing day (t=0), cell culture plates are washed with DPBS and the medium is replaced by 4 ml fresh complete medium.
5. Add 400 μl of Opti-MEM medium in one small plastic tube.
6. Add 8 μl of siRNA oligo (final concentration 40 nM) and aspirate by gently pipetting.
7. Add 12 μl of INTERFERin and aspirate by gently pipetting once again.
8. Vortex for 10 sec at a low-medium speed and let on the bench to incubate for 10 min.
9. The mixture (Opti-MEM, complex of INTERFERin-oligos) is added to the plate dropwise and aspirate by gentle circular movements.
10. Incubate at 37°C and 5% CO_2 conditions
11. After 24 h the medium is changed to fresh without wash (this step can be omitted)

12. After 72 h for siRNA oligo #1, or 96 h for siRNA oligo #2 since silencing, cells are harvested for either immunofluorescence (IF) analysis or RT-qPCR analysis or SDS electrophoresis and Western blot (WB) analysis.
13. For negative control experiment, the protocol is repeated but no oligo is used i.e. mock transfection reaction.

2.2.7 siRNA oligonucleotides

siRNA	Sequence	Manufacturer
Oligo #1	5′- GGCGGCAUCUAUGACUUCATT -3′	Ambion 109789 Silencer® Predesign.
Oligo #2	5′- CGCUAUGAUCUGUACCACATT -3′	Ambion s20403 Silencer® Predesign.

Table 2.15: siRNA oligonucleotides used for silencing

2.2.8 Generating transient transfection cell lines using the calcium phosphate transfection method

Materials

- Cell culture plate with the appropriate cell line up to 80% confluency
- Cell culture plates, 100 mm (Corning BD Falcon, 353003).
- 2x BBS (50 mM BES, 280 mM NaCl, 1.5 mM Na_2HPO_4, pH 6.96)
- 0.25 M $CaCl_2$
- Plasmid of known DNA concentration.
- Plastic tubes 1.5 ml (Eppendorf EP0030120086)
- Complete cell culture medium
- DPBS (Dulbecco’s phosphate-buffered saline) w/o Calcium or Magnesium (Gibco 14190-169).
- Sterile coverslips (Deckglaser cover glasses 12x12 mm)

Methodology

1. 24 h before transfection subculture a confluent cell culture plate and seed 700000-800000 cells for each 100 mm plate for up to 50% confluency on the transfection day (if needed place cvs on the bottom of the plate for cells to grow on).
2. On the day of transfection replace medium with fresh complete medium before the procedure but omit 1ml (7 ml: 8-1 ml).

3. In a 1.5 ml plastic tube add 0.5 ml of 0.25 M $CaCl_2$
4. Add, up to 20 µg of plasmid DNA and aspirate by gently pipetting.
5. Incubate for 5 min on the bench
6. Add 0.5 ml 2x BBS solution dropwise and swirl between fingers to mix the solutions
7. Incubate on bench for another 20 min.
8. Add the mixture in the plate dropwise and aspirate by swirling gently the plate.
9. Incubate at 37°C, 5% CO_2.
10. After 10 h remove medium, wash with DPBS and add fresh medium.
11. After 24 h, transfection is completed and further handling can be applied (Immunofluorescence, SDS-PAGE, WB).

2.2.9 Transfection using the Lipofectamine reagent.

Materials:

- Cell culture plate 100 mm
- Sterile coverslips (Deckglaser cover glasses 12x12 mm)
- DMEM-GlutaMAX (Dulbecco's Modified Eagle Medium) containing 25 mM Glucose, 3.97 mM Glutamine, without Sodium Pyruvate, (Gibco 61965-026).
- FBS (Fetal Bovine Serum) qualified, heat inactivated, (Gibco 10500-064).
- Antibiotics Mixture: Penicillin, 10000 units/mL and Streptomycin, 10000 µg/mL (Gibco 15140-122)
- Sodium Pyruvate, 100 mM, (Gibco 11360-039)
- Complete medium
- DPBS (Dulbecco’s phosphate-buffered saline) w/o Calcium or Magnesium (Gibco 14190-169).
- Opti-MEM cell culture medium (Gibco 51985-026)
- Lipofectamine 2000 reagent (Invitrogen 11668-027)
- Plasmid of known DNA concentration
- Plastic tubes of 1.5 ml (Eppendorf EP0030120086)

Methodology:

1. 24 h prior transfection (t=-24) a confluent cell culture plate is sub-cultured so that at t=0 to be confluent up to 60%. (if needed place cvs on the bottom of the plate for cells to grow).

2. At t=0 remove and replace complete culture medium with fresh consisting only of DMEM-GlutaMAX and FBS at 5% v/v.
3. Label two plastic tubes, the first with “P” plasmid and “L” lipofectamine.
4. Add in both 250 μl Opti-MEM.
5. In the “P” tube add, up to 5μg plasmid and in the “L” tube add, up to 5 μl lipofectamine reagent (1:1).
6. Aspirate gently by pipetting and let both tubes incubate at room temperature for 5 min.
7. Transfer the mixture of the “L” tube to the “P” and aspirate by gently pipetting.
8. Incubate the new mixture at RT for 20 min.
9. Add the mixture of Opti-MEM and Lipofectanine-Plasmid complexes dropwise to the cell culture plate and aspirate with circular movements.
10. The plate is incubated at 37°C, 5% CO_2.
11. At t=4 h the medium is replaced by Complete medium.
12. At t=24 h the cells are transfected and ready for further handling.

2.2.10 Cell viability assays

2.2.10.1 Cell viability assays upon TMEM147 silencing

Materials

- DPBS (Dulbecco’s phosphate-buffered saline) w/o Calcium or Magnesium (Gibco 14190-169).
- 0.25% Trypsine-EDTA (1x) (Gibco 25200-072).
- Trypan Blue Staining Solution (abcam, ab233465)
- Plastic tubes of 1.5 ml (Eppendorf EP0030120086)
- Complete cell culture medium
- Hemocytometer (Weber Scientific, 800.328.8378)

Methodology

1. Subculture cells in a 24x well plate by seeding $15x10^3$ cells in each well
2. Triplicate experiments of TMEM147-silencing, negative control-silencing, and untreated cells are conducted following the silencing protocol in 2.6, as adapted for the 24x well plate format.

3. For each treatment count cell viability at three time points: 24, 48 and 72 h using Trypan Blue Staining solution, each in three different wells on the plate. The counts are also performed at least in triplicate from each well.
4. Cell counting is conducted as follows:
    a. Discard complete medium and wash once with 0.5 ml of DPBS
    b. Add 0.2 ml of 0.25% Trypsine-EDTA (1x), agitate the plate until the surface is covered and incubate at 37°C, 5% CO2, until cells are detached.
    c. Add 0.8 ml complete medium and pipette up and down to break down the cell aggregations and homogenize the mixture.
    d. In a new plastic tube 1.5 ml, add 100 µl of the cell mixture.
    e. Add 100 µl of Trypan Blue Staining solution and pipette to homogenize the new mixture
    f. Place the coverslip on the hemocytometer and gently spread 10 µl of the mixture at each side of the plate.
    g. Give 30 sec to cells to spread evenly, place the hemocytometer under the microscope and observe the cells.
       Dead cells take up the dye due to the loss of membrane function and are labeled as blue while in contrast, the living cells do not take up the dye and are shown as transparent/white
    h. For each side of the hemocytometer, count the cells in the four corner squares and calculate the mean cell number.
    i. Then clean the hemocytometer.
    j. Steps f-i are repeated two more times.
       The resulted six mean values of the viable cells are then used to calculate the final mean cell number which is multiplied by two (1:1 dilution with Trypan Blue Staining solution) represents the number of cells per ml for the experiment investigated.
5. These cell numbers are used to create cell growth plots.

2.2.10.2 Cell viability assays for cholesterol uptake experiment

Materials

- Cell culture plate confluent up to 90% for subculturing
- 24x well plate (Corning CLS3527)

- DPBS (Dulbecco’s phosphate-buffered saline) w/o Calcium or Magnesium (Gibco 14190-169).
- 0.25% Trypsine-EDTA (1x) (Gibco 25200-072).
- Complete cell culture medium
- Complete growth medium omitting FBS addition (serum starvation medium (SS) - Lipid depleted medium)
- Cholesterol solution (Final concentration in well 20 μg/ml)

Methodology

1. Subculture cells in a 24x well plate by seeding 15x10^3 cells in each well
2. Triplicate experiments of TMEM147 silencing and negative control silencing are conducted following silencing protocol as previously described adapted for 24x well cultures.
3. For each treatment the following three conditions are applied after silencing event.
    a. Grow in complete medium for 72 h,
    b. Grow in complete medium for 48 h and then change to serum starvation (SS) medium until 72 h,
    c. Grow in complete medium for 48 h. and change to serum starvation (SS) medium until 72 h with the addition of exogenous cholesterol at a final concentration of 20 μg/ml 8 h prior the completion of 72 h.
4. For each condition and each treatment count cell viability at three time points: 24, 48 and 72 h using Trypan Blue Staining solution as described at 2.2.10.1.

2.3 Protein analysis methods

2.3.1 Protein extraction

Materials

- Cell culture plate with up to 80% confluency
- DPBS (Dulbecco’s phosphate-buffered saline) w/o Calcium or Magnesium (Gibco 14190-144)
- 2x SDS-PAGE sample buffer (200 mM Tris pH 6.8, 20% (v/v) glycerol, 4% (w/v) SDS, 2% (w/v) β-Mercaptoethanol, 0.2% (w/v) Bromophenol Blue)
- 1.5 ml plastic tube (Eppendorf EP0030120086)
- Cell scraper (Corning BD Falcon 353086)

- Insulin syringe (BD Ultra-Fine II 328822)

Methodology

1. Place the cell culture plate on ice and proceed with:
    a. Remove and Discard the cell culture medium from the cell culture plate.
    b. Add 5ml DPBS to wash the remaining medium from the plate.
    c. Completely remove and discard DPBS.
    d. Add 200 μl 1x SDS-PAGE Sample buffer and agitate the plate until the surface is fully covered.
    e. Use the cell scraper to detach the cells from the plate and transfer them in a 1.5 ml plastic tube with a pipette.
2. The mixture of the cells then is lysed combining the use of sound wave short pulses under ice-cold conditions employing a sonicator and passing the lysate through a fine needle syringe (insulin syringe).
3. The tube with the lysate is then boiled to 60°C for 5 min and then centrifuge at 13000 rpm for 2 min.
4. The protein extract is ready for SDS-PAGE electrophoresis or to be stored in -20°C.

2.3.2 Electrophoresis of proteins on Sodium Dodecyl Sulfate Poly-Acrylamide Gel Electrophoresis (SDS-PAGE)

Materials

- dH2O
- Acrylamide:Bis Acrylamide (19:1) 40% (w/v) (Biorad 161-044)
- 1.5 M Tris-HCl, pH 8.8
- 10% (w/v) SDS
- TEMED (N,N,N′,N′-Tetramethylethylenediamine) (Sigma T9281-25ML)
- 1x Running buffer, pH 8.3 25 mM Tris, 192 mM Glycine, 0.1% SDS (w/v)
- 20% isopropanol
- Protein markers (BlueStar Prestained Protein Marker, Bis-Tris 10% w/v MES buffer, Nippon Genetics Europe MWP03)
- Separating Gel (10%)
  Tris-Cl 1.5 M (pH 8.8), Acrylamide 10% (w/v), 47.9% dH2O (v/v), 0.1% SDS (w/v), 0.1% APS (w/v), 0.1% TEMED (v/v)

- Stacking Gel (5%)
  Tris-Cl 0.5 M (pH 6.8), Acrylamide 5% (w/v), 71.375% dH2O (v/v), 0.25% SDS (w/v), 0.1% APS (w/v), 0.125% TEMED (v/v)
- Mini-PROTEAN Electrophoresis System (BIO-RAD 1658001)

Methodology

1. Set the casting apparatus.
2. Prepare the separating gel and immediately after the addition of TEMED pour the mixture between the two glasses leaving enough space for the stacking gel (1-2 cm). To force the top of the gel to be horizontal and to prevent the gel from drying add 5ml of isopropanol between the two glasses. Let the mixture to polymerize and solidify
3. Remove the isopropanol and wash out the remaining traces of isopropanol with distilled water.
4. Prepare the stacking gel leaving for last the addition of TEMED.
5. Immediately after the addition of TEMED pour the mixture between the glasses on top of the separating gel and add the comb making sure no bubbles were trapped.
6. Let the gel to polymerize and solidify
7. Clamp the glasses and the containing gel into the apparatus and fill both buffer chambers with gel running buffer.
8. Cautiously use a long-tipped pipette to load molecular mass protein markers and the protein samples into the wells.
9. Close the lid of the apparatus and apply potential difference of 100 V until the sample's front riches the lower end of the separating gel.

2.3.3 Protein Transfer to Nitrocellulose membrane (Wet Transfer)

Materials

- Nitrocellulose membrane (9x6 cm) (Porablot NCP, Macherey-Nagel 741280)
- Filter paper (10x8 cm)
- Foam pads for liquid transfer
- Transfer buffer (48 mM Tris-HCl, 39 mM Glycine, 20% (v/v) Methanol)
- dH_2O
- Electrophoretically separated proteins on acrylamide gel (casting glasses and the stacking gel are removed).

- Mini Trans-Blot Electrophoretic Transfer Cell (BIO-RAD 170-3930)

Methodology

10. Let the foam pads and the filter papers to soak in cold transfer buffer for at least 10 min until nitrocellulose membrane is ready.
11. Let the nitrocellulose membrane to soak for 2 min in dH_2O and then in transfer buffer for at least 10 min.
12. Open the cassette and on the negative side put sequentially the following: fiber pad, filter paper, gel with electrophoretically separated proteins, nitrocellulose membrane, filter paper and fiber pad. Ensure that no bubbles were entrapped between gel and nitrocellulose membrane by pushing them out with a roller.
13. Close the Mini Gel Holder Cassette, place it in the Mini Trans-Blot Central Core and that in the tank.
14. Place the Bio-Ice Cooling unit in the tank and fill the tank with cold transfer buffer until the cassette is covered.
15. Apply potential difference of 100 V for 1 h.

2.3.4 Western Blot Immunostaining

Materials

- Nitrocellulose membrane with electrophoretically transferred separated proteins
- 1x PBS pH 7.4 Buffer (13.5 mM NaCl, 2.7 mM KCl, 10 mM Na_2HPO_4, 1.75 mM KH_2PO_4)
- PBS/ 0.1% Tween-20 Solution buffer: 1x PBS, 0.1% (v/v) Tween-20
- Blocking buffer:
  - 5% (w/v) skimmed milk in PBS/Tween-20 solution buffer or
  - 0.1% Tween-20 (v/v) in 1x PBS.
- Primary antibody solution in Blocking buffer
- Secondary antibody solution in Blocking buffer
- ECL Buffers:
  - Buffer A: 0.1 M Tris-HCl pH 8.5, 2.5 mM Luminol, 0.45 mM Coumaric Acid
  - Buffer B: 0.1 M Tris-HCl pH 8.5, 0.006% H_2O_2.

Methodology

1. After the protein transfer is complete, remove the nitrocellulose membrane from the cassette and incubate in Blocking buffer for 1h.
2. Wash the membrane for 10 min in PBS/ 0.1% Tween-20.
3. Incubate the membrane in primary antibody solution for 16-18 h at 4°C
4. Wash the membrane three times with PBS/ 0.1% Tween-20 for 10 min each wash.
5. Incubate the membrane in secondary antibody solution for 1h at room temperature.
6. Wash the membrane twice with PBS/ 0.1% Tween-20 for 15 min each wash.
7. Wash the membrane once with PBS for 10 min.
8. Prepare the two ECL buffers and mix them well.
9. Incubate the nitrocellulose membrane for 1 min with the mixed ECL buffer
10. Chemiluminescence signal of the proteins on the nitrocellulose membrane is detected and observed in Syngene G:Box employing GeneSys software.
11. Images are stored for further analysis in digital format (.tiff).

2.3.5 Stripping and reprobing of the nitrocellulose membrane

After the first immunoblotting of the nitrocellulose membrane, the antibody complexes hybridized to the proteins on the membrane can be stripped off and the membrane can be reprobed with antibodies detecting different proteins that could not be detected before.

Materials

- Previously used immunostained nitrocellulose membrane
- 0.2 M NaOH solution
- PBS/ 0.1% Tween-20 Solution buffer: 1x PBS, 0.1% (v/v) Tween-20

Methodology

1. Wash the used membrane once, with PBS/ 0.1 Tween-20 for 5 min.
2. Incubate the membrane for 5-10 min in 0.2 M NaOH solution.
3. Wash the membrane three times in PBS/ 0.1% Tween-20 for 5 min each.
4. When the last wash is finished, follow the Western Blot Immunostaining protocol from the start (Incubation in Blocking Buffer)

2.3.6 Co-Immunoprecipitation (co-IP) analysis of protein interactions.

Materials

- Appropriate cell pellet

- Co-IP solution buffer (50 mM Tris-HCl pH 7.6, 150 mM NaCl, 2 mM EDTA, 1% NP-40, 1x Protease inhibitor)
- 1.5 ml plastic tube (Eppendorf EP0030120086)
- GFP-Trap Agarose beads (Chromotek, gta-20)
- 2x SDS-PAGE Sample buffer (200 mM Tris pH 6.8, 20% (v/v) glycerol, 4% (w/v) SDS, 2% (w/v) β-Mercaptoethanol, 0.2% (w/v) Bromophenol Blue)

Methodology

1. Resuspend the cell pellet in 600 μl of co-IP buffer.
2. Lyse the cells employing sound waves (sonication) in short pulses while the tube is in ice avoiding the formation of foam.
3. Let the tube with the cell lysate rest on ice for 30 min. During this period agitate the container gently twice.
4. Centrifuge the lysate for 30 min at 13000 rpm at 4°C
5. 5 min prior cell extract centrifugation is finished, beads are prepared:
    a. 10 μl of slurry beads mixture (For each reaction) is transferred in a new tube.
    b. Wash the beads by adding 200 μl of co-IP buffer in the tube.
    c. Centrifuge at 1000 rpm for 2 min at room temperature (RT).
    d. Discard the supernatant with cautious
6. Carefully observe if there is a lipid layer floating on the surface of the supernatant after centrifugation and remove.
7. Remove 65 μl of the sample labeled as input and keep on ice
8. Transfer the rest of the supernatant in the tube containing the washed beads.
9. Incubate the beads and the cell extract on a carousel for 2 h at RT.
10. Quantify the protein concentration in the extract of the input sample to normalize input and flow-through loading samples later on in SDS-PAGE.
11. After beads incubation is over centrifuge at 1000 rpm for 2 min at RT
12. Carefully transfer 500 μl of the supernatant in new tube and label as flow-through.
13. Wash the beads three times by adding 500 μl co-IP buffer (protease inhibitor can be omitted at this step from the buffer) incubate on carousel for 2 min and centrifuge at 1000 rpm for 2 min at RT.
14. Discard the supernatant as carefully as possible.
15. Add 30 μl of 1x SDS-PAGE sample buffer in the beads tube (bound fraction).

16. Add appropriate volume of 1x SDS-PAGE Sample buffer in input and flow-through samples.
17. Boil Input, flow-through and beads samples at 60°C for 10 min and centrifuge at 13000 rpm for 5 min at RT.
18. Samples are then separated by SDS-PAGE followed by Western Blot immunostaining (see previous sections).

2.3.7 Protein Quantification using the Image-J software.

Stored images of Western Blot Immunostaining or Immunoprecipitation experiments in tiff format, were processed in Image-J v1.52p software to quantify the detected levels of the different proteins of interest. The software quantifies the intensity of each pixel within the bands of the proteins subtracting the background and the values can be then exported and transferred in excel for further processing and statistical analysis.

2.3.8 Further processing and Statistical analysis of the quantified protein levels.

Protein quantified levels using Image-J prior the statistical analysis, were normalized to the levels of the housekeeping protein GAPDH (protein levels do not change during the different experimental conditions applied). Protein levels from triplicate experiments were used to determine the mean value and the standard error or standard deviation, whereas the statistical significance of the observed altered phenotype was analyzed by student’s t-test.

2.4 Immunofluorescence

2.4.1 Permeabilization and fixation methods

Materials

- Coverslips with cell coverage up to 80%
- Sterile Tweezers
- 1x PBS pH 7.4 Buffer filtered (13.5 mM NaCl, 2.7 mM KCl, 10 mM Na_2HPO_4, 1.75 mM KH_2PO_4)
- PHEM solution filtered: 30 mM HEPES, 60 mM Pipes pH 6.9, 10 mM EGTA, 2 mM MgCl2.
- Fixation solution: Paraformaldehyde (PFA) 4% (w/v) in PHEM ph 8.0
- Permeabilization Solution: 0.5% (v/v) Triton-X in PHEM

- Quenching solution: 50 mM NH4Cl in DPBS
- 12x well plate (Corning CLS353043)
- Filter paper

Methodology

1. Using the sterile tweezers remove each coverslip from the tissue culture plate and wash it twice in PBS by immersing the cvs in a small beaker with PBS
2. Cautiously dry the cvs on a filter paper.
3. Place the cvs in a well from a 12x well plate containing 1-2 ml fixation solution.
4. Incubate in fixation solution for 10 min.
5. Remove the fixation solution and add permeabilization solution for 5 min at RT.
6. Remove the permeabilization solution and add 3 ml PHEM solution to wash three times.
7. When the last wash is finished, add quenching solution and incubate for 10 min at RT.
8. Remove quenching solution and add PBS.
9. Immunofluorescence staining protocol can be immediately initiated or store in 4°C no more than two weeks.

2.4.2 Immunofluorescence Staining

Materials

- Tube Rack covered with Parafilm
- Microscope slides
- Tweezer with fine tip.
- PHEM solution filtered: 30 mM HEPES, 60 mM Pipes pH 6.9, 10 mM EGTA, 2 mM $MgCl_2$.
- Wash solution: Tween-20 0.1% (v/v) in PHEM
- Blocking solution: 2% (w/v) FBS, 2% (w/v) BSA, 0.2% (w/v) fish skin gelatin, in DPBS
- Primary antibody: appropriate dilution of the first antibody in 5% blocking solution
- Secondary antibody: appropriate dilution of the first antibody in 5% blocking solution
- 1x PBS pH 7.4 Buffer filtered: 13.5 mM NaCl, 2.7 mM KCl, 10 mM Na_2HPO_4, 1.75 mM KH_2PO_4.

- Hoechst 1mg/ml (1:10000) for DNA staining.
- Mounting medium for fixing the coverslips on the microscope slide (DABCO).

Methodology

For the following procedure the volume of the solutions used, except washing solutions, are applied directly on the coverslips until they are fully covered (20-30 μl).

1. With the use of a tweezer remove the coverslips from the 12-well plate and place them on a tube-rack covered with parafilm.
2. Immediately after placing each cvs cover them with a droplet of washing solution.
3. When all cvs are placed on the rack remove wash solution add blocking solution and incubate for 1 h at RT to prevent non-specific staining.
4. Remove blocking solution and add the primary antibody at an appropriate dilution, or a mixture of the primary antibodies when double staining is attempted and incubate over night at 4°C.
5. Let 16-18 h to pass and wash the cvs three times with wash solution for 3 min each by completely covering each time the cvs.
6. Apply the appropriate secondary fluorophore antibody specific for the primary antibody and incubate for 1 h at RT.
7. Wash the cvs twice with washing solution for 3 min each and then wash with filtered PBS.
8. Remove PBS and incubate in Hoechst for 10 min at RT, for DNA staining.
9. Wash the cvs with PBS for 3 min.
10. While waiting, on the surface of a clean microscope slide add a droplet of mounting medium.
11. Take the coverslip with the tweezer and carefully discard the remaining liquid by touching its edge on a filter paper and place it upside down on the droplet of mounting medium.
12. Let microscope slides to dry and mounting medium to set for 24 h at RT in a dark place.
13. The slides are then ready for immediate microscopic observation or can be stored in -20°C for future use.

2.4.3 Microscopy

Microscope imaging was performed on an upright fluorescence Carl Zeiss Axiovert 200M microscope and the coverslips were visualized using an Apochromatic x63 magnification and 1.4 NA oil lens and wavelength filters for blue, green (488 nm) and red (568 nm) bands. The images were acquired using the high sensitivity digital camera AxioCam HRc for multicolor fluorescent images along with the Zeiss software Axiovision, v4.8.2.SP2.

A Leica TCS SP2 DMIRE2 confocal microscope using 63x 1.4NA oil immersion objective lens. The images were acquired with LSM Zen or Leica LAS (v.4.1.0) software.

For comparison, all images were taken by maintaining the same acquisition settings across samples.

All images were processed using Adobe CC Photoshop and figures assembled with Adobe Illustrator software.

2.5 Morphometric Analysis

2.5.1 Nuclear alterations after silencing of TMEM147 (LBR staining)

A number of 103 Hela cells images, n=55 control and n=48 siRNA mediated TMEM147 silenced cells, from three independent experiments, were acquired using Leica TCS SP2 DMIRE2 confocal microscope, maintaining the same acquisition settings across control and respective silenced samples. The stacks generated were processed by *Imaris* (Bitplane AG, v 9.2.1) to determine morphological parameters of area volume, oblate ellipticity, prolate ellipticity and sphericity, along with the mean fluorescence Intensity for LBR (green) and Hoechst (blue).

2.5.2 Analysis of ER morphological alterations after silencing of TMEM147 (CLIMP63/RTN4 staining)

A number of 457 Hela cells images, n=225 control and n=232 siRNA mediated TMEM147 silenced cells, from three independent experiments, were acquired using the upright fluorescence Carl Zeiss Axiovert 200M microscope as mentioned earlier. Acquisition settings used across control and respective silenced samples in all images, were kept the same. Afterwards, the images acquired were processed in Image-J v1.52p, to determine the area in pixels, labeled from CLIMP63 staining and RTN4 staining, indicating the flattened cisternae and tubular areas of the ER respectively of each cell after subtracting the signal corresponding to the nucleus area as it was background. In order to do this, the origins of each cell were manually selected as a region of interest (ROI). For each cell thresholding algorithms were applied to determine the area of flattened domains corresponding to CLIMP63 staining and tubular domains corresponding to RTN4. The total area of ER was determined by overlapping the two thresholded areas counting overlapping pixels only once.

2.6 3D rendering

Serial confocal z-stacks of HeLa nuclei of the same three independent silencing experiments (control and treated) were processed in *Imaris* (Bitplane AG, v 9.2.1), to render 3D models. 3D reconstruction of each nucleus was generated using the "new surface" algorithm setting the surface detail magnitude at 0.250μm followed by manual thresholding until voxels covered the entire surface of the nucleus according to LBR labeling. Snapshots of 3D images were acquired to compare the localization of LBR in control and TMEM147-silenced cells.

2.7 Lipidomics

Lipidomic analysis was based on the protocol described in (Özbalci et al., 2013) and was carried out by the group of Prof. B. Brügge at the Biochemistry Center (BZH), University of Heidelberg.

2.8 Cellular cholesterol uptake assay.

Materials

- Cholesterol Uptake Assay Kit (Abcam ab236212)
- 96-well plate (Corning CLS9017)
- Complete medium
- Lipid depleted medium
- Cholesterol transport inhibitor U-18666A

Methodology

To analyze the uptake of cholesterol in control and silenced cells Abcam kit Ab236212 was used. This assay employs NBD-cholesterol (Fluorescently-tagged cholesterol) as a probe to estimate the lipoprotein-mediated cholesterol uptake (Huang et al., 2015, Frolov et al., 2000).

1. Silencing of TMEM147 protocol was conducted as previously described with the appropriate controls.
2. Use a 96-well plate to culture TMEM147 silenced and control silenced cells.
3. After 48 h have passed remove and discard growth medium and then apply the following conditions.
    a. Add complete medium and culture for 24 more h
    b. Add lipid depleted medium and culture for 24 more h
    c. Add lipid depleted medium supplemented with U-18666A at 1 μM for 24 more h
4. In each condition add fluorescently tagged NBD-cholesterol at 20 μg/ml.
5. At the 72 h time point the fluorescence emission was quantified with an FITC/GFP filter set.

2.9 Statistical Evaluation

2.9.1 Statistical analysis of images of nuclear alterations after silencing of TMEM147 (LBR labeling)

The statistical difference between control and silenced cells for the multiple continuous morphometric variables was calculated by MANOVA using Pillai's test at a statistical significance α=5% in Excel (Microsoft Office, 2016) and XLSTAT by Addinsoft. Following MANOVA the parameters were individually analyzed for further statistical significance discoveries by Mann-Whitney test using Prism 8 (Graphpad) and p- value was adjusted by using the false discovery rate approach by the two-stage linear step-up procedure of Benjamini, Krieger and Yekutieli setting the Q=5%.

For the same three independent silencing experiments, the observed increased ER localization of the LBR in silenced treated cells, was tested for statistical significance compared to control cells, by applying two-sided Fisher's exact test in Prism 8.0 (Graphpad).

2.9.2 Statistics on cell growth assay results

The results of the triplicate cell growth assays comprising two treatments and three conditions were processed in excel for mean and s.e.m. Normality of the results was confirmed with Shapiro-Wilk test and then parametric comparisons were used for statistical evaluation with one-way ANOVA based on the two-stage linear step-up procedure of Benjamini, Krieger and Yekutieli (Q=5%) to determine discovery in GraphPad Prism 8.0.

2.9.3 Statistics and group-wise comparisons of images based on DNA staining, CLIMP63 and RTN4 labeling after silencing of TMEM147.

Statistics and group-wise comparisons for image analyses based on DNA, CLIMP63 and RTN4 fluorescence measurements after TMEM147 silencing were based on composite images for a total of 457 HeLa cells. Box-and-whisker diagrams displaying all values were based on raw data for all cells, whereas bar charts and group-wise comparisons were based on data after outlier removal using the 1.5x IQR rule (Tukey, 1977), resulting in evaluable data for 362 HeLa cells (n=177 control, n=185 silenced). These data were tested for statistical significance between untreated and treated cells by MANOVA analysis using Pillai's test at a statistical significance α=5% in Excel (Microsoft Office, 2016) and XLSTAT (Addinsoft).

2.9.4 Statistics on Lipidomics

Data obtained from MS were evaluated using LipidView (ABSciex) and an in-house-developed software (ShinyLipids). Statistical evaluation of comparisons was assessed by multiple t-test with multiple testing correction, based on an FDR of <0.05. For lipidomics, multivariate statistics analyses were performed in MetaboAnalyst version 4.0. All variables were log transformed and scaled by performing mean-centering and division by the standard deviation of each sample. All variables were then subjected to an unsupervised principal component analysis (PCA), generating a scores plot showing the variance in the dataset. The loadings plot for the generated model was used to determine which variables drive the separation between classes. The most discriminant variables were visualized using univariate statistics. For univariate statistics, GraphPad Prism 8.0 software was used. All data were expressed as mean±s.e.m. In GraphPad, one- or two-way ANOVA was performed where appropriate. For one-way ANOVA, Dunnett's post hoc multiple-comparisons test was performed, while for two-way ANOVA, Sidak's post hoc multiple-comparisons test was used.

2.9.5 Statistics on cellular cholesterol uptake assays

Cholesterol uptake assay was conducted in triplicate for each condition. The fluorescence emission was normalized to the concentration of proteins deduced for the same wells using BCA assay. An extra set of experimental conditions were used for the background subtraction for either TMEM147-silenced or control-silenced cells. Excel was used to calculate the mean and s.d. for each condition and statistical significance was determined employing multiple t-tests with multiple testing correction in GraphPad Prism 8.0. using one unpaired t-test per row without assuming a consistent s.d. and applying the two-stage linear step-up procedure of Benjamini, Krieger and Yekutieli (Q=5%) to determine discovery.

2.10 Bioinformatics and Statistical Evaluation

2.10.1 Network analyses

Reported TMEM147 targets, direct, indirect and same-complex interactors, co-regulated and co-expressed proteins were identified and manually curated for redundancy and spurious or erroneous database entries based on the following repositories: APID (Alonso-Lopez et al., 2019), BioGRID, GeneMania (Warde-Farley et al., 2010), GPS-Prot (Fahey et al., 2011), Human Protein Reference Database (Keshava Prasad et al., 2009, Peri et al., 2003), IntAct EMBL-EBI (Orchard et al., 2014), HuRi (Luck et al., 2020), PubMed, Pathwaycommons (Cerami et al., 2011), PINA (Wu et al., 2009, Cowley et al., 2012), Reactome (Jassal et al., 2020), STRING (Szklarczyk et al., 2019), with identifiers and annotations from UniProt (UniProt, 2008).

The resulting list of 98 protein factors plus TMEM147 were used as a list of input proteins in String-db.org 11.0b (https://version-11-0b.string-db.org) (Szklarczyk et al.), applying as settings full network analysis, network edges representing evidence, using all active interaction sources, applying 0.150 as the required interaction score and displaying only the query proteins and no additional layers of secondary interactors. The network output images were manually curated to align unlinked protein factors outside the network, to apply the official HUGO gene symbol where String-db applied alternative protein names and to include the legend.

2.10.2 Pathway reduction

Significant Gene Ontology Molecular Function nodes derived from String-db were imported with their corresponding false discovery rate (FDR) values to the Reduce and Visualize Gene Ontology (REVIGO) (http://revigo.irb.hr) tool (Supek et al.), in order to remove redundant GO terms and interpret more readily the underlying enrichment analysis. The settings applied were the choice of Small (0.5) for the resulting list, the provision of P value (as the most suitable choice) for associated values, the removal of obsolete GO terms, the choice of Homo sapiens as target species and the choice of the default SimRel semantic similarity measure. The resulting output of this analysis is included in the non-redundant GO terms table whereas its graphical representations in TreeMap, Scatterplot and Interactive Function graphs in the corresponding result sections.

2.11 Antibodies

The antibodies used in this thesis are shown in the following table.

Application	Antibody	Species	Dilution	Source
Primary Antibodies				
WB	TMEM147	Mouse	1:7	Haffner et al., 2010
WB, IF	LBR	Rabbit	1:300	Abcam
IF	LAP2β	Mouse	1:500	BD Transduction Labs
WB	emerin	Rabbit	1:300	Abcam
WB	LEM4	Rabbit	1:100	(Asencio et al., 2012)
WB, IF	calnexin	Rabbit	1:200	Santa Cruz
WB	DHCR7	Rabbit	1:300	Acris
WB	GABDH	Mouse	1:500	Santa Cruz
WB, IF	GFP	Rabbit	1:1000	(Yavuz et al., 2010)
IF	CLIMP63	Mouse	1:1000	ALEXIS Biochemicals
IF	RTN4	Rabbit	1:300	Abcam
Secondary Antibodies				
WB	anti-mouse IgG-HRP	Donkey	1:5000	Santa Cruz
	anti-rabbit IgG-HRP	Donkey	1:10000	Santa Cruz
IF	anti-Rabbit IgG Alexa Fluor 488	Donkey	1:1000	Molecular Probes
	anti-Rabbit IgG Alexa Fluor 555	Donkey	1:1000	Molecular Probes
	anti-Mouse IgG Alexa Fluor 555	Donkey	1:1000	Molecular Probes

Table 2.16: List of antibodies

WB: Western Blot Immunostaining, IF Immunofluorescence staining

3

Results

Chapter 3: Results

3.1 TMEM147 localizes at the ER and NE in HeLa cells

One of the topics of interest in our research laboratory is the study of ER morphogenesis in human cells, publishing work on the characterization of TMEM170A, a transmembrane protein present in both ER membranes and the NE (Christodoulou et al., 2016). In this work, expression levels of TMEM170A were found to affect the shape and morphology of the ER. Transmission electron microscopy (TEM) showed that upon depletion of TMEM170A, the ER was disorganized and its symmetrical distribution around the nucleus was lost while aggregates of tubular ER were formed. In contrast, upon TMEM170A upregulation, there was concomitant ER sheet upregulation, suggesting that TMEM170A was a newly-discovered ER-sheet promoting protein. Furthermore, depletion of TMEM170A altered nuclear shape and size, decreased the density of nuclear pore complexes in the nuclear envelope and caused either a reduction in inner nuclear membrane (INM) proteins or their relocalization to the ER. Moreover, the reticulon family protein RTN4, a known inducer of ER tubule formation, was shown to physically interact with TMEM170A while their effect proved to be antagonistic as all three phenotypes (ER subdomain induction, NE formation and nuclear pore complex (NPC) assembly and density) were rescued upon their concurrent downregulation. (Christodoulou et al., 2016).

Extending our research on ER morphology, my own work focused on the characterization of another transmembrane protein in human cells, TMEM147 (NM_032635.4). As a starting point, we wished to revisit the issue of its localization, shown by earlier studies to be at the ER ((Dettmer et al., 2010, Rosemond et al., 2011). Because of the lack of a commercially available anti-TMEM147 antibody performing well in immunofluorescent experiments, we first performed transient transfection experiments in HeLa cells using a full-length construct of TMEM147 tagged with the FLAG epitope at its N-terminus. Our findings show localization of FLAG-TMEM147 at the ER in agreement with previous observations by Dettmer and Rosemond (Dettmer et al., 2010, Rosemond et al., 2011), and also at the nuclear rim (Fig. 3.1A1 and A2), as can also be seen, on closer inspection, in Cos-7 cells in images by Rosemond and co-workers (Rosemond et al., 2011).

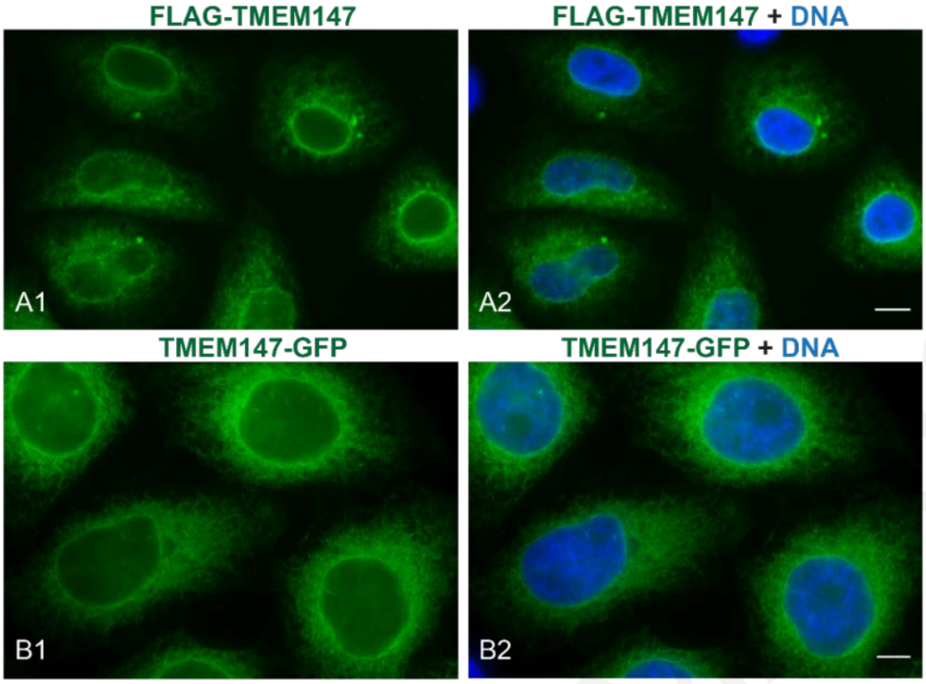

Figure 3.1: Localization of TMEM147 at the ER and NE.
(A1, A2) Labeling of the ER and the NE in immunofluorescence images of HeLa cells transiently transfected with recombinant plasmid vector expressing FLAG-tagged TMEM147. FLAG-TMEM147 corresponds to the green fluorescence whereas, DNA labeling corresponds to blue fluorescence in overlay images.
(B1, B2) Immunofluorescence images of HeLa cells stably expressing GFP tagged TMEM147. Green labeling corresponds to TMEM147-GFP while DNA labeling corresponds to blue fluorescence in overlay images.
For both FLAG- and GFP-TMEM146, localization is at the ER and at the rim of the nucleus.
Scale bars: A1, A2:5 μm; B1, B2: 10 μm

The need of a suitable detection tool of TMEM147 for further experiments, led us to construct a stable TMEM147-GFP HeLa cell line, with a C-terminal GFP fusion of TMEM147. Consistent with our initial observations, this construct showed the same localization as the FLAG-tagged version (Fig. 3.1B1 and B2). Localization of TMEM147-GFP at the ER membranes was confirmed with double labeling for calnexin (Fig. 3.2A1-A3) and at the NE with double labeling for LAP2β (Fig. 3.2B1-B3) as an inner nuclear membrane marker.

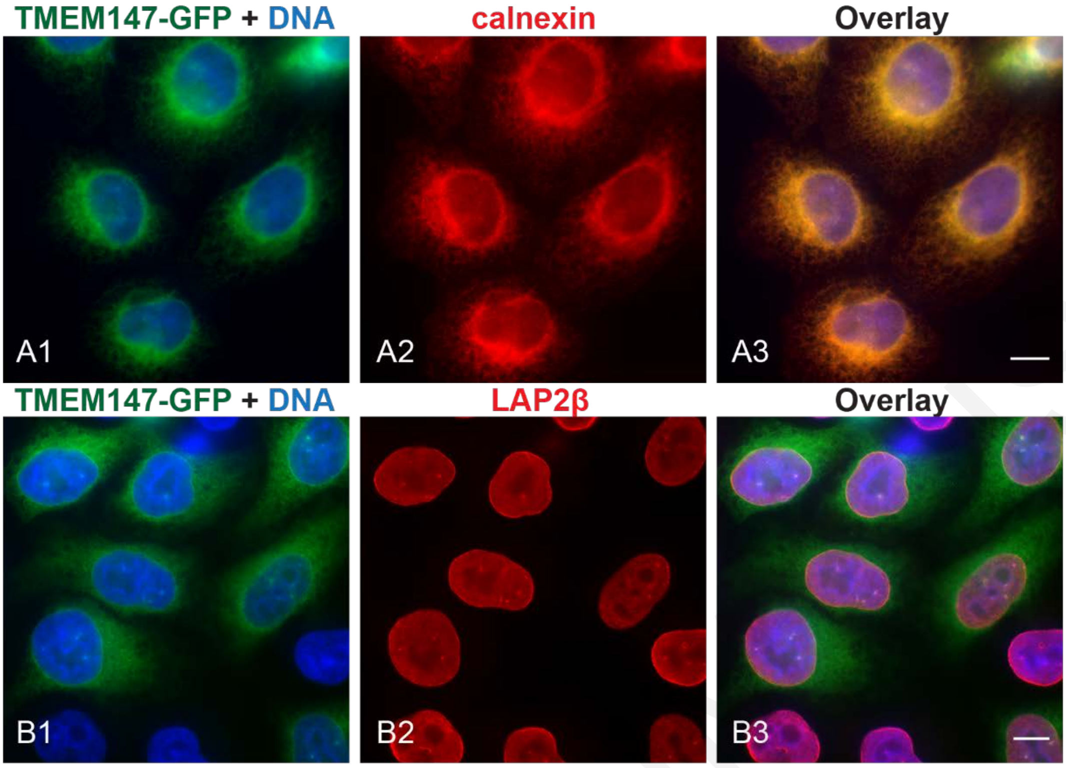

Figure 3.2:Confirmation of TMEM147 localization at the ER and NE.
(A1-A3) Immunofluorescence images of HeLa-TMEM147-GFP cells labeled for the ER marker calnexin. Overlay image (A3), shows calnexin labeling (A2) and TMEM147-GFP labeling (A1) as overlapping regions, confirming the ER localization of TMEM147. Blue staining (A1), corresponds to DNA labeling.
(B1-B3) Immunofluorescence images of HeLa-TMEM147-GFP cells labeled for the INM marker LAP2β. Overlay image (B3), shows LAP2β labeling (B2) and TMEM147-GFP labeling (B1) overlapping on a yellow rim around the nucleus, confirming the NE localization of TMEM147. Blue staining (B1) corresponds to DNA labeling. Scale bars: 10 μm.

3.2 Establishing the conditions for the efficient TMEM147 silencing

After determining the localization of TMEM147 in the ER and NE, we wanted to investigate its functional role in cells and our first approach was by means of siRNA-mediated silencing. We performed TMEM147 silencing in either wt. HeLa or the stable cell line HeLa-TMEM147-GFP and quantified both mRNA and protein levels of TMEM147 by comparing negative control-silenced and TMEM147-silenced cells.

Upon repeated silencing, experimental conditions were optimized, leading to robust silencing of TMEM147 mRNA, as was confirmed by RT-qPCR. Samples of mRNA extract from three independent silencing experiments paired to three mock (negative control, without siRNA, see 2.2.6) silencing experiments using wt. HeLa cells were collected and analyzed by RT-qPCR. The analysis showed that TMEM147 mRNA levels were reduced up to 97.9±1.87% (mean±s.e.m., or reduced to 2.10±1.87%), when expressed as a ratio to the normalized negative control, equal to a 47.42 expression reduction factor. Moreover, statistical analysis of this reduction indicated an extremely significant knockdown effect, with p-value lower than 0.0001 ($p<0.0001$) (Fig. 3.3).

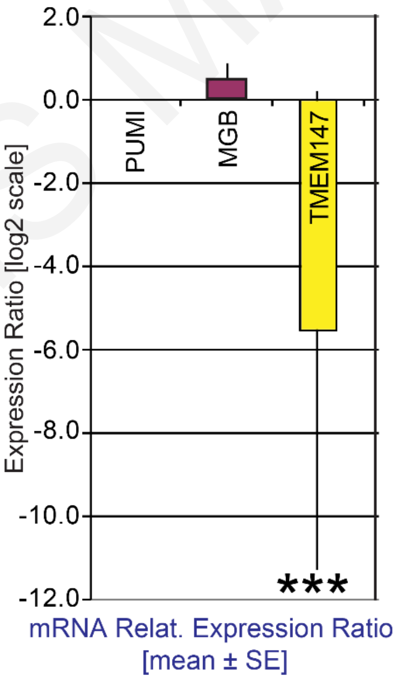

Figure 3.3: Quantification of TMEM147 mRNA levels in TMEM147-silenced wild-type HeLa cells.
The levels of TMEM147 mRNA in silenced HeLa cells was quantified by RT-qPCR in three independent experiments showing a statistically significant decrease to 2.10±1.87% (mean±sem) of negative control silenced cells, $p<0.0001$. For sample normalization purposes, the mRNA level of the housekeeping gene PUM1 was used, and, as an unrelated control, the relative change of the mRNA levels of mammaglobin B-2 (MGB) was also quantified.

Protein extracts from corresponding experiments were also collected in parallel and quantitative Western Blot (WB) analysis was conducted. Native TMEM147 protein levels were detected with the use of a monoclonal antibody, suitable for immunoblotting and kindly provided by Dr. Christof Haffner (Dettmer et al., 2010), showing a significant reduction of TMEM147 protein levels in wt. HeLa silenced cells to 13.36±2.27% (mean±s.d.; p=0.0011) of negative control cells (Fig. 3.4A and B).

Silencing experiments were repeated with the stable cell line HeLa-TMEM147-GFP as well. When WBs were probed by either anti-GFP or anti-TMEM147 antibodies, there was a clear reduction of the signal for both exogenous TMEM147-GFP and endogenous TMEM147, compared with negative controls (Fig. 3.4C). Furthermore, immunofluorescence images acquired from the same silencing experiments of the stable cell line, where GFP signal is used as a proxy for TMEM147-GFP expression, indicated an apparent loss of GFP signal compared with negative control cells (Fig. 3.4D).

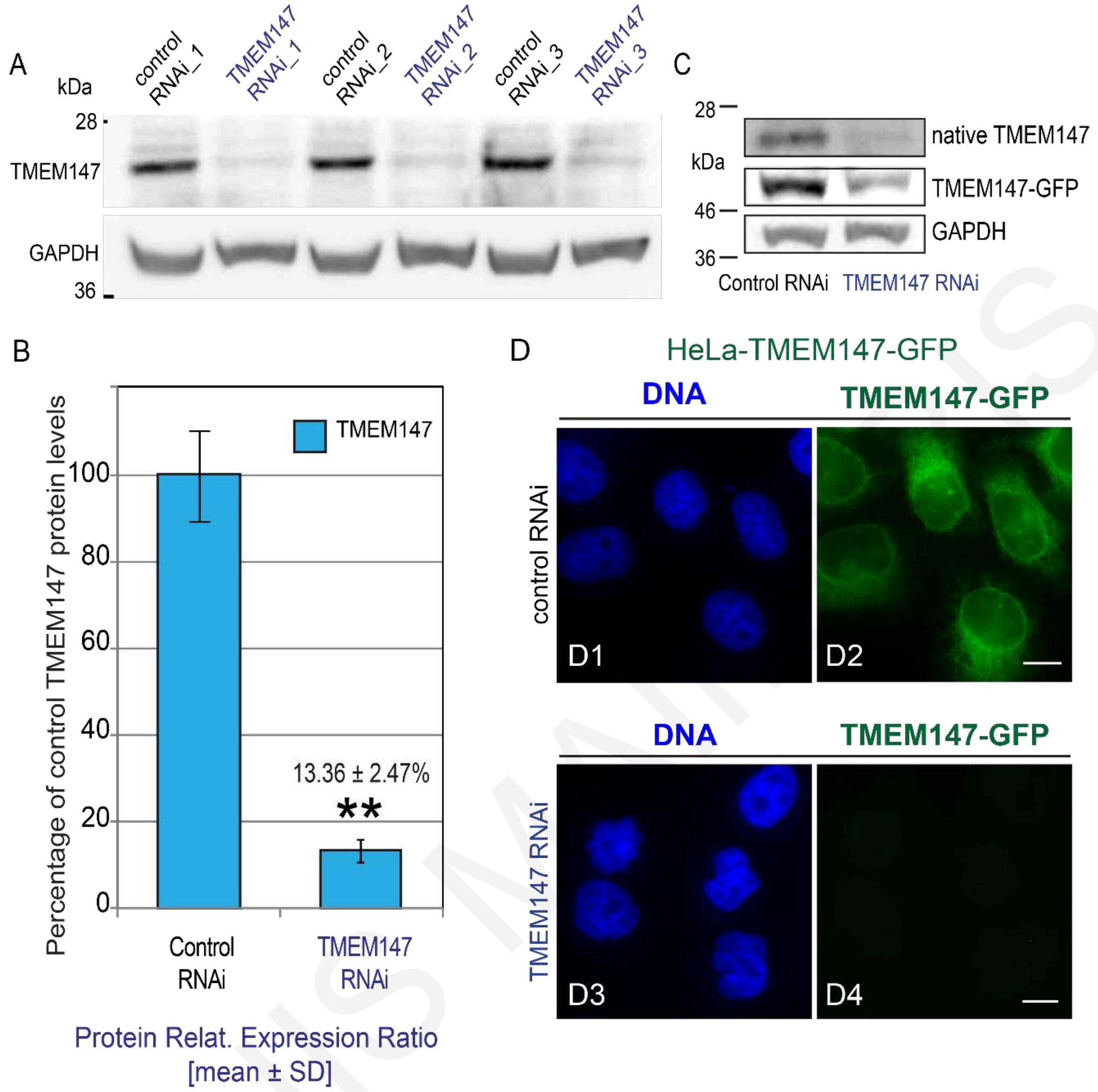

Figure 3.4:Quantification of TMEM147 protein levels in wild-type HeLa cells and further confirmation in HeLa-TMEM147-GFP stable cell line.

Protein extracts of HeLa cells from three independent TMEM147-silencing experiments were analyzed by WB. (A) shows the corresponding drastic downregulation of TMEM147 in 3 independent experiments (upper panel), GAPDH was used for normalization across samples (lower panel). (B) Quantification of the WB analysis shown in A revealed a statistically significant dramatic decrease in TMEM147-protein levels to 13.36±2.47% (mean±s.d.; p=0.0011) compared with negative controls, as assessed by a one-tailed heteroscedastic t-test. Normalization was to the corresponding GAPDH signals, as shown in lower panel of (A).

Silencing of TMEM147 in the stable cell line HeLa-TMEM147-GFP exhibited a protein decrease in both endogenous TMEM147 and exogenous TMEM147-GFP proteins, as shown in WB analysis (C) and observed in immunofluorescence images in (D). Labeling of TMEM147-GFP was used as a proxy for TMEM147in the absence of a suitable antibody for IF. Labeling of TMEM147-GFP is dramatically decreased in silenced cells (D4) compared with the control cells (D2). Image acquisition settings were identical for panels D2 and D4 to allow direct comparison. Blue staining corresponds to DNA labeling (D1 and D3). Scale bars: 10 μm.

3.3 Silencing of TMEM147 downregulates protein levels of Lamin B Receptor (LBR)

Having established the conditions for robust TMEM147 silencing, we subsequently wished to further characterize the resulting phenotypes as a tool for its functional characterization.

An early observation we made in TMEM147 RNAi experiments was that, upon silencing, a cell-death-related phenotype was apparent after 48h post transfection. TMEM147 silencing appeared to be affecting cell growth at the later stages, as cell viability was decreased compared with negative control or untreated cells shown by cell viability experiments (Fig. 3.5).

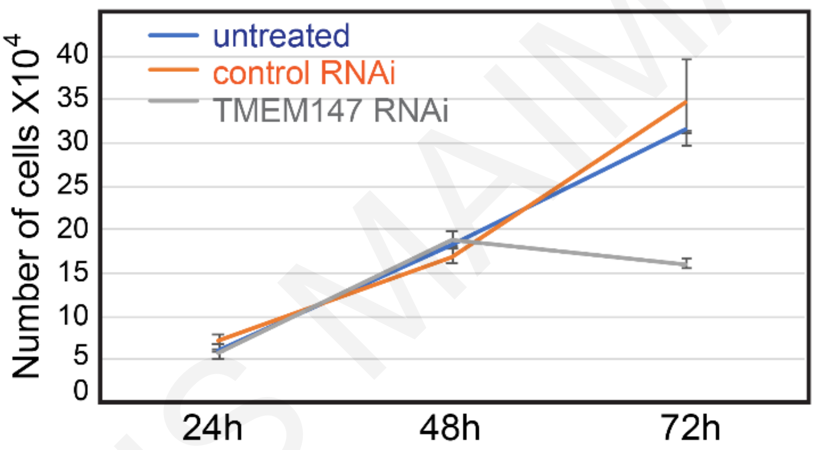

Figure 3.5: Effect of TMEM147 silencing on cell growth.
HeLa cells from three different conditions, untreated, negative control-silenced and TMEM147-silenced, were cultured in triplicate. Cells were seeded in a 24-well plate from an identical starting cell number (7600) and monitored for 72 h. Every 24 h measurements from each culture were taken triplicate and growth curves were constructed. The curves show a clear decline of cell viability after 48 h of silencing, specifically for TMEM147-silenced cells. Number of cells refers to means and bars to the standard deviation of the three experiments.

Furthermore, a striking and consistent observation with TMEM147-silenced cells was a concomitant remarkable reduction of the levels of the INM protein LBR, an effect already detectable at 48h post transfection. At this time point, LBR was severely reduced and WB immunostaining showed a consistent and significant downregulation of its levels when compared with negative control (Fig. 3.6A). Quantification revealed that upon TMEM147 silencing, LBR protein levels were reduced to 9.93±6.23% (mean±s.d., p=0.0065), relative to negative controls (Fig. 3.6B), a reduction comparable to the one observed for TMEM147 itself (Fig. 3.4B). The results were specific for LBR, given that upon TMEM147 downregulation, protein levels of NE protein emerin, or ER transmembrane and chaperone protein calnexin, were not measurably affected (Fig. 3.6A).

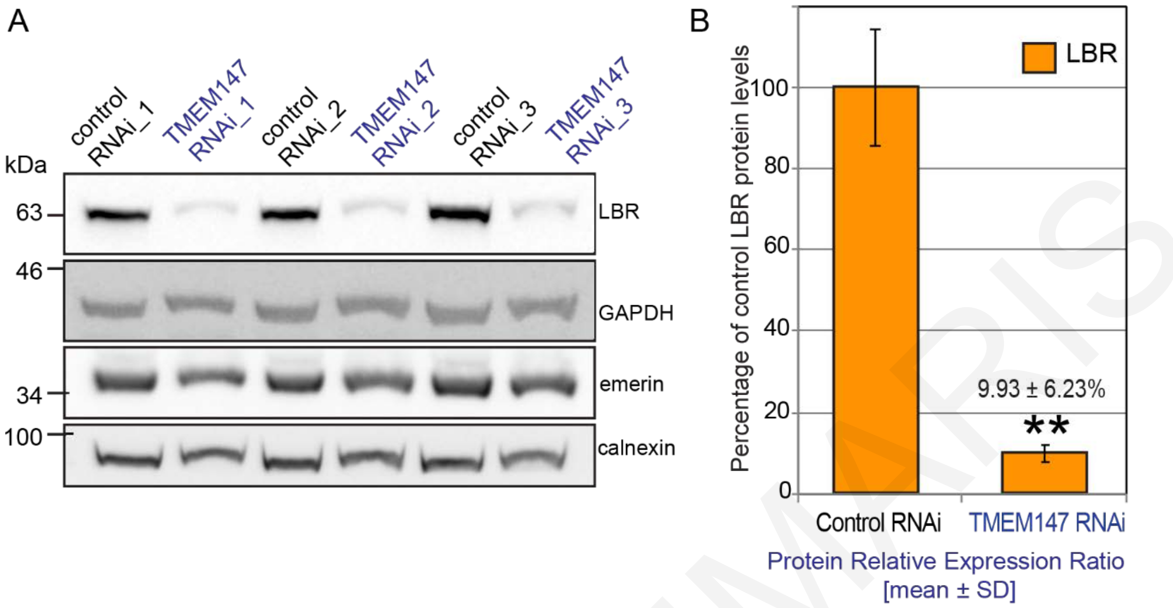

Figure 3.6: Silencing of TMEM147 downregulates protein levels of LBR.
Protein extracts of TMEM147-silenced HeLa cells from three independent experiments were analyzed by WB. (A) TMEM147-silenced cells exhibited a drastic reduction of LBR protein levels compared with controls, while protein levels of emerin (a NE protein) and calnexin (an ER protein) were not affected. (B) Quantification of this analysis revealed that protein levels of LBR (normalized to the GAPDH) had a statistically significant reduction to 9.93±6.23% (mean±s.d.; p=0.0065, as assessed by two-tailed unpaired t-test with Welch's correction).

The TMEM147-silencing effect on LBR was investigated employing confocal and wide-field microscopy in HeLa and HeLa-TMEM147-GFP cells respectively, probed with an anti-LBR antibody. Consistent with WB quantitation, both sets of experiments revealed a reduction in LBR labeling compared with control-silenced cells. Specifically, LBR labeling was barely detectable on the INM of silenced wt. HeLa cells (Fig. 3.7A3, A6 and B2, B5), whereas lamin A, a component of the nuclear lamina, was not affected, clearly demarcating the INM in both knockdown and control cells (Fig. 3.7A2 and A5). The same effect was observed when the stable cell line HeLa-TMEM147-GFP was also silenced for TMEM147; in particular, upon downregulation of TMEM147 and the consequent loss of GFP signal (Fig. 3.7C1 and C4), cells again displayed a decreased LBR-labeling confirming the already observed phenotype (Fig. 3.7C2 and C5).

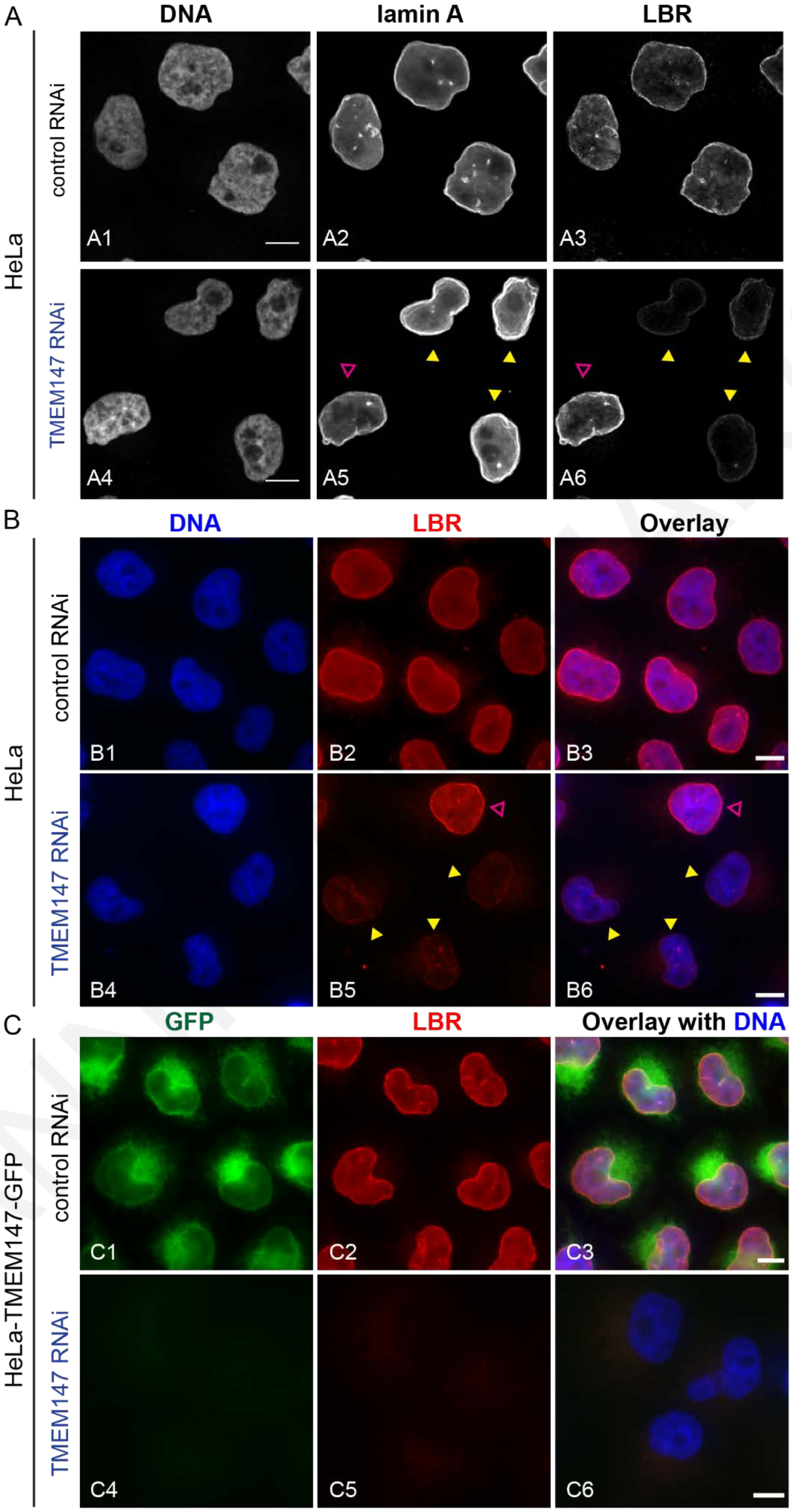

Figure 3.7: Immunofluorescence images of LBR labeling upon TMEM147-silencing.
(A1-A6) Confocal microscopy images of HeLa cells comparing control-silenced cells (A1-A3) and TMEM147-silenced cells (A4-A6). DNA, lamin A (an INM marker protein) and LBR labeling were compared. Panel A6

shows a clear reduction of LBR labeling in silenced cells compared with negative control in panel A3 (yellow arrows showing cells exhibiting LBR reduction; the magenta arrow indicates a non-silenced cell in the population), while Lamin A labeling is not affected (compare A2 and A5).
(B1-B6) Wide field microscopy images of HeLa cells, comparing control silenced(B1-B3) and TMEM147-silenced cells (B4-B6). Blue staining corresponds to DNA and red to LBR labeling. Comparing B2 with B5, shows the reduction of LBR upon downregulation of TMEM147 (yellow arrows showing cells exhibiting LBR reduction while the magenta arrow indicates a non-silenced cell in the population).
(C1-C6) Wide field microscopy images of the stable cell line HeLa-TMEM147-GFP comparing control silenced(C1-C3) with TMEM147-silenced cells (C4-C6). Green staining corresponds to GFP-tagged TMEM147 while red staining to LBR; blue staining indicates the DNA. Like before, GFP-tagged TMEM147 signal is reduced in silenced cells, along with a loss of signal of LBR labeling indicating the negative impact of TMEM147 silencing on LBR protein levels. Scale bars 10 μm.

To further establish the specificity of the TMEM147 silencing-induced downregulation of LBR, and recapitulate our findings so far, an alternative siRNA (#oligo2) molecule was employed. This oligo targets an exon downstream of the target of the oligo used in the silencing experiments mentioned earlier (#oligo1) (Fig. 3.8A). Silencing experiments with this alternative oligo were analyzed by WB, again showing reduced levels of both TMEM147 and LBR (Fig. 3.8B), and by immunofluorescence, where LBR labeling was visibly reduced in silenced cells compared with negative control cells (Fig. 3.8C).

All the above suggest that the reduction of TMEM147 results in a concomitant reduction of LBR protein at the INM.

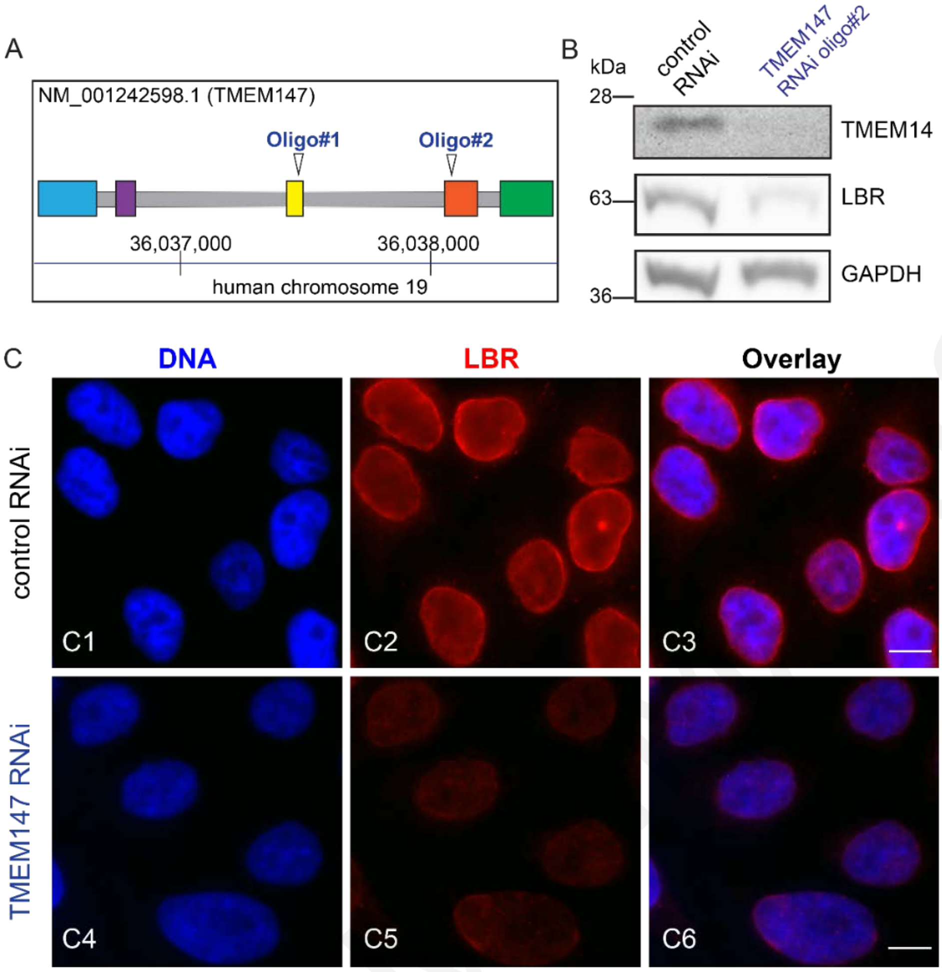

Figure 3.8: Effects of TMEM147-silencing are confirmed by an alternative siRNA silencing oligo
(A) Sketch of the multi-exon mRNA organization of human TMEM147, highlighting the targeting positions of the siRNA oligonucleotide 1 (oligo#1), used for all the silencing experiments and siRNA oligonucleotide 2 (oligo#2) used to confirm the specificity of the silencing phenotypes and in particular the effect on LBR in this figure.
(B) In agreement with oligo#1 (Fig. 3.7), siRNA-silencing with oligo#2, efficiently downregulates TMEM147(top panel), as assessed by WB analysis, and also drastically reduces the protein levels of LBR (middle panel). GAPDH was used in parallel as a loading control.
(C) Immunofluorescence images of HeLa cells silenced with oligo#2, exhibiting simultaneous drastic reduction of LBR labeling. Panels C2 and C5 display a comparison of control-silenced with TMEM147-silenced cells, revealing the reduction of red signal corresponding to LBR labeling. Image acquisition settings were identical for panels C2 and C5 to allow direct comparison. Blue staining corresponds to DNA labeling and overlay images combine LBR and DNA labeling. Scale bars 10 μm.

3.4 Silencing of TMEM147 causes mislocalization of LBR to the ER

So far, we have documented that knocking down TMEM147 in HeLa cells caused an up to 90%, downregulation of LBR protein levels. In literature, decreased levels of LBR have been shown to be related with abnormal granulocyte nucleus, present in Pelger-Huët anomaly, an autosomal dominant disorder characterized by hyposegmented nuclei demonstrating bilobed or rod-like phenotype (Hoffmann et al., 2002) and abnormal chromatin structure exhibiting coarse clumping chromatin (ropy, cordlike) (Waterham et al., 2003). Specifically, the normal 3-4 lobes of differentiated granulocyte nucleus are decreased to 1-2 lobes or even to an ovoid shape, in addition to the reduced NE surface area and mislocalized heterochromatin to the center of the nucleus, rather the periphery (Hoffmann et al., 2002).

To investigate if the TMEM147 silencing treatment in our case also affects the nuclear morphology overall, given the important role of LBR in nuclear organization (as detailed in the Introduction chapter, section 1.3), we sought to analyze the potential nuclear phenotype changes in HeLa cells as a consequence of LBR reduction upon TMEM147 silencing.

To assess this, we conducted 4 independent silencing experiments from which optical sections of 55 control and 48 silenced cells, stained for LBR and DNA, were acquired by confocal microscopy (Fig. 3.9A1-A4). These sections were processed and analyzed with the *Imaris* software, quantifying both the Mean Fluorescence Intensity (MFI) of the two labels and also measuring several nuclear morphological parameters.

MANOVA analysis of these measurements, suggested a significant difference between the control and silenced cells ($p<0.0001$). In particular, analysis of each individual parameter by Mann-Whitney test, suggested that MFI of both LBR and DNA labeling, and the sphericity of the nucleus were significantly altered (area, volume, oblate ellipticity and prolate ellipticity did not report any difference).

The median of LBR MFI labeling was reduced from 24.44 in control to 14.34 (arbitrary units, AU) in TMEM147-silenced cells, a difference which was statistically significant ($p<0.0001$). This result was consistent with the previous quantification of LBR protein levels by WB, confirming the link between LBR reduction and silencing of TMEM147 (Fig. 3.9B1). Interestingly, the median of DNA MFI labeling was also significantly different ($p<0.0001$) between the compared cell populations, showing a reduction from 44.66 to 27.45 AU in control and silenced cells respectively. This reduction of DNA labeling suggested loss of chromatin compaction (Fig. 3.9B2). To confirm this result, control and silenced cells were further stained with an antibody against H3K9 tri-methylated histone 3, which can be used as a marker of heterochromatin and an anchor of chromatin to the nuclear lamina (Mattout et al., 2015). The images of methylated H3 labeling showed a strong reduction of fluorescence intensity in silenced cells, in agreement with the DNA labeling quantification result and consistent with the suggested decrease in heterochromatin regions (Fig. 3.9A5 and A6). Moreover, silencing of TMEM147 and the accompanying LBR reduction altered nuclear morphology by changing its sphericity ($p<0.0001$). This difference is most likely caused by changes in the shape of the INM derived from the reduced levels of its constituent LBR (Fig. 3.9B3).

In addition to the reduced LBR localization at the INM, a more detailed observation of LBR staining in the sections of silenced cells, showed dispersed LBR staining in the ER membranes, away from the INM (Fig. 3.9A2). To better characterize this finding, we rendered 3D-images using the optical sections for all 103 cells of the 4 experiments. These 3D-images showed that when TMEM147 was silenced, a prominent mislocalization of the LBR to the ER membranes was detectable, compared with control cells. Quantification of this mislocalization revealed that when TMEM147 is silenced, LBR-positive staining in the ER membranes increased 6 times, compared with the control cells ($p<0.0001$) (Fig. 3.10A and B; Movie 1; Table 3.1).

Concluding our analyses, the silencing of TMEM147 not only promotes negative regulation of the LBR-expression but also causes the remaining expressed LBR to partition to the ER membranes, rather than correctly localize to the INM. Furthermore, depletion of LBR from the INM is associated with chromatin decompaction (decreased heterochromatin) and an altered nuclear shape (decreased sphericity).

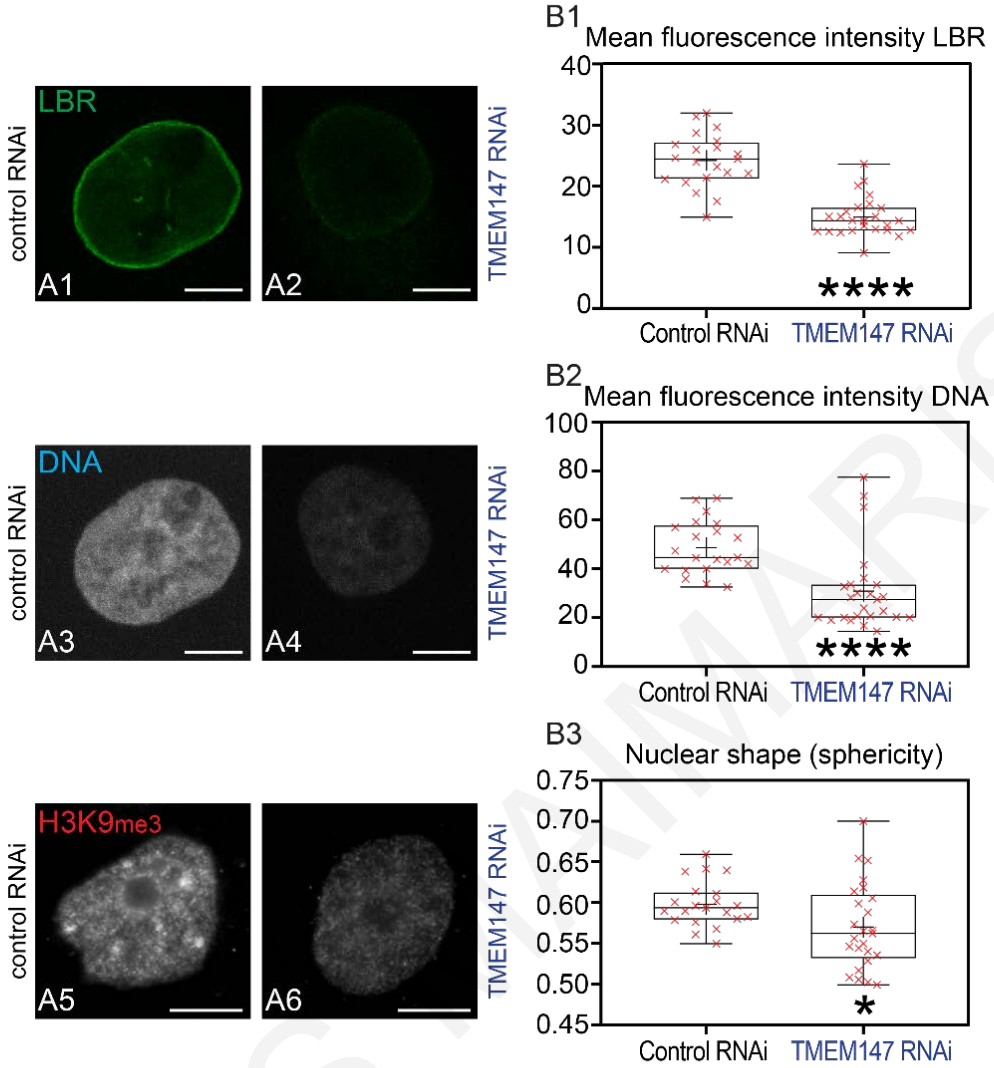

Figure 3.9: TMEM147 silencing induces alterations in nuclear organization.

(A1, A2) Immunofluorescence single confocal image representative of LBR labeling in negative control silenced and TMEM147 -silenced cells using the same image acquisition settings, displays the drastic loss of signal from LBR labeling.

(A3, A4) Confocal images of the same cells as in A1, A2 showing a dramatic reduction of DNA labeling upon downregulation of TMEM147.

(A5, A6) Immunofluorescence widefield images of HeLa cells showing a clear reduction of H3K9me3 heterochromatin labeling in TMEM147-silenced HeLa cells compared with control. Scale bars: 10 µm.

(B series) Immunofluorescence confocal stack images from a total of 103 cells (n=55 control silencing, n=48 TMEM147 siRNA) from four independent silencing experiments were analyzed with Box-and-Whisker plot showing the distribution of mean fluorescence intensity (MFI) of LBR labeling (B1), DNA labeling corresponding to Hoechst staining (B2) and the sphericity of nucleus measured in arbitrary units as defined by the Imaris algorithm(B3). In all Box-and-Whisker plots, whiskers indicate minimum to maximum, boxes indicate 25th to 75th percentile, the central line indicates the median and cross (+) marks the mean value.

(B1) Analysis of mean fluorescence intensity (MFI) corresponding to the LBR labeling. Median value of fluorescence intensity was reduced from 24.44 in control to 14.34 AU in silenced cells. MANOVA analysis revealed significant overall difference of MFI between silencing and control set of cells ($p<0.0001$), furthermore Mann–Whitney U-test with FDR correction ($Q=5\%$) reported the difference in LBR MFI as an extremely significant discovery ($q=0.0002$).

(B2) Analysis of mean fluorescence intensity (MFI) corresponding to the DNA labeling as detected by Hoechst staining. Median value of fluorescence intensity was reduced from 44.66 in control to 27.45 AU in silenced cells, indicative of loss of chromatin compaction. MANOVA analysis revealed significant overall difference of MFI between silencing and control set of cells ($p<0.0001$), furthermore Mann–Whitney U-test with FDR correction ($Q=5\%$) reported the difference in DNA MFI as an extremely significant discovery ($q=0.0002$).

(B3) Analysis of the nuclear sphericity shows a small but statistically significant difference in nuclear shape, comparing control-silenced with TMEM147-silenced cells. Median value of silenced cells is 0.5621 compared with 0.5937 units of control cells. Once again, MANOVA analysis revealed significant overall difference of the sphericity between silenced and control set of cells (p<0.05), furthermore Mann–Whitney U-test with FDR correction (Q=5%) reported the difference in DNA MFI as an extremely significant discovery (q=0.0218).

	№ of cells with NE-localized LBR (% of population)	№ of cells with ER-localized LBR (% of population)	№ cells with unclear localization	Total № of cells
Control RNAi	47 (**85.5%)**	6 (**10.9%)**	2	55
TMEM147 RNAi	15 (**31.3%)**	31 (**64.6%)**	2	48

Table 3.1: Percentages of cells exhibiting LBR labeling at the NE only or partitioning between the NE+ER.

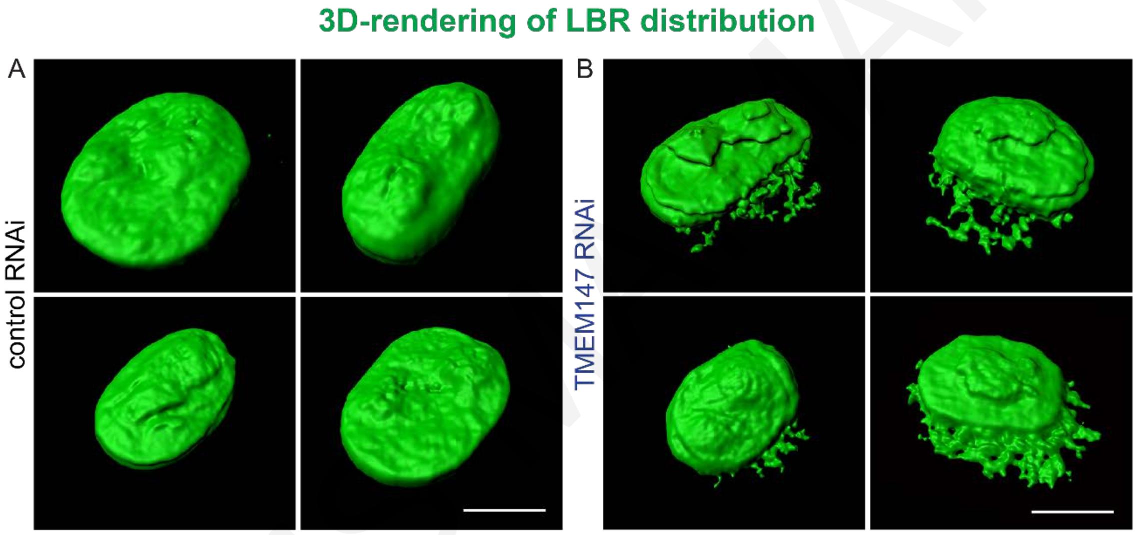

Figure 3.10 3D-rendering images of LBR distribution in NE and ER, comparing control-silenced with TMEM147-silenced HeLa cells

(A, B) Two sets of 3D-rendering optical section stack images with Imaris software comparing the distribution of LBR, indicative of an obvious retention of LBR in the ER upon TMEM147 downregulation. LBR is retained in ER membranes 6 times more frequently than in control cells and this difference is statistically significant, p<0.0001. For illustration purposes, the intensity of the color used does not reflect the change in the MFI of LBR labeling as shown previously (Fig. 3.10A1, A2 and B1).

Scale bars: 10μm. See also the animation clip of LBR distribution in TMEM147-silenced cells.

(Click to: Watch LBR altered distribution after TMEM147-silencing)

3.5 Investigating the interaction between TMEM147 and LBR.

The previous series of experiments described how LBR protein levels were affected by the silencing of TMEM147 and how targeting of LBR was also differentiated. Prompted by these findings, we proceeded with investigating the possibility that the two proteins physically interact by employing co-immunoprecipitation (co-IP) experiments, along with silencing experiments. To investigate this interaction, additional tools needed to be developed and are described here prior to the experiments.

3.5.1 Development of tools for experiments to follow.

3.5.1.1 HeLa-TMEM147-GFP, HeLa-GFP-only and HeLa-LBR$_{238}$-GFP stable cell lines

Development of all three cell lines is described in the “Materials and Methods” chapter (section 2.2.1).

3.5.1.2 Plasmids and strategy:

The following recombinant plasmid constructs were developed as tools for further investigation of the interaction between TMEM147 and LBR employed in the described experimental procedures below. These constructs incorporated either the GFP or FLAG tag.

Appropriate primers were designed (see Materials and Methods section 2.1.22.1) in order to clone the full-length LBR sequence (LBR-GFP) as well as two overlapping truncated constructs. The first was an N-terminal LBR construct containing the first 372 amino acid residues (LBR$_{372}$), and the second, a C-terminal LBR construct, comprising residues 209-615, (LBR$_{209-615}$) (Fig. 3.11).

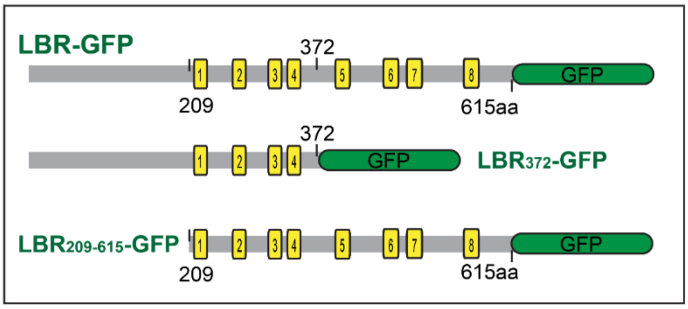

Figure 3.11: GFP tagged LBR constructs.
Graphical illustrations of the full length and truncated constructs of the LBR, all C-terminally tagged with GFP. LBR full length-GFP (LBR-GFP), N-terminal LBR construct (LBR$_{372}$-GFP), and C-terminal LBR construct (LBR$_{209-615}$-GFP).

3.5.1.2.1 Recombinant plasmid vector containing full length LBR tagged with GFP

Total RNA was purified from HeLa cells and used as a template to produce cDNA of the LBR full sequence with LBR-full-FW and LBR-full-RV primers (Fig. 3.12A). The product was then inserted in the pCR2.1-TOPO vector via TOPO cloning, colonies were screened and successful cloning confirmed (Fig. 3.12B).

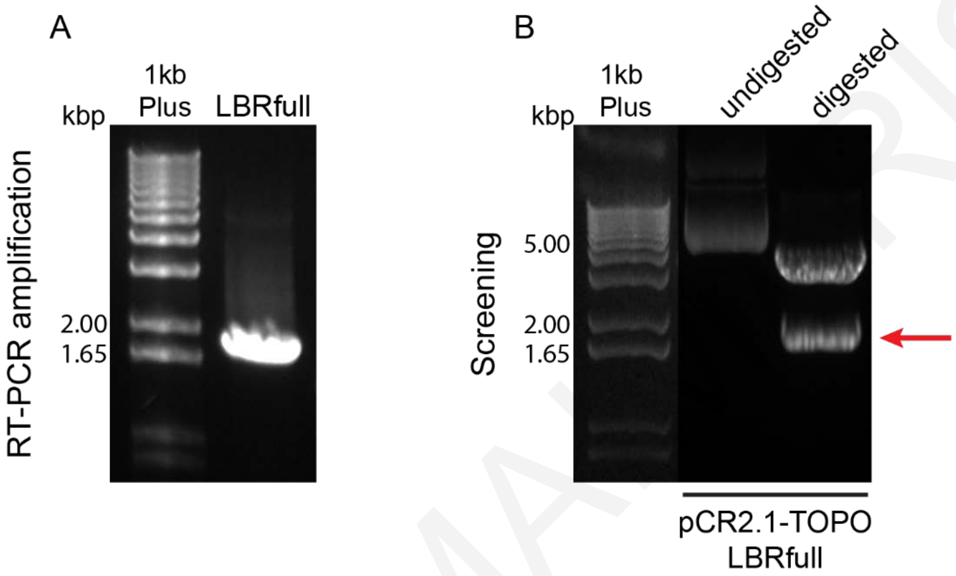

Figure 3.12: Cloning of LBR full length sequence in pCR2.1-TOPO plasmid vector.
(A) agarose gel showing the full length LBR cDNA sequence (expected size 1847bp) after RT- PCR amplification with appropriate primers LBR-full-FW and LBR-full-RV.
(B) agarose gel showing validation and confirmation of successful insertion of cloning product into pCR2.1-TOPO vector with EcoRI/XhoI digest. LBR full sequence is 1847bp (arrow).

To tag the LBR full sequence with GFP, we digested pCR2.1-TOPO-LBRfull and the pEGFP-N1 vector with XhoI/EcoRI, run the digestion products on gel for validation and cut out the appropriate bands. Bands were then gel purified and digested products LBR full and pEGFP-N1 were ligated together. Correct constructs were identified (Fig. 3.13) and in-frame ligation was confirmed by nucleotide sequencing.

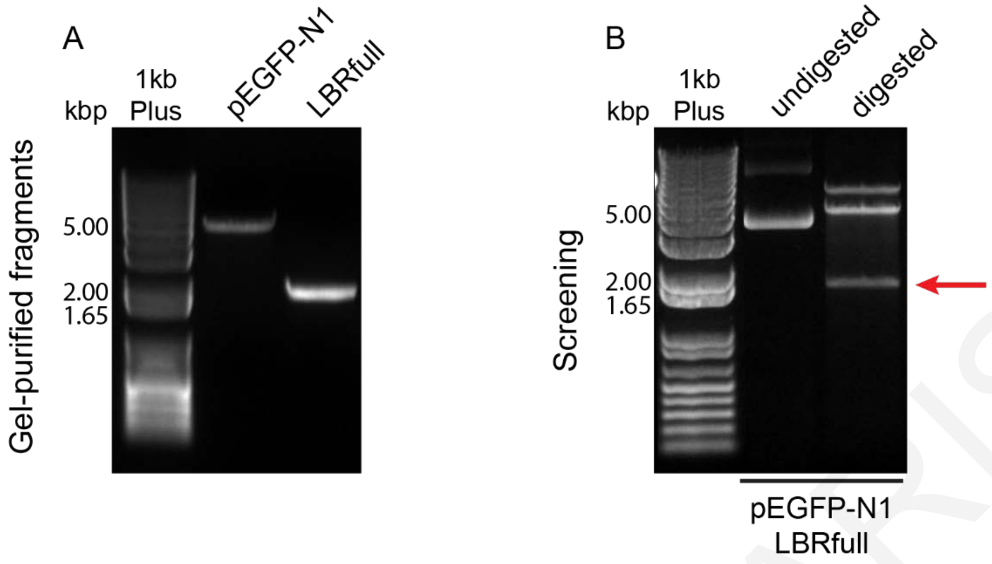

Figure 3.13: Cloning of LBR full sequence into the pEGFP-N1 plasmid vector.
(A) agarose gel showing the gel purified and linearized pEGFP-N1 and LBR full, both digested with EcoRI/XhoI.
(B) agarose gel showing confirmation of successful insertion of LBR full sequence into pEGFP-N1-LBR full. Following EcoRI/XhoI digest, an expected fragment of 1847bp (arrow)

3.5.1.2.2 Recombinant plasmid vectors containing LBR$_{1-372}$- or LBR$_{209-615}$- tagged with GFP

To generate the two overlapping truncated constructs, pEGFP-N1_LBR-full was employed so that the constructs were cloned and amplified with the use of the appropriate primers (see Materials and Methods section 2.1.22.1). The produced PCR products, along with an empty pEGFP-N1 vector were XhoI/EcoRI digested and evaluated on agarose gels. The bands were then cut out of the gel, purified and each construct was ligated with the digested empty pEGFP-N1 vector. Positive clones were identified (Fig. 3.14) and in-frame GFP fusions confirmed by nucleotide sequencing.

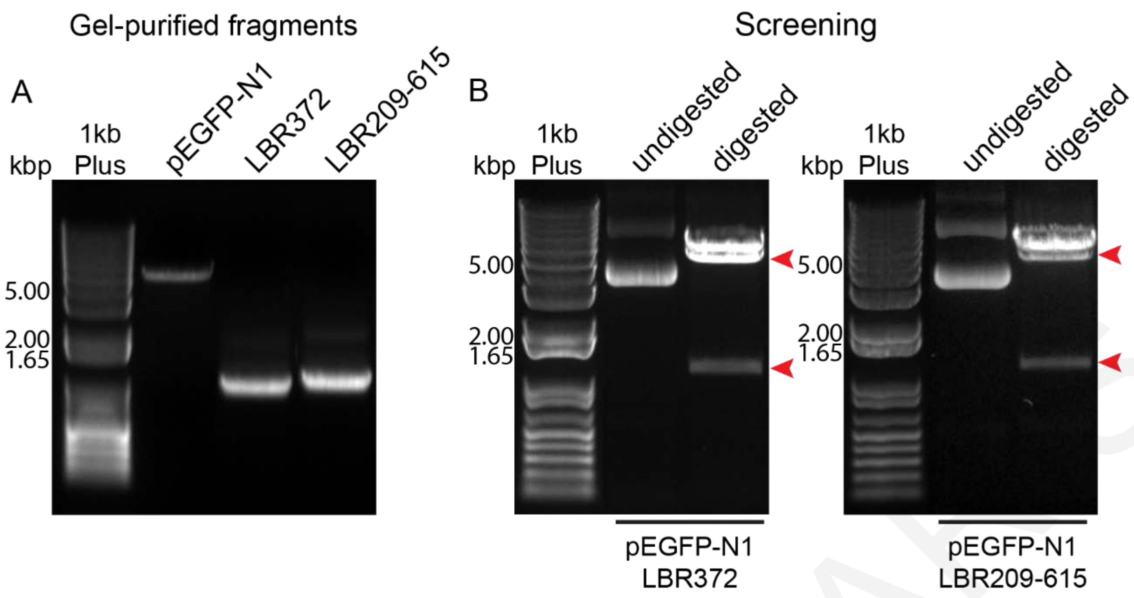

Figure 3.14: Cloning of LBR truncated constructs LBR$_{372}$-GFP and LBR$_{209-615}$-GFP.
(A) agarose gel showing the linearized pEGFP-N1 plasmid vector and PCR-generated fragments of LBR, LBR$_{372}$ and LBR$_{209-615}$, all digested with EcoRI/XhoI.
(B) agarose gel showing confirmation of successful insertion of LBR fragments into pEGFP-N1-LBR$_{372}$-GFP and pEGFP-N1-LBR$_{209-615}$-GFP. Expected fragments following EcoRI/XhoI digests are 1116 bp for LBR$_{372}$, 1218 bp for LBR$_{209-615}$, and 4.7 Kbp for pEGFP-N1 (red arrowheads)

3.5.1.2.3 Recombinant plasmid vector containing LBR full length-, or LBR$_{372}$- or LBR$_{209-615}$- tagged with FLAG.

For the production of the FLAG-tagged versions of LBRfull and the two truncated LBR constructs, we used the already generated recombinant pEGFP-N1-LBRfull, pEGFP-N1-LBR$_{372}$ and pEGFP-N1-LBR$_{209-615}$ plasmids. All three and the empty pFLAG-CMV2 vector were digested in sequence *with* BglII and KpnI following the same procedure as before. Figure 3.15A shows the digested and gel-purified products of LBRfull and pFLAG-CMV2 before ligation and the positive clones identified after screening (Fig. 3.15B). The production of the FLAG-tagged versions of the LBR truncated constructs, LBR$_{372}$ and LBR$_{209-615}$ in pFLAG-CMV2 vector was undertaken by Dr. Andri Christodoulou and provided to me for further experimental use. All positive clones identified and correct in-frame FLAG fusions were confirmed by nucleotide sequencing.

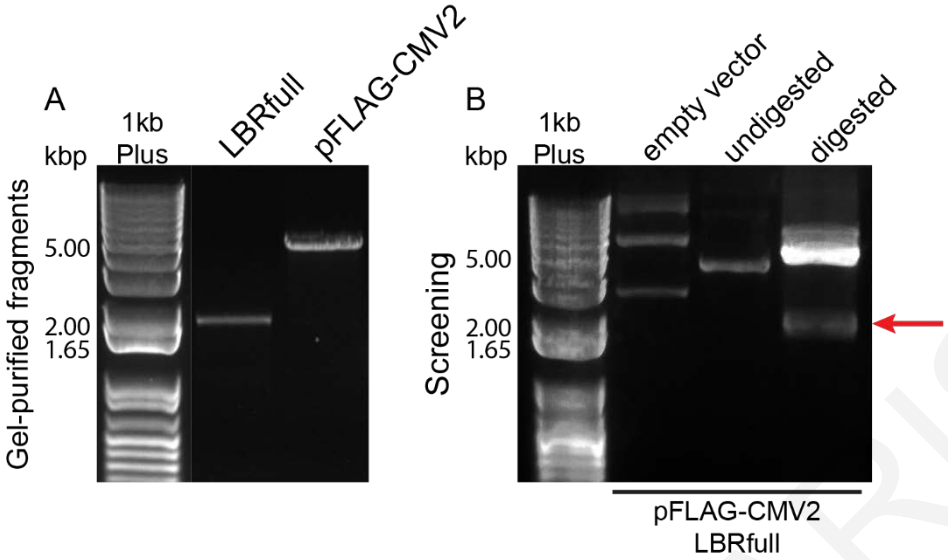

Figure 3.15: Gel-purified fragments of LBR constructs and pFLAG-CMV2 plasmid vector
(A) agarose gel showing the sequential BglII/KpnI-digested and gel purified LBR full and linearized plasmid vector pFLAG-CMV2 just before ligation. LBR full: 1847 bp, pFLAG-CMV2:4.7 kbp.
(B) agarose gel showing confirmation of successful insertion of LBR full into pFLAG-CMV2. Expected fragment following BglII/KpnI digests is LBR full 1847 bp for pFLAG-CMV2-LBRful (red arrow)

All of these generated recombinant plasmid vector constructs were the experimental tools for the results that follow in the next section.

3.5.2 Physical interaction between TMEM147 and LBR proteins

This first round of experiments aimed at probing a physical interaction between the two proteins. Towards this, protein extracts from two HeLa cell lines, stably expressing either a GFP-tagged recombinant TMEM147 construct (HeLa-TMEM147-GFP) or stably expressing the GFP protein (HeLa-GFP-only, as negative control) were immunoprecipitated using anti-GFP beads. Subsequent analysis of the total input and bound fractions by WB with antibodies against GFP or LBR resulted in detecting the endogenous LBR only in the presence of TMEM147-GFP and not in the presence of GFP-only (Figure 3.16 lanes c and d). The co-selection of LBR on the TMEM147-GFP bound fraction was suggestive of a physical interaction between the two proteins, but further proof was necessary.

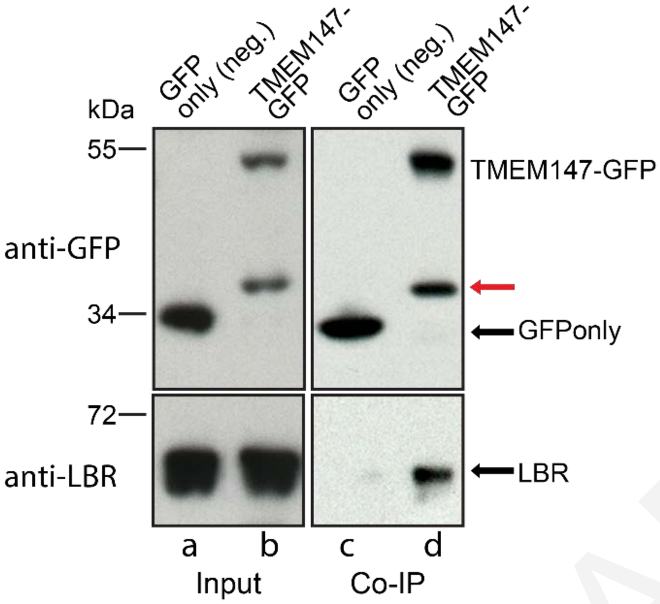

Figure 3.16: Interaction of TMEM147-GFP and LBR proteins by co-IP.
WB analysis of input (lanes a, b) and bound (lanes c, d) fractions of IP analysis using protein extracts of HeLa-TMEM147-GFP and HeLa-GFP only stable cells and employing anti-GFP beads. LBR protein is co- immunoprecipitated only in the presence of TMEM147-GFP (lane d) and not in the presence of GFP only (lane c). The extra band indicated by a red arrow in TMEM147-GFP bound fraction, corresponds to a GFP-containing internal initiation translation product.

To this aim, the two stable cell lines were both transiently transfected with FLAG-tagged recombinant LBR construct (pFLAG-CMV2-LBRfull) and protein extracts were prepared for IP experiments with GFP-Trap agarose beads. WB analysis of the IP fractions detected the FLAG-LBR construct only in the presence of the TMEM147-GFP construct and not in the presence of the GFP-only, confirming the co-selection of TMEM147-GFP with native LBR, seen previously in the bound fraction of the IP (Fig. 3.17, compare lanes c and f).

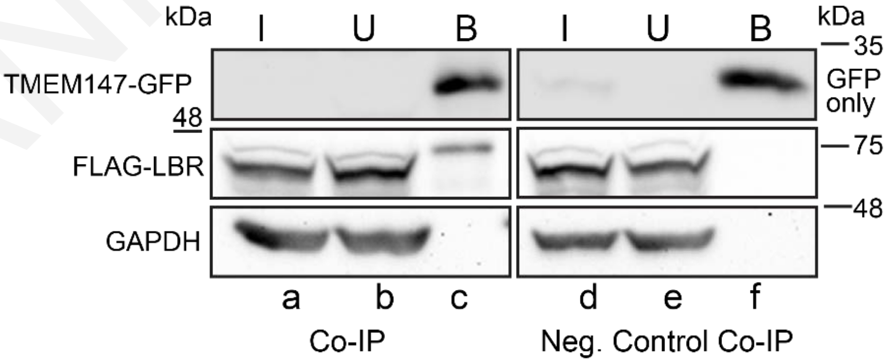

Figure 3.17: Confirmation of TMEM147-LBR interaction.
Protein extracts of HeLa TMEM147-GFP and HeLa-GFP, transiently transfected with LBR-FLAG construct, were immunoprecipitated using anti-GFP beads. Input (I), unbound (U) and bound (B) fractions were analyzed by WB and LBR protein was found to co-immunoprecipitate only in the presence of TMEM147-GFP (lane c) and not of GFP only (lane f), confirming the interaction of TMEM147 and LBR not as unspecific GFP-tag interaction. (GAPDH was used as a loading control)

3.5.3 Mapping of the TMEM147-LBR interaction

As mentioned in the Introduction, LBR is considered to possess two distinct functional domains. Whereas its N-terminal region is implicated in chromatin binding and organization of the nuclear periphery, its C-terminal region is involved in cellular cholesterol biosynthesis. Therefore, LBR can be described as a modular protein, suggesting two distinct functions in two distinct nuclear compartments; N-terminal in the nucleoplasm and C-terminal at the INM. Having found evidence proving the physical interaction between LBR and TMEM147, questions arose as to which functional module of LBR protein was associated with this interaction. To map the functional association between LBR and TMEM147 within the modular structure of LBR, we performed two sets of experiments.

First, we sought to investigate whether the N-terminal region of LBR was implicated in the interaction with TMEM147. We employed a stable HeLa cell line expressing LBR$_{238}$-GFP (Fig. 3.18) subjected it to TMEM147 silencing and assessed protein levels of both the endogenous, full-length, LBR and the GFP-tagged truncated version which consisted of the full LBR N-terminus plus its first transmembrane domain.

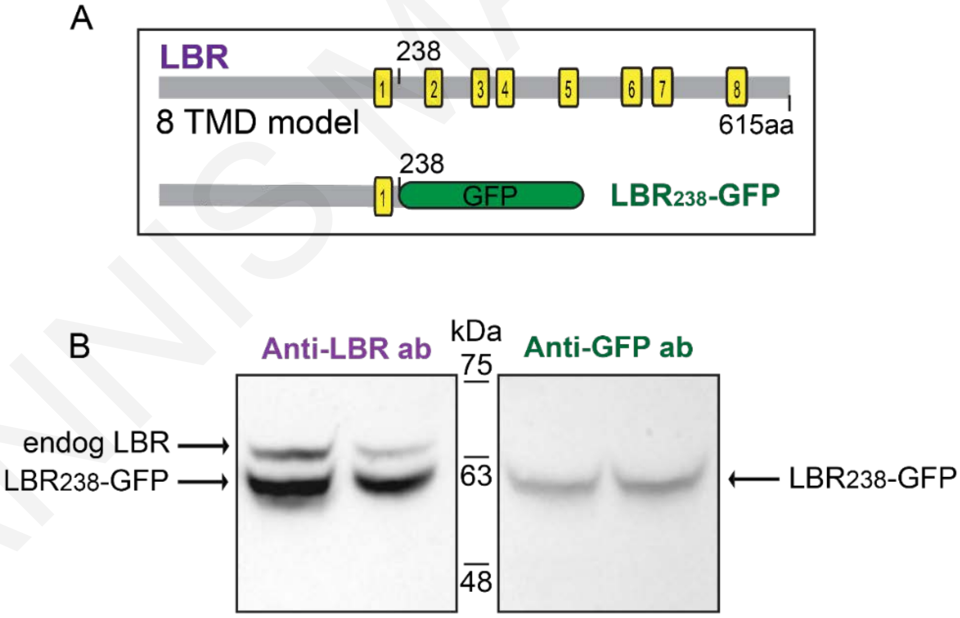

Figure 3.18: HeLa-LBR$_{238}$-GFP cell line characterization
(A) Schematic representation of the LBR N-terminal domain fused to GFP construct, stably expressed in HeLa-LBR$_{238}$-GFP as compared with the full-length sequence of LBR. This N-terminal construct includes the first TM domain of the LBR.
(B) Protein extract of HeLa-LBR$_{238}$-GFP after WB and immunostaining with anti-LBR antibody (left) and anti-GFP antibody (right). On the left panel both endogenous LBR and exogenous LB-GFPR proteins are shown (arrows). The right panel shows that only the exogenous N-terminal domain product is detected with an anti-GFP antibody.

Protein extracts from these experiments were analyzed by quantitative WB in which anti-GFP, anti-LBR and anti-TMEM147 antibodies were used for detection (Fig. 3.19). The analysis of these experiments confirmed, as expected, a significant reduction of both TMEM147 protein levels [top panel Fig. 3.19A; to 22.60% ± 6.81% of negative controls, p=0.0025 (mean±s.d.), Fig. 3.19B] and a significant reduction of the endogenous LBR protein levels to 12.77%±11.58%, p=0.045 of negative controls (Fig. 3.19A and B). In contrast to the visible reduction of the endogenous LBR bands, LBR_{238}-GFP bands did not show a corresponding change in TMEM147-silenced cells, as compared with negative controls: This was obvious both employing anti-LBR antibody or anti-GFP antibody, as can be seen by the lower bands of the first row of the second panel and second row of the first panel, respectively (Fig. 3.19A). Indeed, quantification of the LBR_{238}-GFP protein levels, regardless of the detection method, revealed minor reductions compared with the control (anti-LBR: 96.39%±41.78%, anti-GFP: 77.12%±18.10%, relative to negative controls) that were statistically non-significant (p=0.7, p=0.06 respectively) (Fig. 3.19B).

Considering the overall unchanged protein levels of the N-terminal truncated LBR and, at the same time, the downregulation of full-length LBR upon TMEM147 silencing, it can be suggested that the absence of the C-terminus is essential for the observed protein-protein interaction implying a functional association with the reductase activity domain of the LBR.

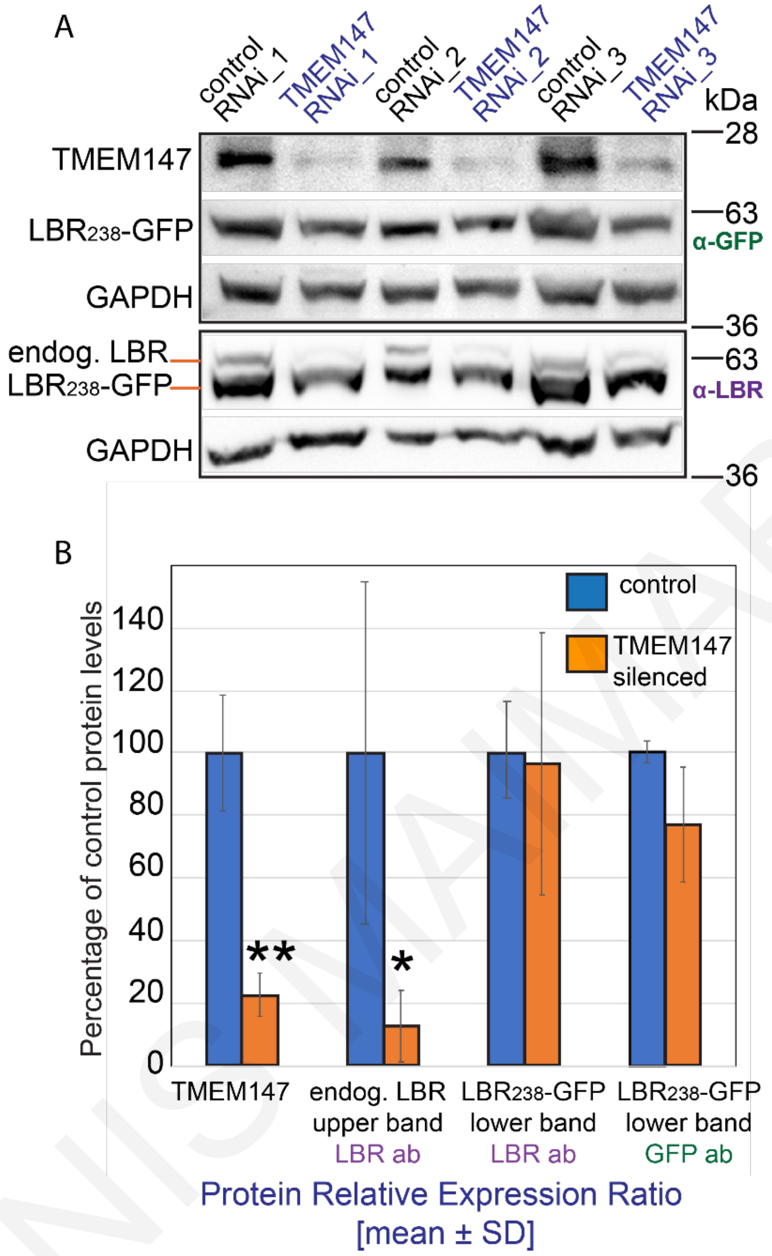

Figure 3.19: N-terminus of LBR is not employed in the interaction between TMEM147 and LBR

Protein extracts from three independent silencing experiments in the stable cell line HeLa LBR238-GFP and negative control cells were analyzed by WB (A) and quantified (B).

(A) Top panel first row, shows a confirmation of the depleted TMEM147 protein-levels in the silencing experiments, compared with negative controls. In the second row of the top panel, using anti-GFP detection, the LBR$_{238}$-GFP truncated product does not exhibit any considerable decrease, compared with control. In the first row of the lower panel, using anti-LBR antibody both endogenous LBR and exogenous LBR-GFP proteins were detected, and, while the endogenous LBR (higher band) exhibits great loss of signal, the LBR238-GFP product (lower band) does not show a corresponding signal reduction. GAPDH in both panels was used as a loading control.

(B) Quantification of WB analysis confirms the reduction of TMEM147 to 22.06±6.81% (mean±s.d.; p=0.002) compared with negative control. Endogenous LBR detected by anti-LBR antibody also shows a reduction to 12.77±11.58% (mean±s.d.; p=0.04). In contrast, protein levels of LBR$_{238}$-GFP, detected on the same panel by anti-LBR antibody shows a very small and statistically non-significant reduction (96.39±41.78%; p=0.7). Minor and non-significant reduction of LBR238-GFP was detected by the anti-GFP antibody (77.12±18.10% p=0.06). The effect of TMEM147 silencing on protein levels was assessed without assuming a consistent s.d. and using individual two-tailed unpaired t-tests for TMEM147, the upper and lower LBR bands and GFP values. All protein signals were normalized to corresponding GAPDH levels.

We next performed a more detailed mapping of the interaction between TMEM147 and LBR; we proceeded with co-IP analysis of protein extracts from wt. HeLa, transiently transfected with overlapping truncated GFP-tagged constructs of LBR. The first construct, pEGFP-N1-LBR$_{372}$-GFP, contained the first 372 amino acids of LBR, while the second construct, pEGFP-N1-LBR$_{209\text{-}615}$-GFP, encompassed the C-terminus of LBR from amino acids 209 to 615 (Fig. 3.11 for construct structure and Fig. 3.20 for their localization).

For comparisons, wt. HeLa were transiently transfected with pEGFP-N1-LBRfull construct and used along with the stable cell lines HeLa-LBR$_{238}$-GFP and HeLa-GFP-only.

All three GFP-tagged LBR constructs localized at the rim of the nuclear envelope (Fig. 3.20) while any observed signal localized at the ER most likely was a result of overexpression.

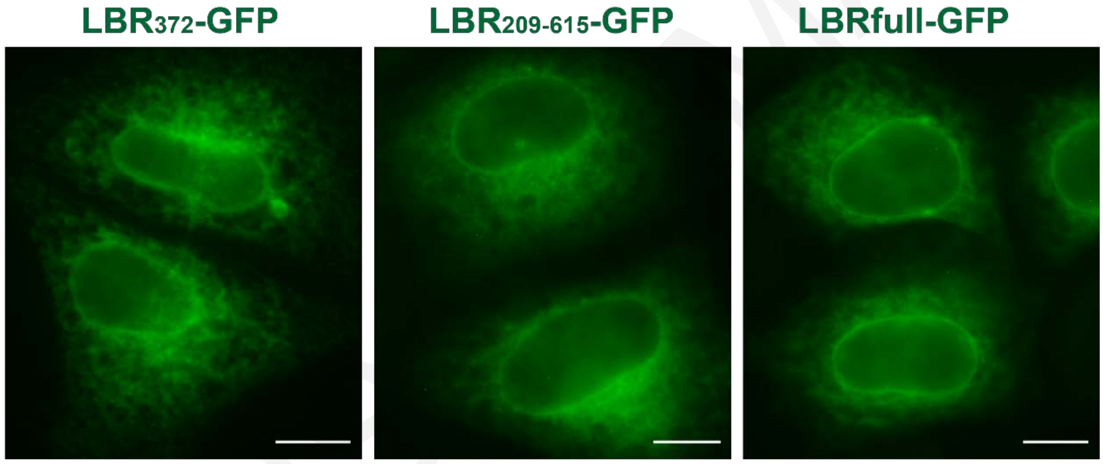

Figure 3.20:Localization of LBR truncated and full-length constructs in transiently transfected HeLa cells.
Wide field microscopy images of transiently transfected HeLa cells with the three LBR constructs: LBR372-GFP, LBR209-615-GFP and LBR full length. All three constructs localized at the NE, indicated by the intense green rim around the nucleus. Signal extension to the ER is a possible effect of overexpression.
Scale bars: 10μm

Upon transfection of HeLa with the three LBR constructs, protein extracts were collected along with extracts from the stable cell lines HeLa-LBR$_{238}$-GFP and HeLa-GFP-only. These extracts were applied in IP experiments where the GFP tagged N-terminal, C-terminal and full-length LBR constructs were immobilized on anti-GFP beads as a bait to screen the extracts for co-selection of the endogenous TMEM147. Input, unbound and bound fractions were then analyzed by WB (Fig. 3.21). As seen in the upper panels of Fig. 3.21A and B, all five extracts display the specific binding of the GFP-tagged versions of LBR in the bound fractions. Endogenous TMEM147 (detected in the middle panels of A and B) appears in the bound fractions of LBR$_{\text{full}}$-GFP and the C-terminal truncation LBR$_{209\text{-}615}$-GFP, exhibiting an equally strong signal, indicative of the co-selection. In contrast, the signal observed in the N-terminal truncation LBR$_{372}$-GFP bound fraction is very weak and barely detectable, by comparison. Consistently, a barely detectable TMEM147 signal is also manifested with HeLa-LBR$_{238}$-GFP, the other N-terminal truncated LBR product (Fig 3.21 B left middle panel). As expected, the HeLa-GFP-only, did not show any evidence of TMEM147 signal at all, thus no indication of co-selection (Fig 3.21 B right middle panel).

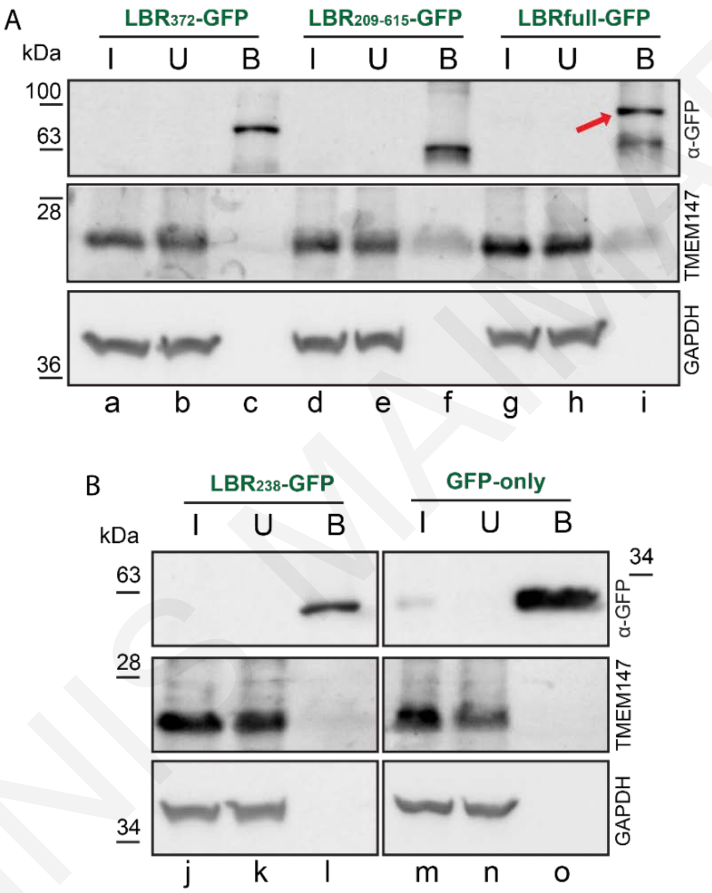

Figure 3.21: Interaction between TMEM147-LBR is mediated by the C-terminus of LBR.
Protein extracts of Hela cells transiently transfected with LBR full length-GFP, LBR372-GFP and LBR209-615-GFP constructs (A) and protein extracts from stable cell lines HeLa-LBR238-GFP and HeLa-GFP only (B), were used for IP experiments, using anti-GFP beads immobilizing the GFP tagged versions of LBR as a bait to select the endogenous TMEM147. Input (I), unbound (U) and bound (B) fractions were then analyzed with WB and anti-GFP, anti-TMEM147 and anti-GAPDH antibodies were used for the detection of the corresponding proteins. Transfection with full length GFP-tagged LBR and HeLa-LBR238-GFP were used as a positive and negative control, respectively.
Top panels of A and B show the detection of GFP-tagged constructs in the bound fractions, verifying the immobilization of GFP-tagged bait (red arrow points to full-length-LBR).
Middle panel shows the detection of immunoprecipitated TMEM147 in the bound fractions. Obvious co-selection occurs in the sample of LBR full length-GFP (lane i) as expected and in the bound fraction of C-terminal truncated construct of LBR with a comparable strength (lane f). The N-terminal truncated construct (lane c) exhibits only a barely detectable signal for TMEM147 co-immunoprecipitation. Signal is also barely detectable in HeLa-LBR238-GFP (lane l) and absent in the negative control HeLa-GFP only (lane o), bound fractions.
Lower panel of GABDH serves as loading control for comparison purposes.

These results infer an interaction between TMEM147 and particularly with the C-terminus of the LBR. Moreover, the unique topology of the LBR, comprising two distinct regions, in two distinct organelle compartments; the first oriented to the nucleoplasmic domain and the second to the INM domain facing the perinuclear space, each one encompassing characteristic functional activity, reinforces the conclusion that the functional interaction between TMEM147 and LBR is localized at the C-terminus of LBR, subsequently implicating TMEM147 in the regulation of the C-14 sterol reductase activity present at the C-terminus of LBR.

3.6 TMEM147 regulates DHCR7 a key reductase in cholesterol biosynthesis

Having documented an interaction between TMEM147 and LBR, specifically with its C-terminal sterol reductase activity domain, we subsequently wanted to further investigate whether downregulation of TMEM147 affects other key sterol reductases of the cellular cholesterol synthesis pathway, additional to LBR.

In this context, a highly promising TMEM147 interactor candidate not only because of its enzymatic activity but also its common localization at the ER and NE, seemed to be the 7-dehydrocholesterol reductase, DHCR7 which catalyzes the last step in the pathway of cholesterol biosynthesis (Koczok et al., 2019).

For this purpose, protein extracts from TMEM147-silencing experiments in HeLa cells were analyzed by quantitative WB and the levels of DHCR-7 were determined as detected by an anti-DHCR7 antibody. Compared with control extracts, DHCR-7 protein levels of the TMEM147-silenced cells showed a reduction, quantified to 32.78±7.98% of negative controls and statistically significant ($p=0.026$) (Fig.3.22A and B). In agreement with this downregulation, were the results of a corresponding analysis with the stable cell line HeLa-TMEM147-GFP, showing a reduction of DHCR7 protein levels to 36.80±19.25% of controls (Fig. 3.22C and D; $p=0.04$).

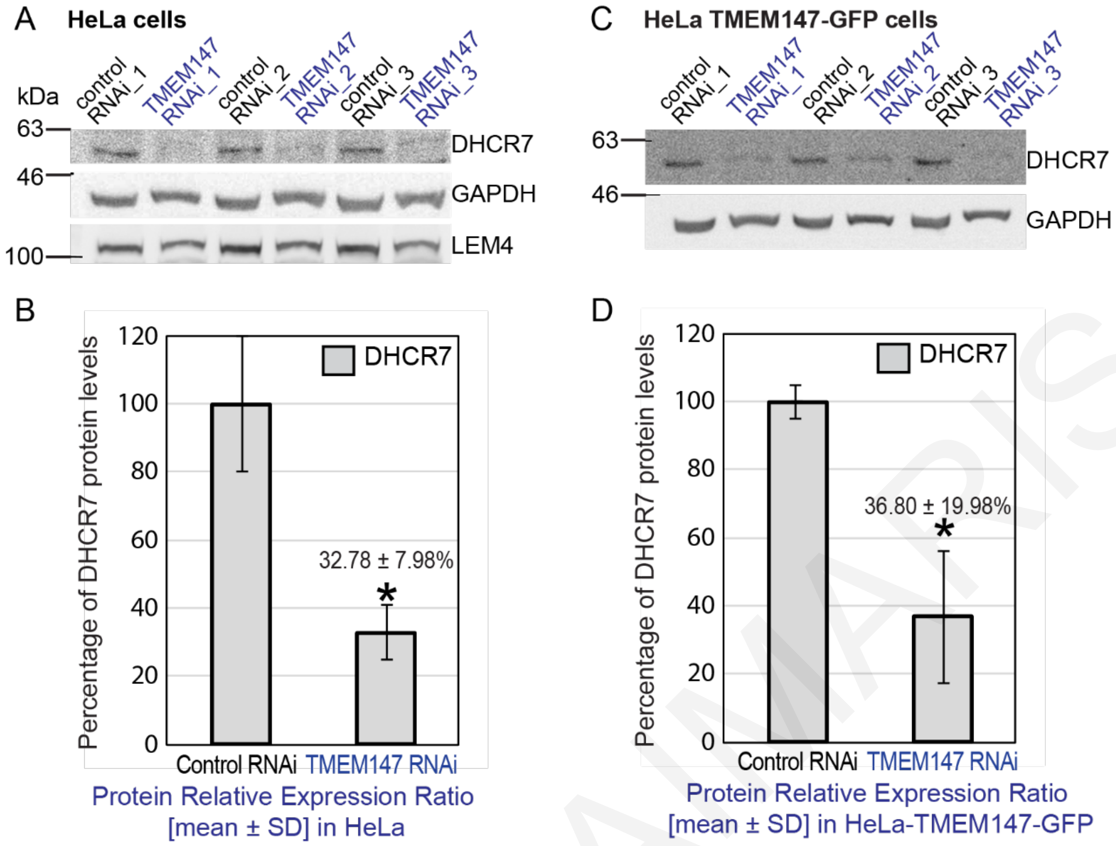

Figure 3.22: DHCR7 protein levels are downregulated upon TMEM147-silencing.
Protein extracts in triplicate TMEM147-silencing experiments were analyzed and quantified with WB regarding sterol reductase DHCR7. Protein extracts were derived from both wt. HeLa (A, B) and HeLa-TMEM147-GFP cell line (C, D). Top panels in A and C show a clear reduction of DHCR7 signal in silenced extracts compared with control-silencing but not in the ER integral protein LEM4, used as negative control. Quantification of this reduction shows it to be statistically significant in both cell lines, down to 32.78±7.98% compared with negative control (100±20.01%; mean±s.d.; p=0.026) and 36.80±19.25% compared with negative control (100±5.76%; mean±s.d.; p=0.04), respectively, as assessed by a two-tailed heteroscedastic t-test. GAPDH was used as a loading control.

Parallel to the silencing experiments investigating DHCR7 as a likely interactor of TMEM147, we carried out a full proteomic analysis of proteins that co-immunoprecipitated by anti-GFP IP with TMEM147-GFP and GFP-only by liquid chromatography coupled with tandem mass spectrometry (Fig. 3.23). The results were affirmative to our aforementioned findings, revealing not only the DHCR7 among the MS hits but also LBR and sterol reductase TM7SF2, another component of the cellular cholesterol biosynthetic pathway. This protein catalyzes a NADPH-dependent reduction step at an earlier stage of the pathway than DHCR7; a step catalyzed also by LBR (Bennati et al., 2006b). Moreover, our work was further validated by the discovery of other known interactors of TMEM147 such as Nicalin (NCLN) and NOMO (Dettmer et al., 2010) (Fig. 3.23A+B). Therefore, DHCR7 is a novel addition to the interacting partners of TMEM147, with similar to LBR effects by TMEM147 depletion.

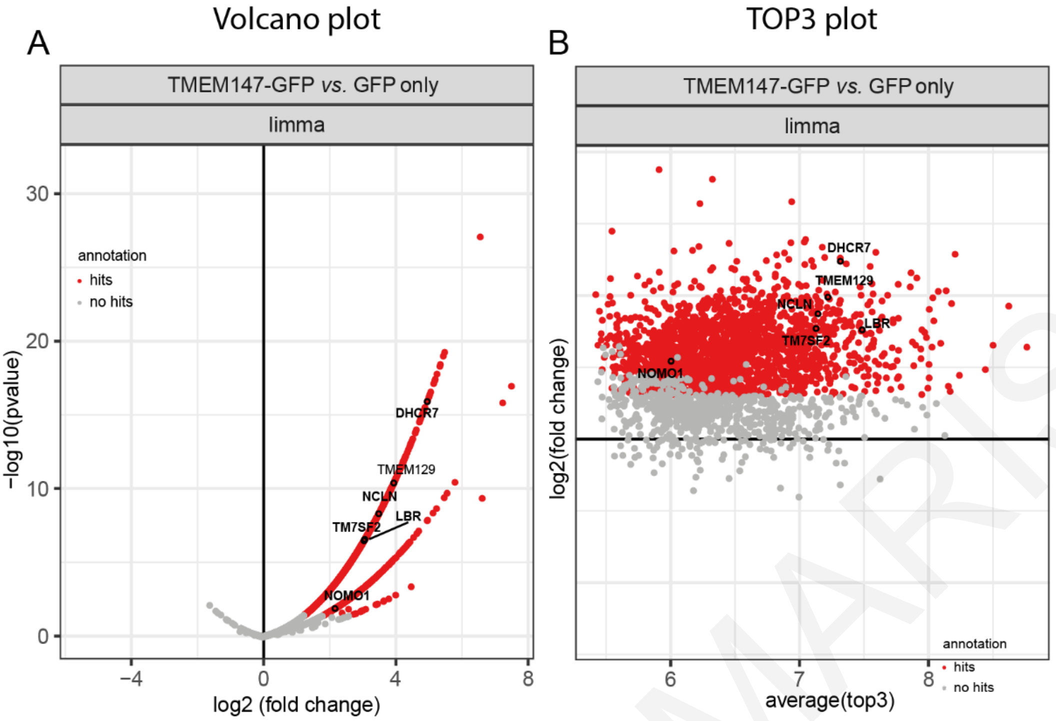

Figure 3.23: Proteomic analysis of the TMEM147 interactome.
Protein extracts of stable cell lines HeLa-TMEM147-GFP and HeLa-GFP only were immunoprecipitated with anti-GFP beads immobilizing the GFP-tagged TMEM147 or GFP as bait and screened for possible interactors by Dr Andri Christodoulou in our laboratory. Extracted peptides from the bound fraction were subjected to liquid chromatography coupled with tandem spectrometry for protein identification by Dr Mandy Rettel and bioinformatic analysis of the results was performed by Dr Frank Stein, both at the EMBL Proteomic Facility in Heidelberg, Germany.
(A, B) Volcano plot and TOP3 plot showing the hit proteins of TMEM147 MS analysis with GFP-only as a negative control. Among the hit proteins identified were DHCR7, LBR, TM7SF2, and also the already known TMEM147 interactors NOMO and NCLN.

Having found that TMEM147 physically interacts with both LBR and DHCR7 at the protein level, downregulating their levels, we questioned whether this is an effect on the transcriptional level. Towards this direction was our further quantification experiments by RT-qPCR, also including TM7SF2. This analysis revealed that both LBR and DHCR7 mRNA levels were reduced by 3.29- and 3.84-fold respectively, a reduction statistically significant ($p<0.0001$) compared with control mRNA levels of PUM1. Specifically, LBR mRNA levels were reduced to 30.40±26.08% whereas DHCR7 levels were reduced to 26.0±24.04% (Fig. 3.24). In contrast to this reduction were the findings for TM7SF2. The mRNA levels of this reductase remained essentially unaffected (Fig. 3.24).

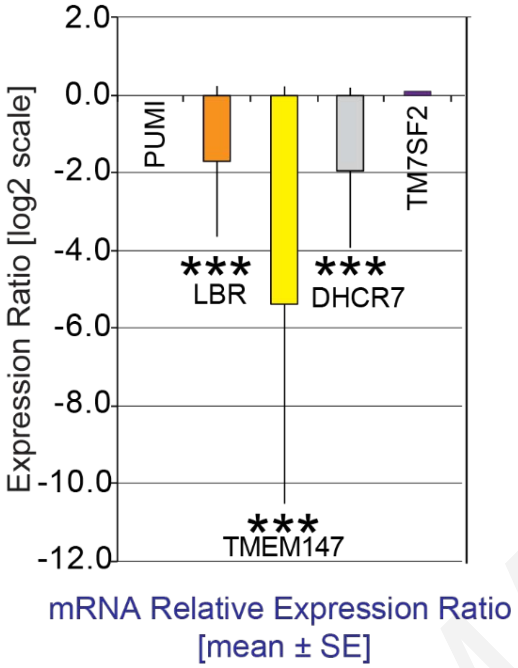

Figure 3.24: RT-qPCR quantification of sterol reductases upon TMEM147 silencing.
Gene expression from three independent TMEM147-silencing experiments of HeLa cells was assessed by RT-qPCR showing that knockdown of TMEM147 downregulates expression levels of both LBR and DHCR7 but not of TM7SF2. Both reductions are statistically significant ($p<0.0001$) exhibiting LBR reduction to 30.40±26.08% (mean±s.e.m.) and DHCR7 to 26.0±24.04% compared with negative control. TM7SF2 expression levels were not affected by TMEM147 silencing. PUM1 was used as reference gene for normalization. Error bars correspond to the s.e.m. of triplicate analysis.

These three TMEM147 protein novel interactors (LBR, DHCR7 and TM7SF2), comprise a reductase activity domain and they are implicated in the biosynthesis of cholesterol. On this basis, we proceeded to a new quantitative analysis of their mRNA levels upon TMEM147-silencing, but this time cells were seeded and cultured in parallel, either in medium continuously supplemented with lipids (72 h culture) or in complete medium for the first 48 h and then replaced with serum starvation medium for the last 24 h before sampling; mRNA levels of TMEM147 were also quantified (Fig. 3.25). This analysis showed that expression levels of both TMEM147 and LBR in serum starvation conditions remained unchanged as Tsai et al. reported for LBR under these conditions (Tsai et al., 2016). Additionally, the previously found decreased mRNA levels of TMEM147 and LBR upon TMEM147-silencing, showed the same downregulation under lipid restrictive conditions as well, respectively. However, the already documented unresponsiveness, in the absence of TMEM147, of expression levels of TM7SF2 in complete medium conditions, showed a statistically significant elevation by a 0.5 factor in lipid restrictive conditions. This increase was also present upon downregulation of TMEM147 in lipid restrictive conditions corroborating the independence of this reductase of TMEM147 expression levels (in silenced conditions the elevation is slightly lower than 0.5-fold but still statistically significant). Furthermore, analysis of DHCR7 gene expression levels, showed a remarkable and statistically significant increase under serum starvation conditions of greater magnitude than TM7SF2. Specifically, the mRNA levels of DHCR7 reductase were elevated by a 2.5 factor under lipid depleted conditions, either comparing negative control cells or TMEM147-silenced cells indicating its importance when lipid uptake is deficit.

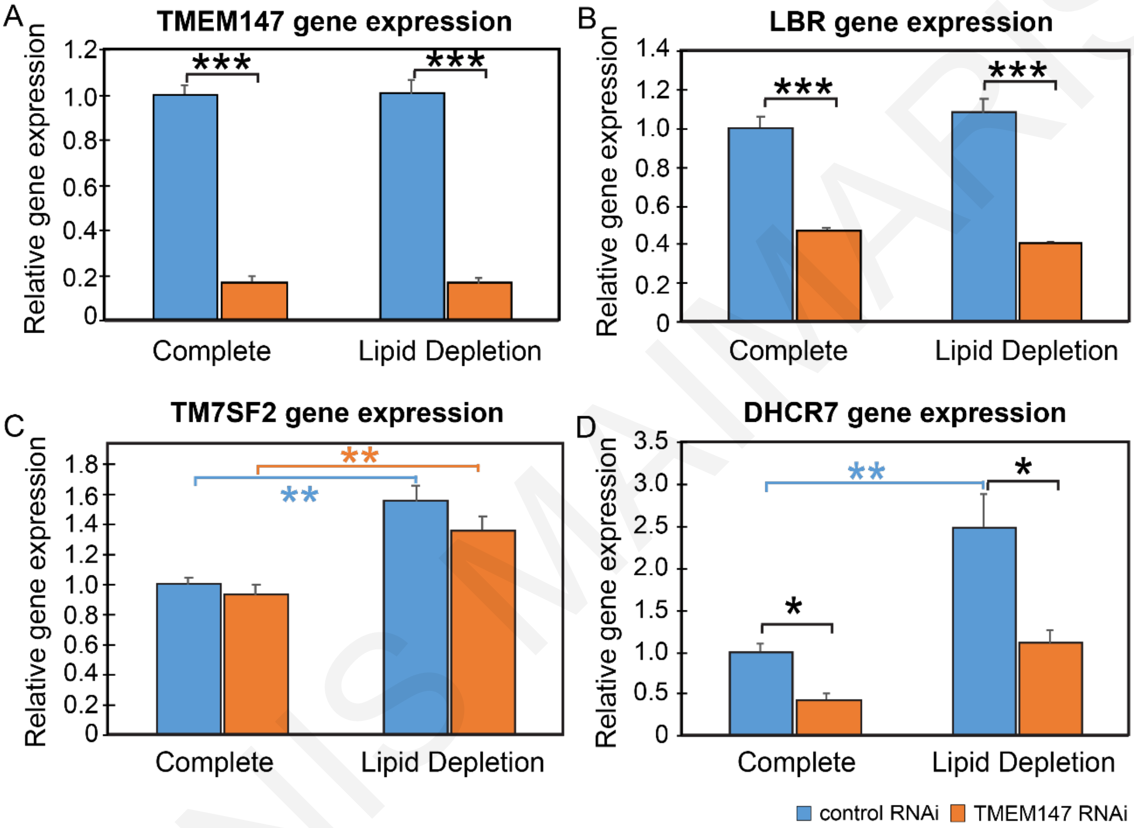

Figure 3.25: RT-qPCR quantification of sterol reductases upon TMEM147 silencing under lipid-depleted conditions.

Gene expression from three independent sets of parallel TMEM147-silencing experiments of cells grown in either complete medium for 72h, or for 48h followed by 24h serum starvation (lipid depleted condition) was assessed by RT-qPCR. Common base method (Ganger et al., 2017) was used to calculate the values in order to be directly comparable and expressed as a ratio to the normalized mean control value with error bars corresponding to SE (mean±s.e.).

(A, B) show that, non-withstanding the reduction caused by TMEM147 silencing, TMEM147 and LBR gene expression levels appear unaffected by the composition of the growth medium. In each comparison, the difference between silenced and negative control-silenced levels was statistically significant ($p<0.001$).

(C) The expression levels of TM7SF2 are increased when cells were grown in lipid depletion medium up to 0.5-times ($p<0.01$), compared with complete medium growth, for both control-silenced or TMEM147-silenced treatment. Moreover, as previously seen, TM7SF2 expression levels are not affected by TMEM147 (and consequent LBR) knockdown (see also Fig. 3.24).

(D) Similar to LBR, DHCR7 gene expression levels are greatly downregulated upon TMEM147 silencing treatment conditions (as seen previously in Fig. 3.24) in either medium. Furthermore, lipid restrictive conditions induce a 2.5-times increase in DHCR7 gene expression levels in either silencing treatment (control-silencing: from 1.00±0.10 to 2.49±0.40 upon lipid restriction; $p=0.007$ and TMEM147-silencing: from 0.44±0.07 medium to 1.11±0.15 upon lipid restriction; $p=0.01$).

3.7 Silencing of TMEM147 impacts cellular cholesterol homeostasis

The proven interaction of TMEM147 with both LBR and DHCR7, the nature of these proteins and their role in cholesterol biosynthesis prompted us to further investigate how downregulation of TMEM147 may affect the overall cellular cholesterol biosynthesis.

Therefore, in collaboration with the Biochemistry Center at the University of Heidelberg (Prof. B. Brügger), we conducted a full lipidome profile analysis, including cholesterol and cholesteryl esters (CE), specifically quantifying the cholesteryl esters species (CEs) profile (Table 6.1 in the Appendix). Cell extracts from TMEM147-silenced cells, control-silenced and untreated cells in triplicate experiments were profiled and the lipidomic data were validated using principal component analysis (PCA). This multivariate analysis, specifically the scores plot, indicated two distinguishable lipid profiles; the first assigned to control-silenced and untreated cells and the second to the silenced cells as can be observed by the great distance between the lipid profiles around the principal component 1 (Fig. 3.26A). Indicative of the variables influencing this separation, is the loadings plot which detected that cholesterol and cholesteryl esters were significant to this separation (Fig. 3.26B). Somewhat surprisingly, free cholesterol showed a small but significant increase from 14.43±0.16 in negative control cells to 16.36±0.45 mol% ($p<0.05$) in TMEM147-silenced cells, while, at the same time, the total levels of cholesteryl esters were greatly reduced from 9.74±1.83 to 5.80±1.68 mol% respectively ($p=0.05$) (Fig. 3.26C). In more detail, the profile of cholesteryl ester species revealed both upregulations and downregulations with upregulations in polyunsaturated long fatty-acyl chains of the esterified cholesterol and downregulations in saturated and short lipid species (Fig. 3.26D).

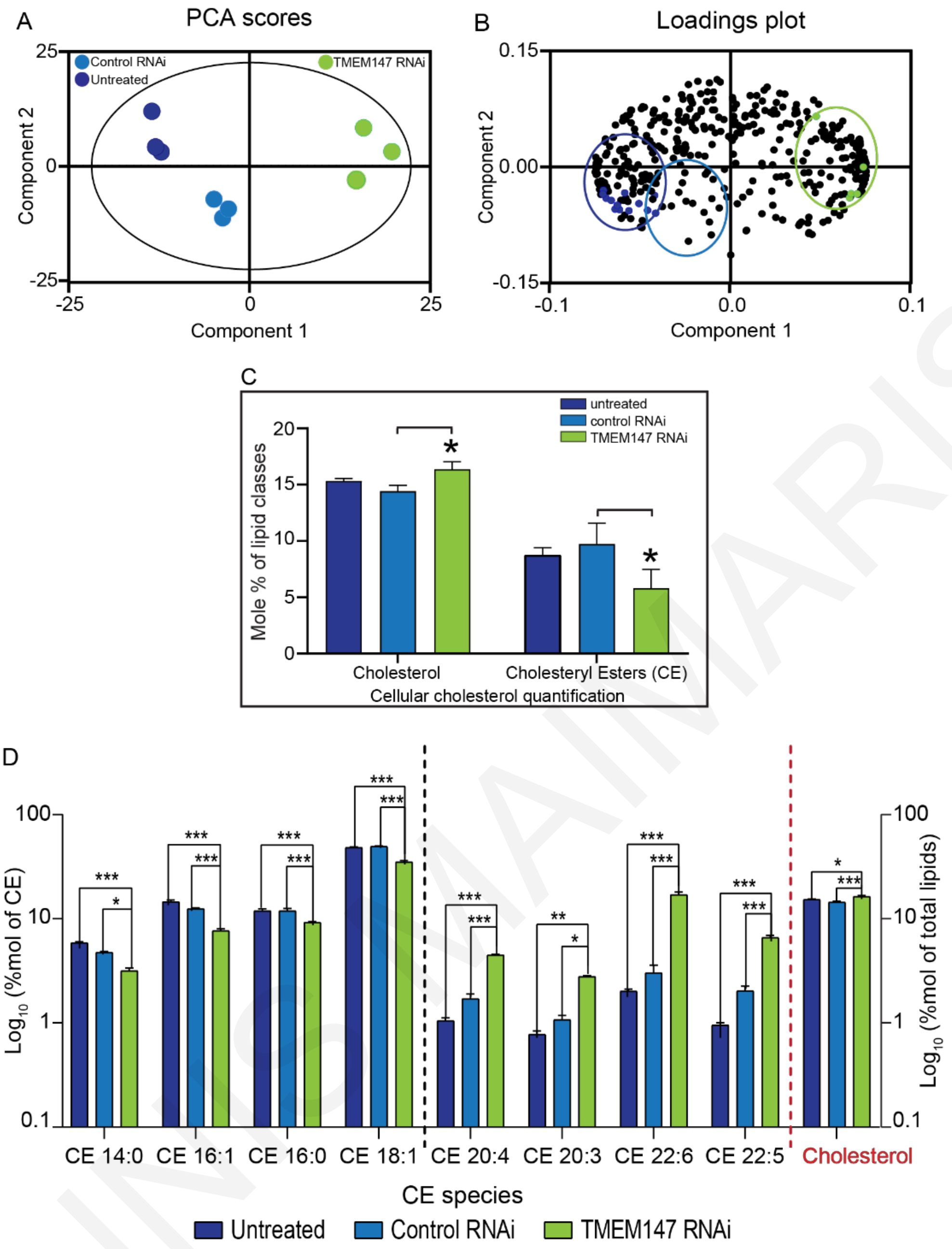

Figure 3.26 Lipidomic analysis to investigate the effect of TMEM147-silencing in HeLa cells

Total lipid extracts from HeLa cells under TMEM147-silencing, control-silencing treatments or untreated cells, in triplicate were analyzed by LC/MS to profile their lipidomic content in the laboratory of Prof. Britta Brügger at the University of Heidelberg, Germany. Bioinformatics analysis of the results was carried out by Dr Evelina Charidemou at the University of Cyprus.

(A) Principal component analysis (PCA) scores plot indicative of two groups depending on the lipidic content (lipid profile) of each treatment. Principal component one, clearly separates TMEM147-silencing treatment group from both control-silencing and untreated cells groups, suggesting a difference in the two grouped lipidic profiles.

(B) Loading scores plot indicates which lipid species are influencing the discovered separation in PCA scores plot.

(C) An analytical view of the lipid species influencing the difference between the two groups revealed total free cholesterol and Cholesteryl esters (CE) as the effecting factors. Levels of total free cellular cholesterol and total CE, revealed statistically significant changes for both, comparing control- with TMEM147-silenced treatment. Cholesterol levels were moderately increased while CE levels exhibit a greater reduction [(14.43±0.16 to 16.36±0.45 mol% ($p<0.05$), 9.74±1.83 to 5.80±1.68 mol% ($p=0.05$) respectively, (mean±s.d.)].

*(D) A detailed view of the most important CE species and how their levels are affected upon treatment. Upregulation is common in polyunsaturated long fatty-acyl chains of the esterified cholesterol, in contrast to downregulation commonly seen in saturated and short lipid species. The comparison of total free cholesterol levels is included. Data are presented as mean±sem and analyzed by 2-way ANOVA with post hoc Tukey's multiple-comparisons test; *$p \leq 0.05$, ** $p \leq 0.01$, *** $p \leq 0.001$ n = 3/group.*

ER and residential enzymes, by hosting cholesterol biosynthetic reactions and cholesterol esterification reactions, have a key role in maintaining cholesterol at its physiological levels, contributing this way to its homeostatic control. When cholesterol accumulates in the cell, its levels are regulated by esterification of excess free cholesterol to cholesteryl esters. When free cholesterol levels are low, either its corresponding biosynthetic pathway is activated employing acetyl-CoA, or hydrolysis of CEs restores its levels. This mechanism renders the concentration of the CEs an indicator of the available intracellular free cholesterol (Luo et al., 2020)

Thus, our findings of downregulated sterol reductase activity (LBR and DHCR7) upon depletion of TMEM147, is consistent with the observed decrease in the concentration of cholesteryl esters. Furthermore, total free cellular cholesterol levels were maintained, and even slightly elevated, under the same conditions as a result of both biosynthetic ability and absorption from the growth medium.

To investigate and determine to what extend cholesterol absorbed from the medium contributes to cholesterol availability in TMEM147-silenced cells, we carried out cholesterol uptake assays. Fluorescently-labeled cholesterol was used in cholesterol uptake assays to detect and compare total free cholesterol levels of control-silenced and TMEM147-silenced cells at different growth conditions: complete medium, lipid depleted medium and lipid depleted medium supplemented with cholesterol transport inhibitor U18666A. This inhibitor has been shown to decrease the movement of cholesterol to ER impairing the biosynthesis of cholesterol while maintaining at the same time the uptake at high levels and it is used as a positive control for increased cholesterol uptake (Sparrow et al., 1999).

Normalized cholesterol uptake results showed a considerable and statistically significant elevation of the uptake upon TMEM147-downregulation in all three conditions, relative to control. Specifically, cholesterol uptake of TMEM147-silenced cells was elevated 2.3-fold in complete medium, relative to control cells. Additionally, cholesterol uptake of silenced cells in restrictive medium conditions was twice the uptake of control cells in the same conditions (Fig. 3.27). Both results were indicative of cholesterol biosynthetic impairment in silenced cells and explanatory of the low levels of cholesteryl esters in TMEM147-

silenced cells and slightly elevated levels of free cholesterol quantified in lipidomics analysis (Fig. 3.26C).

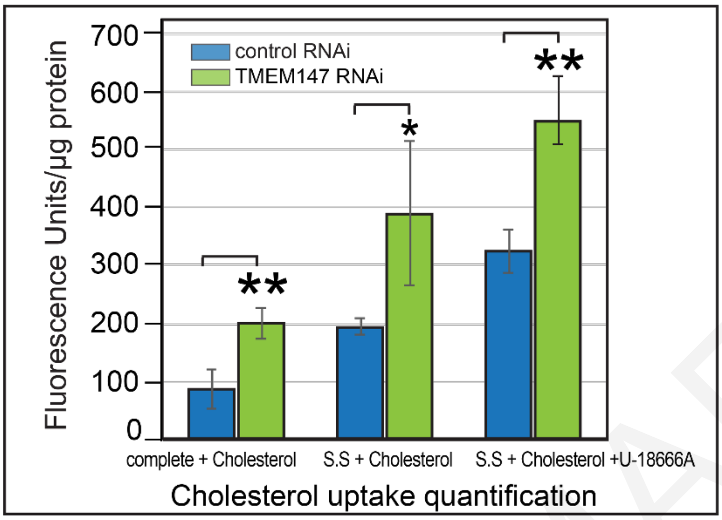

Figure 3.27: Cholesterol uptake assays.
Cholesterol uptake was determined in three different conditions comparing control-silenced with TMEM147-silenced HeLa cells. Cells were grown in complete, lipid depleted or lipid depleted medium in the presence of cholesterol uptake inhibitor U-18666A (1 µM). Fluorescent cholesterol was added in each growth medium to measure cholesterol uptake as quantified by fluorescence emission. Measurements were normalized to protein content in each well and background fluorescence was subtracted from equivalent measurements per condition without cholesterol. In all conditions there was a statistically significant increase in cholesterol uptake comparing the two treatments, suggestive of a cholesterol synthesis impairment upon TMEM147-silencing and a contribution via uptake for regulating total cellular free cholesterol levels. Cholesterol uptake levels in complete medium were raised from 86.58±35.65 to 199.39±26.14, in lipid-depleted medium from193.50±14.17 to 388.43±123.93, and in restrictive medium+ U-18666A from 324.22±36.85 to 548.80±56.17 emission units/µg protein (mean±s.d.; q=0.006, q=0.019, q=0.005, respectively). Statistical discovery was determined by applying the two-stage linear step-up procedure of Benjamini, Krieger and Yekutieli (Q=5%), upon calculating the statistical significance by multiple t-tests with multiple testing correction using one unpaired t-test per row without assuming a consistent s.d.in GraphPad Prism 8.0.

Therefore, these findings suggested that cells growing in the absence of TMEM147 showed impaired cholesterol synthesis, emphasizing the key role of DHCR7 and LBR in this metabolic pathway. This impairment in silenced cells, appeared to be counterbalanced by enhanced cholesterol endocytosis.

These conclusions were strengthened by results from cholesterol rescue growth assays. In these experiments, cells were cultured in three different media; complete medium for a total of 72 hours, complete medium for the first 48 hours replaced by lipid depleted medium for 24 more hours, and the same medium as before (48 h complete + 24 h s.s.) with the addition of cholesterol for the last 8 hours. Cells were counted and their viability was determined every 24 hours. As has been shown in previous growth experiments, silencing of TMEM147 induces a dramatic decline in cell growth after 48 hours (Fig. 3.5). This phenotype was also observed in these experiments after 48 hours growing in complete medium in either condition. However, adding in the restrictive medium exogenous cholesterol for the last 8 hours, resulted in restored cell numbers compared with those observed at 48 h (Fig. 3.28B). At the same time, adding cholesterol to the restrictive medium of control-silenced cells had only a small impact on cell growth (Fig. 3.28A). Noteworthy is the observation that, whereas application of restrictive conditions at 48 hours had a crucial effect on the growth rate of control-silenced cells, the same conditions on TMEM147-silenced cells did not alter the already ongoing destructive impact on cell viability observed due to the silencing of TMEM147 (Fig. 3.28A and B).

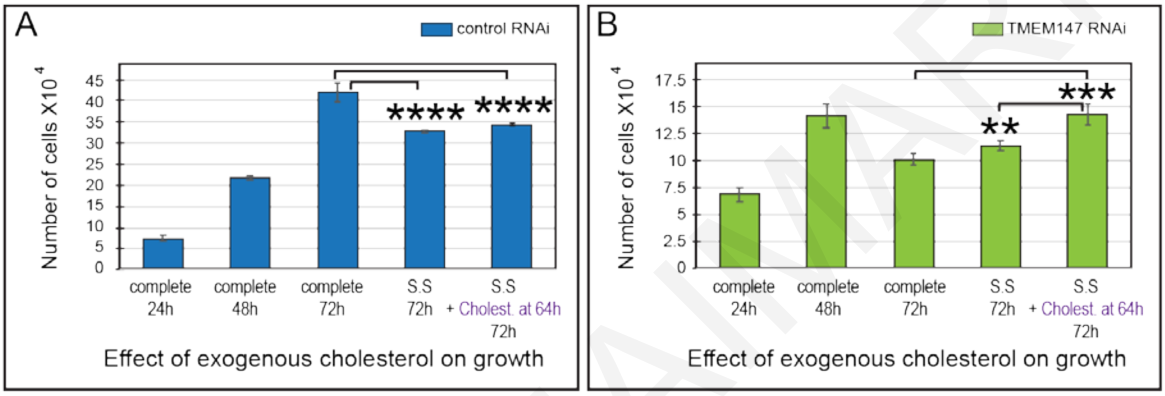

Figure 3.28:Cholesterol dependent growth rescue assays.
Cell viability was determined in three different conditions comparing control-silenced (A) with TMEM147-silenced (B) HeLa cells in triplicate. Cells were identically seeded and grown in complete medium for 72 h, or in complete medium for 48 h followed by 24 h serum starvation, or in complete medium for 48 h followed by serum starvation for 24 h followed by addition of cholesterol for the last 8 h. Cell growth was monitored for a total of 72 h and counted every 24 h (three timepoints). The results show that both control and TMEM147-silenced cells had comparable cell growth until 48 h, at which point cell viability started to decline in TMEM147-silenced cells in any of the three conditions. Addition of cholesterol to the serum-starved conditions of TMEM147-silenced cells 8 hours prior to last time point resulted in an increase of the cell numbers, restoring viability levels (rescue) to levels similar to those observed at 48 h of the same treatment [TMEM147-silenced cells in complete medium at 48 h $(14.06\pm1.13)*10^4$ vs. TMEM147-silenced cells in complete medium at 72 h $(10.10\pm0.48)*10^4$ vs. $(11.35\pm0.48)*10^4$ vs SS supplemented with cholesterol at 72 h $(14.27\pm0.95)*10^4$). Statistical significance: TMEM147-silenced 72 h SS vs. 72 h SS+Chol **p=0.0046, and for 72 h compl. vs. 72 h SS+Chol. ***p=0.0003] Control-silenced cells, upon restrictive conditions, show a statistically significant reduction in growth which is not rescued after the addition of cholesterol at the same time point as in (B) (Control-silenced in complete at 72 h compared to SS at 72 h or control-silenced in complete at 72 h compared with SS supplemented with cholesterol at 72 h: both p<0.0001). Values represent mean±s.d. Shapiro–Wilk test was used to confirm normality of the results before applying one-way ANOVA for parametric comparisons to determine statistical discovery based on the two-stage linear step-up procedure of Benjamini, Krieger and Yekutieli (Q=5%) in GraphPad Prism 8.0.

3.8 Silencing of TMEM147 alters ER structure

In the final segment of the Results chapter, further work is presented that addresses the question of any additional impact on the ER structure and function by TMEM147 depletion. Specifically, we sought to further investigate the impact of this depletion on two ER key structural proteins: RTN4 and CLIMP63. These proteins were selected as RTN4 is associated with the generation of curved areas (tubules) and CLIMP63 with the maintenance and stabilization of the flattened regions (sheets) (Shibata et al., 2010), thus representing the two morphologically distinct domains of the ER.

Antibodies against RTN4 and CLIMP63 were employed to label these proteins and related ER domains in HeLa TMEM147-silenced cells in an attempt to investigate the ER surface area and composition. At the same time, LBR labeling was used for confirmation of TME147 silencing, and Hoechst 33342 as a marker of nuclear size and DNA, independent of LBR.

Upon TMEM147-silencing, ER labeling was significantly changed, relative to controls. An initial morphological assessment of immunofluorescence signals revealed that the signal of both protein targets was elevated and topologically expanded. Specifically, labeling of CLIMP63 increased and expanded, suggesting a denser ER network and an increase of the flattened surface area (Fig. 3.29, panels A1, A4 and B1, B4). In agreement with the increased density of the ER network, brighter RTN4 labeling was observed, suggestive of an increase of the curved edges of the flat cisternae and tubular area at the periphery of the ER (Fig. 3.29, panels B2, B5). These observed increases in the labeling intensity and area of both RTN4 and CLIMP63, additionally suggested an overall expansion of the ER density and ER surface area (Fig. 3.29, panels B3, B6).

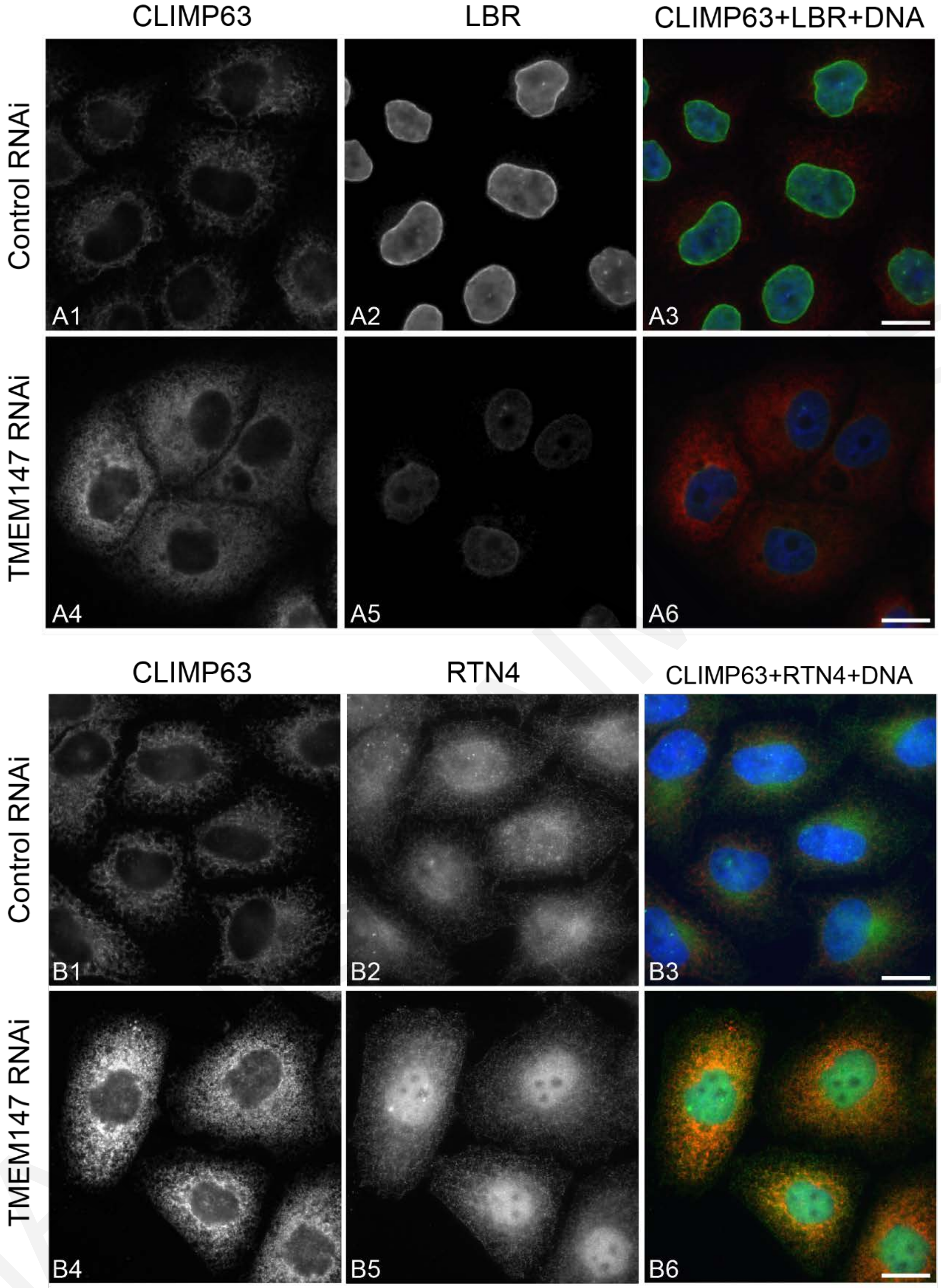

Figure 3.29: Immunofluorescence imaging of ER markers in control and TMEM147-silenced HeLa cells.
Indicative wide field immunofluorescence images of control-silenced and TMEM147-silenced HeLa cells.
(A1, A4,B1, B4) CLIMP63 labeling, showing an increase in the intensity and expansion of the ER surface area in TMEM147-silenced cells, relative to controls.
(A2, A5) LBR labeling, showing downregulation of the LBR, manifested in TMEM147-silenced HeLa cells.
(A3-A6) Overlay images of CLIMP63 (red), LBR (green) and DNA (blue). LBR nuclear rim signal is markedly reduced in TMEM147-silenced cells.
(B2-B5) RTN4 labeling, showing signal elevation and expansion of the ER surface area in TMEM147-silenced cells.
(B3-B6) Overlay images of CLIMP63 (red), RTN4 (green) and DNA (blue g). Yellow areas represent colocalization of CLIMP63 and RTN4.
Scale bars: 20 μm.

3.9 Quantification of ER morphological alterations in TMEM147-silenced cells

To quantify these observations concerning CLIMP63 and RTN4 and thus of ER composition and surface area after TMEM147-silencing, we conducted quantitative morphometric microscopy analyses from three independent silencing experiments, based on images acquired with identical, non-saturating exposure settings (Fig. 3.30A). Area analyses were performed for a total of 457 cells (n=232 silenced, n=225 negative control) for three independent fluorescent channels after labelling with α-CLIMP63, α-RTN4 antibodies and Hoechst 33342 staining (Fig. 3.30B).

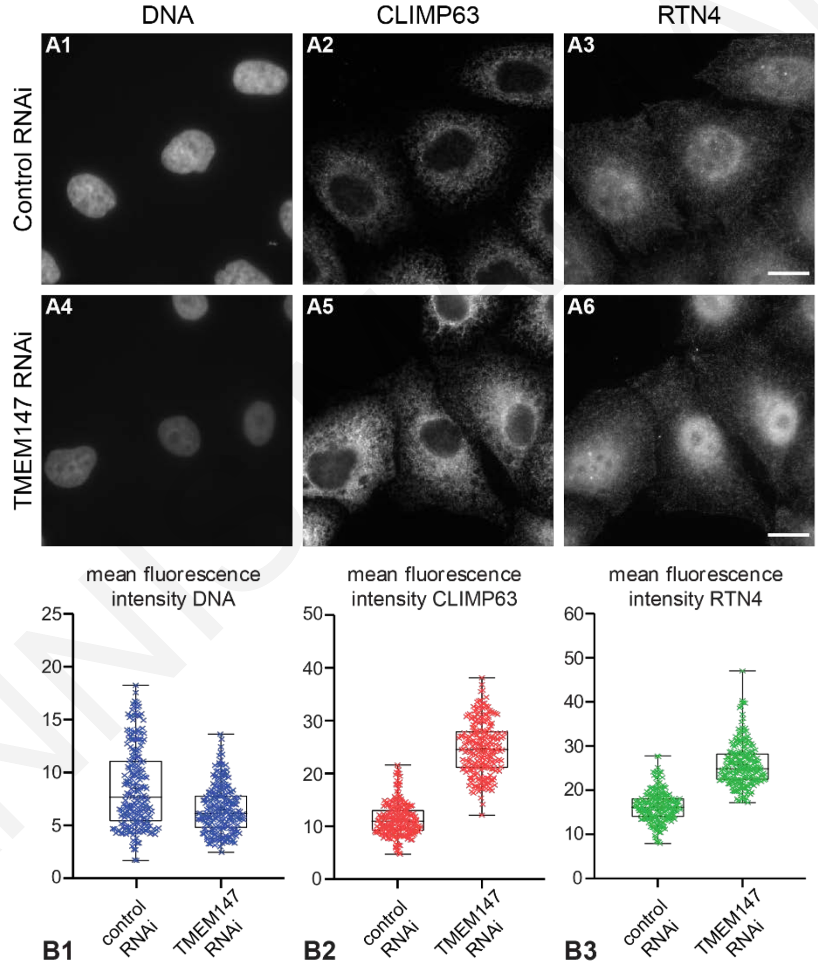

Figure 3.30: StatQuantification of immunofluorescence imaging after TMEM147 silencing.
(A) Representative wide field immunofluorescence images of control-silenced and TMEM147-silenced HeLa cells labeled for DNA, CLIMP63 and RTN4 from three independent experiments as assessed in Image-J for morphometric analyses. Scale bars: 20 µm.
(B) Box-and-whisker diagrams of mean fluorescence intensities (MFI) for DNA, CLIMP63 and RTN4. Each diagram shows the distribution of MFI values measured for DNA staining and indirect labeling of CLIMP63 and RTN4, before the removal of outlier values from a total of 457 cells (n=225 negative control, n=232 TMEM147-silenced) from three independent experiments. Whiskers indicate minimum to maximum; boxes indicate 25th to 75th percentile the interquartile range including the values processed for the following statistical analysis; and the central line indicates the mean value.

Mean Fluorescence Intensity (MFI). Analysis of MFI for DNA staining confirmed our previous finding (section 3.4, Fig. 3.9A3, A4 and B2) that silencing of TMEM147 promotes a loss of chromatin compaction, with a significant decrease of the DNA signal after silencing (Fig. 3.31, p<0.0001). In contrast, MFI for both ER markers, CLIMP63 and RTN4, significantly increased compared with negative control cells by 122.9% (p<0.0001) and 60.3% (p<0.0001), respectively, suggesting an increased density of the ER network and increased levels of both markers in ER membranes after TMEM147 silencing.

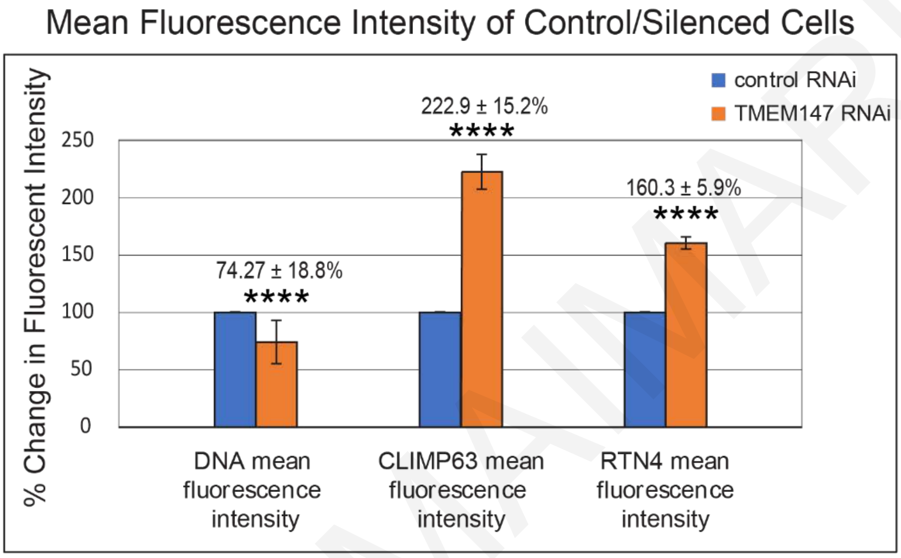

Figure 3.31: Mean fluorescence intensity
*Bar chart of mean fluorescence intensity (MFI) percentage changes of DNA staining, CLIMP63- and RTN4-labeling of triplicate control-silenced compared with TMEM147-silenced HeLa cells experiments. As previously shown downregulation of TMEM147 decreases the compaction of DNA as can be seen by the decrease of DNA labeling. CLIMP63 labeling markedly increases more than twice compared with the control (122.9±15.2% increase), while RTN4 increases 0.5-fold compared with control (60.3±5.9%). (mean±s.d.;****p<0.0001). The analysis was assessed on data for 362 HeLa cells (n=177 control, n=185 silenced) after outlier removal using 1.5x IQR rule (Tukey, 1977). For the statistical significance MANOVA analysis was applied for silenced and control cells using Pillai's test at a statistical significance α=5% in Excel (Microsoft Office, 2016) and XLSTAT (Addinsoft).*

Surface area analysis. Corresponding analysis of nuclear surface area, ER total surface area and ER flat and tubular domain surface areas revealed differential effects of TMEM147 silencing. While treatment had no effect on the surface area of the cell nucleus, it increased total ER surface area by 46.97% compared with control cells (p<0.0001) (Fig. 3.32). Based on the universally fixed ratio of nuclear area to cell size (a.k.a. nucleoplasmic ratio) (Cantwell and Nurse, 2019a, Hara, 2020), this observation indicated that TMEM147-silencing, while resulting in an almost 50% expansion of labelled ER area and a likely increase in ER density, as indicated by MFI measurements, did not increase overall cell size, with clear implications for the intracellular organization and transport of non-ER organelles. Moreover, the increase in ER area was not contributed in equal measure by both ER domains, with an area increase of flat ER cisternae by 100.13% ($p<0.0001$) and with a more conservative increase of the tubular ER area by 41.39% (Fig. 3.32, $p<0.0001$).

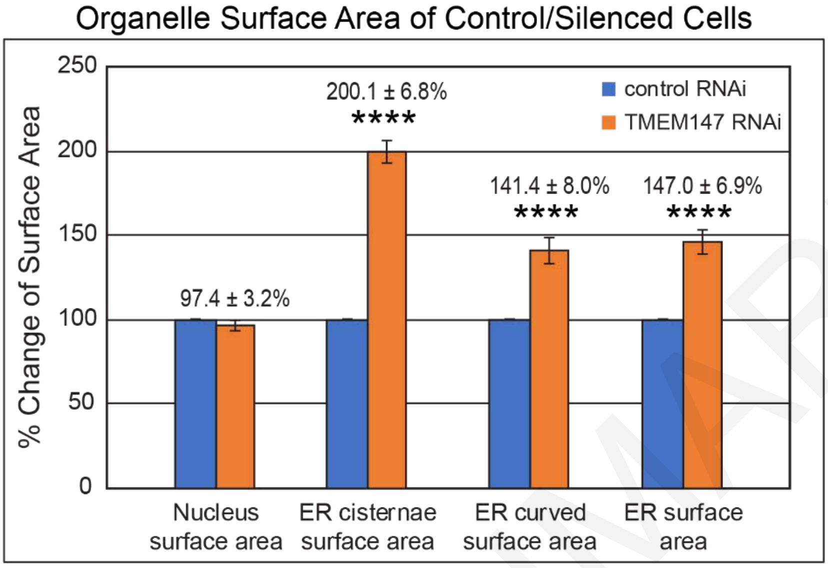

Figure 3.32 Organelle surface area quantification

Bar chart of organelle surface area percentage changes of nucleus (measured as DNA), ER flat cisternae (measured as CLIMP63), ER curved areas (measured as RTN4) and total ER surface area (measured as the overlap-corrected union of CLIMP63 and RTN4 areas) for TMEM147- vs control-silencing from triplicate experiments. As previously shown, nuclear area is not affected in the absence of TMEM147. Surface area of flat sheets area is doubled compared with control-silenced (100.1±6.8%, $p<0.0001$), while tubular ER area is more moderately increased (41.4±8.0%, $p<0.0001$). Overall, the total ER surface area expansion in silenced cells increased to 147.0±6.9% of the total surface area observed in negative control cells ($p<0.0001$). (mean±s.d.). The analysis was assessed on data for 362 HeLa cells (n=177 control, n=185 silenced) after outlier removal using 1.5x IQR rule (Tukey, 1977). For the statistical significance MANOVA analysis was applied for silenced and control cells using Pillai's test at a statistical significance $\alpha=5\%$ in Excel (Microsoft Office, 2016) and XLSTAT (Addinsoft).

ER Domain Surface Area Ratios. Differential area increases for flat and curved areas predictably resulted in a change of the area ratio for both ER domains, compared with untreated cells (Fig. 3.33). The ratio of curved surface area to the total ER surface area comparing silenced-treated with control-treated cells had no difference, implying a proportional increase of the curved domains to the overall ER surface increase (Fig. 3.32). At the same time, the ratio of cisternal surface area to the total ER surface area had a statistically significant increase in silenced treated cells when compared with control-treated cells, to 134.2±4.2% ($p<0.0001$). Additionally, silenced- vs. control-treated cells had an increased ratio of flat surface area to curved surface area, to 139.8±6.0%. All three results clearly indicate that upon silencing of TMEM147 the expansion of flat cisternal areas is disproportionate comparing to curved areas, in addition to an overall increase of ER surface area and network density.

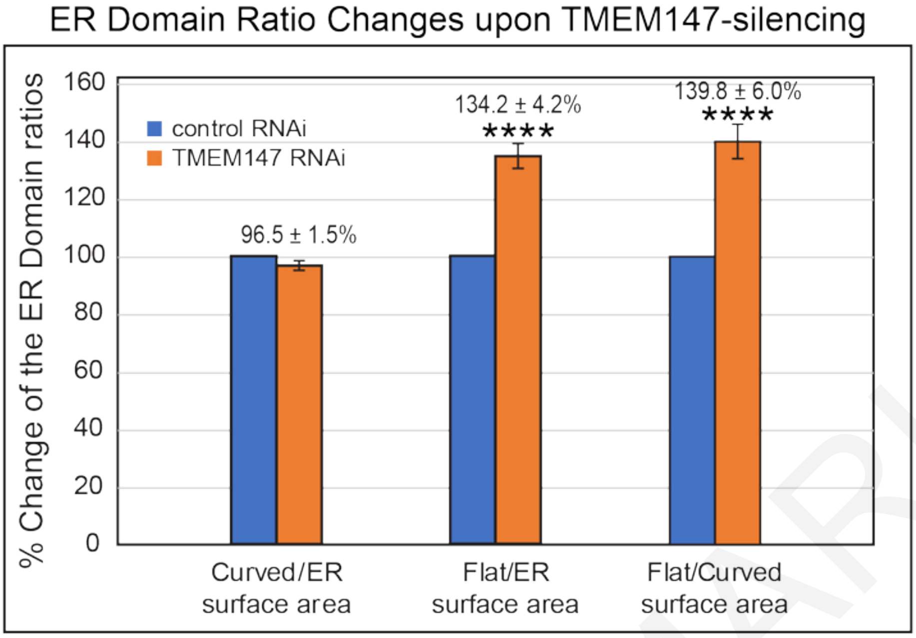

Figure 3.33: ER-domain ratio changes chart.
Bar chart of percentage changes in ER-domain ratios. Curved area corresponds to RTN4, flat area to CLIMP63 and ER to overlap-corrected union of CLIMP63 and RTN4 areas. Experiments were conducted in triplicate. Tubular area of silenced cells changes slightly, suggesting that ratio of tubular area to the total area of ER does not change, either in the presence or not of TMEM147. Downregulation of TMEM147 increased the ratio of flat sheet areas over the total area of ER (34.2±4.2%, $p<0.0001$) suggesting that the ER area expansion is contributed mainly from the flat sheet domain. The ratio of sheet area over tubular area of TMEM147-silenced cells compared with control cells changes with the sheet area changing in a greater magnitude than tubular area (39.8±6.0%, $p<0.0001$). (mean±s.d.). The analysis was assessed on data for 362 HeLa cells (n=177 control, n=185 silenced) after outlier removal using 1.5x IQR rule (Tukey, 1977). For the statistical significance MANOVA analysis was applied for silenced and control cells using Pillai's test at a statistical significance α=5% in Excel (Microsoft Office, 2016) and XLSTAT (Addinsoft)

3.10 Data mining to compile TMEM147 interactors

Our findings regarding the role of TMEM147 in cholesterol homeostasis and furthermore its apparent inhibitory effect on ER size and density suggested a wide range of additional future research investigation targets. In order to identify the most promising targets and experimental strategies for future investigations and to allow deeper insight into potential functional roles of TMEM147, we finally conducted a thorough and comprehensive datamining investigation of interaction and association databases and of the literature, in order to identify all known TMEM147 interactions and associations. Data from eleven different databases and literature were collected, compared and sorted before integration. This investigation revealed 98 interactors of TMEM147 (Table 3.2; for full annotations see Table 6.2 in the Appendix), which were used in subsequent network and pathway analysis.

Gene Symbol[a] [String-db ID][b]	Uniprot Id[c]	Interaction type[d]	GO IDs[e]	GO Group/ Context[f]	Protein[g]	Db found[h]
ABHD16A	O95870	A			Phosphatidylserine lipase ABHD16A	A,B,C,D,E,G,F,J
ABI3	Q9P2A4	A			ABI gene family member 3	A,B,D,E,G,F,I,J
AVPR2	P30518	B	4888, 8528, 38023, 4930	A	Vasopressin V2 receptor	C
BCAP31	P51572	F			B-cell receptor-associated protein 31	C
BRF2	Q9HAW0	B			Transcription factor IIIB 50 kDa subunit	A,D,F,I,J
CAPNS1	P04632	F			Calpain small subunit 1	C
CASP4	P49662	B			Caspase-4	A,D,F,J
CCDC47	Q96A33	A			PAT complex subunit CCDC47	H
CD40	P25942	A	4888, 38023	A	Tumor necrosis factor receptor superfamily member 5	A,B,G,F,I,J
CD79A	P11912	A	4888, 38023	A	B-cell antigen receptor complex-associated protein alpha chain	A,B,G,F,I,J
CGN	Q9P2M7	B			Cingulin	A
CHRM3	P20309	A	4888, 38023, 8227, 4930	A	Muscarinic acetylcholine receptor M3	C,H
CLDN7	O95471	A			Claudin-7	A,B,G,F,I,J
CLN8	Q9UBY8	A			Protein CLN8	A,B,D,H,J
CLRN1	P58418	A			Clarin-1	A,B,D,H,J
COX6B1	P14854	F	22890, 15077	B	Cytochrome c oxidase subunit 6B1	C
CREB3L1	Q96BA8	A			Cyclic AMP-responsive element-binding protein 3-like protein 1	A,B,D,G,F,I,J,K
CXCR2	P25025	A	4888, 8528, 38023, 4930	A	C-X-C chemokine receptor type 2	A,B,G,F,I,J,K
DHCR7	Q9UBM7	A	16628	C	7-dehydrocholesterol reductase	H
DPM3	Q9P2X0	A			Dolichol-phosphate mannosyltransferase subunit 3	A,B,G,F,I,J
EBP	Q15125	A	4888, 38023, 16860, 16863	A,C	3-beta-hydroxysteroid-Delta(8),Delta(7)-isomerase	A,B,G,F,I,J,K
EFNA4	P52798	A	4888, 38023	A	Ephrin-A4	A,B,G,F,I,J
EIF3K	Q9UBQ5	F	43022	D	Eukaryotic translation initiation factor 3 subunit K	C
ENPP4	Q9Y6X5	A			Bis(5'-adenosyl)-triphosphatase ENPP4	A,B,G,F,J
F11R	Q9Y624	A			Junctional adhesion molecule A	A,B,G,F,J,K
FASN	P49327	G	16628	C	Fatty acid synthase	B
FFAR2	O15552	A	4888, 38023, 4930	A	Free fatty acid receptor 2	A,B,G,F,J,K
FOXF2	Q12947	E			Forkhead box protein F2	I
GJA8	P48165	A			Gap junction alpha-8 protein	A,B,G,F,J
GLP1R	P43220	A	4888, 8528, 38023, 4930	A	Glucagon-like peptide 1 receptor	A,B,D,G,H,J
GOLM1	Q8NBJ4	A			Golgi membrane protein 1	A,B,G,F,J
GPR101	Q96P66	A	4888, 38023, 8227, 4930	A	Probable G-protein coupled receptor 101	A,B,G,F,J
GPR37L1	O60883	A	4888, 8528, 38023, 4930	A	G-protein coupled receptor 37-like 1	A,B,G,F,J,K
GPR42	O15529	A	4888, 38023, 4930	A	G-protein coupled receptor 42	B,G,F,I,J
GPR61	Q9BZJ8	A	4888, 38023, 4930	A	G-protein coupled receptor 61	A,B,G,F,J
HTR2C	P28335	A	4888, 38023, 8227, 4930	A	5-hydroxytryptamine receptor 2C	A,B,D,G,F,J
IER3IP1	Q9Y5U9	C			Immediate early response 3-interacting protein 1	L
IL3RA	P26951	A	4888, 38023	A	Interleukin-3 receptor subunit alpha	A,B,G,F,J,K
KASH5 [CCDC155]	Q8N6L0	A			Protein KASH5	A,B,G,F,I,J
LBR	Q14739	A	16628	C	Delta (14) - Sterol Reductase LBR	H

LDLRAD1	Q5T700	A			Low-density lipoprotein receptor class A domain-containing protein 1	A,B,D,G,F,J
LEF1	Q9UJU2	E	38023	A	Lymphoid enhancer-binding factor 1	I
LEUTX	A8MZ59	A			Paired-like homeodomain transcription factor LEUTX	A,B,G,F,I,J
LHFPL2	Q6ZUX7	A			LHFPL tetraspan subfamily member 2 protein	A,B,G,F,J
LRRFIP2	Q9Y608	B			Leucine-rich repeat flightless-interacting protein 2	A
MIF	P14174	F	16860, 16863	C	Macrophage migration inhibitory factor	C
MPRIP	Q6WCQ1	B			Myosin phosphatase Rho-interacting protein	A
MTCH2	Q9Y6C9	C			Mitochondrial carrier homolog 2	L
MTIF3	Q9H2K0	A	43022	D	Translation initiation factor IF-3, mitochondrial	A,B,G,F,I,J,K
MUC1	P15941	A			Mucin-1	A,B,G,F,I,J
NCLN	Q969V3	A			Nicalin	C,H,L
NFKB1	P19838	A			Nuclear factor NF-kappa-B p105 subunit	H
NHP2	Q9NX24	F			H/ACA ribonucleoprotein complex subunit 2	C
NOMO		A			NODAL modulator	H
PACC1 [TMEM206]	Q9H813	A			Proton-activated chloride channel	A,B,D,G,F,J
PDCD1LG2	Q9BQ51	A			Programmed cell death 1 ligand 2	A,B,G,F,I,J
PHPT1	Q9NRX4	F			14 kDa phosphohistidine phosphatase	L
PLEKHG3	A1L390	B			Pleckstrin homology domain-containing family G member 3	A
POLE4	Q9NR33	F			DNA polymerase epsilon subunit 4	C
POLR2I	P36954	F			DNA-directed RNA polymerase II subunit RPB9	C
PPP1R9A	Q9ULJ8	B			Neurabin-1	A
PSCA	O43653	A			Prostate stem cell antigen	A,B,G
PSENEN	Q9NZ42	F			Gamma-secretase subunit PEN-2	L
PVR	P15151	A	38023	A	Poliovirus receptor	A,B,G,F,J,K
RABAC1	Q9UI14	F			Prenylated Rab acceptor protein 1	C
RBM42	Q9BTD8	F			RNA-binding protein 42	C
RMDN3	Q96TC7	A			Regulator of microtubule dynamics protein 3	A,B,G,F,J
RNF185	Q96GF1	A			E3 ubiquitin-protein ligase RNF185	A,B,G,F,J
RTKN	Q9BST9	B			Rhotekin	A
RUVBL2	Q9Y230	F			RuvB-like 2	C
SCAMP4	Q969E2	A			Secretory carrier-associated membrane protein 4	A,B,G,J
SEC61A1	P61619	A	43022	D	Protein transport protein Sec61 subunit alpha isoform 1	H
SHISA3	A0PJX4	A			Protein shisa-3 homolog	A,B,G,F,J
SLC10A1	Q14973	A	15294, 15370, 15291, 15081, 46873, 1901618, 22890, 15077	B	Sodium/bile acid cotransporter	A,B,G,F,J,K
SLC12A7	Q9Y666	A	15296, 15377, 15294, 15291, 46873, 22890, 15077	B	Solute carrier family 12 member 7	A,B,G,F,J
SLC13A4	Q9UKG4	A	15296, 15373, 15294, 15370, 15291, 15081, 46873, 22890, 15077	B	Solute carrier family 13 member 4	A,B,G,F,I,J,K
SLC22A1	O15245	A	15296, 15373, 15377, 5277, 5330, 5334, 8513, 15294, 15370, 15651, 15291, 15081, 46873, 1901618, 22890, 15077	B	Solute carrier family 22 member 1	A,B

SLC22A2	O15244	A	15296, 15373, 15377, 5277, 5330, 5334, 8513, 15294, 15370, 15651, 15291, 15081, 46873, 1901618, 22890, 15077	B	Solute carrier family 22 member 2	A,B
SLC41A1	Q8IVJ1	A	15291, 15081, 46873, 22890, 15077	B	Solute carrier family 41 member 1	H
STOML2	Q9UJZ1	F			Stomatin-like protein 2, mitochondrial	C
SUSD3	Q96L08	A			Sushi domain-containing protein 3	A,B,G,F,I,J
SYNE4	Q8N205	A			Nesprin-4	A,B,D,G,F,I,J
TACR1	P25103	A	4888, 8528, 38023, 4930	A	Substance-P receptor	A,B,G,F,I,J,K
TBCB	Q99426	F			Tubulin-folding cofactor B	C
TEX29	Q8N6K0	A			Testis-expressed protein 29	A,B,G,F,J
TMCO1	Q9UM00	A	46873, 22890	B,D	Calcium load-activated calcium channel	H
TMEM14B	Q9NUH8	A			Transmembrane protein 14B	A,B,G,F,J
TMEM237	Q96Q45	A			Transmembrane protein 237	A,B,G,F,J
TMEM248	Q9NWD8	A			Transmembrane protein 248	A,B,G,F,I,J
TMEM252	Q8N6L7	A			Transmembrane protein 252	A,B,G,F,I,J
TMEM42	Q69YG0	A			Transmembrane protein 42	A,B,G,F,J
TMEM52B	Q4KMG9	A			Transmembrane protein 52B	A,B,G,F,I,J
TPI1	P60174	F	16860	C	Triosephosphate isomerase	C
TRAPPC3	O43617	F			Trafficking protein particle complex subunit 3	C
TRPC6	Q9Y210	H	46873, 22890	B	Short transient receptor potential channel 6	B,H,J
TSPAN12	O95859	A			Tetraspanin-12	A,B,G,F,J
YIPF6	Q96EC8	C			Protein YIPF6	L

Table 3.2: Curated list of reported TMEM147 associations and interactions.

This manually curated, non-redundant list of proteins as retrieved from twelve different repositories is the basis for network and pathway enrichment analyses. An annotated version of this table is provided in Table 6.2 in the Appendix.

[a] *Official gene symbol according to the HUGO Gene Nomenclature Committee (HGNC).*

[b] *The associated STRING ID used in STRING analysis, if different from the official gene symbol.*

[c] *Protein UniProt ID.*

[d] *Nature of discovered TMEM147 interactions: [A] direct physical interaction: the interaction is at the protein-protein level; [B] physical interaction: co-existence in a stable complex; [C] indirect physical interaction: both proteins have a common direct physical interactor; [D] functional association: the combined function with TMEM147 affects the corresponding phenotype; [E] expression regulation: the interactor controls the expression of TMEM147; [F] genetic: significant co-regulation, protein expression dependency or intercellular co-localization with TMEM147; [G] positive modifier: the phenotype is more severe when both are defective; [H] negative modifier: the phenotype is milder when both are defective.*

[e] *Gene Ontology ID with format GO: ####### after removal of "GO:" and leading zeros for the sake of compactness.*

[f] *Representative non-redundant Gene Ontology category according to REVIGO: [A] G-protein coupled receptor activity; [B] Transmembrane transport; [C] Oxidoreductase activity; [D] Ribosome binding.*

[g] *Protein name as found in UniProt.*

[h] *Query sources: [A] APID; [B] BioGRID; [C] GeneMania; [D] GPS-Prot; [E] Human Protein Reference Database; [F] IntAct EMBL-EBI; [G] HuRi; [H] PubMed; [I] Pathwaycommons; [J] PINA3; [K] Reactome; [L] STRING*

3.11 Network analyses of reported TMEM147-associated proteins

The previously generated input-list of TMEM147 interactors, co-actors, targets and effectors was employed in network analysis using STRING-db (Szklarczyk et al., 2019), in order to produce a comprehensive network of TMEM147-associated factors and pathways (Fig. 3.34A). The analysis showed that for twelve of our list components, even if they were identified from the other repositories as TMEM147 interactors, String-db analysis gave back no connected association with TMEM147, or any of the other 86 components. Moreover, if the analysis in String-db was conducted by employing TMEM147 as a single input protein, the result would be a ten-member network compared with our list-based analysis and the 87 out of 98 interactors discoveries (Fig. 3.34B). Both LBR and DHCR7 were included in these exclusions. Remarkable as it is, this observation was of no surprise and indicative that even if the String-db analysis tool is constantly updated and exceptionally powerful and versatile, it cannot be used as a complete repository of interactions; indicating that provision of manually curated input lists leads to more accurate results, free of misinterpretations of an automated machine search, and hence should be preferable.

Pathway-based analyses in String-db then revealed several pathway categories with statistically significant enrichment in the supplied list of TMEM147-associated proteins, including 25 GO Molecular Function terms, 21 GO Cellular Component terms, 6 GO Biological Process terms, 7 UniProt Annotated Keyword terms, 3 PubMed Reference Publications, 1 Reactome pathway, 1 Pfam Protein Domain (Tables 6.3-6.9 in the Appendix). As particularly informative for further analysis, the significantly enriched GO Molecular Function nodes were then exported to REVIGO (Supek et al., 2011) for content simplification and redundant GOs integration.

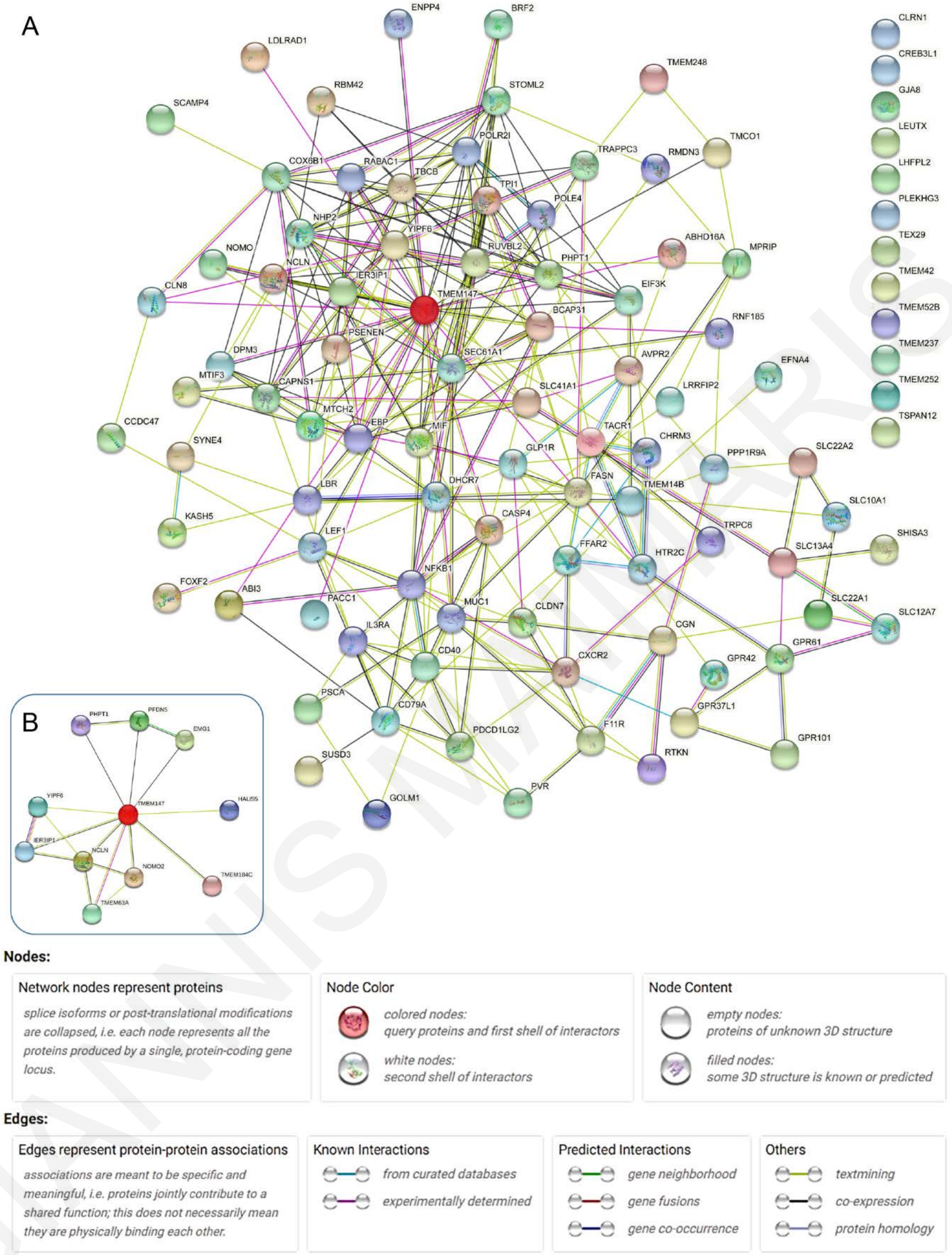

Nodes:

Network nodes represent proteins

splice isoforms or post-translational modifications are collapsed, i.e. each node represents all the proteins produced by a single, protein-coding gene locus.

Node Color

colored nodes:
query proteins and first shell of interactors

white nodes:
second shell of interactors

Node Content

empty nodes:
proteins of unknown 3D structure

filled nodes:
some 3D structure is known or predicted

Edges:

Edges represent protein-protein associations

associations are meant to be specific and meaningful, i.e. proteins jointly contribute to a shared function; this does not necessarily mean they are physically binding each other.

Known Interactions

from curated databases

experimentally determined

Predicted Interactions

gene neighborhood

gene fusions

gene co-occurrence

Others

textmining

co-expression

protein homology

Figure 3.34: Network analysis for TMEM147-associated proteins.
(A) Primary network of proteins, based on our manually curated list of known interactions and reports for TMEM147 (indicated by transparent red overlay), as analyzed in String-db 11.0b. Proteins without interaction in the String-db 11.0b database are aligned at the top right.
(B) Primary network of TMEM147-associated proteins as held in String-d 11.0b, based on TMEM147 as input. The color code for underlying database information used by String-db is given in the in-figure legend. Of note, no white nodes are present, because network analysis was restricted to query proteins.

3.12 Pathway analysis for the TMEM147 gene network

REVIGO simplified the complete list of Molecular Function GO terms provided by STRING-db analysis (Table 6.3 in the Appendix) by removing the redundant terms and clustering them in 7 functional groups of GO terms as a summary of a pathway-based analysis for all currently known TMEM147-associated proteins (Table 3.3). These 7 groups were also represented in a Scatterplot graph and their interconnections were represented in an interactive map as well (Fig. 6.1 in the Appendix).

GO term ID	Name	Frequency	Value	Uniqueness	Dispensability
GO:0015296	anion:cation symporter activity	0.121%	-2.6576	0.38	0.00
GO:0016628	oxidoreductase activity, acting on CH-CH group of donors, NAD or NADP as acceptor	0.160%	-1.6271	0.98	0.00
GO:0043022	ribosome binding	0.364%	-1.4685	1.00	0.00
GO:0008528	G protein-coupled peptide receptor activity	0.817%	-1.6271	0.80	0.00
GO:0016860	intramolecular oxidoreductase activity	0.298%	-1.4750	0.93	0.13
GO:1901618	Organic hydroxy compound transmembrane transporter activity	0.287%	-1.4685	0.54	0.41
GO:0015651	quaternary ammonium group transmembrane transporter activity	0.061%	-1.6271	0.47	0.45

Table 3.3: Reduction of pathway complexity for TMEM147.
Reduction of Gene Ontology Molecular Function terms for TMEM147 interactors based on enriched Gene Ontology Molecular Functions terms identified by String-db 11.0b, as assessed by REVIGO with target a "Small" output list.

In an attempt of even more simplified conclusions, the resulting non-redundant GO terms can be further clustered, based on color coding, as shown in TreeMap provided by REVIGO (Fig. 3.35). In conclusion, our analysis showed that TMEM147 could be associated with 4 Molecular Function GO term-clusters: [A] G protein-coupled receptor activity, [B] Transmembrane transport, [C] Oxidoreductase activity and [D] Ribosome binding.

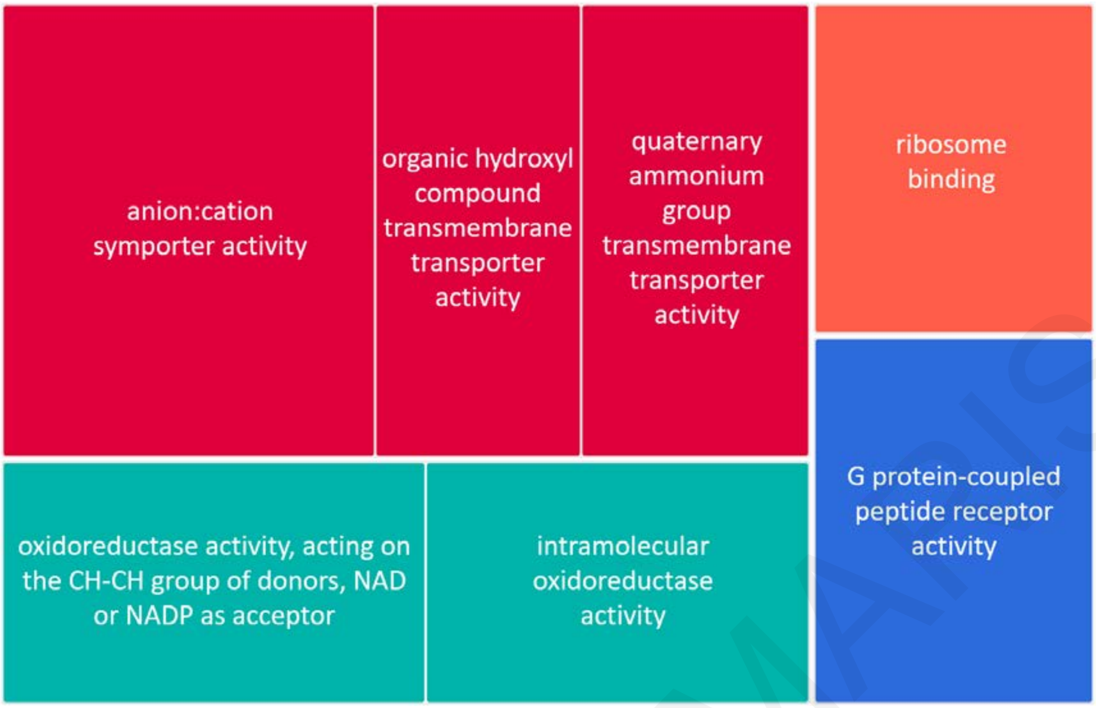

Figure 3.35: Reduction of pathway complexity for TMEM147 using TreeMap.
This TreeMap shows the non-redundant Gene Ontology Molecular Function terms for TMEM147 interactors, generated by REVIGO as in table 7, with color coding clustering for further simplicity. The four clusters identified in REVIGO depending on their color codes are: RED: Transmembrane transport; ORANGE: Ribosome binding; BLUE: G protein-coupled receptor activity; TURQUOISE: Oxidoreductase activity.

Taken together this bioinformatics analysis, the initial 25 GO terms identified by STRING-db, implicating TMEM147 in various molecular functions, were clustered to seven subsets by removing the redundant terms in REVIGO and then simplified even more down to four parental terms (color code in TreeMap, Fig.3.35). These four parental GO terms summarize the molecular functions associated with TMEM147, as interpreted from the long list of interactors presented earlier and provide a general notion of the functions that may this protein be involved in. This analysis though, can also be read in the opposite direction, especially for proteins that are not well characterized but interaction data are provided via untargeted studies. Specifically, the four GO terms associated with TMEM147 and their related child-terms in this analysis, can be used as a reference tool for future insight. Through this list further studies on TMEM147 can be targeted either towards a specific direction in an already initiated study field like its association with G-protein coupled receptor (muscarinic receptor (Rosemond et al., 2011)) or dive into a field that TMEM147 was not yet implicated, like its potential role in uptake and release of Ca^{2+} from the ER as the symporter activity GO terms suggest.

3.13 Contribution Acknowledgment

At the end of this Results chapter, I would like to acknowledge the help and contribution of other members of the laboratory in this work. In particular I would like to credit and thank Dr Andri Christodoulou (biochemical work), Dr Evelina Aristodemou (lipidomics analysis), Dr Carsten W. Lederer (bioinformatic analysis), undergraduate student Andri Makrigiorgi and lab associate Renos Georgiou for their experimental input.

3.14 Publications

The work presented in this Chapter was published as follows and reprints are included in the Appendix (Sections 6.1 and 6.2):

Publication 1

TMEM147 interacts with lamin B receptor, regulates its localization and levels, and affects cholesterol homeostasis.

Andri Christodoulou, Giannis Maimaris, Andri Makrigiorgi, Evelina Charidemou, Christian Lüchtenborg, Antonis Ververis, Renos Georgiou, Carsten W Lederer, Christof Haffner, Britta Brügger, Niovi Santama.

J Cell Sci. 2020 Aug 21;133(16):jcs245357

doi: 10.1242/jcs.245357.

PMID: 32694168.

Publication 2

Regulation of ER Composition and Extent, and Putative Action in Protein Networks by ER/NE Protein TMEM147.

Giannis Maimaris, Andri Christodoulou, Niovi Santama, Carsten Werner Lederer.

Int J Mol Sci. 2021 Sep 23;22(19):10231.

doi: 10.3390/ijms221910231.

PMID: 34638576.

4

Discussion

Chapter 4: Discussion

Previous studies have shown that TMEM147 is a core component and stabilizer of the membrane complex Nicalin-NOMO, which acts as a modulator of the NODAL signal transduction pathway controlling early embryonic development in *Zebrafish*. Additionally, trafficking and proper folding of muscarinic receptor 3 (M3R) in COS-7 cells, have been shown to be impaired upon downregulation of TMEM147. More recently, it has been implicated in regulating the activation of NF-κB transcription factors, as a response of the immune system to infection in chondrocytes of the joints during the development of rheumatoid arthritis.

During our studies for the characterization of TMEM147, we found that this ER membrane and INM resident protein physically and functionally interacts with LBR, an extensively studied protein with a dual role in tethering and organizing heterochromatin to nuclear lamina and in cholesterol biosynthesis. We found that upon siRNA mediated downregulation of TMEM147, both gene and protein expression of LBR were markedly reduced while at the same time it was mislocalized to the ER membranes. Mapping the interaction of TMEM147-LBR, we found that the C-terminal domain of LBR where its sterol reductase activity resides, is essential in contrast to its N-terminal domain where this dual activity protein tethers and organizes heterochromatin. Investigating how this might affect the overall cholesterol homeostasis, our lipidomics analysis showed that TMEM147 downregulation alters the levels of cholesteryl esters, levels of free cellular cholesterol and its uptake in cells. Consequently, TMEM147 can be suggested as a regulator of cholesterol homeostasis in cells.

Cholesterol has been shown to be essential for cells not only maintaining and regulating fluidity, rigidity and permeability of the lipid bilayers but also vital for the proper signaling during cell differentiation in embryonic developmental stages in mammals. It is also important in insulating the axons of nerves, mediating a faster signal transport along the nerve axis as it forms myelin sheath. Homeostasis of cholesterol includes a fine regulation between the *de novo* synthesis, the uptake of cholesterol via membrane receptor endocytosis and the esterification of its excess amounts. Downregulation of TMEM147 has been shown to increase the uptake of cholesterol, consistent with the decreased levels of LBR and DHCR7, most probably as a response to the impaired cholesterol biosynthesis and the decreased levels of cholesteryl esters (esters are hydrolyzed as a response to low cholesterol levels). Compared with other work showing that cell growth declined only at the concurrent LBR depletion and cholesterol uptake impairment (Tsai et al., 2016), our results show that even if cholesterol is supplied in the medium, silencing of TMEM147 alone has detrimental results in cell viability (Fig. 3.28). Most probably this can be explained because in the absence of TMEM147 the cellular changes are to such an extent that cannot be restored back to normal just by restoring cellular total free cholesterol levels.

In addition to the interaction of TMEM147 with LBR, both IP experiments and MS analysis has shown that there is an interaction at the protein level with two other reductases, DHCR7 and TM7SF2 both catalyzing reactions in cholesterol biosynthesis pathway. In particular, whereas LBR and TM7SF2 catalyze the same step, DHCR7 participates in an upstream catalytic step and also in the last step of cholesterol synthesis. Upon TMEM147 depletion, DHCR7 like LBR showed the same negative regulation response, whereas under lipid depleted conditions this reductase is upregulated to 2.5-fold. DHCR7 mutations have been implicated in Smith-Lemli-Opitz syndrome (SLOS), but despite the vast data on this syndrome only a little is known concerning its interaction with LBR. On the basis of our results, it could be proposed that TMEM147 regulates both LBR and DHCR7 in a positive way affecting both in the transcriptional and translational level but the mechanism underlying this interaction remains to be found.

Although TMEM147 downregulation affects both LBR and DHCR7 gene expression, our results show that it does not affect TM7SF2 levels. Both TM7SF2 and LBR catalyze the same step in the biosynthetic pathway of cholesterol but this differential response when TMEM147 is depleted reveals that the transcriptional regulation of these two reductases is distinct. This differential gene expression regulation between TM7SF2 and LBR was also observed in other studies where in HeLa cells among other cell lines, LBR expression was unaffected under either normal or lipid restrictive conditions in contrast to upregulated levels of TM7SF2 in the absence of lipids (Tsai et al., 2016). Additionally, homozygous TM7SF2 knock out mice had also unaffected levels of LBR (Bennati et al., 2006b). This distinct regulation in not only at the gene expression level but also in the post-translational level as elevated cholesterol levels or pathway intermediates decreased the half-life of TM7SF2 but not of LBR (Capell-Hattam et al., 2020). Conclusively, even if these two reductases share a common Delta-14 reductase activity and catalyze the same biosynthetic step of cholesterol biosynthesis, in the absence of LBR, TM7SF2 cannot compensate for cholesterol synthesis as Wassif et al., proposed (Wassif et al., 2007).

In addition to the negative regulation of LBR levels and its consequent absence from the nuclear rim upon TMEM147 downregulation, LBR labeling was also shifted to the ER membranes in contrast to the negative control cells from where it is normally absent

(Nikolakaki et al., 2017). Similar retention of the LBR to the ER is also observed upon depletion of nucleoporin ELYS or when phosphorylation of the LBR N-terminal domain was inhibited (Clever et al., 2012, Mimura et al., 2016, Nikolakaki et al., 1996, Tseng and Chen, 2011). This observation is thus not entirely unexpected as ER compartment is dedicated to translation, proper folding and targeting of transmembrane proteins while nuclear pore complexes facilitate their lateral diffusion from the ER to the INM, through peripheral channels of the complexes, of which the ELYS component also acts on protein phosphatases regulating their activity. Therefore, although LBR retention in the ER membranes is not entirely unexpected, the detected cholesterol synthesis impairment is not clear whether it may depend on LBR localization. If proper localization of LBR in the INM is required for its reductase activity hence cholesterol synthesis, then its altered localization upon TMEM147-silencing might be an additional contribution to the reduction of cholesterol synthesis.

Phenotypic nuclear-related alterations are not limited to the decreased LBR rim labeling or its mislocalization to the ER. Here, we report that upon downregulation of TMEM147, nuclear sphericity changes, accompanied by loss of chromatin compaction. These phenotypes have also been shown in other work and seem to be related with specific cell developmental stages. It has been documented that during differentiation of the specific immune system cell line granulocytes, LBR is upregulated and this is related to adoption of a 3-4 lobulated nuclear morphology and the retention of heterochromatin to the periphery of the nucleus (Olins et al., 2008). Consistent with this, is the reported NE growth induced by invaginations and the formation of membrane stacks as a result of LBR upregulation (Ma et al., 2007). In contrast, truncated or impaired-activity mutant forms of LBR resulting in depleted wt. LBR in granulocytes of Pelger-Huët patients have been shown to be related with hypolobulated nuclei. Moreover, the related ichthyosis syndrome in mice is manifested by ovoid nuclei and heterochromatin oriented towards the center of the nucleoplasm while euchromatin is moved to the periphery (Shultz et al., 2003, Hoffmann et al., 2007). Nuclear shape alterations and redistribution of the heterochromatin to the nucleoplasm have also been reported in myeloid cells, where the severity of the phenotype is dependent on the hetero- or homozygosity state of the mutant LBR allele when *in vitro* differentiation is induced (Hoffmann et al., 2007).

In this work beside nuclear phenotypic changes we report that TMEM147 depletion also induces structural alterations to the ER. Investigating CLIMP63 and RTN4, as ER flat and tubular subdomain markers respectively, we report that TMEM147 depletion affects the composition, the size and presumably the structure and density of the ER. Labeling intensity of both markers is markedly increased followed by an increase in their corresponding surface area. In particular, the intensity increase of CLIMP63 is greater than RTN4 and the ratio between flat and tubular areas is also increased. CLIMP63 regulates the formation of flat ER areas by acting as a spacer that maintains the opposing membranes of the ER sheets, whereas RTNs are present in every tubular ER domain constructing and maintaining the membrane curvature by integrating their wedge-like hydrophobic hairpins to the outer lipid leaflet (Shibata et al., 2010, Zhang and Hu, 2016). More importantly, recent ultrastructural microscope studies revealed that these, two ER markers dynamically regulate the formation of nanodomains with evidence of opposing impact on spatial localization of these nanodomains in the peripheral ER tubules (Gao et al., 2019). In the same context, our initial work can be further expanded by microscope ultrastructural analysis to reveal how differences in intensity and ER staining can be reflected in membrane network or differential expression of CLIMP63 and RTN4 upon TMEM147 depletion. While ER network seems to be expanded and denser, at the same time the overall cell size remained unaffected between TMEM147-silenced and negative control silenced cells, according to nucleocytoplasmic ratio and the constant nuclear size (Cantwell and Nurse, 2019b, Hara, 2020). In this context, an indirect effect of TMEM147 depletion can be the defective intracellular organization and/or transportation of other organelles.

Not many years after the first study on TMEM147 (Dettmer et al., 2010), this residential transmembrane protein of ER and NE has been associated with a number of diverse interactions. In an attempt to compile all known TMEM147 associations towards a better understanding of its functional relations in cells, we manually curated a list of reported interactors, regulators and mediators by datamining an extensive list of online available databases and literature. All gene networks and pathways identified were then statistically evaluated and simplified and, as a result, we have a list of the most related proteins and important pathways involving TMEM147. This pathway enrichment analysis and the following removal of redundant pathways highlighted a small list of four functional clusters indicating the most important associations of TMEM147 (color coded TreeMap plot (Fig. 3.35)). The first of the four key clusters indicated by REVIGO (Supek et al., 2011), was the *G-protein coupled receptor function,* in agreement with its regulation function of muscarinic receptor 3 (Rosemond et al., 2011). The second cluster was *Ribosome binding,* which indicates the role of Nicalin-NOMO-TMEM147 complex and specifically TMEM147 facilitating the co-translational translocation in the translocon complex (McGilvray et al., 2020). *Oxidoreductase activity,* implies TMEM147 relations with proteins involved in cholesterol synthesis consistent with our previously mentioned results, whereas the fourth cluster *Transmembrane transport*, indicates the role of TMEM147 transporting proteins into the membrane a role established in Nicalin-NOMO-TMEM147 complex and its association with the ribosome binding translocon complex. The last indicated channel attribute of TMEM147 as a component of the translocon complex can be further examined regarding its own activity on the ER and the potent role as a transport channel with a possible relation in Ca^{2+} uptake and release from the smooth tubular ER.

Regarding the individual interactors and their associated network created in STRING-db, TMEM147 is represented as the major hub protein with minor hubs within the network. Evaluating this network, hub protein factors with high connectivity can imply major key mediators or regulators of TMEM147. Such proteins include emopamil binding protein (EBP), CD40, NFKB1. EBP, like TMEM147 is also a residential protein of ER and NE and comprises an isomerase activity catalyzing the conversion of δ8 sterols to their δ7 isomers in cholesterol biosynthesis. Furthermore, DHCR7 and EBP form a bifunctional complex and present coordinated transcription (de Medina et al., 2010). These data can suggest that, like LBR and DHCR7, even more proteins in the cholesterol synthesis are likely to be affected by TMEM147. Similarly, CD40 with a role in mediating immune responses (Takada et al., 2019), and NFKB1 as a regulator of innate immunity can be further associated with TMEM147 as it has been shown that the latter activates NF-κB in the development of rheumatoid arthritis (Ota et al., 2020).

Our overall findings can be summarized in Fig. 4.1. The figure illustrates that TMEM147 is implicated at different levels in physical and functional association with LBR and DHCR7, key components in cholesterol biosynthesis, it highlights the potential role of TMEM147 in morphogenesis of both NE and ER subdomains, and includes insights of likely novel interactors stemming from our network analysis. Taken together, these different aspects indicate the importance of further studies to unravel the underlying interactions and understand their molecular mechanisms as future research objectives.

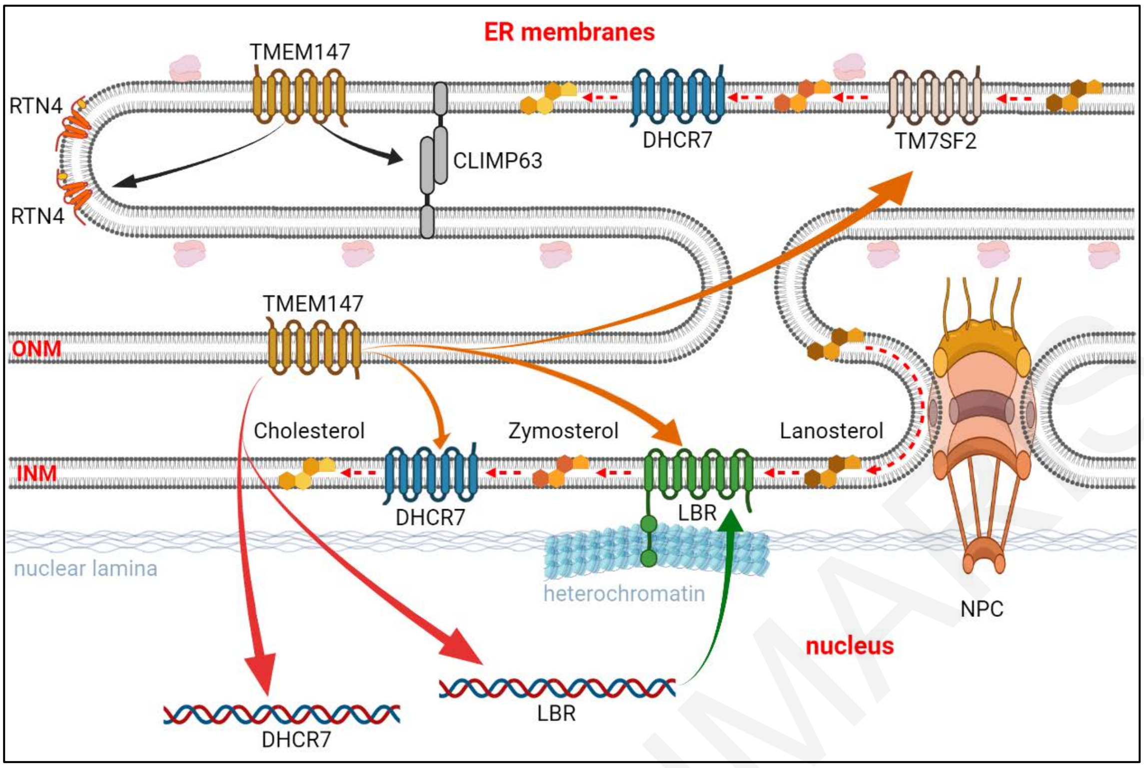

Figure 4.1: Schematic summary representation of our findings regarding the functions of TMEM147. *TMEM147 is involved in the regulation of the levels of the ER structural proteins RTN4 and CLIMP63 (black arrows). TMEM147 also physically interacts with DHCR7 and LBR (orange arrows), while exhibiting a co-ordinate gene expression (red arrows). Green arrow indicates the impact on the localization for LBR. TMEM147 also physically interacts with TM7SF2 (orange arrow). Synthesis of cholesterol, occurs at the ER and NE membranes and all three reductases, TM7SF2, LBR and DHCR7, catalyze key steps of cholesterol biosynthesis. (Created with BioRender.com.)*

5

Bibliography

Chapter 5: Bibliography

ALONSO-LOPEZ, D., CAMPOS-LABORIE, F. J., GUTIERREZ, M. A., LAMBOURNE, L., CALDERWOOD, M. A., VIDAL, M. & DE LAS RIVAS, J. 2019. APID database: redefining protein-protein interaction experimental evidences and binary interactomes. *Database (Oxford),* 2019.

ANDRULIS, E. D., NEIMAN, A. M., ZAPPULLA, D. C. & STERNGLANZ, R. 1998. Perinuclear localization of chromatin facilitates transcriptional silencing. *Nature,* 394**,** 592-5.

ANWAR, K., KLEMM, R. W., CONDON, A., SEVERIN, K. N., ZHANG, M., GHIRLANDO, R., HU, J., RAPOPORT, T. A. & PRINZ, W. A. 2012. The dynamin-like GTPase Sey1p mediates homotypic ER fusion in S. cerevisiae. *J Cell Biol,* 197**,** 209-17.

APPELBAUM, J., BLOBEL, G. & GEORGATOS, S. D. 1990. In vivo phosphorylation of the lamin B receptor. Binding of lamin B to its nuclear membrane receptor is affected by phosphorylation. *J Biol Chem,* 265**,** 4181-4.

ASENCIO, C., DAVIDSON, I. F., SANTARELLA-MELLWIG, R., LY-HARTIG, T. B., MALL, M., WALLENFANG, M. R., MATTAJ, I. W. & GORJÁNÁCZ, M. 2012. Coordination of kinase and phosphatase activities by Lem4 enables nuclear envelope reassembly during mitosis. *Cell,* 150**,** 122-35.

BARLOWE, C., ORCI, L., YEUNG, T., HOSOBUCHI, M., HAMAMOTO, S., SALAMA, N., REXACH, M. F., RAVAZZOLA, M., AMHERDT, M. & SCHEKMAN, R. 1994. COPII: a membrane coat formed by Sec proteins that drive vesicle budding from the endoplasmic reticulum. *Cell,* 77**,** 895-907.

BATES, S. R. & ROTHBLAT, G. H. 1974. Regulation of cellular sterol flux and synthesis by human serum lipoproteins. *Biochim Biophys Acta,* 360**,** 38-55.

BAUMANN, O. & WALZ, B. 2001. Endoplasmic reticulum of animal cells and its organization into structural and functional domains. *International Review of Cytology.* Academic Press.

BENNATI, A. M., CASTELLI, M., DELLA FAZIA, M. A., BECCARI, T., CARUSO, D., SERVILLO, G. & ROBERTI, R. 2006a. Sterol dependent regulation of human TM7SF2 gene expression: role of the encoded 3beta-hydroxysterol Delta14-reductase in human cholesterol biosynthesis. *Biochim Biophys Acta,* 1761**,** 677-85.

BENNATI, A. M., CASTELLI, M., DELLA FAZIA, M. A., BECCARI, T., CARUSO, D., SERVILLO, G. & ROBERTI, R. 2006b. Sterol dependent regulation of human TM7SF2 gene expression: role of the encoded 3beta-hydroxysterol Delta14-reductase in human cholesterol biosynthesis. *Biochimica et Biophysica Acta (BBA) - Molecular and Cell Biology of Lipids,* 1761**,** 677-685.

BERNALES, S., MCDONALD, K. L. & WALTER, P. 2006. Autophagy counterbalances endoplasmic reticulum expansion during the unfolded protein response. *PLoS Biol,* 4**,** e423.

BLASSBERG, R., MACRAE, J. I., BRISCOE, J. & JACOB, J. 2016. Reduced cholesterol levels impair Smoothened activation in Smith-Lemli-Opitz syndrome. *Hum Mol Genet,* 25**,** 693-705.

BLOBEL, G. 1980. Intracellular protein topogenesis. *Proc Natl Acad Sci U S A,* 77**,** 1496-500.

BONIFACINO, J. S. & GLICK, B. S. 2004. The mechanisms of vesicle budding and fusion. *Cell,* 116**,** 153-66.

BOUCHER, L., OUZOUNIS, C. A., ENRIGHT, A. J. & BLENCOWE, B. J. 2001. A genome-wide survey of RS domain proteins. *RNA,* 7**,** 1693-701.

BRAAKMAN, I. & HEBERT, D. N. 2013. Protein folding in the endoplasmic reticulum. *Cold Spring Harb Perspect Biol,* 5**,** a013201.

BRADY, J. P., CLARIDGE, J. K., SMITH, P. G. & SCHNELL, J. R. 2015. A conserved amphipathic helix is required for membrane tubule formation by Yop1p. *Proc Natl Acad Sci U S A,* 112**,** E639-48.

BROWN, M. S. & GOLDSTEIN, J. L. 1984. How LDL receptors influence cholesterol and atherosclerosis. *Sci Am,* 251**,** 58-66.

CANTWELL, H. & NURSE, P. 2019a. Unravelling nuclear size control. *Current Genetics,* 65**,** 1281-1285.

CANTWELL, H. & NURSE, P. 2019b. Unravelling nuclear size control. *Curr Genet,* 65**,** 1281-1285.

CAPELL-HATTAM, I. M., SHARPE, L. J., QIAN, L., HART-SMITH, G., PRABHU, A. V. & BROWN, A. J. 2020. Twin enzymes, divergent control: The cholesterogenic enzymes DHCR14 and LBR are differentially regulated transcriptionally and post-translationally. *J Biol Chem,* 295**,** 2850-2865.

CERAMI, E. G., GROSS, B. E., DEMIR, E., RODCHENKOV, I., BABUR, O., ANWAR, N., SCHULTZ, N., BADER, G. D. & SANDER, C. 2011. Pathway Commons, a web resource for biological pathway data. *Nucleic Acids Res,* 39**,** D685-90.

CERQUEIRA, N. M., OLIVEIRA, E. F., GESTO, D. S., SANTOS-MARTINS, D., MOREIRA, C., MOORTHY, H. N., RAMOS, M. J. & FERNANDES, P. A. 2016. Cholesterol Biosynthesis: A Mechanistic Overview. *Biochemistry,* 55**,** 5483-5506.

CHEN, S., NOVICK, P. & FERRO-NOVICK, S. 2012. ER network formation requires a balance of the dynamin-like GTPase Sey1p and the Lunapark family member Lnp1p. *Nat Cell Biol,* 14**,** 707-16.

CHEN, S., NOVICK, P. & FERRO-NOVICK, S. 2013. ER structure and function. *Curr Opin Cell Biol,* 25**,** 428-33.

CHRISTODOULOU, A., SANTARELLA-MELLWIG, R., SANTAMA, N. & MATTAJ, I. W. 2016. Transmembrane protein TMEM170A is a newly discovered regulator of ER and nuclear envelope morphogenesis in human cells. *J Cell Sci,* 129**,** 1552-65.

CHUNG, J., TORTA, F., MASAI, K., LUCAST, L., CZAPLA, H., TANNER, L. B., NARAYANASWAMY, P., WENK, M. R., NAKATSU, F. & CAMILLI, P. D. 2015. PI4P/phosphatidylserine countertransport at ORP5- and ORP8-mediated ER–plasma membrane contacts. *Science,* 349**,** 428-432.

CLEVER, M., FUNAKOSHI, T., MIMURA, Y., TAKAGI, M. & IMAMOTO, N. 2012. The nucleoporin ELYS/Mel28 regulates nuclear envelope subdomain formation in HeLa cells. *Nucleus,* 3**,** 187-199.

COHEN, S. 2018. Lipid Droplets as Organelles. *Int Rev Cell Mol Biol,* 337**,** 83-110.

COURVALIN, J. C., SEGIL, N., BLOBEL, G. & WORMAN, H. J. 1992. The lamin B receptor of the inner nuclear membrane undergoes mitosis-specific phosphorylation and is a substrate for p34cdc2-type protein kinase. *J Biol Chem,* 267**,** 19035-8.

COWLEY, M. J., PINESE, M., KASSAHN, K. S., WADDELL, N., PEARSON, J. V., GRIMMOND, S. M., BIANKIN, A. V., HAUTANIEMI, S. & WU, J. 2012. PINA v2.0: mining interactome modules. *Nucleic Acids Res,* 40**,** D862-5.

DE LA LLERA-MOYA, M., ROTHBLAT, G. H., CONNELLY, M. A., KELLNER-WEIBEL, G., SAKR, S. W., PHILLIPS, M. C. & WILLIAMS, D. L. 1999. Scavenger receptor BI (SR-BI) mediates free cholesterol flux independently of HDL tethering to the cell surface. *J Lipid Res,* 40**,** 575-80.

DE MEDINA, P., PAILLASSE, M. R., SEGALA, G., POIROT, M. & SILVENTE-POIROT, S. 2010. Identification and pharmacological characterization of cholesterol-5,6-epoxide hydrolase as a target for tamoxifen and AEBS ligands. *Proceedings of the National Academy of Sciences,* 107**,** 13520-13525.

DESHAIES, R. J., SANDERS, S. L., FELDHEIM, D. A. & SCHEKMAN, R. 1991. Assembly of yeast Sec proteins involved in translocation into the endoplasmic reticulum into a membrane-bound multisubunit complex. *Nature,* 349, 806-8.

DETTMER, U., KUHN, P. H., ABOU-AJRAM, C., LICHTENTHALER, S. F., KRUGER, M., KREMMER, E., HAASS, C. & HAFFNER, C. 2010. Transmembrane protein 147 (TMEM147) is a novel component of the Nicalin-NOMO protein complex. *J Biol Chem,* 285, 26174-81.

DI SCALA, F., DUPUIS, L., GAIDDON, C., DE TAPIA, M., JOKIC, N., GONZALEZ DE AGUILAR, J. L., RAUL, J. S., LUDES, B. & LOEFFLER, J. P. 2005. Tissue specificity and regulation of the N-terminal diversity of reticulon 3. *Biochem J,* 385, 125-34.

EISENBERG-BORD, M., SHAI, N., SCHULDINER, M. & BOHNERT, M. 2016. A Tether Is a Tether Is a Tether: Tethering at Membrane Contact Sites. *Developmental Cell,* 39, 395-409.

ELLENBERG, J., SIGGIA, E. D., MOREIRA, J. E., SMITH, C. L., PRESLEY, J. F., WORMAN, H. J. & LIPPINCOTT-SCHWARTZ, J. 1997. Nuclear membrane dynamics and reassembly in living cells: targeting of an inner nuclear membrane protein in interphase and mitosis. *J Cell Biol,* 138, 1193-206.

ENDO, A. 2010. A historical perspective on the discovery of statins. *Proceedings of the Japan Academy. Series B, Physical and biological sciences,* 86, 484-493.

ENGLISH, A. R. & VOELTZ, G. K. 2013. Endoplasmic reticulum structure and interconnections with other organelles. *Cold Spring Harb Perspect Biol,* 5, a013227.

ENSEMBL. 2021. *Gene expression* [Online]. Available: https://asia.ensembl.org/Homo_sapiens/Gene/ExpressionAtlas?db=core;g=ENSG00000105677;r=19:35545600-35547526 [Accessed].

EVANS, E. A., GILMORE, R. & BLOBEL, G. 1986. Purification of microsomal signal peptidase as a complex. *Proc Natl Acad Sci U S A,* 83, 581-5.

FAHEY, M. E., BENNETT, M. J., MAHON, C., JÄGER, S., PACHE, L., KUMAR, D., SHAPIRO, A., RAO, K., CHANDA, S. K., CRAIK, C. S., FRANKEL, A. D. & KROGAN, N. J. 2011. GPS-Prot: A web-based visualization platform for integrating host-pathogen interaction data. *BMC Bioinformatics,* 12, 298.

FARESE, R. V., JR. & WALTHER, T. C. 2009. Lipid droplets finally get a little R-E-S-P-E-C-T. *Cell,* 139, 855-60.

FITZKY, B. U., WITSCH-BAUMGARTNER, M., ERDEL, M., LEE, J. N., PAIK, Y. K., GLOSSMANN, H., UTERMANN, G. & MOEBIUS, F. F. 1998. Mutations in the Delta7-sterol reductase gene in patients with the Smith-Lemli-Opitz syndrome. *Proc Natl Acad Sci U S A,* 95, 8181-6.

FOSTER, L. J., DE HOOG, C. L., ZHANG, Y., ZHANG, Y., XIE, X., MOOTHA, V. K. & MANN, M. 2006. A mammalian organelle map by protein correlation profiling. *Cell,* 125, 187-99.

FRIEDMAN, J. R. & VOELTZ, G. K. 2011. The ER in 3D: a multifunctional dynamic membrane network. *Trends Cell Biol,* 21, 709-17.

FROLOV, A., PETRESCU, A., ATSHAVES, B. P., SO, P. T., GRATTON, E., SERRERO, G. & SCHROEDER, F. 2000. High density lipoprotein-mediated cholesterol uptake and targeting to lipid droplets in intact L-cell fibroblasts. A single- and multiphoton fluorescence approach. *J Biol Chem,* 275, 12769-80.

GANGER, M. T., DIETZ, G. D. & EWING, S. J. 2017. A common base method for analysis of qPCR data and the application of simple blocking in qPCR experiments. *BMC Bioinformatics,* 18, 534.

GAO, G., ZHU, C., LIU, E. & NABI, I. R. 2019. Reticulon and CLIMP-63 regulate nanodomain organization of peripheral ER tubules. *PLoS biology,* 17, e3000355-e3000355.

GILLOTTE, K. L., DAVIDSON, W. S., LUND-KATZ, S., ROTHBLAT, G. H. & PHILLIPS, M. C. 1998. Removal of cellular cholesterol by pre-beta-HDL involves plasma membrane microsolubilization. *J Lipid Res,* 39**,** 1918-28.

GILMORE, R., BLOBEL, G. & WALTER, P. 1982. Protein translocation across the endoplasmic reticulum. I. Detection in the microsomal membrane of a receptor for the signal recognition particle. *J Cell Biol,* 95**,** 463-9.

GOLDSTEIN, J. L., ANDERSON, R. G. & BROWN, M. S. 1982. Receptor-mediated endocytosis and the cellular uptake of low density lipoprotein. *Ciba Found Symp***,** 77-95.

GOLDSTEIN, J. L. & BROWN, M. S. 1985. The LDL receptor and the regulation of cellular cholesterol metabolism. *J Cell Sci Suppl,* 3**,** 131-7.

GOLDSTEIN, J. L. & BROWN, M. S. 2009. The LDL receptor. *Arterioscler Thromb Vasc Biol,* 29**,** 431-8.

GRANDPRE, T., NAKAMURA, F., VARTANIAN, T. & STRITTMATTER, S. M. 2000. Identification of the Nogo inhibitor of axon regeneration as a Reticulon protein. *Nature,* 403**,** 439-44.

GUARDA, A., BOLOGNESE, F., BONAPACE, I. M. & BADARACCO, G. 2009. Interaction between the inner nuclear membrane lamin B receptor and the heterochromatic methyl binding protein, MeCP2. *Exp Cell Res,* 315**,** 1895-903.

HAFFNER, C., DETTMER, U., WEILER, T. & HAASS, C. 2007. The Nicastrin-like protein Nicalin regulates assembly and stability of the Nicalin-nodal modulator (NOMO) membrane protein complex. *J Biol Chem,* 282**,** 10632-8.

HARA, Y. 2020. Specialization of nuclear membrane in eukaryotes. *J Cell Sci,* 133.

HASHEMI, H. F. & GOODMAN, J. M. 2015. The life cycle of lipid droplets. *Curr Opin Cell Biol,* 33**,** 119-24.

HELLE, S. C. J., KANFER, G., KOLAR, K., LANG, A., MICHEL, A. H. & KORNMANN, B. 2013. Organization and function of membrane contact sites. *Biochimica et Biophysica Acta (BBA) - Molecular Cell Research,* 1833**,** 2526-2541.

HIRANO, Y., HIZUME, K., KIMURA, H., TAKEYASU, K., HARAGUCHI, T. & HIRAOKA, Y. 2012. Lamin B receptor recognizes specific modifications of histone H4 in heterochromatin formation. *J Biol Chem,* 287**,** 42654-63.

HOFFMANN, K., DREGER, C. K., OLINS, A. L., OLINS, D. E., SHULTZ, L. D., LUCKE, B., KARL, H., KAPS, R., MULLER, D., VAYA, A., AZNAR, J., WARE, R. E., SOTELO CRUZ, N., LINDNER, T. H., HERRMANN, H., REIS, A. & SPERLING, K. 2002. Mutations in the gene encoding the lamin B receptor produce an altered nuclear morphology in granulocytes (Pelger-Huet anomaly). *Nat Genet,* 31**,** 410-4.

HOFFMANN, K., SPERLING, K., OLINS, A. L. & OLINS, D. E. 2007. The granulocyte nucleus and lamin B receptor: avoiding the ovoid. *Chromosoma,* 116**,** 227-235.

HOLMER, L., PEZHMAN, A. & WORMAN, H. J. 1998. The human lamin B receptor/sterol reductase multigene family. *Genomics,* 54**,** 469-76.

HU, J., SHIBATA, Y., VOSS, C., SHEMESH, T., LI, Z., COUGHLIN, M., KOZLOV, M. M., RAPOPORT, T. A. & PRINZ, W. A. 2008. Membrane proteins of the endoplasmic reticulum induce high-curvature tubules. *Science,* 319**,** 1247-50.

HU, J., SHIBATA, Y., ZHU, P. P., VOSS, C., RISMANCHI, N., PRINZ, W. A., RAPOPORT, T. A. & BLACKSTONE, C. 2009. A class of dynamin-like GTPases involved in the generation of the tubular ER network. *Cell,* 138**,** 549-61.

HUANG, H., MCINTOSH, A. L., LANDROCK, K. K., LANDROCK, D., STOREY, S. M., MARTIN, G. G., GUPTA, S., ATSHAVES, B. P., KIER, A. B. & SCHROEDER, F. 2015. Human

FABP1 T94A variant enhances cholesterol uptake. *Biochimica et Biophysica Acta (BBA) - Molecular and Cell Biology of Lipids,* 1851**,** 946-955.

ISTVAN, E. S., PALNITKAR, M., BUCHANAN, S. K. & DEISENHOFER, J. 2000. Crystal structure of the catalytic portion of human HMG-CoA reductase: insights into regulation of activity and catalysis. *Embo j,* 19**,** 819-30.

IWAHASHI, J., KAWASAKI, I., KOHARA, Y., GENGYO-ANDO, K., MITANI, S., OHSHIMA, Y., HAMADA, N., HARA, K., KASHIWAGI, T. & TOYODA, T. 2002. Caenorhabditis elegans reticulon interacts with RME-1 during embryogenesis. *Biochem Biophys Res Commun,* 293**,** 698-704.

JASSAL, B., MATTHEWS, L., VITERI, G., GONG, C., LORENTE, P., FABREGAT, A., SIDIROPOULOS, K., COOK, J., GILLESPIE, M., HAW, R., LONEY, F., MAY, B., MILACIC, M., ROTHFELS, K., SEVILLA, C., SHAMOVSKY, V., SHORSER, S., VARUSAI, T., WEISER, J., WU, G., STEIN, L., HERMJAKOB, H. & D'EUSTACHIO, P. 2020. The reactome pathway knowledgebase. *Nucleic Acids Res,* 48**,** D498-D503.

JIRA, P. E., WATERHAM, H. R., WANDERS, R. J., SMEITINK, J. A., SENGERS, R. C. & WEVERS, R. A. 2003. Smith-Lemli-Opitz syndrome and the DHCR7 gene. *Ann Hum Genet,* 67**,** 269-80.

JUREVICS, H. & MORELL, P. 1995. Cholesterol for synthesis of myelin is made locally, not imported into brain. *J Neurochem,* 64**,** 895-901.

KELLEY, R. L., ROESSLER, E., HENNEKAM, R. C., FELDMAN, G. L., KOSAKI, K., JONES, M. C., PALUMBOS, J. C. & MUENKE, M. 1996. Holoprosencephaly in RSH/Smith-Lemli-Opitz syndrome: does abnormal cholesterol metabolism affect the function of Sonic Hedgehog? *Am J Med Genet,* 66**,** 478-84.

KESHAVA PRASAD, T. S., GOEL, R., KANDASAMY, K., KEERTHIKUMAR, S., KUMAR, S., MATHIVANAN, S., TELIKICHERLA, D., RAJU, R., SHAFREEN, B., VENUGOPAL, A., BALAKRISHNAN, L., MARIMUTHU, A., BANERJEE, S., SOMANATHAN, D. S., SEBASTIAN, A., RANI, S., RAY, S., HARRYS KISHORE, C. J., KANTH, S., AHMED, M., KASHYAP, M. K., MOHMOOD, R., RAMACHANDRA, Y. L., KRISHNA, V., RAHIMAN, B. A., MOHAN, S., RANGANATHAN, P., RAMABADRAN, S., CHAERKADY, R. & PANDEY, A. 2009. Human Protein Reference Database--2009 update. *Nucleic Acids Res,* 37**,** D767-72.

KLOPFENSTEIN, D. R., KAPPELER, F. & HAURI, H. P. 1998. A novel direct interaction of endoplasmic reticulum with microtubules. *EMBO J,* 17**,** 6168-77.

KOCZOK, K., GURUMURTHY, C. B., BALOGH, I., KORADE, Z. & MIRNICS, K. 2019. Subcellular localization of sterol biosynthesis enzymes. *J Mol Histol,* 50**,** 63-73.

KROGH, A., LARSSON, B., VON HEIJNE, G. & SONNHAMMER, E. L. 2001. Predicting transmembrane protein topology with a hidden Markov model: application to complete genomes. *J Mol Biol,* 305**,** 567-80.

KWON, H. J., ABI-MOSLEH, L., WANG, M. L., DEISENHOFER, J., GOLDSTEIN, J. L., BROWN, M. S. & INFANTE, R. E. 2009. Structure of N-Terminal Domain of NPC1 Reveals Distinct Subdomains for Binding and Transfer of Cholesterol. *Cell,* 137**,** 1213-1224.

LECHNER, M. S., SCHULTZ, D. C., NEGOREV, D., MAUL, G. G. & RAUSCHER, F. J., 3RD 2005. The mammalian heterochromatin protein 1 binds diverse nuclear proteins through a common motif that targets the chromoshadow domain. *Biochem Biophys Res Commun,* 331**,** 929-37.

LEMMENS, I. H., KAS, K., MERREGAERT, J. & VAN DE VEN, W. J. M. 1998. Identification and Molecular Characterization ofTM7SF2in the FAUNA Gene Cluster on Human Chromosome 11q13. *Genomics,* 49**,** 437-442.

LIN, S., SUN, S. & HU, J. 2012. Molecular basis for sculpting the endoplasmic reticulum membrane. *Int J Biochem Cell Biol,* 44**,** 1436-43.

LIOKATIS, S., EDLICH, C., SOUPSANA, K., GIANNIOS, I., PANAGIOTIDOU, P., TRIPSIANES, K., SATTLER, M., GEORGATOS, S. D. & POLITOU, A. S. 2012. Solution structure and molecular interactions of lamin B receptor Tudor domain. *J Biol Chem,* 287, 1032-42.

LONG, J. C. & CACERES, J. F. 2009. The SR protein family of splicing factors: master regulators of gene expression. *Biochem J,* 417, 15-27.

LU, R. & WANG, G. G. 2013. Tudor: a versatile family of histone methylation 'readers'. *Trends Biochem Sci,* 38, 546-55.

LUCK, K., KIM, D.-K., LAMBOURNE, L., SPIROHN, K., BEGG, B. E., BIAN, W., BRIGNALL, R., CAFARELLI, T., CAMPOS-LABORIE, F. J., CHARLOTEAUX, B., CHOI, D., COTÉ, A. G., DALEY, M., DEIMLING, S., DESBULEUX, A., DRICOT, A., GEBBIA, M., HARDY, M. F., KISHORE, N., KNAPP, J. J., KOVÁCS, I. A., LEMMENS, I., MEE, M. W., MELLOR, J. C., POLLIS, C., PONS, C., RICHARDSON, A. D., SCHLABACH, S., TEEKING, B., YADAV, A., BABOR, M., BALCHA, D., BASHA, O., BOWMAN-COLIN, C., CHIN, S.-F., CHOI, S. G., COLABELLA, C., COPPIN, G., D'AMATA, C., DE RIDDER, D., DE ROUCK, S., DURAN-FRIGOLA, M., ENNAJDAOUI, H., GOEBELS, F., GOEHRING, L., GOPAL, A., HADDAD, G., HATCHI, E., HELMY, M., JACOB, Y., KASSA, Y., LANDINI, S., LI, R., VAN LIESHOUT, N., MACWILLIAMS, A., MARKEY, D., PAULSON, J. N., RANGARAJAN, S., RASLA, J., RAYHAN, A., ROLLAND, T., SAN-MIGUEL, A., SHEN, Y., SHEYKHKARIMLI, D., SHEYNKMAN, G. M., SIMONOVSKY, E., TAŞAN, M., TEJEDA, A., TROPEPE, V., TWIZERE, J.-C., WANG, Y., WEATHERITT, R. J., WEILE, J., XIA, Y., YANG, X., YEGER-LOTEM, E., ZHONG, Q., ALOY, P., BADER, G. D., DE LAS RIVAS, J., GAUDET, S., HAO, T., RAK, J., TAVERNIER, J., HILL, D. E., VIDAL, M., ROTH, F. P. & CALDERWOOD, M. A. 2020. A reference map of the human binary protein interactome. *Nature,* 580, 402-408.

LUO, J., JIANG, L.-Y., YANG, H. & SONG, B.-L. 2019a. Intracellular Cholesterol Transport by Sterol Transfer Proteins at Membrane Contact Sites. *Trends in Biochemical Sciences,* 44, 273-292.

LUO, J., JIANG, L., YANG, H. & SONG, B. L. 2017. Routes and mechanisms of post-endosomal cholesterol trafficking: A story that never ends. *Traffic,* 18, 209-217.

LUO, J., JIANG, L. Y., YANG, H. & SONG, B. L. 2019b. Intracellular Cholesterol Transport by Sterol Transfer Proteins at Membrane Contact Sites. *Trends Biochem Sci,* 44, 273-292.

LUO, J., YANG, H. & SONG, B.-L. 2020. Mechanisms and regulation of cholesterol homeostasis. *Nature Reviews Molecular Cell Biology,* 21, 225-245.

MA, Y., CAI, S., LV, Q., JIANG, Q., ZHANG, Q., , S., ZHAI, Z. & ZHANG, C. 2007. Lamin B receptor plays a role in stimulating nuclear envelope production and targeting membrane vesicles to chromatin during nuclear envelope assembly through direct interaction with importin β. *Journal of Cell Science,* 120, 520-530.

MAKATSORI, D., KOURMOULI, N., POLIOUDAKI, H., SHULTZ, L. D., MCLEAN, K., THEODOROPOULOS, P. A., SINGH, P. B. & GEORGATOS, S. D. 2004. The inner nuclear membrane protein lamin B receptor forms distinct microdomains and links epigenetically marked chromatin to the nuclear envelope. *J Biol Chem,* 279, 25567-73.

MATTOUT, A., CABIANCA, D. S. & GASSER, S. M. 2015. Chromatin states and nuclear organization in development — a view from the nuclear lamina. *Genome Biology,* 16, 174.

MAURER-STROH, S., DICKENS, N. J., HUGHES-DAVIES, L., KOUZARIDES, T., EISENHABER, F. & PONTING, C. P. 2003. The Tudor domain 'Royal Family': Tudor, plant Agenet, Chromo, PWWP and MBT domains. *Trends Biochem Sci,* 28, 69-74.

MAXFIELD, F. R. & MENON, A. K. 2006. Intracellular sterol transport and distribution. *Curr Opin Cell Biol,* 18, 379-85.

MCGILVRAY, P. T., ANGHEL, S. A., SUNDARAM, A., ZHONG, F., TRNKA, M. J., FULLER, J. R., HU, H., BURLINGAME, A. L. & KEENAN, R. J. 2020. An ER translocon for multi-pass membrane protein biogenesis. *Elife,* 9.

MEYER, D. I., KRAUSE, E. & DOBBERSTEIN, B. 1982. Secretory protein translocation across membranes-the role of the "docking protein'. *Nature,* 297**,** 647-50.

MIMURA, Y., TAKAGI, M., CLEVER, M. & IMAMOTO, N. 2016. ELYS regulates the localization of LBR by modulating its phosphorylation state. *Journal of Cell Science,* 129**,** 4200-4212.

MOEBIUS, F. F., FITZKY, B. U., LEE, J. N., PAIK, Y. K. & GLOSSMANN, H. 1998. Molecular cloning and expression of the human delta7-sterol reductase. *Proc Natl Acad Sci U S A,* 95**,** 1899-902.

MOREIRA, E. F., JAWORSKI, C. J. & RODRIGUEZ, I. R. 1999. Cloning of a novel member of the reticulon gene family (RTN3): gene structure and chromosomal localization to 11q13. *Genomics,* 58**,** 73-81.

NCBI-ACEVIEW. 2021, February 10. Available: https://www.ncbi.nlm.nih.gov/ieb/research/acembly/av.cgi?db=human&term=tmem147&submit=Go [Accessed 10 February 2021].

NCBI. 2021, November 9. Available: https://www.ncbi.nlm.nih.gov/nuccore/NM_032635.4,NM_001242597.2,NM_001242598.2 [Accessed 9 June 2020].

NIKOLAKAKI, E., MYLONIS, I. & GIANNAKOUROS, T. 2017. Lamin B Receptor: Interplay between Structure, Function and Localization. *Cells,* 6.

NIKOLAKAKI, E., SIMOS, G., GEORGATOS, S. D. & GIANNAKOUROS, T. 1996. A nuclear envelope-associated kinase phosphorylates arginine-serine motifs and modulates interactions between the lamin B receptor and other nuclear proteins. *J Biol Chem,* 271**,** 8365-72.

NIKONOV, A. V., HAURI, H. P., LAURING, B. & KREIBICH, G. 2007. Climp-63-mediated binding of microtubules to the ER affects the lateral mobility of translocon complexes. *J Cell Sci,* 120**,** 2248-58.

OERTLE, T., HUBER, C., VAN DER PUTTEN, H. & SCHWAB, M. E. 2003a. Genomic structure and functional characterisation of the promoters of human and mouse nogo/rtn4. *J Mol Biol,* 325**,** 299-323.

OERTLE, T., KLINGER, M., STUERMER, C. A. & SCHWAB, M. E. 2003b. A reticular rhapsody: phylogenic evolution and nomenclature of the RTN/Nogo gene family. *FASEB J,* 17**,** 1238-47.

OLINS, A. L., RHODES, G., WELCH, D. B., ZWERGER, M. & OLINS, D. E. 2010. Lamin B receptor: multi-tasking at the nuclear envelope. *Nucleus,* 1**,** 53-70.

OLINS, A. L., ZWERGER, M., HERRMANN, H., ZENTGRAF, H., SIMON, A. J., MONESTIER, M. & OLINS, D. E. 2008. The human granulocyte nucleus: Unusual nuclear envelope and heterochromatin composition. *European Journal of Cell Biology,* 87**,** 279-290.

ORCHARD, S., AMMARI, M., ARANDA, B., BREUZA, L., BRIGANTI, L., BROACKES-CARTER, F., CAMPBELL, N. H., CHAVALI, G., CHEN, C., DEL-TORO, N., DUESBURY, M., DUMOUSSEAU, M., GALEOTA, E., HINZ, U., IANNUCCELLI, M., JAGANNATHAN, S., JIMENEZ, R., KHADAKE, J., LAGREID, A., LICATA, L., LOVERING, R. C., MELDAL, B., MELIDONI, A. N., MILAGROS, M., PELUSO, D., PERFETTO, L., PORRAS, P., RAGHUNATH, A., RICARD-BLUM, S., ROECHERT, B., STUTZ, A., TOGNOLLI, M., VAN ROEY, K., CESARENI, G. & HERMJAKOB, H. 2014. The MIntAct project--IntAct as a common curation platform for 11 molecular interaction databases. *Nucleic Acids Res,* 42**,** D358-63.

ORSO, G., PENDIN, D., LIU, S., TOSETTO, J., MOSS, T. J., FAUST, J. E., MICARONI, M., EGOROVA, A., MARTINUZZI, A., MCNEW, J. A. & DAGA, A. 2009. Homotypic fusion of ER membranes requires the dynamin-like GTPase atlastin. *Nature,* 460**,** 978-83.

OTA, M., TANAKA, Y., NAKAGAWA, I., JIANG, J. J., ARIMA, Y., KAMIMURA, D., ONODERA, T., IWASAKI, N. & MURAKAMI, M. 2020. Role of Chondrocytes in the

Development of Rheumatoid Arthritis Via Transmembrane Protein 147-Mediated NF-κB Activation. *Arthritis Rheumatol,* 72**,** 931-942.

ÖZBALCI, C., SACHSENHEIMER, T. & BR¼GGER, B. 2013. Quantitative Analysis of Cellular Lipids by Nano-Electrospray Ionization Mass Spectrometry. *In:* RAPAPORT, D. & HERRMANN, J. M. (eds.) *Membrane Biogenesis: Methods and Protocols.* Totowa, NJ: Humana Press.

PALADE, G. E. 1955. Studies on the endoplasmic reticulum. II. Simple dispositions in cells in situ. *J Biophys Biochem Cytol,* 1**,** 567-82.

PALADE, G. E. & PORTER, K. R. 1954. Studies on the endoplasmic reticulum. I. Its identification in cells in situ. *J Exp Med,* 100**,** 641-56.

PERI, S., NAVARRO, J. D., AMANCHY, R., KRISTIANSEN, T. Z., JONNALAGADDA, C. K., SURENDRANATH, V., NIRANJAN, V., MUTHUSAMY, B., GANDHI, T. K., GRONBORG, M., IBARROLA, N., DESHPANDE, N., SHANKER, K., SHIVASHANKAR, H. N., RASHMI, B. P., RAMYA, M. A., ZHAO, Z., CHANDRIKA, K. N., PADMA, N., HARSHA, H. C., YATISH, A. J., KAVITHA, M. P., MENEZES, M., CHOUDHURY, D. R., SURESH, S., GHOSH, N., SARAVANA, R., CHANDRAN, S., KRISHNA, S., JOY, M., ANAND, S. K., MADAVAN, V., JOSEPH, A., WONG, G. W., SCHIEMANN, W. P., CONSTANTINESCU, S. N., HUANG, L., KHOSRAVI-FAR, R., STEEN, H., TEWARI, M., GHAFFARI, S., BLOBE, G. C., DANG, C. V., GARCIA, J. G., PEVSNER, J., JENSEN, O. N., ROEPSTORFF, P., DESHPANDE, K. S., CHINNAIYAN, A. M., HAMOSH, A., CHAKRAVARTI, A. & PANDEY, A. 2003. Development of human protein reference database as an initial platform for approaching systems biology in humans. *Genome Res,* 13**,** 2363-71.

PFAFFL, M. W., HORGAN, G. W. & DEMPFLE, L. 2002. Relative expression software tool (REST) for group-wise comparison and statistical analysis of relative expression results in real-time PCR. *Nucleic Acids Res,* 30**,** e36.

PHILLIPS, M. C. 2014. Molecular mechanisms of cellular cholesterol efflux. *J Biol Chem,* 289**,** 24020-9.

PHILLIPS, M. C., JOHNSON, W. J. & ROTHBLAT, G. H. 1987. Mechanisms and consequences of cellular cholesterol exchange and transfer. *Biochim Biophys Acta,* 906**,** 223-76.

PORTER, K. R. & PALADE, G. E. 1957. Studies on the endoplasmic reticulum. III. Its form and distribution in striated muscle cells. *J Biophys Biochem Cytol,* 3**,** 269-300.

PRAKASH, A., SENGUPTA, S., APARNA, K. & KASBEKAR, D. P. 1999. The erg-3 (sterol Δ14,15-reductase) gene of Neurospora crassa: generation of null mutants by repeat-induced point mutation and complementation by proteins chimeric for human lamin B receptor sequences. *Microbiology,* 145**,** 1443-1451.

PRINZ, W. A. 2014. Bridging the gap: Membrane contact sites in signaling, metabolism, and organelle dynamics. *Journal of Cell Biology,* 205**,** 759-769.

PUHKA, M., VIHINEN, H., JOENSUU, M. & JOKITALO, E. 2007. Endoplasmic reticulum remains continuous and undergoes sheet-to-tubule transformation during cell division in mammalian cells. *J Cell Biol,* 179**,** 895-909.

PYRPASOPOULOU, A., MEIER, J., MAISON, C., SIMOS, G. & GEORGATOS, S. D. 1996. The lamin B receptor (LBR) provides essential chromatin docking sites at the nuclear envelope. *EMBO J,* 15**,** 7108-19.

RAPOPORT, T. A. 2007. Protein translocation across the eukaryotic endoplasmic reticulum and bacterial plasma membranes. *Nature,* 450**,** 663-9.

REINHART, M. P., BILLHEIMER, J. T., FAUST, J. R. & GAYLOR, J. L. 1987. Subcellular localization of the enzymes of cholesterol biosynthesis and metabolism in rat liver. *J Biol Chem,* 262**,** 9649-55.

ROEBROEK, A. J., CONTRERAS, B., PAULI, I. G. & VAN DE VEN, W. J. 1998. cDNA cloning, genomic organization, and expression of the human RTN2 gene, a member of a gene family encoding reticulons. *Genomics,* 51**,** 98-106.

ROSEMOND, E., ROSSI, M., MCMILLIN, S. M., SCARSELLI, M., DONALDSON, J. G. & WESS, J. 2011. Regulation of M(3) muscarinic receptor expression and function by transmembrane protein 147. *Mol Pharmacol,* 79**,** 251-61.

SANKARANARAYANAN, S., ORAM, J. F., ASZTALOS, B. F., VAUGHAN, A. M., LUND-KATZ, S., ADORNI, M. P., PHILLIPS, M. C. & ROTHBLAT, G. H. 2009. Effects of acceptor composition and mechanism of ABCG1-mediated cellular free cholesterol efflux. *Journal of lipid research,* 50**,** 275-284.

SANTAMA, N., ER, C. P., ONG, L. L. & YU, H. 2004. Distribution and functions of kinectin isoforms. *J Cell Sci,* 117**,** 4537-49.

SCHEKMAN, R. & ORCI, L. 1996. Coat proteins and vesicle budding. *Science,* 271**,** 1526-33.

SCHULER, E., LIN, F. & WORMAN, H. J. 1994. Characterization of the human gene encoding LBR, an integral protein of the nuclear envelope inner membrane. *J Biol Chem,* 269**,** 11312-7.

SCHWARZ, D. S. & BLOWER, M. D. 2016. The endoplasmic reticulum: structure, function and response to cellular signaling. *Cell Mol Life Sci,* 73**,** 79-94.

SCHWEIZER, A., ERICSSON, M., BACHI, T., GRIFFITHS, G. & HAURI, H. P. 1993. Characterization of a novel 63 kDa membrane protein. Implications for the organization of the ER-to-Golgi pathway. *J Cell Sci,* 104 (Pt 3)**,** 671-83.

SEVER, N., SONG, B. L., YABE, D., GOLDSTEIN, J. L., BROWN, M. S. & DEBOSE-BOYD, R. A. 2003a. Insig-dependent ubiquitination and degradation of mammalian 3-hydroxy-3-methylglutaryl-CoA reductase stimulated by sterols and geranylgeraniol. *J Biol Chem,* 278**,** 52479-90.

SEVER, N., YANG, T., BROWN, M. S., GOLDSTEIN, J. L. & DEBOSE-BOYD, R. A. 2003b. Accelerated degradation of HMG CoA reductase mediated by binding of insig-1 to its sterol-sensing domain. *Mol Cell,* 11**,** 25-33.

SHIBATA, Y., HU, J., KOZLOV, M. M. & RAPOPORT, T. A. 2009. Mechanisms shaping the membranes of cellular organelles. *Annu Rev Cell Dev Biol,* 25**,** 329-54.

SHIBATA, Y., SHEMESH, T., PRINZ, W. A., PALAZZO, A. F., KOZLOV, M. M. & RAPOPORT, T. A. 2010. Mechanisms determining the morphology of the peripheral ER. *Cell,* 143**,** 774-88.

SHIBATA, Y., VOELTZ, G. K. & RAPOPORT, T. A. 2006. Rough sheets and smooth tubules. *Cell,* 126**,** 435-9.

SHIBATA, Y., VOSS, C., RIST, J. M., HU, J., RAPOPORT, T. A., PRINZ, W. A. & VOELTZ, G. K. 2008. The reticulon and DP1/Yop1p proteins form immobile oligomers in the tubular endoplasmic reticulum. *J Biol Chem,* 283**,** 18892-904.

SHULTZ, L. D., LYONS, B. L., BURZENSKI, L. M., GOTT, B., SAMUELS, R., SCHWEITZER, P. A., DREGER, C., HERRMANN, H., KALSCHEUER, V., OLINS, A. L., OLINS, D. E., SPERLING, K. & HOFFMANN, K. 2003. Mutations at the mouse ichthyosis locus are within the lamin B receptor gene: a single gene model for human Pelger-Huët anomaly. *Hum Mol Genet,* 12**,** 61-9.

SILVE, S., DUPUY, P.-H., FERRARA, P. & LOISON, G. 1998. Human lamin B receptor exhibits sterol C14-reductase activity in Saccharomyces cerevisiae. *Biochimica et Biophysica Acta (BBA) - Lipids and Lipid Metabolism,* 1392**,** 233-244.

SINGH, R., KAUSHIK, S., WANG, Y., XIANG, Y., NOVAK, I., KOMATSU, M., TANAKA, K., CUERVO, A. M. & CZAJA, M. J. 2009. Autophagy regulates lipid metabolism. *Nature,* 458**,** 1131-5.

SMITH, J. D., LE GOFF, W., SETTLE, M., BRUBAKER, G., WAELDE, C., HORWITZ, A. & ODA, M. N. 2004. ABCA1 mediates concurrent cholesterol and phospholipid efflux to apolipoprotein A-I. *J Lipid Res,* 45**,** 635-44.

SONG, B. L., JAVITT, N. B. & DEBOSE-BOYD, R. A. 2005. Insig-mediated degradation of HMG CoA reductase stimulated by lanosterol, an intermediate in the synthesis of cholesterol. *Cell Metab,* 1**,** 179-89.

SONI, K. G., MARDONES, G. A., SOUGRAT, R., SMIRNOVA, E., JACKSON, C. L. & BONIFACINO, J. S. 2009. Coatomer-dependent protein delivery to lipid droplets. *Journal of cell science,* 122**,** 1834-1841.

SOTO-ACOSTA, R., BAUTISTA-CARBAJAL, P., CERVANTES-SALAZAR, M., ANGEL-AMBROCIO, A. H. & DEL ANGEL, R. M. 2017. DENV up-regulates the HMG-CoA reductase activity through the impairment of AMPK phosphorylation: A potential antiviral target. *PLoS Pathog,* 13**,** e1006257.

SPARROW, S. M., CARTER, J. M., RIDGWAY, N. D., COOK, H. W. & BYERS, D. M. 1999. U18666A inhibits intracellular cholesterol transport and neurotransmitter release in human neuroblastoma cells. *Neurochem Res,* 24**,** 69-77.

SUPEK, F., BOSNJAK, M., SKUNCA, N. & SMUC, T. 2011. REVIGO summarizes and visualizes long lists of gene ontology terms. *PLoS One,* 6**,** e21800.

SZKLARCZYK, D., GABLE, A. L., LYON, D., JUNGE, A., WYDER, S., HUERTA-CEPAS, J., SIMONOVIC, M., DONCHEVA, N. T., MORRIS, J. H., BORK, P., JENSEN, L. J. & MERING, C. V. 2019. STRING v11: protein-protein association networks with increased coverage, supporting functional discovery in genome-wide experimental datasets. *Nucleic Acids Res,* 47**,** D607-D613.

TAKADA, Y. K., YU, J., SHIMODA, M. & TAKADA, Y. 2019. Integrin Binding to the Trimeric Interface of CD40L Plays a Critical Role in CD40/CD40L Signaling. *The Journal of Immunology,* 203**,** 1383-1391.

TERASAKI, M., SHEMESH, T., KASTHURI, N., KLEMM, R. W., SCHALEK, R., HAYWORTH, K. J., HAND, A. R., YANKOVA, M., HUBER, G., LICHTMAN, J. W., RAPOPORT, T. A. & KOZLOV, M. M. 2013a. Stacked endoplasmic reticulum sheets are connected by helicoidal membrane motifs. *Cell,* 154**,** 285-96.

TERASAKI, M., SHEMESH, T., KASTHURI, N., KLEMM, R. W., SCHALEK, R., HAYWORTH, K. J., HAND, A. R., YANKOVA, M., HUBER, G., LICHTMAN, J. W., RAPOPORT, T. A. & KOZLOV, M. M. 2013b. Stacked endoplasmic reticulum sheets are connected by helicoidal membrane motifs. *Cell,* 154**,** 285-296.

THIAM, A. R., FARESE, R. V., JR. & WALTHER, T. C. 2013. The biophysics and cell biology of lipid droplets. *Nat Rev Mol Cell Biol,* 14**,** 775-86.

THUAHNAI, S. T., LUND-KATZ, S., DHANASEKARAN, P., DE LA LLERA-MOYA, M., CONNELLY, M. A., WILLIAMS, D. L., ROTHBLAT, G. H. & PHILLIPS, M. C. 2004. Scavenger receptor class B type I-mediated cholesteryl ester-selective uptake and efflux of unesterified cholesterol. Influence of high density lipoprotein size and structure. *J Biol Chem,* 279**,** 12448-55.

TSAI, P. L., ZHAO, C., TURNER, E. & SCHLIEKER, C. 2016. The Lamin B receptor is essential for cholesterol synthesis and perturbed by disease-causing mutations. *Elife,* 5.

TSENG, L.-C. & CHEN, R.-H. 2011. Temporal control of nuclear envelope assembly by phosphorylation of lamin B receptor. *Molecular Biology of the Cell,* 22**,** 3306-3317.

TUKEY, J. W. 1977. *Exploratory Data Analysis,* Reading, Mass., Addison-Wesley Pub. Co.

UNIPROT, C. 2008. The universal protein resource (UniProt). *Nucleic Acids Res,* 36**,** D190-5.

VAN DE VELDE, H. J., ROEBROEK, A. J., SENDEN, N. H., RAMAEKERS, F. C. & VAN DE VEN, W. J. 1994. NSP-encoded reticulons, neuroendocrine proteins of a novel gene family associated with membranes of the endoplasmic reticulum. *J Cell Sci,* 107 (Pt 9)**,** 2403-16.

VERATTI, E. 1902. Investigations on the fine structure of striated muscle fiber read before the Reale Istituto Lombardo, 13 March 1902. *J Biophys Biochem Cytol,* 10(4)Suppl, 1-59.

VOELTZ, G. K., PRINZ, W. A., SHIBATA, Y., RIST, J. M. & RAPOPORT, T. A. 2006. A class of membrane proteins shaping the tubular endoplasmic reticulum. *Cell,* 124, 573-86.

VOELTZ, G. K., ROLLS, M. M. & RAPOPORT, T. A. 2002. Structural organization of the endoplasmic reticulum. *EMBO Rep,* 3, 944-50.

WALTER, P. & BLOBEL, G. 1981. Translocation of proteins across the endoplasmic reticulum. II. Signal recognition protein (SRP) mediates the selective binding to microsomal membranes of in-vitro-assembled polysomes synthesizing secretory protein. *J Cell Biol,* 91, 551-6.

WALTER, P., IBRAHIMI, I. & BLOBEL, G. 1981. Translocation of proteins across the endoplasmic reticulum. I. Signal recognition protein (SRP) binds to in-vitro-assembled polysomes synthesizing secretory protein. *J Cell Biol,* 91, 545-50.

WARDE-FARLEY, D., DONALDSON, S. L., COMES, O., ZUBERI, K., BADRAWI, R., CHAO, P., FRANZ, M., GROUIOS, C., KAZI, F., LOPES, C. T., MAITLAND, A., MOSTAFAVI, S., MONTOJO, J., SHAO, Q., WRIGHT, G., BADER, G. D. & MORRIS, Q. 2010. The GeneMANIA prediction server: biological network integration for gene prioritization and predicting gene function. *Nucleic Acids Res,* 38, W214-20.

WASSIF, C. A., BROWNSON, K. E., STERNER, A. L., FORLINO, A., ZERFAS, P. M., WILSON, W. K., STAROST, M. F. & PORTER, F. D. 2007. HEM dysplasia and ichthyosis are likely laminopathies and not due to 3β-hydroxysterol Δ14-reductase deficiency. *Human Molecular Genetics,* 16, 1176-1187.

WASSIF, C. A., MASLEN, C., KACHILELE-LINJEWILE, S., LIN, D., LINCK, L. M., CONNOR, W. E., STEINER, R. D. & PORTER, F. D. 1998. Mutations in the human sterol delta7-reductase gene at 11q12-13 cause Smith-Lemli-Opitz syndrome. *Am J Hum Genet,* 63, 55-62.

WATERHAM, H. R., KOSTER, J., MOOYER, P., NOORT GV, G., KELLEY, R. I., WILCOX, W. R., WANDERS, R. J., HENNEKAM, R. C. & OOSTERWIJK, J. C. 2003. Autosomal recessive HEM/Greenberg skeletal dysplasia is caused by 3 beta-hydroxysterol delta 14-reductase deficiency due to mutations in the lamin B receptor gene. *Am J Hum Genet,* 72, 1013-7.

WATERHAM, H. R., WIJBURG, F. A., HENNEKAM, R. C., VREKEN, P., POLL-THE, B. T., DORLAND, L., DURAN, M., JIRA, P. E., SMEITINK, J. A., WEVERS, R. A. & WANDERS, R. J. 1998. Smith-Lemli-Opitz syndrome is caused by mutations in the 7-dehydrocholesterol reductase gene. *Am J Hum Genet,* 63, 329-38.

WEST, M., ZUREK, N., HOENGER, A. & VOELTZ, G. K. 2011a. A 3D analysis of yeast ER structure reveals how ER domains are organized by membrane curvature. *The Journal of cell biology,* 193, 333-346.

WEST, M., ZUREK, N., HOENGER, A. & VOELTZ, G. K. 2011b. A 3D analysis of yeast ER structure reveals how ER domains are organized by membrane curvature. *J Cell Biol,* 193, 333-46.

WESTRATE, L. M., LEE, J. E., PRINZ, W. A. & VOELTZ, G. K. 2015. Form follows function: the importance of endoplasmic reticulum shape. *Annu Rev Biochem,* 84, 791-811.

WILFLING, F., WANG, H., HAAS, J. T., KRAHMER, N., GOULD, T. J., UCHIDA, A., CHENG, J.-X., GRAHAM, M., CHRISTIANO, R., FRÖHLICH, F., LIU, X., BUHMAN, K. K., COLEMAN, R. A., BEWERSDORF, J., FARESE, R. V. & WALTHER, T. C. 2013. Triacylglycerol synthesis enzymes mediate lipid droplet growth by relocalizing from the ER to lipid droplets. *Developmental cell,* 24, 384-399.

WOLINS, N. E., QUAYNOR, B. K., SKINNER, J. R., SCHOENFISH, M. J., TZEKOV, A. & BICKEL, P. E. 2005. S3-12, Adipophilin, and TIP47 package lipid in adipocytes. *J Biol Chem,* 280, 19146-55.

WONG, L. H., ČOPIČ, A. & LEVINE, T. P. 2017. Advances on the Transfer of Lipids by Lipid Transfer Proteins. *Trends in Biochemical Sciences,* 42, 516-530.

WORMAN, H. J., YUAN, J., BLOBEL, G. & GEORGATOS, S. D. 1988. A lamin B receptor in the nuclear envelope. *Proc Natl Acad Sci U S A,* 85**,** 8531-4.

WU, J., VALLENIUS, T., OVASKA, K., WESTERMARCK, J., MAKELA, T. P. & HAUTANIEMI, S. 2009. Integrated network analysis platform for protein-protein interactions. *Nat Methods,* 6**,** 75-7.

YANG, Y. S. & STRITTMATTER, S. M. 2007. The reticulons: a family of proteins with diverse functions. *Genome Biol,* 8**,** 234.

YAVUZ, S., SANTARELLA-MELLWIG, R., KOCH, B., JAEDICKE, A., MATTAJ, I. W. & ANTONIN, W. 2010. NLS-mediated NPC functions of the nucleoporin Pom121. *FEBS Lett,* 584**,** 3292-8.

YE, Q. & WORMAN, H. J. 1994. Primary structure analysis and lamin B and DNA binding of human LBR, an integral protein of the nuclear envelope inner membrane. *J Biol Chem,* 269**,** 11306-11.

YONEYAMA, M. T., N.; KOSHIBA, S.; INOUE, M.; KIGAWA, T.; YOKOYAMA, S. 2006. Solusion structure of the Tudor domain of human Lamin-B receptor. *Riken Structural Genomics/Proteomics Initiative (RSGI).*

ZECHNER, R., MADEO, F. & KRATKY, D. 2017. Cytosolic lipolysis and lipophagy: two sides of the same coin. *Nat Rev Mol Cell Biol,* 18**,** 671-684.

ZHANG, H. & HU, J. 2016. Shaping the Endoplasmic Reticulum into a Social Network. *Trends Cell Biol,* 26**,** 934-943.

ZHANG, K. & KAUFMAN, R. J. 2003. Unfolding the toxicity of cholesterol. *Nature Cell Biology,* 5**,** 769-770.

ZHANG, M., WU, F., SHI, J., ZHU, Y., ZHU, Z., GONG, Q. & HU, J. 2013. ROOT HAIR DEFECTIVE3 family of dynamin-like GTPases mediates homotypic endoplasmic reticulum fusion and is essential for Arabidopsis development. *Plant Physiol,* 163**,** 713-20.

ZHENG, H., KUNST, L., HAWES, C. & MOORE, I. 2004. A GFP-based assay reveals a role for RHD3 in transport between the endoplasmic reticulum and Golgi apparatus. *Plant J,* 37**,** 398-414.

ZUREK, N., SPARKS, L. & VOELTZ, G. 2011. Reticulon short hairpin transmembrane domains are used to shape ER tubules. *Traffic,* 12**,** 28-41.

6

Appendix

Table 6.1: Quantification of the full lipidome profile, including cholesterol and cholesteryl esters of TMEM147-silenced cells, control-silenced and untreated cells in triplicate.

Group mol%	PC O-30:2	PC O-30:1	PC O-30:0	PC 30:2	PC 30:1	PC 30:0	PC O-32:2	PC O-32:1	PC O-32:0	PC 32:3	PC 32:2	PC 32:1	PC 32:0	PC O-34:3
UNTREAT_A	0.0087	0.0949	0.4146	0.0362	0.6390	1.5990	0.1649	1.3337	1.1675	0.0314	0.7667	5.2673	1.2908	0.0631
UNTREAT_B	0.0083	0.1152	0.4597	0.0326	0.6881	1.6491	0.1931	1.4954	1.2829	0.0265	0.8827	5.9259	1.3642	0.0827
UNTREAT_C	0.0103	0.1355	0.4691	0.0294	0.7032	1.6497	0.2238	1.5421	1.3042	0.0270	0.8518	5.8809	1.4092	0.0935
NEG_A	0.0087	0.0703	0.2085	0.0243	0.5226	1.2586	0.1091	0.6744	0.6460	0.0300	0.7948	4.9995	1.2913	0.0458
NEG_B	0.0123	0.0924	0.2156	0.0292	0.5808	1.4153	0.1341	0.7649	0.6295	0.0343	0.8019	5.4126	1.3547	0.0564
NEG_C	0.0143	0.1084	0.2222	0.0325	0.6239	1.4721	0.1649	0.8343	0.6890	0.0372	0.8872	5.9360	1.3953	0.0612
SilTMEM147_A	0.0149	0.1130	0.2056	0.0324	0.4741	1.5298	0.1368	0.6674	0.6461	0.0399	0.5720	4.9106	1.8770	0.0484
SilTMEM147_B	0.0151	0.1246	0.2053	0.0307	0.4911	1.5802	0.1509	0.7087	0.6358	0.0415	0.5946	5.1171	1.9328	0.0558
SilTMEM147_C	0.0146	0.1098	0.1920	0.0292	0.4507	1.4396	0.1485	0.6242	0.6348	0.0362	0.5255	4.5093	1.7910	0.0509
Group mol%	PC O-34:2	PC O-34:1	PC O-34:0	PC 34:3	PC 34:2	PC 34:1	PC 34:0	PC O-36:6	PC O-36:5	PC O-36:4	PC O-36:3	PC O-36:2	PC O-36:1	PC O-36:0
UNTREAT_A	0.5912	2.2266	0.3469	0.2066	3.3246	6.6362	0.0676	0.0256	0.0937	0.1648	0.1691	0.5974	0.3179	0.0686
UNTREAT_B	0.6714	2.2580	0.3124	0.2055	3.5462	7.0410	0.0939	0.0364	0.0963	0.1663	0.1801	0.5856	0.3388	0.0594
UNTREAT_C	0.7081	2.2876	0.2972	0.2072	3.5158	7.0125	0.0779	0.0347	0.0989	0.1730	0.1815	0.6018	0.3388	0.0536
NEG_A	0.3915	1.3985	0.1764	0.2081	3.0262	7.0385	0.0713	0.0296	0.0686	0.1048	0.1006	0.4123	0.2510	0.0338
NEG_B	0.4033	1.3104	0.1755	0.2248	3.1846	7.0351	0.0953	0.0361	0.0919	0.1288	0.1069	0.4071	0.2446	0.0434
NEG_C	0.4701	1.4417	0.1871	0.2497	3.5290	7.8436	0.1033	0.0475	0.1146	0.1507	0.1305	0.4490	0.2733	0.0414
SilTMEM147_A	0.3342	1.2133	0.2743	0.2384	2.5114	8.2433	0.1971	0.0813	0.1881	0.1735	0.1167	0.4013	0.4261	0.0512
SilTMEM147_B	0.3552	1.2390	0.2679	0.2473	2.6227	8.5798	0.2077	0.0902	0.2128	0.1803	0.1208	0.4229	0.4391	0.0505
SilTMEM147_C	0.3302	1.1298	0.2573	0.2091	2.2858	7.5854	0.1856	0.0867	0.1999	0.1534	0.1064	0.3714	0.3951	0.0409
Group mol%	PC 36:6	PC 36:5	PC 36:4	PC 36:3	PC 36:2	PC 36:1	PC 36:0	PC O-38:6	PC O-38:5	PC O-38:4	PC O-38:3	PC O-38:2	PC O-38:1	PC 38:7
UNTREAT_A	0.0181	0.1228	0.2295	0.4138	3.0072	0.4425	0.0431	0.1083	0.1523	0.0610	0.0380	0.0717	0.0355	0.0289
UNTREAT_B	0.0277	0.1324	0.2634	0.4722	3.4713	0.5160	0.0404	0.1272	0.1489	0.0689	0.0423	0.0820	0.0400	0.0378
UNTREAT_C	0.0299	0.1331	0.2619	0.4701	3.4150	0.5115	0.0457	0.1308	0.1555	0.0658	0.0432	0.0813	0.0351	0.0345
NEG_A	0.0453	0.2283	0.4164	0.5747	3.2699	0.6809	0.0281	0.0932	0.1354	0.0743	0.0378	0.0651	0.0392	0.0478
NEG_B	0.0398	0.2201	0.4210	0.5285	3.0136	0.6128	0.0409	0.0943	0.1212	0.0591	0.0377	0.0597	0.0303	0.0483
NEG_C	0.0460	0.2438	0.4779	0.5815	3.3249	0.6627	0.0484	0.1201	0.1372	0.0675	0.0398	0.0678	0.0280	0.0578
SilTMEM147_A	0.0779	0.5931	0.9491	0.7643	3.1593	1.5695	0.0598	0.1675	0.2011	0.1281	0.0638	0.0822	0.0445	0.0742
SilTMEM147_B	0.0827	0.6225	1.0003	0.8096	3.3049	1.6651	0.0742	0.1908	0.2198	0.1344	0.0659	0.0877	0.0457	0.0856
SilTMEM147_C	0.0779	0.5674	0.8946	0.7272	3.0897	1.5786	0.0630	0.1830	0.2068	0.1280	0.0614	0.0827	0.0453	0.0758
Group mol%	PC 38:6	PC 38:5	PC 38:4	PC 38:3	PC 38:2	PC 38:1	PC 38:0	PC O-40:1	PC 40:7	PC 40:6	PC 40:5	PC 40:4	LPC 14:1	LPC 14:0
UNTREAT_A	0.1518	0.2086	0.1231	0.0742	0.1677	0.0192	0.0361	0.0000	0.0817	0.0616	0.0280	0.0085	0.0098	0.0437
UNTREAT_B	0.1528	0.2280	0.1344	0.0709	0.1721	0.0230	0.0437	0.0087	0.0732	0.0688	0.0323	0.0096	0.0032	0.0239
UNTREAT_C	0.1528	0.2189	0.1293	0.0725	0.1743	0.0278	0.0461	0.0118	0.0749	0.0700	0.0320	0.0114	0.0039	0.0340
NEG_A	0.2643	0.4252	0.2519	0.0769	0.0937	0.0362	0.0313	0.0287	0.1329	0.1170	0.0674	0.0182	0.0084	0.0291
NEG_B	0.2581	0.4027	0.2268	0.0749	0.1335	0.0303	0.0344	0.0304	0.1303	0.1201	0.0556	0.0167	0.0000	0.0210
NEG_C	0.2851	0.4437	0.2564	0.0916	0.1429	0.0268	0.0396	0.0283	0.1399	0.1317	0.0599	0.0146	0.0000	0.0147
SilTMEM147_A	0.6308	1.0044	0.6862	0.1857	0.1240	0.0262	0.0506	0.0450	0.2760	0.2905	0.1311	0.0315	0.0028	0.0239
SilTMEM147_B	0.6674	1.0662	0.7461	0.1993	0.1468	0.0394	0.0528	0.0543	0.2882	0.3009	0.1366	0.0379	0.0019	0.0199
SilTMEM147_C	0.5946	0.9479	0.6630	0.1873	0.1391	0.0340	0.0455	0.0416	0.2568	0.2819	0.1340	0.0343	0.0015	0.0223

Group mol%	LPC 16:1	LPC 16:0	LPC 18:3	LPC 18:2	LPC 18:1	LPC 18:0	LPC 20:6	LPC 20:5	LPC 20:4	LPC 20:3	LPC 20:2	LPC 20:1	LPC 20:0	LPC 22:6
UNTREAT_A	0.1366	0.2433	0.0101	0.0381	0.4096	0.1362	0.0121	0.0320	0.0401	0.0209	0.0307	0.1767	0.0127	0.0375
UNTREAT_B	0.0876	0.1544	0.0032	0.0231	0.2872	0.1068	0.0021	0.0138	0.0306	0.0128	0.0222	0.1372	0.0053	0.0211
UNTREAT_C	0.1534	0.2377	0.0065	0.0392	0.4317	0.0573	0.0033	0.0127	0.0318	0.0151	0.0147	0.0576	0.0069	0.0199
NEG_A	0.0742	0.1737	0.0013	0.0262	0.2709	0.0788	0.0060	0.0306	0.0696	0.0139	0.0218	0.1015	0.0008	0.0310
NEG_B	0.1375	0.2304	0.0035	0.0334	0.3693	0.0517	0.0002	0.0197	0.0497	0.0147	0.0083	0.0429	0.0000	0.0203
NEG_C	0.0878	0.1516	0.0034	0.0222	0.2245	0.0311	0.0016	0.0130	0.0310	0.0095	0.0049	0.0233	0.0000	0.0120
SilTMEM147_A	0.1104	0.2428	0.0042	0.0428	0.3477	0.1451	0.0020	0.0610	0.1113	0.0319	0.0174	0.0652	0.0000	0.0384
SilTMEM147_B	0.1018	0.2315	0.0040	0.0459	0.3762	0.1179	0.0023	0.0646	0.1161	0.0332	0.0132	0.0444	0.0014	0.0386
SilTMEM147_C	0.0511	0.1182	0.0018	0.0230	0.1291	0.0521	0.0000	0.0334	0.0567	0.0209	0.0064	0.0207	0.0021	0.0191
Group mol%	LPC 22:5	LPC 22:4	LPC 22:3	LPC 22:2	LPC 22:1	SM 34:2;2	SM 34:1;2	SM 34:0;2	SM 36:2;2	SM 36:1;2	SM 36:0;2	SM 38:2;2	SM 38:1;2	SM 38:0;2
UNTREAT_A	0.0473	0.0480	0.0267	0.0124	0.0071	0.0554	0.6265	0.0192	0.0224	0.0873	0.0000	0.0114	0.0000	0.0000
UNTREAT_B	0.0301	0.0351	0.0090	0.0036	0.0072	0.0535	0.6321	0.0086	0.0317	0.0747	0.0000	0.0147	0.0000	0.0000
UNTREAT_C	0.0254	0.0176	0.0043	0.0056	0.0077	0.0526	0.6563	0.0134	0.0382	0.0766	0.0000	0.0098	0.0000	0.0000
NEG_A	0.0416	0.0470	0.0253	0.0059	0.0100	0.0607	0.7544	0.0346	0.0373	0.0752	0.0000	0.0000	0.0000	0.0000
NEG_B	0.0269	0.0213	0.0014	0.0012	0.0026	0.0691	0.8356	0.0306	0.0361	0.1245	0.0000	0.0152	0.0000	0.0000
NEG_C	0.0153	0.0135	0.0021	0.0019	0.0021	0.0726	0.8700	0.0310	0.0414	0.1184	0.0000	0.0184	0.0000	0.0000
SilTMEM147_A	0.0700	0.0870	0.0143	0.0020	0.0065	0.0603	0.4983	0.0037	0.0407	0.1956	0.0000	0.0201	0.0432	0.0000
SilTMEM147_B	0.0588	0.0597	0.0084	0.0026	0.0058	0.0609	0.5259	0.0129	0.0420	0.2150	0.0000	0.0113	0.0239	0.0000
SilTMEM147_C	0.0270	0.0240	0.0033	0.0043	0.0046	0.0495	0.4458	0.0038	0.0355	0.1866	0.0000	0.0266	0.0000	0.0000
Group mol%	SM 40:2;2	SM 40:1;2	SM 40:0;2	SM 42:3;2	SM 42:2;2	SM 42:1;2	SM 42:0;2	PE 32:2	PE 32:1	PE O-34:3	PE O-34:2	PE O-34:1	PE 34:2	PE 34:1
UNTREAT_A	0.1319	0.2896	0.0000	0.2458	1.1670	0.3089	0.0104	0.1834	1.3312	0.0255	0.1663	0.2735	1.8601	3.4600
UNTREAT_B	0.1339	0.0396	0.0000	0.2283	1.0170	0.2731	0.0069	0.1871	1.1544	0.0264	0.2175	0.2682	1.7978	3.3535
UNTREAT_C	0.1274	0.0560	0.0000	0.2547	1.0626	0.2916	0.0074	0.1846	1.1454	0.0414	0.2360	0.2719	1.7447	3.1800
NEG_A	0.1089	0.1672	0.0000	0.2133	1.1257	0.2826	0.0000	0.2026	0.8898	0.0250	0.2165	0.2797	1.7122	2.9245
NEG_B	0.1315	0.1626	0.0020	0.2265	1.0999	0.2980	0.0018	0.1651	0.8843	0.0353	0.2014	0.2323	1.6771	2.7818
NEG_C	0.1363	0.1291	0.0096	0.2284	1.1681	0.3273	0.0097	0.1563	0.8663	0.0369	0.2568	0.2393	1.7485	2.8782
SilTMEM147_A	0.1394	0.2502	0.0000	0.1695	1.0548	0.3450	0.0126	0.0426	0.3959	0.0206	0.1259	0.1310	0.6703	1.6711
SilTMEM147_B	0.1691	0.1453	0.0000	0.1958	1.0852	0.3407	0.0073	0.0473	0.3947	0.0211	0.1496	0.1390	0.6818	1.7335
SilTMEM147_C	0.1495	0.2052	0.0000	0.1528	0.9911	0.3257	0.0150	0.0520	0.3942	0.0244	0.1591	0.1439	0.7401	1.7650
Group mol%	PE O-36:6	PE O-36:5	PE O-36:4	PE O-36:3	PE O-36:2	PE O-36:1	PE 36:5	PE 36:4	PE 36:3	PE 36:2	PE 36:1	PE 36:0	PE O-38:6	PE O-38:5
UNTREAT_A	0.0764	0.0928	0.0362	0.0660	0.2537	0.2518	0.1425	0.3163	0.4700	3.3021	1.9937	0.0525	0.1115	0.0820
UNTREAT_B	0.0534	0.1210	0.0441	0.0676	0.2492	0.2591	0.1298	0.3112	0.4430	3.3161	1.8704	0.0801	0.1258	0.1002
UNTREAT_C	0.0833	0.1488	0.0563	0.0866	0.2541	0.2444	0.1359	0.3034	0.4367	3.1344	1.9060	0.0869	0.1582	0.1241
NEG_A	0.0433	0.1482	0.0559	0.0508	0.2978	0.2663	0.1581	0.3515	0.5523	5.0581	2.1953	0.0163	0.1759	0.1397
NEG_B	0.0740	0.1751	0.0598	0.0687	0.2486	0.2213	0.1710	0.3392	0.4869	4.8607	1.9985	0.0968	0.1613	0.1461
NEG_C	0.0970	0.2073	0.0557	0.0852	0.2920	0.2556	0.1788	0.3667	0.5313	5.1146	2.0727	0.1310	0.2047	0.1663
SilTMEM147_A	0.1093	0.1871	0.0367	0.0468	0.1481	0.1974	0.2206	0.3579	0.3143	3.3260	1.6132	0.0990	0.1652	0.1554
SilTMEM147_B	0.1292	0.2147	0.0412	0.0530	0.1714	0.1967	0.2244	0.3784	0.3883	3.5692	1.6669	0.1254	0.2002	0.1824
SilTMEM147_C	0.1218	0.2401	0.0477	0.0731	0.2033	0.2249	0.2115	0.3380	0.4008	3.8966	1.8654	0.1320	0.2362	0.2117

Group mol%	PE O-38:4	PE O-38:3	PE O-38:2	PE O-38:1	PE O-38:0	PE 38:6	PE 38:5	PE 38:4	PE 38:3	PE 38:2	PE 38:1	PE 38:0	PE O-40:6	PE O-40:5
UNTREAT_A	0.0445	0.0140	0.0689	0.0489	0.0306	0.2190	0.7006	0.8588	0.1559	0.1672	0.0482	0.0274	0.0312	0.0339
UNTREAT_B	0.0477	0.0251	0.0659	0.0423	0.0329	0.2209	0.6713	0.9469	0.1384	0.1471	0.0495	0.0365	0.0340	0.0178
UNTREAT_C	0.0543	0.0236	0.0630	0.0491	0.0408	0.2206	0.6934	0.8994	0.1569	0.1658	0.0652	0.0451	0.0405	0.0265
NEG_A	0.0726	0.0171	0.0502	0.0318	0.0351	0.3149	0.9571	1.2059	0.1319	0.1598	0.0525	0.0522	0.0577	0.0229
NEG_B	0.0535	0.0176	0.0582	0.0320	0.0365	0.2994	0.8626	1.1129	0.1605	0.1495	0.0561	0.0405	0.0439	0.0279
NEG_C	0.0508	0.0215	0.0562	0.0334	0.0325	0.3043	0.9144	1.1864	0.1630	0.1436	0.0663	0.0478	0.0488	0.0349
SilTMEM147_A	0.0824	0.0223	0.0526	0.0364	0.0414	0.4200	1.0941	1.4089	0.1871	0.0904	0.0564	0.0329	0.0559	0.0385
SilTMEM147_B	0.0888	0.0240	0.0592	0.0254	0.0380	0.4595	1.2398	1.6212	0.2128	0.1058	0.0540	0.0474	0.0571	0.0396
SilTMEM147_C	0.0925	0.0341	0.0590	0.0373	0.0462	0.4174	1.1661	1.5504	0.1752	0.1092	0.0559	0.0475	0.0558	0.0400
Group mol%	PE O-40:4	PE O-40:3	PE O-40:2	PE O-40:1	PE 40:7	PE 40:6	PE 40:5	PE 40:4	PE 40:3	PS 32:3	PS 32:2	PS 32:1	PS O-34:2	PS O-34:1
UNTREAT_A	0.0239	0.0183	0.0157	0.0431	0.1504	0.3031	0.0901	0.0502	0.0240	0.0156	0.0296	0.1979	0.0014	0.0613
UNTREAT_B	0.0134	0.0142	0.0095	0.0221	0.1329	0.2623	0.1156	0.0295	0.0135	0.0050	0.0003	0.1584	0.0000	0.0656
UNTREAT_C	0.0145	0.0256	0.0254	0.0376	0.1402	0.2702	0.1117	0.0382	0.0151	0.0085	0.0059	0.1753	0.0066	0.0647
NEG_A	0.0225	0.0102	0.0142	0.0175	0.1965	0.3318	0.1485	0.0577	0.0111	0.0057	0.0128	0.1204	0.0014	0.0413
NEG_B	0.0155	0.0150	0.0117	0.0257	0.1641	0.3000	0.1167	0.0479	0.0151	0.0005	0.0000	0.1151	0.0000	0.0395
NEG_C	0.0214	0.0117	0.0072	0.0230	0.1606	0.3170	0.1312	0.0529	0.0115	0.0054	0.0000	0.1098	0.0000	0.0369
SilTMEM147_A	0.0187	0.0164	0.0180	0.0420	0.1877	0.3080	0.1268	0.0425	0.0095	0.0115	0.0051	0.0560	0.0000	0.0246
SilTMEM147_B	0.0179	0.0123	0.0092	0.0220	0.2000	0.3595	0.1299	0.0532	0.0126	0.0000	0.0000	0.0502	0.0000	0.0288
SilTMEM147_C	0.0328	0.0136	0.0144	0.0368	0.2128	0.3413	0.1419	0.0538	0.0142	0.0132	0.0038	0.0512	0.0051	0.0175
Group mol%	PS 34:2	PS 34:1	PS 34:0	PS O-36:2	PS O-36:1	PS 36:4	PS 36:3	PS 36:2	PS 36:1	PS 36:0	PS O-38:3	PS O-38:2	PS O-38:1	PS 38:7
UNTREAT_A	0.1785	0.9738	0.0264	0.0125	0.1186	0.0223	0.0382	0.5610	1.5322	0.0045	0.0116	0.0171	0.0448	0.0068
UNTREAT_B	0.1478	0.9953	0.0242	0.0220	0.1119	0.0194	0.0405	0.5436	1.5027	0.0000	0.0081	0.0264	0.0325	0.0039
UNTREAT_C	0.1676	1.0330	0.0215	0.0323	0.1352	0.0205	0.0428	0.5595	1.6094	0.0171	0.0164	0.0252	0.0340	0.0109
NEG_A	0.1153	0.9107	0.0377	0.0204	0.1073	0.0188	0.0359	0.7059	2.2207	0.0000	0.0178	0.0192	0.0354	0.0000
NEG_B	0.1001	0.8178	0.0249	0.0173	0.1162	0.0176	0.0328	0.5468	1.8895	0.0000	0.0071	0.0159	0.0278	0.0005
NEG_C	0.1110	0.8451	0.0410	0.0120	0.1039	0.0174	0.0411	0.5673	1.9491	0.0000	0.0056	0.0193	0.0269	0.0036
SilTMEM147_A	0.0491	0.5351	0.0398	0.0092	0.1272	0.0192	0.0332	0.3835	2.1302	0.0000	0.0048	0.0133	0.0454	0.0021
SilTMEM147_B	0.0428	0.5389	0.0228	0.0083	0.1276	0.0138	0.0300	0.4197	2.2851	0.0000	0.0101	0.0129	0.0296	0.0000
SilTMEM147_C	0.0353	0.5051	0.0376	0.0080	0.1231	0.0139	0.0216	0.4354	2.1243	0.0000	0.0156	0.0212	0.0409	0.0047
Group mol%	PS 38:6	PS 38:5	PS 38:4	PS 38:3	PS 38:2	PS 38:1	PS 38:0	PS O-40:2	PS O-40:1	PS O-40:0	PS 40:6	PS 40:5	PS 40:4	PS 40:3
UNTREAT_A	0.0175	0.0335	0.0719	0.0582	0.1015	0.0728	0.0000	0.0223	0.0024	0.0224	0.1021	0.0484	0.0062	0.0109
UNTREAT_B	0.0144	0.0347	0.0731	0.0657	0.0883	0.0529	0.0003	0.0068	0.0079	0.0106	0.0743	0.0467	0.0208	0.0178
UNTREAT_C	0.0238	0.0413	0.0898	0.0656	0.1026	0.0651	0.0072	0.0136	0.0143	0.0143	0.0749	0.0672	0.0298	0.0253
NEG_A	0.0338	0.0424	0.0979	0.0768	0.0948	0.0815	0.0049	0.0053	0.0106	0.0173	0.1039	0.0898	0.0378	0.0105
NEG_B	0.0143	0.0378	0.0764	0.0833	0.0856	0.0579	0.0000	0.0088	0.0052	0.0131	0.0988	0.0643	0.0299	0.0159
NEG_C	0.0162	0.0393	0.0893	0.0751	0.0885	0.0575	0.0000	0.0080	0.0074	0.0131	0.1162	0.0695	0.0358	0.0147
SilTMEM147_A	0.0241	0.0665	0.1320	0.1454	0.0597	0.0610	0.0042	0.0102	0.0114	0.0153	0.1930	0.0886	0.0421	0.0224
SilTMEM147_B	0.0274	0.0709	0.1582	0.1533	0.0601	0.0686	0.0000	0.0023	0.0060	0.0168	0.2112	0.0939	0.0446	0.0137
SilTMEM147_C	0.0324	0.0881	0.1436	0.1598	0.0765	0.0654	0.0000	0.0191	0.0106	0.0173	0.2058	0.0967	0.0495	0.0277

Group mol%	PS 40:1	PS O-42:3	PS O-42:2	PS O-42:1	PS O-42:0	PS 42:6	PS 42:5	PS 42:4	PS 42:2	PS 42:1	PI 32:1	PI 32:0	PI 34:2	PI 34:1
UNTREAT_A	0.0399	0.0000	0.0142	0.0052	0.0116	0.0062	0.0000	0.0151	0.0251	0.0156	0.0518	0.0190	0.2681	0.4205
UNTREAT_B	0.0214	0.0029	0.0141	0.0069	0.0022	0.0041	0.0035	0.0028	0.0167	0.0079	0.0527	0.0139	0.2545	0.3967
UNTREAT_C	0.0411	0.0101	0.0106	0.0113	0.0095	0.0112	0.0120	0.0106	0.0244	0.0175	0.0640	0.0211	0.2646	0.3847
NEG_A	0.0519	0.0000	0.0107	0.0072	0.0060	0.0000	0.0042	0.0064	0.0295	0.0358	0.0504	0.0119	0.1828	0.3673
NEG_B	0.0342	0.0015	0.0088	0.0041	0.0018	0.0035	0.0039	0.0012	0.0202	0.0103	0.0491	0.0134	0.2053	0.3804
NEG_C	0.0228	0.0037	0.0043	0.0033	0.0012	0.0054	0.0026	0.0022	0.0253	0.0102	0.0458	0.0128	0.2085	0.3779
SilTMEM147_A	0.0370	0.0045	0.0053	0.0078	0.0085	0.0059	0.0144	0.0080	0.0153	0.0157	0.0221	0.0074	0.0846	0.1616
SilTMEM147_B	0.0369	0.0010	0.0005	0.0052	0.0000	0.0074	0.0028	0.0010	0.0158	0.0121	0.0212	0.0038	0.0741	0.1521
SilTMEM147_C	0.0359	0.0023	0.0170	0.0086	0.0034	0.0154	0.0031	0.0070	0.0234	0.0201	0.0213	0.0140	0.0832	0.1514
Group mol%	PI 34:0	PI O-36:3	PI O-36:2	PI O-36:1	PI 36:4	PI 36:3	PI 36:2	PI 36:1	PI O-38:3	PI O-38:2	PI 38:5	PI 38:4	PI 38:3	PI 38:2
UNTREAT_A	0.0556	0.0104	0.0503	0.0474	0.0453	0.0838	0.8680	0.7517	0.0283	0.0643	0.2124	0.4340	0.2381	0.2191
UNTREAT_B	0.0456	0.0037	0.0363	0.0429	0.0298	0.0832	0.9526	0.7649	0.0180	0.0675	0.1801	0.3576	0.2203	0.1940
UNTREAT_C	0.0480	0.0086	0.0469	0.0476	0.0342	0.0803	0.9604	0.7397	0.0211	0.0681	0.1808	0.3779	0.2289	0.2040
NEG_A	0.0468	0.0049	0.0253	0.0424	0.0505	0.0789	0.7762	0.7400	0.0138	0.0543	0.2805	0.7277	0.2479	0.1323
NEG_B	0.0486	0.0021	0.0298	0.0355	0.0435	0.0729	0.7360	0.7501	0.0194	0.0392	0.2584	0.6883	0.2878	0.1382
NEG_C	0.0494	0.0055	0.0346	0.0376	0.0484	0.0733	0.7827	0.7376	0.0158	0.0527	0.2833	0.7239	0.2756	0.1468
SilTMEM147_A	0.0250	0.0000	0.0224	0.0294	0.0660	0.0636	0.5175	0.4687	0.0129	0.0565	0.3091	1.4350	0.4484	0.1034
SilTMEM147_B	0.0170	0.0000	0.0175	0.0271	0.0652	0.0596	0.4659	0.4798	0.0150	0.0368	0.3442	1.5977	0.5040	0.1074
SilTMEM147_C	0.0230	0.0056	0.0203	0.0293	0.0599	0.0658	0.4892	0.5297	0.0056	0.0380	0.3099	1.5290	0.5042	0.1187
Group mol%	PI O-40:4	PI O-40:3	PI 40:6	PI 40:5	PI 40:4	PI 40:3	PI 40:2	PG 30:1	PG 30:0	PG O-32:1	PG O-32:0	PG 32:2	PG 32:1	PG 32:0
UNTREAT_A	0.0119	0.0281	0.0525	0.0771	0.0794	0.0395	0.0406	0.0030	0.0043	0.0006	0.0000	0.0031	0.0138	0.0043
UNTREAT_B	0.0124	0.0270	0.0514	0.0675	0.0518	0.0326	0.0325	0.0011	0.0031	0.0006	0.0006	0.0015	0.0163	0.0067
UNTREAT_C	0.0170	0.0335	0.0595	0.0768	0.0613	0.0332	0.0404	0.0017	0.0058	0.0011	0.0021	0.0013	0.0150	0.0105
NEG_A	0.0177	0.0197	0.0537	0.0887	0.0837	0.0249	0.0241	0.0010	0.0014	0.0005	0.0009	0.0018	0.0105	0.0029
NEG_B	0.0112	0.0251	0.0547	0.0844	0.0749	0.0285	0.0194	0.0000	0.0019	0.0002	0.0000	0.0010	0.0099	0.0039
NEG_C	0.0168	0.0273	0.0589	0.0966	0.0802	0.0289	0.0221	0.0004	0.0024	0.0000	0.0000	0.0012	0.0090	0.0052
SilTMEM147_A	0.0238	0.0353	0.1386	0.1542	0.1047	0.0339	0.0000	0.0013	0.0032	0.0000	0.0007	0.0023	0.0077	0.0030
SilTMEM147_B	0.0219	0.0354	0.1408	0.1646	0.1054	0.0296	0.0000	0.0000	0.0008	0.0000	0.0000	0.0024	0.0043	0.0011
SilTMEM147_C	0.0164	0.0358	0.1381	0.1437	0.1025	0.0325	0.0140	0.0013	0.0012	0.0004	0.0000	0.0013	0.0049	0.0026
Group mol%	PG O-34:2	PG O-34:1	PG O-34:0	PG 34:3	PG 34:2	PG 34:1	PG 34:0	PG O-36:2	PG O-36:1	PG 36:4	PG 36:3	PG 36:2	PG 36:1	PG 38:6
UNTREAT_A	0.0006	0.0022	0.0007	0.0014	0.0131	0.1204	0.0000	0.0013	0.0057	0.0017	0.0037	0.0240	0.0310	0.0015
UNTREAT_B	0.0000	0.0030	0.0009	0.0012	0.0138	0.1555	0.0000	0.0021	0.0060	0.0021	0.0007	0.0213	0.0366	0.0007
UNTREAT_C	0.0000	0.0044	0.0023	0.0007	0.0150	0.1546	0.0001	0.0032	0.0064	0.0027	0.0031	0.0194	0.0391	0.0000
NEG_A	0.0000	0.0012	0.0005	0.0007	0.0109	0.1140	0.0000	0.0020	0.0055	0.0041	0.0000	0.0146	0.0327	0.0000
NEG_B	0.0000	0.0019	0.0007	0.0008	0.0129	0.1285	0.0007	0.0012	0.0046	0.0017	0.0012	0.0192	0.0385	0.0003
NEG_C	0.0000	0.0015	0.0004	0.0007	0.0118	0.1348	0.0001	0.0010	0.0046	0.0016	0.0012	0.0162	0.0375	0.0002
SilTMEM147_A	0.0000	0.0016	0.0010	0.0032	0.0095	0.0694	0.0019	0.0017	0.0054	0.0027	0.0075	0.0208	0.0332	0.0041
SilTMEM147_B	0.0000	0.0014	0.0004	0.0021	0.0092	0.0678	0.0000	0.0009	0.0035	0.0027	0.0062	0.0159	0.0304	0.0009
SilTMEM147_C	0.0000	0.0006	0.0020	0.0017	0.0067	0.0693	0.0003	0.0029	0.0046	0.0028	0.0059	0.0193	0.0411	0.0006

Group mol%	PG 38:5	PG 38:4	PG 38:3	PG 38:2	PA 32:2	PA 32:1	PA 32:0	PA O-34:2	PA O-34:1	PA 34:3	PA 34:2	PA 34:1	PA O-36:2	PA O-36:1
UNTREAT_A	0.0012	0.0011	0.0027	0.0007	0.0000	0.0605	0.0255	0.0000	0.0195	0.0000	0.0442	0.1801	0.0042	0.0093
UNTREAT_B	0.0009	0.0003	0.0007	0.0009	0.0000	0.0437	0.0230	0.0000	0.0126	0.0000	0.0288	0.1236	0.0015	0.0028
UNTREAT_C	0.0029	0.0028	0.0029	0.0025	0.0000	0.0428	0.0224	0.0000	0.0161	0.0000	0.0305	0.1251	0.0097	0.0100
NEG_A	0.0021	0.0023	0.0000	0.0011	0.0000	0.0124	0.0201	0.0000	0.0000	0.0000	0.0118	0.0838	0.0000	0.0023
NEG_B	0.0010	0.0008	0.0008	0.0009	0.0000	0.0130	0.0213	0.0000	0.0000	0.0000	0.0049	0.0702	0.0000	0.0000
NEG_C	0.0010	0.0011	0.0006	0.0007	0.0000	0.0161	0.0208	0.0000	0.0000	0.0000	0.0084	0.0754	0.0000	0.0000
SilTMEM147_A	0.0032	0.0017	0.0009	0.0015	0.0000	0.0023	0.0179	0.0000	0.0000	0.0000	0.0000	0.0526	0.0000	0.0000
SilTMEM147_B	0.0018	0.0016	0.0009	0.0002	0.0000	0.0000	0.0121	0.0000	0.0000	0.0000	0.0000	0.0281	0.0000	0.0000
SilTMEM147_C	0.0018	0.0029	0.0013	0.0003	0.0000	0.0088	0.0213	0.0000	0.0000	0.0000	0.0011	0.0672	0.0000	0.0012
Group mol%	PA 36:4	PA 36:3	PA 36:2	PA 36:1	PA 38:6	PA 38:5	PA 38:4	PA 38:3	p16:0a16:1	p16:0a18:2	p16:0a18:1	p16:0a20:5	p16:0a20:4	p16:0a20:3
UNTREAT_A	0.0051	0.0166	0.1243	0.1983	0.0012	0.0031	0.0045	0.0059	0.1829	0.0992	0.7184	0.4912	0.9017	0.1089
UNTREAT_B	0.0000	0.0000	0.0767	0.0912	0.0000	0.0000	0.0013	0.0009	0.2240	0.0920	0.6247	0.5365	0.6771	0.1107
UNTREAT_C	0.0020	0.0082	0.0833	0.1033	0.0003	0.0043	0.0072	0.0073	0.2163	0.0836	0.6636	0.5178	0.8010	0.0862
NEG_A	0.0000	0.0000	0.0499	0.1435	0.0000	0.0000	0.0016	0.0002	0.1479	0.0914	0.7052	0.5357	1.1282	0.1180
NEG_B	0.0000	0.0000	0.0415	0.0852	0.0000	0.0000	0.0025	0.0000	0.1560	0.0757	0.6878	0.5395	1.1289	0.1200
NEG_C	0.0000	0.0000	0.0476	0.0972	0.0000	0.0000	0.0001	0.0004	0.1704	0.0906	0.6641	0.5675	1.1752	0.1405
SilTMEM147_A	0.0023	0.0000	0.0345	0.1576	0.0000	0.0000	0.0065	0.0055	0.1597	0.1317	0.7819	0.9482	1.7530	0.1497
SilTMEM147_B	0.0000	0.0000	0.0111	0.0374	0.0000	0.0000	0.0002	0.0000	0.0931	0.0877	0.4373	0.7599	1.2585	0.1285
SilTMEM147_C	0.0000	0.0008	0.0518	0.2057	0.0000	0.0036	0.0127	0.0122	0.0737	0.0641	0.4413	0.7495	1.2717	0.1066
Group mol%	p16:0a20:2	p16:0a20:1	p16:0a22:6	p16:0a22:5	p16:0a22:4	p16:0a22:3	p16:0a22:2	p16:0a22:1	p18:1a16:1	p18:1a16:0	p18:1a18:2	p18:1a18:1	p18:1a18:0	p18:1a20:5
UNTREAT_A	0.0149	0.0282	0.5482	0.5090	0.1060	0.0211	0.0122	0.0000	0.0844	0.1450	0.0419	0.2699	0.0149	0.1995
UNTREAT_B	0.0304	0.0251	0.4776	0.4616	0.0630	0.0312	0.0382	0.0092	0.0752	0.1466	0.0517	0.3085	0.0018	0.2611
UNTREAT_C	0.0438	0.0418	0.5101	0.4788	0.0855	0.0370	0.0151	0.0012	0.1077	0.1713	0.0342	0.2501	0.0073	0.1298
NEG_A	0.0028	0.0200	0.4897	0.4586	0.0445	0.0111	0.0053	0.0000	0.0775	0.2185	0.0262	0.2462	0.0026	0.1360
NEG_B	0.0000	0.0274	0.4746	0.4858	0.0664	0.0040	0.0125	0.0046	0.0706	0.1744	0.0268	0.2252	0.0113	0.1992
NEG_C	0.0008	0.0229	0.4886	0.4743	0.0372	0.0214	0.0100	0.0048	0.0625	0.2063	0.0373	0.2472	0.0084	0.1674
SilTMEM147_A	0.0102	0.0260	0.7702	0.5630	0.0608	0.0282	0.0110	0.0060	0.0689	0.2043	0.0388	0.2642	0.0085	0.3332
SilTMEM147_B	0.0011	0.0195	0.4946	0.3505	0.0419	0.0189	0.0084	0.0104	0.0444	0.1314	0.0218	0.1939	0.0047	0.3043
SilTMEM147_C	0.0173	0.0114	0.4919	0.2895	0.0306	0.0093	0.0020	0.0000	0.0417	0.1230	0.0303	0.1778	0.0017	0.2521
Group mol%	p18:1a20:4	p18:1a20:3	p18:1a20:2	p18:1a20:1	p18:1a20:0	p18:1a22:6	p18:1a22:5	p18:1a22:4	p18:1a22:3	p18:1a22:2	p18:0a16:1	p18:0a18:2	p18:0a18:1	p18:0a20:5
UNTREAT_A	0.2294	0.0200	0.0058	0.0000	0.0014	0.1703	0.0976	0.0153	0.0100	0.0052	0.0764	0.0450	0.2385	0.2286
UNTREAT_B	0.2442	0.0394	0.0172	0.0309	0.0000	0.1862	0.1420	0.0503	0.0212	0.0522	0.1053	0.0508	0.1574	0.2300
UNTREAT_C	0.2132	0.0409	0.0095	0.0257	0.0000	0.1378	0.1194	0.0208	0.0245	0.0000	0.0726	0.0299	0.2855	0.2317
NEG_A	0.3143	0.0250	0.0006	0.0054	0.0000	0.1256	0.0815	0.0109	0.0009	0.0021	0.0649	0.0451	0.2350	0.2706
NEG_B	0.3239	0.0317	0.0021	0.0103	0.0070	0.1390	0.1030	0.0149	0.0119	0.0053	0.0790	0.0449	0.2963	0.2866
NEG_C	0.3669	0.0325	0.0000	0.0138	0.0002	0.1491	0.1045	0.0135	0.0142	0.0000	0.0938	0.0524	0.2523	0.2348
SilTMEM147_A	0.5486	0.0496	0.0065	0.0079	0.0041	0.2074	0.1299	0.0310	0.0017	0.0066	0.0702	0.0468	0.3174	0.4807
SilTMEM147_B	0.4962	0.0490	0.0051	0.0041	0.0048	0.1610	0.0940	0.0288	0.0074	0.0000	0.0436	0.0536	0.2413	0.4691
SilTMEM147_C	0.4515	0.0288	0.0037	0.0072	0.0002	0.1785	0.0849	0.0100	0.0078	0.0044	0.0439	0.0391	0.2510	0.4677

Group mol%	p18:0a20:4	p18:0a20:3	p18:0a20:2	p18:0a20:1	p18:0a22:6	p18:0a22:5	p18:0a22:4	p18:0a22:3	p18:0a22:2	Cer 34:1;2	Cer 36:1;2	Cer 38:1;2	Cer 40:2;2	Cer 40:1;2
UNTREAT_A	0.3121	0.0573	0.0153	0.0000	0.2461	0.2419	0.0245	0.0230	0.0000	0.0300	0.0053	0.0047	0.0034	0.0250
UNTREAT_B	0.2798	0.0637	0.0526	0.0000	0.1552	0.0000	0.0871	0.0675	0.0933	0.0326	0.0069	0.0023	0.0037	0.0179
UNTREAT_C	0.3107	0.0409	0.0148	0.0000	0.1823	0.2030	0.0430	0.0450	0.0000	0.0374	0.0076	0.0011	0.0039	0.0188
NEG_A	0.4976	0.0430	0.0084	0.0000	0.1993	0.1536	0.0150	0.0116	0.0000	0.0400	0.0127	0.0026	0.0030	0.0276
NEG_B	0.5465	0.0573	0.0037	0.0226	0.1887	0.1519	0.0233	0.0295	0.0222	0.0464	0.0102	0.0022	0.0031	0.0214
NEG_C	0.5044	0.0644	0.0167	0.0062	0.2207	0.1777	0.0225	0.0162	0.0133	0.0425	0.0094	0.0025	0.0031	0.0242
SilTMEM147_A	0.9934	0.0698	0.0061	0.0096	0.3786	0.2352	0.0170	0.0168	0.0092	0.0272	0.0185	0.0087	0.0067	0.0456
SilTMEM147_B	0.8667	0.0651	0.0209	0.0000	0.2450	0.1644	0.0203	0.0397	0.0045	0.0276	0.0219	0.0070	0.0071	0.0496
SilTMEM147_C	0.8330	0.0740	0.0141	0.0000	0.2635	0.1633	0.0224	0.0276	0.0000	0.0234	0.0194	0.0081	0.0070	0.0450
Group mol%	Cer 40:2;3	Cer 42:2;2	Cer 42:1;2	HexCer 34:1;2	HexCer 36:1;2	HexCer 38:1;2	HexCer 38:2;3	HexCer 40:2;2	HexCer 40:1;2	HexCer 40:3;3	HexCer 40:2;3	HexCer 40:1;3	HexCer 42:3;2	HexCer 42:2;2
UNTREAT_A	0.0047	0.0912	0.0561	0.0209	0.0044	0.0015	0.0014	0.0064	0.0344	0.0058	0.0115	0.0069	0.0072	0.1148
UNTREAT_B	0.0058	0.0832	0.0592	0.0169	0.0044	0.0020	0.0008	0.0070	0.0360	0.0068	0.0109	0.0113	0.0039	0.1189
UNTREAT_C	0.0071	0.0909	0.0621	0.0178	0.0057	0.0013	0.0009	0.0051	0.0365	0.0083	0.0132	0.0088	0.0044	0.1261
NEG_A	0.0062	0.0775	0.0548	0.0233	0.0116	0.0053	0.0027	0.0134	0.0510	0.0051	0.0184	0.0069	0.0070	0.1900
NEG_B	0.0053	0.0815	0.0578	0.0329	0.0090	0.0027	0.0006	0.0101	0.0699	0.0065	0.0165	0.0071	0.0069	0.1843
NEG_C	0.0057	0.0818	0.0561	0.0323	0.0106	0.0045	0.0019	0.0102	0.0639	0.0098	0.0194	0.0080	0.0066	0.1937
SilTMEM147_A	0.0093	0.1056	0.0845	0.0542	0.1044	0.0578	0.0060	0.0662	0.4689	0.0471	0.0739	0.0254	0.0363	0.6810
SilTMEM147_B	0.0105	0.1137	0.0900	0.0572	0.0921	0.0508	0.0059	0.0600	0.4509	0.0405	0.0690	0.0213	0.0380	0.6590
SilTMEM147_C	0.0143	0.1103	0.0964	0.0504	0.0770	0.0513	0.0051	0.0543	0.4222	0.0403	0.0717	0.0263	0.0280	0.5948
Group mol%	HexCer 42:1;2	HexCer 42:3;3	HexCer 42:2;3	HexCer 42:1;3	Hex2Cer 34:1;2	Hex2Cer 36:1;2	Hex2Cer 36:1;3	Hex2Cer 38:1;2	Hex2Cer 38:2;3	Hex2Cer 40:1;2	Hex2Cer 40:2;3	Hex2Cer 40:1;3	Hex2Cer 42:2;2	Hex2Cer 42:1;2
UNTREAT_A	0.0946	0.0050	0.0093	0.0285	0.0116	0.0229	0.0000	0.0104	0.0057	0.0165	0.0075	0.0167	0.0215	0.0233
UNTREAT_B	0.0966	0.0051	0.0087	0.0294	0.0118	0.0084	0.0035	0.0040	0.0041	0.0262	0.0169	0.0144	0.0313	0.0271
UNTREAT_C	0.1049	0.0042	0.0101	0.0269	0.0148	0.0138	0.0082	0.0077	0.0088	0.0284	0.0205	0.0186	0.0378	0.0248
NEG_A	0.1758	0.0080	0.0092	0.0168	0.0250	0.0417	0.0000	0.0103	0.0058	0.0372	0.0174	0.0165	0.0615	0.0475
NEG_B	0.1622	0.0061	0.0091	0.0162	0.0127	0.0093	0.0032	0.0039	0.0032	0.0314	0.0166	0.0092	0.0537	0.0475
NEG_C	0.1743	0.0062	0.0111	0.0245	0.0159	0.0178	0.0035	0.0048	0.0044	0.0370	0.0174	0.0099	0.0463	0.0432
SilTMEM147_A	0.5100	0.0164	0.0199	0.0331	0.0124	0.0176	0.0075	0.0083	0.0063	0.0449	0.0165	0.0142	0.0527	0.0411
SilTMEM147_B	0.5086	0.0141	0.0256	0.0371	0.0109	0.0106	0.0065	0.0043	0.0033	0.0313	0.0184	0.0097	0.0499	0.0404
SilTMEM147_C	0.4800	0.0189	0.0192	0.0296	0.0120	0.0153	0.0083	0.0082	0.0000	0.0365	0.0116	0.0139	0.0500	0.0483

Group mol%	Hex2Cer 42:2;3	Hex2Cer 42:1;3	Chol	CE 14:1	CE 14:0	CE 15:0	CE 16:2	CE 16:1	CE 16:0	CE 17:1	CE 17:0	CE 18:3	CE 18:2	CE 18:1
UNTREAT_A	0.0099	0.0000	15.5644	0.0935	0.5082	0.0938	0.0340	1.2703	0.8872	0.1784	0.0970	0.0785	0.2148	3.8865
UNTREAT_B	0.0191	0.0241	15.1545	0.0883	0.5532	0.0840	0.0254	1.3058	1.1936	0.1701	0.1226	0.0546	0.2184	4.6976
UNTREAT_C	0.0234	0.0255	15.2496	0.0942	0.4845	0.0763	0.0308	1.2500	1.0608	0.1665	0.1158	0.0561	0.1900	4.1297
NEG_A	0.0185	0.0173	13.8655	0.0968	0.5238	0.0669	0.0345	1.3178	1.3327	0.1955	0.1495	0.0802	0.2431	5.1317
NEG_B	0.0133	0.0155	14.5520	0.0974	0.5103	0.0728	0.0341	1.3349	1.3742	0.1933	0.1177	0.0792	0.2643	5.6233
NEG_C	0.0140	0.0130	14.8694	0.0730	0.3571	0.0424	0.0266	0.9857	0.8112	0.1440	0.0786	0.0710	0.1961	3.7365
SilTMEM147_A	0.0196	0.0202	15.6047	0.0339	0.1678	0.0455	0.0170	0.4044	0.4536	0.0661	0.0685	0.0422	0.1354	1.7799
SilTMEM147_B	0.0102	0.0140	16.8775	0.0299	0.1283	0.0448	0.0147	0.3268	0.4384	0.0678	0.0656	0.0360	0.1123	1.5509
SilTMEM147_C	0.0137	0.0184	16.6146	0.0466	0.2618	0.0762	0.0358	0.6190	0.7150	0.1191	0.0991	0.0711	0.1934	2.8443
Group mol%	CE 18:0	CE 19:1	CE 20:4	CE 20:3	CE 20:2	CE 20:1	CE 22:6	CE 22:5	DAG 30:1	DAG 30:0	DAG 32:2	DAG 32:1	DAG 32:0	DAG 34:2
UNTREAT_A	0.1508	0.0849	0.0983	0.0742	0.0404	0.1708	0.1822	0.0865	0.0132	0.0234	0.0157	0.1280	0.0592	0.1414
UNTREAT_B	0.1654	0.0740	0.0954	0.0661	0.0498	0.2626	0.1807	0.0873	0.0126	0.0237	0.0199	0.1038	0.0536	0.0982
UNTREAT_C	0.1474	0.0706	0.0814	0.0620	0.0463	0.2168	0.1651	0.0761	0.0062	0.0156	0.0144	0.0795	0.0506	0.0712
NEG_A	0.2280	0.0915	0.1809	0.1038	0.0581	0.2615	0.2431	0.1987	0.0041	0.0154	0.0102	0.0654	0.0359	0.0750
NEG_B	0.2177	0.0784	0.1527	0.1062	0.0598	0.2457	0.2917	0.1933	0.0082	0.0176	0.0095	0.0480	0.0387	0.0659
NEG_C	0.1072	0.0568	0.1556	0.0978	0.0416	0.1630	0.3159	0.1882	0.0020	0.0101	0.0070	0.0296	0.0247	0.0310
SilTMEM147_A	0.0931	0.0454	0.2224	0.1347	0.0448	0.1001	0.8568	0.3415	0.0061	0.0113	0.0000	0.0421	0.0314	0.0350
SilTMEM147_B	0.1005	0.0343	0.2100	0.1353	0.0389	0.0858	0.8688	0.3247	0.0005	0.0025	0.0047	0.0000	0.0120	0.0000
SilTMEM147_C	0.1389	0.0643	0.3471	0.2127	0.0616	0.1432	1.1952	0.4698	0.0054	0.0117	0.0056	0.0482	0.0327	0.0293
Group mol%	DAG 34:1	DAG 34:0	DAG 36:5	DAG 36:4	DAG 36:3	DAG 36:2	DAG 36:1	DAG 36:0	DAG 38:6	DAG 38:5	DAG 38:4	DAG 38:3	DAG 38:2	DAG 38:1
UNTREAT_A	0.1749	0.1922	0.0111	0.0281	0.0254	0.2393	0.4197	0.3060	0.0155	0.0162	0.0119	0.0384	0.0968	1.4012
UNTREAT_B	0.1695	0.1108	0.0000	0.0113	0.0147	0.2247	0.2585	0.1850	0.0000	0.0000	0.0000	0.0143	0.0482	0.7254
UNTREAT_C	0.1178	0.1202	0.0003	0.0182	0.0145	0.2014	0.2642	0.1761	0.0000	0.0017	0.0048	0.0229	0.0457	0.7139
NEG_A	0.1022	0.1397	0.0034	0.0111	0.0127	0.1498	0.3906	0.3169	0.0000	0.0032	0.0108	0.0384	0.0792	1.3861
NEG_B	0.0778	0.1434	0.0063	0.0155	0.0078	0.1402	0.3843	0.3174	0.0000	0.0130	0.0121	0.0328	0.0753	1.1580
NEG_C	0.0542	0.0806	0.0000	0.0218	0.0039	0.1747	0.2117	0.1218	0.0000	0.0000	0.0029	0.0185	0.0365	0.5477
SilTMEM147_A	0.0569	0.0632	0.0001	0.0107	0.0128	0.1728	0.1375	0.1509	0.0000	0.0003	0.0112	0.0162	0.0480	0.4786
SilTMEM147_B	0.0145	0.0168	0.0000	0.0073	0.0000	0.0746	0.0389	0.0288	0.0000	0.0000	0.0073	0.0000	0.0000	0.0822
SilTMEM147_C	0.0733	0.0850	0.0012	0.0153	0.0064	0.1647	0.2693	0.1613	0.0000	0.0031	0.0055	0.0195	0.0438	0.6114

Group mol%	DAG 40:6	DAG 40:5	DAG 40:4	DAG 40:3	DAG 40:2	DAG 40:1	DAG 40:0	TAG 44:0	TAG 44:1	TAG 45:0	TAG 46:0	TAG 46:1	TAG 46:2	TAG 47:0
UNTREAT_A	0.0146	0.0389	0.0386	0.0028	0.0232	0.0752	0.0049	0.0232	0.0046	0.0309	0.0486	0.0148	0.0045	0.0384
UNTREAT_B	0.0044	0.0119	0.0121	0.0000	0.0086	0.0414	0.0026	0.0014	0.0000	0.0007	0.0088	0.0064	0.0014	0.0083
UNTREAT_C	0.0033	0.0201	0.0160	0.0012	0.0119	0.0382	0.0035	0.0049	0.0008	0.0046	0.0079	0.0054	0.0003	0.0088
NEG_A	0.0040	0.0558	0.0506	0.0012	0.0206	0.0604	0.0077	0.0010	0.0004	0.0040	0.0000	0.0047	0.0009	0.0008
NEG_B	0.0034	0.0817	0.0493	0.0000	0.0209	0.0618	0.0144	0.0048	0.0022	0.0043	0.0082	0.0068	0.0021	0.0050
NEG_C	0.0000	0.0235	0.0210	0.0002	0.0065	0.0233	0.0017	0.0026	0.0017	0.0043	0.0074	0.0060	0.0011	0.0051
SiITMEM147_A	0.0031	0.1165	0.0683	0.0013	0.0149	0.0259	0.0018	0.0031	0.0014	0.0037	0.0040	0.0055	0.0026	0.0017
SiITMEM147_B	0.0000	0.0456	0.0177	0.0000	0.0045	0.0025	0.0000	0.0020	0.0016	0.0050	0.0039	0.0055	0.0012	0.0023
SiITMEM147_C	0.0093	0.1137	0.0683	0.0007	0.0204	0.0418	0.0107	0.0018	0.0004	0.0067	0.0028	0.0027	0.0008	0.0000
Group mol%	TAG 47:1	TAG 48:0	TAG 48:1	TAG 48:2	TAG 48:3	TAG 49:0	TAG 49:1	TAG 49:2	TAG 50:0	TAG 50:1	TAG 50:2	TAG 50:3	TAG 51:0	TAG 51:1
UNTREAT_A	0.0053	0.0492	0.0398	0.0123	0.0037	0.0228	0.0218	0.0030	0.0225	0.0694	0.0548	0.0098	0.0103	0.0224
UNTREAT_B	0.0055	0.0238	0.0328	0.0103	0.0020	0.0074	0.0219	0.0039	0.0165	0.0811	0.0454	0.0079	0.0000	0.0132
UNTREAT_C	0.0031	0.0178	0.0243	0.0018	0.0001	0.0069	0.0202	0.0032	0.0127	0.0539	0.0180	0.0027	0.0021	0.0114
NEG_A	0.0000	0.0113	0.0190	0.0053	0.0016	0.0027	0.0064	0.0025	0.0113	0.0445	0.0295	0.0071	0.0000	0.0074
NEG_B	0.0046	0.0145	0.0232	0.0071	0.0018	0.0062	0.0121	0.0024	0.0112	0.0440	0.0235	0.0051	0.0032	0.0091
NEG_C	0.0000	0.0156	0.0247	0.0024	0.0029	0.0047	0.0119	0.0051	0.0144	0.0479	0.0227	0.0036	0.0040	0.0069
SiITMEM147_A	0.0009	0.0280	0.0187	0.0103	0.0023	0.0060	0.0084	0.0049	0.0263	0.0623	0.0571	0.0198	0.0000	0.0107
SiITMEM147_B	0.0013	0.0118	0.0209	0.0055	0.0019	0.0027	0.0085	0.0027	0.0131	0.0557	0.0325	0.0052	0.0000	0.0123
SiITMEM147_C	0.0000	0.0074	0.0182	0.0103	0.0041	0.0026	0.0075	0.0020	0.0056	0.0364	0.0434	0.0081	0.0062	0.0078
Group mol%	TAG 51:2	TAG 51:3	TAG 52:0	TAG 52:1	TAG 52:2	TAG 52:3	TAG 52:4	TAG 52:5	TAG 53:0	TAG 53:1	TAG 53:2	TAG 53:3	TAG 54:0	TAG 54:1
UNTREAT_A	0.0214	0.0017	0.0159	0.0375	0.0762	0.0784	0.0475	0.0202	0.0044	0.0174	0.0092	0.0052	0.0143	0.0058
UNTREAT_B	0.0164	0.0022	0.0068	0.0365	0.0645	0.0217	0.0003	0.0000	0.0000	0.0007	0.0057	0.0031	0.0032	0.0062
UNTREAT_C	0.0100	0.0000	0.0090	0.0276	0.0421	0.0110	0.0016	0.0000	0.0005	0.0003	0.0027	0.0012	0.0048	0.0040
NEG_A	0.0081	0.0000	0.0056	0.0221	0.0371	0.0199	0.0004	0.0000	0.0000	0.0001	0.0038	0.0036	0.0016	0.0031
NEG_B	0.0088	0.0011	0.0067	0.0185	0.0216	0.0119	0.0047	0.0013	0.0008	0.0015	0.0041	0.0035	0.0047	0.0036
NEG_C	0.0107	0.0002	0.0090	0.0242	0.0195	0.0097	0.0004	0.0000	0.0000	0.0000	0.0054	0.0013	0.0049	0.0040
SiITMEM147_A	0.0113	0.0013	0.0155	0.0451	0.0918	0.0562	0.0320	0.0235	0.0010	0.0026	0.0100	0.0092	0.0062	0.0112
SiITMEM147_B	0.0104	0.0002	0.0091	0.0403	0.0516	0.0222	0.0052	0.0021	0.0010	0.0004	0.0082	0.0065	0.0016	0.0124
SiITMEM147_C	0.0122	0.0006	0.0015	0.0241	0.0587	0.0308	0.0051	0.0004	0.0000	0.0008	0.0076	0.0096	0.0019	0.0032

Group mol%	TAG 54:2	TAG 54:3	TAG 54:4	TAG 54:5	TAG 54:6	TAG 55:1	TAG 55:2	TAG 55:3	TAG 56:0	TAG 56:1	TAG 56:2	TAG 56:3	TAG 56:4	TAG 56:5
UNTREAT_A	0.0047	0.0000	0.0325	0.0773	0.0264	0.0092	0.0010	0.0011	0.0098	0.0172	0.0034	0.0071	0.0024	0.0048
UNTREAT_B	0.0052	0.0000	0.0000	0.0000	0.0000	0.0007	0.0000	0.0003	0.0009	0.0119	0.0030	0.0060	0.0011	0.0022
UNTREAT_C	0.0119	0.0000	0.0004	0.0000	0.0003	0.0006	0.0002	0.0008	0.0020	0.0077	0.0025	0.0044	0.0009	0.0019
NEG_A	0.0063	0.0000	0.0000	0.0000	0.0000	0.0053	0.0008	0.0009	0.0001	0.0054	0.0017	0.0039	0.0021	0.0038
NEG_B	0.0013	0.0000	0.0000	0.0005	0.0019	0.0143	0.0000	0.0009	0.0030	0.0082	0.0015	0.0043	0.0031	0.0034
NEG_C	0.0000	0.0000	0.0000	0.0000	0.0000	0.0074	0.0000	0.0006	0.0020	0.0026	0.0021	0.0024	0.0014	0.0043
SilTMEM147_A	0.0178	0.0000	0.0190	0.0163	0.0088	0.0232	0.0035	0.0042	0.0001	0.0000	0.0021	0.0137	0.0074	0.0135
SilTMEM147_B	0.0065	0.0000	0.0000	0.0033	0.0000	0.0144	0.0000	0.0017	0.0007	0.0000	0.0021	0.0062	0.0037	0.0115
SilTMEM147_C	0.0023	0.0000	0.0000	0.0037	0.0000	0.0446	0.0000	0.0029	0.0000	0.0000	0.0024	0.0049	0.0084	0.0237
Group mol%	TAG 56:6	TAG 56:7	TAG 58:1	TAG 58:2	TAG 58:3	TAG 58:4	TAG 58:5	TAG 58:6	TAG 58:7	TAG 58:8	TAG 58:9	TAG 59:3	TAG 59:4	TAG 60:0
UNTREAT_A	0.0000	0.0089	0.0055	0.0057	0.0016	0.0007	0.0000	0.0001	0.0174	0.0046	0.0000	0.0004	0.0014	0.0037
UNTREAT_B	0.0000	0.0028	0.0000	0.0015	0.0015	0.0000	0.0000	0.0004	0.0024	0.0000	0.0000	0.0000	0.0006	0.0016
UNTREAT_C	0.0000	0.0020	0.0013	0.0031	0.0010	0.0000	0.0000	0.0010	0.0063	0.0006	0.0008	0.0001	0.0006	0.0014
NEG_A	0.0005	0.0050	0.0002	0.0016	0.0006	0.0000	0.0000	0.0002	0.0023	0.0029	0.0010	0.0000	0.0006	0.0015
NEG_B	0.0000	0.0054	0.0011	0.0023	0.0007	0.0000	0.0000	0.0010	0.0065	0.0087	0.0017	0.0000	0.0012	0.0014
NEG_C	0.0000	0.0047	0.0007	0.0020	0.0000	0.0001	0.0000	0.0009	0.0040	0.0000	0.0010	0.0000	0.0007	0.0000
SilTMEM147_A	0.0098	0.0196	0.0000	0.0004	0.0017	0.0000	0.0000	0.0015	0.0083	0.0002	0.0015	0.0000	0.0000	0.0010
SilTMEM147_B	0.0090	0.0114	0.0000	0.0015	0.0016	0.0000	0.0000	0.0006	0.0043	0.0000	0.0007	0.0000	0.0004	0.0016
SilTMEM147_C	0.0093	0.0209	0.0000	0.0015	0.0015	0.0000	0.0000	0.0017	0.0073	0.0036	0.0033	0.0000	0.0004	0.0006
Group mol%	TAG 60:1	TAG 60:2	TAG 60:3	TAG 60:4	TAG 60:5	TAG 60:7								
UNTREAT_A	0.0019	0.0038	0.0000	0.0024	0.0036	0.0111								
UNTREAT_B	0.0011	0.0011	0.0002	0.0006	0.0000	0.0018								
UNTREAT_C	0.0012	0.0016	0.0000	0.0003	0.0018	0.0041								
NEG_A	0.0008	0.0007	0.0000	0.0003	0.0011	0.0014								
NEG_B	0.0012	0.0025	0.0000	0.0012	0.0034	0.0062								
NEG_C	0.0008	0.0011	0.0000	0.0004	0.0014	0.0030								
SilTMEM147_A	0.0000	0.0000	0.0000	0.0000	0.0000	0.0001								
SilTMEM147_B	0.0006	0.0007	0.0000	0.0000	0.0000	0.0007								
SilTMEM147_C	0.0000	0.0008	0.0000	0.0010	0.0002	0.0006								

Table 6.2: Annotated curated list of reported TMEM147 associations and interactions.

Gene Symbol[a] [String-db ID][b]	Gene Name	Manual annotation combining multiple sources	References outside String-db
ABHD16A	abhydrolase domain containing 16A, phospholipase	- This alpha/beta-sheet hydrolase domain-containing protein by introns sequence similarity mediates the hydrolysis of phosphatidylserine to generate lysophosphatidylserine (LPS). In bibliography this protein has showed monoacylglycerol lipase activity, with preference for 1-(9Z,12Z-octadecadienoyl)-glycerol (1-LG) and 2-glyceryl-15-deoxy-Delta(12,14)-prostaglandin J2 (15d-PGJ2-G), but no activity towards diacylglycerol, triacylglycerol or lysophosphatidylserine lipase (PMID: 25290914).	PMID: 25290914
ABI3	ABI family member 3	- By introns sequence similarity the protein inhibits tumor metastasis while *in vitro* experiments showed reduced cell motility (PMID: 11956071).	PMID: 11956071
AVPR2	arginine vasopressin receptor 2	- Belongs to the G-protein coupled receptor 1 family. Vasopressin/oxytocin receptor subfamily. The activity of this receptor is mediated by G proteins which activate adenylate cyclase. Involved in renal water reabsorption (PMID: 19440390). RNAi-mediated knockdown of TMEM147 augments vasopressin-2-receptor-mediated carbachol stimulation of cell proliferation, associated with an increase in AVPR2 cell surface density, indicating TMEM147 as a potent negative regulator of AVPR2 function, most likely by ER-localized interaction of AVPR2 and TMEM147 (PMID: 21056967).	PMID: 21056967
BCAP31	B cell receptor associated protein 31	- Bibliography states it is an abundant Endoplasmic Reticulum protein with chaperone function. It also has a role in the export of secreted proteins along with recognition of abnormally folded proteins and targeting them to the ER associated-degradation (ERAD)pathway (PMID: 9396746, PMID: 18287538). - Under ER stress conditions delocalizes from the ER-mitochondria contact sites and binds to BCL2. The same paper states that it stimulates the translocation of NDUFS4 and NDUFB11 from the cytosol to the mitochondria via interaction with TOMM40 (PMID: 31206022).Another publication involves the protein in CASP8-mediated apoptosis (PMID: 10958671). By introns sequence similarity it is attributed the role of a cargo receptor and the export of transmembrane proteins.	PMID: 9396746, PMID: 18287538 PMID: 31206022, PMID: 10958671

BRF2	BRF2 RNA polymerase III transcription initiation factor subunit	- This is a general activator of RNA polymerase III transcription, exclusively required in transcription of genes with promoter elements upstream of the initiation sites (PMID: 11040218, PMID: 11121026, PMID: 11564744, PMID: 26638071). - Under oxidative stress conditions down-regulates the expression of target genes while its overexpression under these conditions protects cells against apoptosis. In the absence of these oxidative stress conditions functions as an activator regulating gene expression (PMID: 26638071).	PMID: 11040218, PMID: 11121026, PMID: 11564744, PMID: 26638071
CAPNS1	calpain small subunit 1	- Regulatory subunit of the calcium-regulated non-lysosomal thiol-protease which catalyzes limited proteolysis of substrates involved in cytoskeletal remodeling and signal transduction (UniProt).	UniProt
CASP4	caspase 4	- Inflammatory caspase that acts as an essential effector of NLRP3 inflammasome-dependent CASP1 activation and IL1B and IL18 secretion in response to non-canonical activators, such as UVB radiation, cholera enterotoxin subunit B and cytosolic LPS (PMID:23516580, PMID:24879791, PMID:25119034, PMID:22246630, PMID:26174085, PMID:26173988, PMID:26508369, PMID:25964352). - Thiol protease that cleaves a tetrapeptide after an Asp residue at position P1 (PMID:7797510, PMID:23516580). - Independently of NLRP3 inflammasome and CASP1, promotes pyroptosis, through GSDMD cleavage and activation, followed by IL1A, IL18 and HMGB1 release in response to non-canonical inflammasome activators (PMID:26375003, PMID:32109412). - Plays a crucial role in the restriction of Salmonella typhimurium replication in colonic epithelial cells during infection: in later stages of the infection, LPS from cytosolic Salmonella triggers CASP4 activation, which catalyzes cleavage of GSDMD, resulting in pyroptosis of infected cells and their extrusion into the gut lumen, as well as in IL18 secretion (PMID:25121752, PMID:26375003, PMID:25964352, PMID:32109412). - Cleavage of GSDMD is not strictly dependent on the consensus cleavage site but depends on an exosite interface on CASP4 that recognizes and binds the Gasdermin-D, C-terminal (GSDMD-CT) part (PMID:32109412). - Pyroptosis limits bacterial replication, while cytokine secretion promotes the recruitment and activation of immune cells and triggers mucosal inflammation (PMID:25121752, PMID:26375003, PMID:25964352). - Involved in LPS-induced IL6 secretion; this activity may not require caspase enzymatic activity (PMID:26508369). - Involved in cell death induced by endoplasmic reticulum stress and by treatment with cytotoxic APP peptides found Alzheimer's patient brains (PMID:15123740, PMID:22246630, PMID:23661706). - Activated by direct binding to LPS without the need of an upstream sensor (PMID:25119034). - Does not directly process IL1B (PMID:7743998, PMID:7797510, PMID:7797592). - During non-canonical inflammasome activation, cuts CGAS and may play a role in the regulation of antiviral innate immune activation (PMID:28314590).	PMID: 23516580, PMID: 24879791, PMID: 25119034, PMID: 22246630, PMID: 26174085, PMID: 26173988, PMID: 26508369, PMID: 25964352' PMID: 7797510, PMID: 26375003, PMID: 32109412, PMID: 25121752, PMID: 15123740, PMID: 23661706, PMID: 7743998, PMID: 7797592, PMID: 28314590

CCDC47	coiled-coil domain containing 47	- Auxiliary protein of Sec61 ER translocon complex along with TMCO1, Nicalin-TMEM147-NOMO complex and core Sec61A1 channel involved in multi-pass membrane protein transport into the ER membrane and biogenesis (PMID:32820719). - Regulator of Calcium ion homeostasis in ER (PMID:30401460). - Involved in ER-associated degradation (ERAD) pathway (PMID:25009997). - Component of the PAT complex, an endoplasmic reticulum (ER)-resident membrane multiprotein complex that facilitates multi-pass membrane proteins insertion into membranes. The PAT complex acts as an intramembrane chaperone by directly interacting with nascent transmembrane domains (TMDs), releasing its substrates upon correct folding, and is needed for optimal biogenesis of multi-pass membrane proteins. WDR83OS/Asterix is the substrate-interacting subunit of the PAT complex, whereas CCDC47 is required to maintain the stability of WDR83OS/Asterix. The PAT complex favors the binding to TMDs with exposed hydrophilic amino acids within the lipid bilayer and provides a membrane-embedded partially hydrophilic environment in which the first transmembrane domain binds (PMID:32814900).	PMID: 32820719, PMID: 30401460, PMID: 25009997, PMID: 32814900
CD40	CD40 molecule	- This tumor necrosis factor acts as a receptor for TNFSF5/CD40LG (PMID:31331973), while by intron sequence similarity transduces TRAF6- and MAP3K8-mediated signals that activate ERK in macrophages and B cells, leading to induction of immunoglobulin secretion.	PMID: 31331973
CD79A	CD79a molecule	- Required in cooperation with CD79B for initiation of the signal transduction cascade activated by binding of antigen to the B-cell antigen receptor complex (BCR) which leads to internalization of the complex, trafficking to late endosomes and antigen presentation. Also required for BCR surface expression and for efficient differentiation of pro- and pre-B-cells. Stimulates SYK autophosphorylation and activation. Binds to BLNK, bringing BLNK into proximity with SYK and allowing SYK to phosphorylate BLNK. Also interacts with and increases activity of some Src-family tyrosine kinases. Represses BCR signaling during development of immature B-cells (PMID: 8617796, PMID: 9057631)	PMID: 8617796, PMID: 9057631
CGN	cingulin	- Probably plays a role in the formation and regulation of the tight junction (TJ) paracellular permeability barrier (UniProt).	UniProt
CHRM3	cholinergic receptor muscarinic 3	- The muscarinic acetylcholine receptor 3 (M3R) mediates various cellular responses, including inhibition of adenylate cyclase, breakdown of phosphoinositides and modulation of potassium channels through the action of G proteins. - TMEM147 represents a potent negative regulator of M3R function by impairing receptor's trafficking to the cell surface membrane retaining it to the ER (PMID: 21056967).	PMID: 21056967

CLDN7	claudin 7	- By introns sequence similarity plays a major role in tight junction-specific obliteration of the intercellular space.	
CLN8	CLN8 transmembrane ER and ERGIC protein	- ER resident transmembrane protein involved in neuronal ceroid lipofuscinosis (neurodegenerative disease) (PMID: 23142642). - TMEM147 was identified as an interactor of CLN8 in a membrane based SU-Y2H screening (PMID: 23142642). - Could play a role in cell proliferation during neuronal differentiation and in protection against cell death (PMID: 19431184).	PMID: 23142642, PMID: 19431184
CLRN1	clarin 1	- May have a role in the excitatory ribbon synapse junctions between hair cells and cochlear ganglion cells and presumably also in analogous synapses within the retina (PMID: 12080385).	PMID: 12080385
COX6B1	cytochrome c oxidase subunit 6B1	- By introns sequence similarity functions as a component of the cytochrome c oxidase, the last enzyme in the mitochondrial electron transport chain which drives oxidative phosphorylation.	
CREB3L1	cAMP responsive element binding protein 3 like 1	- This protein functions as a transcription factor involved in unfolded protein response (UPR) binding the DNA consensus sequence 5'-GTGXGCXGC-3' (PMID:21767813). - Furthermore it is required for TGFB1 to activate genes involved in the assembly of collagen extracellular matrix (PMID:25310401)	PMID: 21767813, PMID: 25310401
CXCR2	C-X-C motif chemokine receptor 2	- UniProt states this chemokine is a G-protein coupled receptor which binds with high affinity to interleukin-8 in order to activate neutrophils including a phosphatidylinositol-calcium second messenger system. Also binds with high affinity to CXCL3, GRO/MGSA and NAP-2.	UniProt
DHCR7	7-dehydrocholesterol reduct-ase	- Sterol reductase catalyzing the C7-C8 double bond of two intermediates in late, post-squalene and smooth ER-localized steps of cholesterol biosynthesis pathway (PMID: 32694168).	PMID: 32694168
DPM3	dolichyl-phosphate mannosyltransferase subunit 3, regulatory	- This transferase functions as a stabilizer subunit of the dolichol-phosphate mannose (DPM) synthase complex; tethers catalytic subunit DPM1 to the ER (PMID: 10835346).	PMID: 10835346

EBP	EBP cholestenol delta-isomerase	- This isomerase catalyzes the conversion of Delta8-sterols to their corresponding Delta7-isomers (PMID: 8798407, PMID: 9894009, PMID: 12760743).	PMID: 8798407, PMID: 9894009, PMID: 12760743
EFNA4	ephrin A4	- UniProt states ephrin A4 is a cell surface ligand anchored to the membrane by a glycosylphosphatidylinositol group. Upon binding to its tyrosine kinase receptor have been implicated in mediating developmental events such as migration, repulsion and adhesion during neuronal, vascular and epithelial development. Binding to receptors residing on adjacent cells lead to contact-dependent bidirectional signaling to neighboring cells. Also, might play a role in the interaction between activated B-lymphocytes and dendritic cells in tonsils.	UniProt
EIF3K	eukaryotic translation initiation factor 3 subunit K	- It is a component of the eukaryotic translation initiation factor 3 (eIF-3) complex, which is required for several steps in the initiation of protein synthesis (PMID:17581632, PMID:25849773, PMID:27462815).	PMID: 17581632, PMID: 25849773, PMID: 27462815
ENPP4	ectonucleotide pyrophosphatase/ phosphodiesterase 4	- A phosphatase that hydrolyzes extracellular Ap3A into AMP and ADP, and Ap4A into AMP and ATP. Acts as a procoagulant, mediating platelet aggregation at the site of nascent thrombus via release of ADP from Ap3A and activation of ADP receptors (PMID: 22995898, PMID: 24338010).	PMID: 22995898, PMID: 24338010
F11R	F11 receptor	- Seems to play a role in epithelial tight junction formation. Appears early in primordial forms of cell junctions and recruits PARD3 (PMID:11489913). - Ligand for integrin alpha-L/beta-2 involved in memory T-cell and neutrophil transmigration (PMID:11812992). - Involved in platelet activation (PMID:10753840).	PMID: 11489913, PMID: 11812992, PMID: 10753840
FASN	fatty acid synthase	- Catalyzes the *de novo* biosynthesis of long-chain saturated fatty acids starting from acetyl-CoA and malonyl-CoA in the presence of NADPH. It contains 7 catalytic activities and a site for the binding of the prosthetic group 4'-phosphopantetheine of the acyl carrier protein ([ACP]) domain (PMID: 7567999, PMID: 8962082, PMID: 9356448, PMID: 16215233, PMID: 16969344, PMID: 26851298).	PMID: 7567999, PMID: 8962082, PMID: 9356448, PMID: 16215233, PMID: 16969344, PMID: 26851298
FFAR2	free fatty acid receptor 2	- This formerly known G protein-coupled receptor 43, is activated by a major product of dietary fiber digestion, the short chain fatty acids (SCFAs), and plays a role in the regulation of whole-body energy homeostasis and in intestinal immunity (PMID:12496283, PMID:12711604, PMID:23589301).	PMID: 12496283, PMID: 12711604, PMID: 23589301

FOXF2	forkhead box F2	- This protein is a probable transcription activator for a number of lung-specific genes (PMID:8626802). Furthermore, it mediates up-regulation of the E3 ligase IRF2BPL and drives ubiquitination and degradation of CTNNB1 (PMID:29374064).	PMID: 8626802, PMID: 29374064
GJA8	gap junction protein alpha 8	- Structural component of the eye lens gap junctions, the connexons which are dodecameric transmembrane channels that connect the cytoplasm of adjoining cells. Via its central pores small molecules and ions diffuse from one cell to a neighboring one (PMID:18006672, PMID:19756179).	PMID: 18006672, PMID: 19756179
GLP1R	glucagon like peptide 1 receptor	- Upon ligand binding on this G-protein coupled receptor a signal cascade is activated leading to the activation of adenylyl cyclase and increased intracellular cAMP levels that regulate insulin secretion (PMID:8405712, PMID:8216285, PMID:7517895, PMID:19861722, PMID:26308095, PMID:27196125, PMID:28514449). TMEM147 suppresses cAMP production levels mediated by GLP1R activation, in a ligand-independent manner (PMID: 23864651).	PMID: 8405712, PMID: 8216285, PMID: 7517895, PMID: 19861722, PMID: 26308095, PMID: 27196125, PMID: 28514449, PMID: 23864651
GOLM1	golgi membrane protein 1	- Unknown function. Cellular response protein to viral infection; Belongs to the GOLM1/CASC4 family (UniProt).	UniProt
GPR101	G protein-coupled receptor 101	- Orphan receptor	Orphan receptor
GPR37L1	G protein-coupled receptor 37 like 1	- This protein belongs to the G-protein coupled receptor family (PMID:27072655) and has been shown to bind the neuroprotective and glioprotective factor prosaposin (PSAP), leading to endocytosis followed by an ERK phosphorylation cascade (PMID:23690594).However, other studies have shown that prosaposin does not increase its activity (PMID:27072655, PMID:28688853). - By introns sequence similarity participates in the regulation of postnatal cerebellar development modulating the Shh pathway, regulates baseline blood pressure in females and protects against cardiovascular stress in males. By similarity it also mediates inhibition of astrocyte glutamate transporters and reduction in neuronal N-methyl-D-aspartate receptor activity.	PMID: 27072655, PMID: 23690594, PMID: 27072655, PMID: 28688853

GPR42	G protein-coupled receptor 42	- Probable G protein-coupled receptor that may be activated by a major product of dietary fiber digestion, the short chain fatty acids (SCFAs), and that may play a role in the regulation of whole-body energy homeostasis and/or in intestinal immunity (PMID: 19630535).	PMID: 19630535
GPR61	G protein-coupled receptor 61	- This orphan G-protein coupled receptor, constitutively activates the G(s)-alpha/cAMP signaling pathway. It also shows a reciprocal regulatory interaction with the melatonin receptor MTNR1B most likely through receptor heteromerization (PMID:28827538). - By sequence similarity may be involved in the regulation of food intake and body weight.	PMID: 28827538
HTR2C	5-hydroxytryptamine receptor 2C	- G-protein coupled receptor for 5-hydroxytryptamine (serotonin). Also functions as a receptor for various drugs and psychoactive substances, including ergot alkaloid derivatives, 1-2,5,-dimethoxy-4-iodophenyl-2-aminopropane (DOI) and lysergic acid diethylamide (LSD). Ligand binding causes a conformation change that triggers signaling via guanine nucleotide-binding proteins (G proteins) and modulates the activity of down-stream effectors. Beta-arrestin family members inhibit signaling via G proteins and mediate activation of alternative signaling pathways. Signaling activates a phosphatidylinositol-calcium second messenger system that modulates the activity of phosphatidylinositol 3-kinase and down-stream signaling cascades and promotes the release of Ca2+ ions from intracellular stores. Regulates neuronal activity via the activation of short transient receptor potential calcium channels in the brain, and thereby modulates the activation of pro-opiomelacortin neurons and the release of CRH that then regulates the release of corticosterone. Plays a role in the regulation of appetite and eating behavior, responses to anxiogenic stimuli and stress. Plays a role in insulin sensitivity and glucose homeostasis (PMID: 7895773, PMID: 12970106, PMID: 18703043, PMID: 19057895).	PMID: 7895773, PMID: 12970106, PMID: 18703043, PMID: 19057895
IER3IP1	immediate early response 3 interacting protein 1	- A study has shown that it is a regulator of the endoplasmic reticulum secretion that acts as a key determinant of brain size. it is required for secretion of extracellular matrix proteins and it is required for correct brain development by depositing sufficient extracellular matrix proteins for tissue integrity and the proliferation of neural progenitors (PMID:33122427). BY sequence similarity acts as a regulator of the unfolded protein response (UPR).	PMID: 33122427
IL3RA	interleukin 3 receptor subunit alpha	- Receptor of interleukin-3 (UniProt)	UniProt

KASH5 [CCDC155]	KASH domain containing 5	- By introns sequence similarity KASH5 functions as a component of the LINC (Linker of Nucleoskeleton and Cytoskeleton) complex, involved in the connection between the nuclear lamina and the cytoskeleton playing an important role in the transmission of mechanical forces across the nuclear envelope and in nuclear movement and positioning.	
LBR	lamin B receptor	- N-terminal domain (1-208) organizes the nuclear lamina and the heterochromatin by anchoring the lamina and the heterochromatin to the inner nuclear membrane. - C-terminal domain (208-615) contains sterol reductase activity catalyzing the reduction of the C14-unsaturated bond of lanosterol, as part of the metabolic pathway leading to cholesterol biosynthesis (PMID:9630650, PMID:12618959, PMID:16784888, PMID:21327084, PMID:27336722). - Functional link of TMEM147 with effect on nuclear shape, LBR has NE/ER distribution and affects cholesterol homeostasis (PMID: 32694168). - By sequence similarity mediates the activation of NADPH oxidases, perhaps by maintaining critical levels of cholesterol required for membrane lipid raft formation during neutrophil differentiation.	PMID: 9630650, PMID: 12618959, PMID: 16784888, PMID: 21327084, PMID: 27336722, PMID: 32694168
LDLRAD1	low density lipoprotein receptor class A domain containing 1		
LEF1	lymphoid enhancer binding factor 1	- Transcription factor that binds DNA in a sequence-specific manner (PMID:2010090).	PMID: 2010090
LEUTX	leucine twenty homeobox	- While its isoform 2 showed no transcriptional activity (PMID: 27578796), isoform 1 is a paired-like homeobox transcription factor, binding to a 36 bp DNA elements containing a 5'-TAATCC-3' sequence motif, referred to as EEA motif (EGA-enriched Alu-motif), present in the promoters of target genes, acting as a regulator of embryo genome activation in embryogenesis (PMID:27578796, PMID:30479355).	PMID: 27578796, PMID: 30479355
LHFPL2	LHFPL tetraspan subfamily member 2	- By introns sequence similarity plays a role in male and female fertility specifically involved in distal reproductive tract development.	

LRRFIP2	LRR binding FLII interacting protein 2	- May function as activator of the canonical Wnt signaling pathway, in association with DVL3, upstream of CTNNB1/beta-catenin. Positively regulates Toll-like receptor (TLR) signaling in response to agonist probably by competing with the negative FLII regulator for MYD88-binding (PMID: 15677333, PMID: 19265123).	PMID: 15677333, PMID: 19265123
MIF	macrophage migration inhibitory factor	- It is a pro-inflammatory cytokine, involved in the innate immune response to bacterial pathogens. It is a mediator in regulating the function of macrophages in host defense (PMID: 15908412, PMID: 17443469, PMID: 23776208).	PMID: 15908412, PMID: 17443469, PMID: 23776208
MPRIP	myosin phosphatase Rho interacting protein	- It is required for regulating actin cytoskeleton by RhoA and ROCK1 and targets myosin phosphatase to the same region. Depletion leads to an increased number of stress fibers in smooth muscle cells while its overexpression or its F-actin-binding region leads to disassembly of stress fibers in neuronal cells (PMID: 15545284, PMID: 16257966).	PMID: 15545284, PMID: 16257966
MTCH2	mitochondrial carrier 2	- Induces mitochondrial depolarization (UniProt).	UniProt
MTIF3	mitochondrial translational initiation factor 3	- This mitochondrial IF-3 binds to the 28S ribosomal subunit and shifts the equilibrium between 55S ribosomes and their 39S and 28S subunits in favor of the free subunits, thus enhancing the availability of 28S subunits on which protein synthesis initiation begins (PMID: 12095986).	PMID: 12095986
MUC1	mucin 1, cell surface associated	- O-glycosylated protein that play an essential role in forming protective mucous barriers on epithelial surfaces. Also play a role in intracellular signaling. It is proteolytically cleaved into alpha and beta subunits that form a heterodimeric complex. - Alpha subunit at the N-terminus has cell adhesive properties acting both as an adhesion and anti-adhesion protein, providing a protective layer on epithelial cells against bacterial and enzyme attack. The C-terminal beta subunit is involved in cell signaling through phosphorylation and protein-protein interactions. In activated T-cells, influences directly or indirectly the Ras/MAPK pathway. Promotes tumor progression. Regulates TP53-mediated transcription and determines cell fate in the genotoxic stress response. Binds, together with KLF4, the PE21 promoter element of TP53 and represses TP53 activity (UniProt).	UniProt
NCLN	nicalin	- Nicastrin-like protein, part of the Nicalin-TMEM147-NOMO complex, accessory proteins along with TMOC1, CCDC47 and core Sec61A1 channel comprising Sec61 ER translocon complex (PMID:32820719). - May antagonize Nodal signaling and subsequent organization of axial structures during mesodermal patterning (PMID: 17261586).	PMID: 32820719, PMID: 17261586

NFKB1	nuclear factor kappa B subunit 1	- Protein transcription factor regulating innate immunity - it is activated upon several cell stress responses such as inflammation, immunity, differentiation, cell growth, tumorigenesis and apoptosis via transcription of DNA and cytokine production. - homo or heterodimer protein complex - family of 5 proteins containing two conserved domains, RHD (Rel homology domain: DNA binding domain and dimerization domain) and Nuclear Localization signal (NLS) (PMID: 15485931). - TMEM147 positively regulates the NF-kB activity, acting as a scaffold of the higher protein complex including breakpoint cluster region, Casein kinase 2 and NF-kB-p65 (PMID: 31785076).	PMID: 15485931, PMID: 31785076
NHP2	NHP2 ribonucleoprotein	- Required for ribosome biogenesis and telomere maintenance. Part of the H/ACA small nucleolar ribonucleoprotein (H/ACA snoRNP) complex, which catalyzes pseudouridylation of rRNA. This involves the isomerization of uridine such that the ribose is subsequently attached to C5, instead of the normal N1. Each rRNA can contain up to 100 pseudouridine ('psi') residues, which may serve to stabilize the conformation of rRNAs. May also be required for correct processing or intranuclear trafficking of TERC, the RNA component of the telomerase reverse transcriptase (TERT) holoenzyme (PMID: 15044956).	PMID: 15044956
NOMO	NODAL modulator	- There are 3 copies of the NOMO gene (NOMO1, 2, 3) extremely similar. Additionally, NOMO2 has 3 isoforms, products of alternative splicing. Both findings make the individual characterization difficult. - Part of the Nicalin-TMEM147-NOMO complex, accessory proteins along with TMOC1, CCDC47 and core Sec61A1 channel comprising Sec61 ER translocon complex. - May antagonize Nodal signaling and subsequent organization of axial structures during mesodermal patterning, via its interaction with NCLN	PMID: 32820719
PACC1 [TMEM206]	proton activated chloride channel 1	- Proton-activated chloride channel mediating chloride influx and subsequent cell swelling in response to extracellular acidic pH (acidosis-induced cell death) (PMID:31023925, PMID:31318332).	PMID: 31023925, PMID: 31318332
PDCD1LG2	programmed cell death 1 ligand 2	- By sequence similarity it is involved in the costimulatory signal, essential for T-cell proliferation and IFNG production in a PDCD1-independent manner. Interaction with PDCD1 inhibits T-cell proliferation by blocking cell cycle progression and cytokine production.	
PHPT1	phosphohistidine phosphatase 1	- Exhibits phosphohistidine phosphatase activity (PMID: 19836471, PMID: 25574816).	PMID: 19836471, PMID: 25574816

PLEKHG3	pleckstrin homology and RhoGEF domain containing G3		
POLE4	DNA polymerase epsilon 4, accessory subunit	- A study showed is an accessory component of the DNA polymerase epsilon complex (PMID:10801849). By introns sequence similarity participates in DNA repair and in chromosomal DNA replication.	PMID: 10801849
POLR2I	RNA polymerase II subunit I	- Experimental evidence and sequence similarity this is a DNA-dependent RNA polymerase catalyzes the transcription of DNA into RNA using the four ribonucleoside triphosphates as substrates. Component of RNA polymerase II which synthesizes mRNA precursors and many functional non-coding RNAs. Pol II is the central component of the basal RNA polymerase II transcription machinery. It is composed of mobile elements that move relative to each other. RPB9 is part of the upper jaw surrounding the central large cleft and thought to grab the incoming DNA template (PMID: 9852112).	PMID: 9852112
PPP1R9A	protein phosphatase 1 regulatory subunit 9A	- By sequence similarity binds along the sides of actin filaments (F-actin) and shows cross-linking activity. May be involved in neurite formation and inhibition of protein phosphatase 1-alpha activity.	
PSCA	prostate stem cell antigen	- May be involved in the regulation of cell proliferation having a cell-proliferation inhibition activity *in vitro* (PMID: 18488030). Furthermore, may act as a modulator of nicotinic acetylcholine receptors (nAChRs) activity. *In vitro* inhibits nicotine-induced signaling probably implicating alpha-3:beta-2- or alpha-7-containing nAChRs (PMID: 25680266).	PMID: 18488030, PMID: 25680266
PSENEN	presenilin enhancer, gamma-secretase subunit	- Belongs to the PEN-2 family and it is essential subunit of the gamma-secretase complex, an endoprotease complex that catalyzes the intramembrane cleavage of integral membrane proteins such as Notch receptors and APP (amyloid-beta precursor protein) (PMID:12522139, PMID:12763021, PMID:12740439, PMID:12679784, PMID:24941111, PMID:30598546, PMID:30630874). - The gamma-secretase complex plays a role in Notch and Wnt signaling cascades and regulation of downstream processes via its role in processing key regulatory proteins, and by regulating cytosolic CTNNB1 levels (Probable). PSENEN modulates both endoproteolysis of presenilin and gamma-secretase activity (PMID:12522139, PMID:12763021, PMID:12740439, PMID:12679784, PMID:24941111).	PMID: 12522139, PMID: 12763021, PMID: 12740439, PMID: 12679784, PMID: 24941111, PMID: 30598546, PMID: 30630874

PVR	PVR cell adhesion molecule	- Mediates NK cell adhesion and triggers NK cell effector functions. Binds two different NK cell receptors: CD96 and CD226. These interactions accumulate at the cell-cell contact site, leading to the formation of a mature immunological synapse between NK cell and target cell. This may trigger adhesion and secretion of lytic granules and IFN-gamma and activate cytotoxicity of activated NK cells. May also promote NK cell-target cell modular exchange, and PVR transfer to the NK cell (PMID: 15471548, PMID: 15607800).	PMID: 15471548, PMID: 15607800
RABAC1	Rab acceptor 1	- By sequence similarity it is a general Rab protein regulator required for vesicle formation from the Golgi complex. May control vesicle docking and fusion by mediating the action of Rab GTPases to the SNARE complexes. In addition, it inhibits the removal of Rab GTPases from the membrane by GDI.	
RBM42	RNA binding motif protein 42	- By introns sequence similarity binds (via the RRM domain) to the 3'-untranslated region (UTR) of CDKN1A mRNA.	
RMDN3	regulator of microtubule dynamics 3	- Involved in cellular calcium homeostasis regulation. May participate in differentiation and apoptosis of keratinocytes. Overexpression induces apoptosis (PMID: 16820967, PMID: 22131369).	PMID: 16820967, PMID: 22131369
RNF185	ring finger protein 185	- E3 ubiquitin-protein ligase that regulates selective mitochondrial autophagy by mediating 'Lys-63'-linked polyubiquitination of BNIP1 (PMID:21931693).Acts in the endoplasmic reticulum (ER)-associated degradation (ERAD) pathway, which targets misfolded proteins that accumulate in the endoplasmic reticulum (ER) for ubiquitination and subsequent proteasome-mediated degradation, protecting cells from ER stress-induced apoptosis (PMID:27485036). Responsible for the cotranslational ubiquitination and degradation of CFTR in the ERAD pathway preferentially associated with the E2 enzymes UBE2J1 and UBE2J2 (PMID:24019521).	PMID: 21931693, PMID: 27485036, PMID: 24019521
RTKN	rhotekin	- Studies showed it mediates Rho signaling to activate NF-kappa-B and may confer increased resistance to apoptosis to cells in gastric tumorigenesis Moreover, may play a novel role in the organization of septin structures (PMID: 10940294, PMID: 15480428, PMID: 16007136).	PMID: 10940294, PMID: 15480428, PMID: 16007136

RUVBL2	RuvB like AAA ATPase 2	- Possesses single-stranded DNA-stimulated ATPase and ATP-dependent DNA helicase (5' to 3') activity (PMID:10428817, PMID:17157868). - It is a component of the NuA4 histone acetyltransferase complex which is involved in transcriptional activation of selected genes principally by acetylation of nucleosomal histones H4 and H2A. This complex may be required for the activation of transcriptional programs associated with oncogene and proto-oncogene mediated growth induction, tumor suppressor mediated growth arrest and replicative senescence, apoptosis, and DNA repair (PMID:14966270). - Component of a SWR1-like complex that specifically mediates the removal of histone H2A.Z/H2AZ1 from the nucleosome (PMID:24463511). - Proposed core component of the chromatin remodeling INO80 complex which exhibits DNA- and nucleosome-activated ATPase activity and catalyzes ATP-dependent nucleosome sliding (PMID:16230350, PMID:21303910). - Plays an essential role in oncogenic transformation by MYC and also modulates transcriptional activation by the LEF1/TCF1-CTNNB1 complex (PMID:10882073, PMID:16014379). - May also inhibit the transcriptional activity of ATF2 (PMID:11713276). - May play a role in regulating the composition of the U5 snRNP complex (PMID:28561026). - Involved in the endoplasmic reticulum (ER)-associated degradation (ERAD) pathway where it negatively regulates expression of ER stress response genes (PMID:25652260).	PMID: 10428817, PMID: 17157868, PMID: 14966270, PMID: 24463511, PMID: 16230350, PMID: 21303910, PMID: 10882073, PMID: 16014379, PMID: 11713276 PMID: 28561026, PMID: 25652260
SCAMP4	secretory carrier membrane protein 4	- By similarity probably it is involved in membrane protein trafficking.	
SEC61A1	SEC61 translocon subunit alpha 1	- Core component of Sec61 channel-forming translocon complex that mediates transport of signal peptide-containing precursor polypeptides across endoplasmic reticulum (ER) - Critical role in controlling cellular calcium ions homeostasis via passive efflux from the ER lumen to the cytosol (PMID: 32820719).	PMID: 32820719
SHISA3	shisa family member 3	- By introns sequence similarity plays an essential role in the maturation of presomitic mesoderm cells by individual attenuation of both FGF and WNT signaling.	
SLC10A1	solute carrier family 10 member 1	- It belongs to the bile acid:sodium symporter (BASS) family. The hepatic sodium/bile acid uptake system exhibits broad substrate specificity and transports various non-bile acid organic compounds as well. It is strictly dependent on the extracellular presence of sodium (PMID: 23150796).	PMID: 23150796

SLC12A7	solute carrier family 12 member 7	- Mediates electroneutral potassium-chloride cotransport when activated by cell swelling. Important for the survival of cochlear outer and inner hair cells and the maintenance of the organ of Corti (PMID: 10913127).	PMID: 10913127
SLC13A4	solute carrier family 13 member 4	- Sodium/sulfate cotransporter that mediates sulfate reabsorption in the high endothelial venules (HEV) (PMID: 10535998, PMID: 15607730).	PMID: 10535998, PMID: 15607730
SLC22A1	solute carrier family 22 member 1	- Translocates a broad array of organic cations with various structures and molecular weights including the model compounds MPP, TEA, NMN, ASP, the endogenous compounds choline, guanidine, histamine, epinephrine, adrenaline, noradrenaline and dopamine, and the drugs quinine, and metformin. The transport of organic cations is inhibited by a broad array of compounds like tetramethylammonium (TMA), cocaine, lidocaine, NMDA receptor antagonists, atropine, prazosin, cimetidine, TEA and NMN, guanidine, cimetidine, choline, procainamide, quinine, tetrabutylammonium, and tetrapentylammonium. - The translocation of cations follows an electrogenic and pH-independent manner across the plasma membrane in both directions. It is regulated by various intracellular signaling pathways including inhibition by protein kinase A activation, and endogenously activation by the calmodulin complex, the calmodulin-dependent kinase II and LCK tyrosine kinase (PMID: 9260930, PMID: 9187257, PMID: 11388889, PMID: 9655880, PMID: 11408531, PMID: 15389554, PMID: 16272756, PMID: 16581093).	PMID: 9260930, PMID: 9187257, PMID: 11388889, PMID: 9655880, PMID: 11408531, PMID: 15389554, PMID: 16272756, PMID: 16581093
SLC22A2	solute carrier family 22 member 2	- Mediates tubular uptake of organic compounds from circulation (PMID: 9260930, PMID: 12089365). This transporter is a major determinant of the anticancer activity of oxaliplatin and may contribute to antitumor specificity (PMID: 16951202).	PMID: 9260930, PMID: 12089365, PMID: 16951202
SLC41A1	solute carrier family 41 member 1	- Na+/Mg+ ion exchanger involved in pathophysiology of various disease conditions acting as a predominant Mg2+ efflux system at the plasma membrane (PMID:22031603).	PMID: 22031603
STOML2	stomatin like 2	- Mitochondrial protein that probably regulates the biogenesis and the activity of mitochondria evidently acting in the organization of functional microdomains in mitochondrial membranes. Therefore, may play a role into several biological processes including cell migration, cell proliferation, T-cell activation, cellular response to stress and calcium homeostasis through negative regulation of calcium efflux from mitochondria (PMID: 17121834, PMID: 19597348, PMID: 19944461, PMID: 21746876).	PMID: 17121834, PMID: 19597348, PMID: 19944461, PMID: 21746876

SUSD3	sushi domain containing 3	- May play a role in breast tumorigenesis by promoting estrogen-dependent cell proliferation, cell-cell interactions and migration (PMID: 24413080).	PMID: 24413080
SYNE4	spectrin repeat containing nuclear envelope family member 4	- By sequence similarity functions as a LINC complex component involved in connection between the nuclear lamina and the cytoskeleton. It also resembles as a kinesin cargo providing a functional binding site for kinesin-1 at the nuclear envelope. Hence may contribute to the establishment of secretory epithelial morphology by promoting kinesin-dependent apical migration of the centrosome and Golgi apparatus and basal localization of the nucleus	
TACR1	tachykinin receptor 1	- This is a receptor for the tachykinin neuropeptide substance P. It is probably associated with G proteins that activate a phosphatidylinositol-calcium second messenger system. The rank order of affinity of this receptor to tachykinins is: substance P > substance K > neuromedin-K (UniProt).	UniProt
TBCB	tubulin folding cofactor B	- It binds to alpha-tubulin folding intermediates after their interaction with cytosolic chaperonin in the pathway leading from newly synthesized tubulin to properly folded heterodimer (PMID:9265649). - By similarity it is probably involved in regulation of tubulin heterodimer dissociation, negatively regulating axonal growth.	PMID: 9265649
TEX29	testis expressed 29		
TMCO1	transmembrane and coiled-coil domains 1	- Auxiliary protein of Sec61 ER translocon complex along with CCDC47, Nicalin-TMEM147-NOMO complex and core Sec61A1 channel (PMID:32820719). - ER Calcium-load storage regulator (PMID:27212239).	PMID: 32820719 PMID: 27212239
TMEM14B	transmembrane protein 14B	- Primate-specific protein involved in cortical expansion and folding in the developing neocortex. May drive neural progenitor proliferation through nuclear translocation of IQGAP1, which in turn promotes G1/S cell cycle transitions (PMID: 29033352).	PMID: 29033352
TMEM237	transmembrane protein 237	- Component of the transition zone in primary cilia, required for ciliogenesis (PMID: 22152675).	PMID: 22152675
TMEM248	transmembrane protein 248		
TMEM252	transmembrane protein 252		

TMEM42	transmembrane protein 42		
TMEM52B	transmembrane protein 52B		
TPI1	triosephosphate isomerase 1	- Triosephosphate isomerase catalyzes the interconversion between dihydroxyacetone phosphate (DHAP) and D-glyceraldehyde-3-phosphate (G3P) in glycolysis and gluconeogenesis (PMID: 18562316). - By introns sequence similarity it is also responsible for the non-negligible production of methylglyoxal a reactive cytotoxic side-product that modifies and can alter proteins, DNA and lipids.	PMID: 18562316
TRAPPC3	trafficking protein particle complex subunit 3	- May play a role in vesicular transport from endoplasmic reticulum to Golgi (PMID: 9564032).	PMID: 9564032
TRPC6	transient receptor potential cation channel subfamily C member 6	- Widely expressed ion channel, mediating intracellular calcium concentration increase, leading to activation of signaling pathways (PMID:19936226, PMID:23291369). - TRPC6-GOF (gain-of-function) mutations lead to autosomal-dominant focal segmental glomerulosclerosis (PMID: 31266804). - TMEM147 was identified as an interactor of TRPC6 protein along with NCLN, NOMO1,NOMO2, NOMO3 in a CRISPR/Cas screening (PMID: 31266804).	PMID: 19936226, PMID: 23291369, PMID: 31266804
TSPAN12	tetraspanin 12	- Acts as a regulator of the MMP14/MT1-MMP membrane proteinase-dependent cleavage activity and the ADAM10 membrane proteinase-dependent cleavage activity of amyloid precursor protein (APP) (PMID: 19587294, PMID: 19211836). - By sequence similarity also functions as a regulator of norrin (NDP) cell surface receptor signal transduction in retinal vascularization.	PMID: 19587294, PMID: 19211836
YIPF6	Yip1 domain family member 6	- May be required for stable YIPF1 and YIPF2 protein expression (PMID: 28286305).	PMID: 28286305

---

[a] *Official gene symbol according to the HUGO Gene Nomenclature Committee (HGNC).*

[b] *The associated STRING ID used in STRING analysis, if different from the official gene symbol*

Table 6.3 GO Molecular Function terms

GO term ID	Term Description	Observed gene count	Back-ground gene count	Strength	False discovery rate	Matching proteins in your network (IDs)	Matching proteins in your network (labels)
GO:0015296	anion:cation symporter activity	4	20	1.6	0.0022	9606.ENSP00000264930,9606.ENSP00000297282,9606.ENSP00000355920,9606.ENSP00000355930	SLC12A7,SLC13A4,SLC22A2,SLC22A1
GO:0015373	anion:sodium symporter activity	3	14	1.63	0.0151	9606.ENSP00000297282,9606.ENSP00000355920,9606.ENSP00000355930	SLC13A4,SLC22A2,SLC22A1
GO:0015377	cation:chloride symporter activity	3	17	1.55	0.0166	9606.ENSP00000264930,9606.ENSP00000355920,9606.ENSP00000355930	SLC12A7,SLC22A2,SLC22A1
GO:0004888	transmembrane signaling receptor activity	16	1226	0.42	0.0236	9606.ENSP00000221972,9606.ENSP00000255380,9606.ENSP00000276198,9606.ENSP00000298110,9606.ENSP00000303522,9606.ENSP00000319635,9606.ENSP00000327890,9606.ENSP00000351805,9606.ENSP00000356251,9606.ENSP00000361359,9606.ENSP00000362353,9606.ENSP00000414378,9606.ENSP00000417052,9606.ENSP00000432456,9606.ENSP00000473159,9606.ENSP00000473212	CD79A,CHRM3,HTR2C,GPR101,TACR1,CXCR2,IL3RA,AVPR2,GPR37L1,CD40,GLP1R,EFNA4,EBP,GPR61,FFAR2,GPR42
GO:0005277	acetylcholine transmembrane transporter activity	2	3	2.12	0.0236	9606.ENSP00000355920,9606.ENSP00000355930	SLC22A2,SLC22A1
GO:0005330	dopamine:sodium symporter activity	2	5	1.9	0.0236	9606.ENSP00000355920,9606.ENSP00000355930	SLC22A2,SLC22A1
GO:0005334	norepinephrine:sodium symporter activity	2	3	2.12	0.0236	9606.ENSP00000355920,9606.ENSP00000355930	SLC22A2,SLC22A1
GO:0008513	secondary active organic cation transmembrane transporter activity	2	3	2.12	0.0236	9606.ENSP00000355920,9606.ENSP00000355930	SLC22A2,SLC22A1

GO:0008528	G protein-coupled peptide receptor activity	5	132	0.88	0.0236	9606.ENSP00000303522,9606.ENSP00000319635,9606.ENSP00000351805,9606.ENSP00000356251,9606.ENSP00000362353	TACR1,CXCR2,AVPR2,GPR37L1,GLP1R
GO:0015294	solute:cation symporter activity	5	110	0.96	0.0236	9606.ENSP00000216540,9606.ENSP00000264930,9606.ENSP00000297282,9606.ENSP00000355920,9606.ENSP00000355930	SLC10A1,SLC12A7,SLC13A4,SLC22A2,SLC22A1
GO:0015370	solute:sodium symporter activity	4	82	0.99	0.0236	9606.ENSP00000216540,9606.ENSP00000297282,9606.ENSP00000355920,9606.ENSP00000355930	SLC10A1,SLC13A4,SLC22A2,SLC22A1
GO:0015651	quaternary ammonium group transmembrane transporter activity	2	8	1.7	0.0236	9606.ENSP00000355920,9606.ENSP00000355930	SLC22A2,SLC22A1
GO:0016628	oxidoreductase activity, acting on the CH-CH group of donors, NAD or NADP as acceptor	3	26	1.36	0.0236	9606.ENSP00000304592,9606.ENSP00000339883,9606.ENSP00000347717	FASN,LBR,DHCR7
GO:0038023	signaling receptor activity	18	1429	0.4	0.0236	9606.ENSP00000221972,9606.ENSP00000255380,9606.ENSP00000265165,9606.ENSP00000276198,9606.ENSP00000298110,9606.ENSP00000303522,9606.ENSP00000319635,9606.ENSP00000327890,9606.ENSP00000351805,9606.ENSP00000356251,9606.ENSP00000361359,9606.ENSP00000362353,9606.ENSP00000402060,9606.ENSP00000414378,9606.ENSP00000417052,9606.ENSP00000432456,9606.ENSP00000473159,9606.ENSP00000473212	CD79A,CHRM3,LEF1,HTR2C,GPR101,TACR1,CXCR2,IL3RA,AVPR2,GPR37L1,CD40,GLP1R,PVR,EFNA4,EBP,GPR61,FFAR2,GPR42
GO:0015291	secondary active transmembrane transporter activity	6	235	0.71	0.0268	9606.ENSP00000216540,9606.ENSP00000264930,9606.ENSP00000297282,9606.ENSP00000355920,9606.ENSP00000355930,9606.ENSP00000356105	SLC10A1,SLC12A7,SLC13A4,SLC22A2,SLC22A1,SLC41A1
GO:0015081	sodium ion transmembrane transporter activity	5	164	0.78	0.0291	9606.ENSP00000216540,9606.ENSP00000297282,9606.ENSP00000355920,9606.ENSP00000355930,9606.ENSP00000356105	SLC10A1,SLC13A4,SLC22A2,SLC22A1,SLC41A1
GO:0016860	intramolecular oxidoreductase activity	3	47	1.11	0.0335	9606.ENSP00000215754,9606.ENSP00000229270,9606.ENSP00000417052	MIF,TPI1,EBP

GO:0008227	G protein-coupled amine receptor activity	3	48	1.1	0.034	9606.ENSP00000255380,9606.ENSP00000276198,9606.ENSP00000298110	CHRM3,HTR2C,GPR101
GO:0016863	intramolecular oxidoreductase activity, transposing C=C bonds	2	12	1.52	0.034	9606.ENSP00000215754,9606.ENSP00000417052	MIF,EBP
GO:0043022	ribosome binding	3	50	1.08	0.034	9606.ENSP00000243253,9606.ENSP00000248342,9606.ENSP00000370508	SEC61A1,EIF3K,MTIF3
GO:0046873	metal ion transmembrane transporter activity	8	458	0.54	0.034	9606.ENSP00000216540,9606.ENSP00000264930,9606.ENSP00000297282,9606.ENSP00000340913,9606.ENSP00000355920,9606.ENSP00000355930,9606.ENSP00000356105,9606.ENSP00000480514	SLC10A1,SLC12A7,SLC13A4,TRPC6,SLC22A2,SLC22A1,SLC41A1,TMCO1
GO:1901618	organic hydroxy compound transmembrane transporter activity	3	48	1.1	0.034	9606.ENSP00000216540,9606.ENSP00000355920,9606.ENSP00000355930	SLC10A1,SLC22A2,SLC22A1
GO:0004930	G protein-coupled receptor activity	11	824	0.43	0.0393	9606.ENSP00000255380,9606.ENSP00000276198,9606.ENSP00000298110,9606.ENSP00000303522,9606.ENSP00000319635,9606.ENSP00000351805,9606.ENSP00000356251,9606.ENSP00000362353,9606.ENSP00000432456,9606.ENSP00000473159,9606.ENSP00000473212	CHRM3,HTR2C,GPR101,TACR1,CXCR2,AVPR2,GPR37L1,GLP1R,GPR61,FFAR2,GPR42
GO:0022890	inorganic cation transmembrane transporter activity	9	598	0.48	0.0426	9606.ENSP00000216540,9606.ENSP00000246554,9606.ENSP00000264930,9606.ENSP00000297282,9606.ENSP00000340913,9606.ENSP00000355920,9606.ENSP00000355930,9606.ENSP00000356105,9606.ENSP00000480514	SLC10A1,COX6B1,SLC12A7,SLC13A4,TRPC6,SLC22A2,SLC22A1,SLC41A1,TMCO1
GO:0015077	monovalent inorganic cation transmembrane transporter activity	7	390	0.55	0.0451	9606.ENSP00000216540,9606.ENSP00000246554,9606.ENSP00000264930,9606.ENSP00000297282,9606.ENSP00000355920,9606.ENSP00000355930,9606.ENSP00000356105	SLC10A1,COX6B1,SLC12A7,SLC13A4,SLC22A2,SLC22A1,SLC41A1

Table 6.4 GO Cellular Component terms

GO term ID	Term description	Observed gene count	Background gene count	Strength	False discovery rate	Matching proteins in your network (IDs)	Matching proteins in your network (labels)
GO:0031224	intrinsic component of membrane	69	5316	0.41	2.48E-16	9606.ENSP00000216540,9606.ENSP00000221972,9606.ENSP00000222008,9606.ENSP00000222284,9606.ENSP00000222747,9606.ENSP00000225726,9606.ENSP00000243253,9606.ENSP00000246117,9606.ENSP00000255380,9606.ENSP00000256433,9606.ENSP00000260385,9606.ENSP00000264930,9606.ENSP00000276198,9606.ENSP00000283547,9606.ENSP00000287667,9606.ENSP00000297282,9606.ENSP00000298110,9606.ENSP00000301258,9606.ENSP00000303222,9606.ENSP00000303522,9606.ENSP00000306564,9606.ENSP00000316007,9606.ENSP00000316130,9606.ENSP00000318066,9606.ENSP00000319635,9606.ENSP00000320508,9606.ENSP00000326445,9606.ENSP00000327890,9606.ENSP00000328182,9606.ENSP00000329158,9606.ENSP00000339883,9606.ENSP00000340668,9606.ENSP00000340913,9606.ENSP00000347717,9606.ENSP00000351805,9606.ENSP00000353475,9606.ENSP00000355920,9606.ENSP00000355930,9606.ENSP00000356105,9606.ENSP00000356251,9606.ENSP00000357005,9606.ENSP00000357384,9606.ENSP00000358238,9606.ENSP00000360411,9606.ENSP00000361359,9606.ENSP00000362353,9606.ENSP00000364621,9606.ENSP00000366528,9606.ENSP00000369702,9606.ENSP00000371348,9606.ENSP00000373364,9606.ENSP00000379282,9606.ENSP00000380855,9606.ENSP00000386264,9606.ENSP00000392330,9606.ENSP00000402060,9606.ENSP00000404220,9606.ENSP00000414378,9606.ENSP00000417052,9606.ENSP00000417573,9606.ENSP00000420658,9606.ENSP00000432456,9606.ENSP00000438863,9606.ENSP00000468411,9606.ENSP00000473159,9606.ENSP00000473212,9606.ENSP00000480514,9606.ENSP00000481956,9606.ENSP00000484824	SLC10A1,CD79A,RABAC1,TMEM147,TSPAN12,CCDC47,SEC61A1,NCLN,CHRM3,IER3IP1,RMDN3,SLC12A7,HTR2C,TEX29,NOMO1,SLC13A4,GPR101,PSCA,MTCH2,TACR1,TMEM42,SCAMP4,SYNE4,ENPP4,CXCR2,RNF185,SHISA3,IL3RA,CLN8,CLRN1,LBR,TMEM248,TRPC6,DHCR7,AVPR2,CLDN7,SLC22A2,SLC22A1,SLC41A1,GPR37L1,F11R,DPM3,GJA8,LDLRAD1,CD40,GLP1R,SUSD3,TMEM252,LHFPL2,TMEM52B,GOLM1,ABHD16A,PDCD1LG2,TMEM237,BCAP31,PVR,CCDC155,EFNA4,EBP,YIPF6,TMEM14B,GPR61,TMEM206,PSENEN,FFAR2,GPR42,TMCO1,CREB3L1,MUC1

GO:0016021	integral component of membrane	67	5155	0.41	8.13E-16	9606.ENSP00000216540,9606.ENSP00000221972,9606.ENSP00000222008,9606.ENSP00000222284,9606.ENSP00000222747,9606.ENSP00000225726,9606.ENSP00000243253,9606.ENSP00000246117,9606.ENSP00000255380,9606.ENSP00000256433,9606.ENSP00000260385,9606.ENSP00000264930,9606.ENSP00000276198,9606.ENSP00000283547,9606.ENSP00000287667,9606.ENSP00000297282,9606.ENSP00000298110,9606.ENSP00000303222,9606.ENSP00000303522,9606.ENSP00000306564,9606.ENSP00000316007,9606.ENSP00000316130,9606.ENSP00000318066,9606.ENSP00000319635,9606.ENSP00000320508,9606.ENSP00000326445,9606.ENSP00000327890,9606.ENSP00000328182,9606.ENSP00000329158,9606.ENSP00000339883,9606.ENSP00000340668,9606.ENSP00000340913,9606.ENSP00000347717,9606.ENSP00000351805,9606.ENSP00000353475,9606.ENSP00000355920,9606.ENSP00000355930,9606.ENSP00000356105,9606.ENSP00000356251,9606.ENSP00000357005,9606.ENSP00000357384,9606.ENSP00000358238,9606.ENSP00000360411,9606.ENSP00000361359,9606.ENSP00000362353,9606.ENSP00000364621,9606.ENSP00000366528,9606.ENSP00000369702,9606.ENSP00000371348,9606.ENSP00000373364,9606.ENSP00000379282,9606.ENSP00000380855,9606.ENSP00000386264,9606.ENSP00000392330,9606.ENSP00000402060,9606.ENSP00000404220,9606.ENSP00000417052,9606.ENSP00000417573,9606.ENSP00000420658,9606.ENSP00000432456,9606.ENSP00000438863,9606.ENSP00000468411,9606.ENSP00000473159,9606.ENSP00000473212,9606.ENSP00000480514,9606.ENSP00000481956,9606.ENSP00000484824	SLC10A1,CD79A,RABAC1,TMEM147,TSPAN12,CCDC47,SEC61A1,NCLN,CHRM3,IER3IP1,RMDN3,SLC12A7,HTR2C,TEX29,NOMO1,SLC13A4,GPR101,MTCH2,TACR1,TMEM42,SCAMP4,SYNE4,ENPP4,CXCR2,RNF185,SHISA3,IL3RA,CLN8,CLRN1,LBR,TMEM248,TRPC6,DHCR7,AVPR2,CLDN7,SLC22A2,SLC22A1,SLC41A1,GPR37L1,F11R,DPM3,GJA8,LDLRAD1,CD40,GLP1R,SUSD3,TMEM252,LHFPL2,TMEM52B,GOLM1,ABHD16A,PDCD1LG2,TMEM237,BCAP31,PVR,CCDC155,EBP,YIPF6,TMEM14B,GPR61,TMEM206,PSENEN,FFAR2,GPR42,TMCO1,CREB3L1,MUC1
GO:0016020	membrane	77	8420	0.26	8.28E-11	9606.ENSP00000216540,9606.ENSP00000221972,9606.ENSP00000222008,9606.ENSP00000222284,9606.ENSP00000222747,9606.ENSP00000225726,9606.ENSP00000243253,9606.ENSP00000246117,9606.ENSP00000246533,9606.ENSP00000246554,9606.ENSP00000255380,9606.ENSP00000256433,9606.ENSP00000260385,9606.ENSP00000264930,9606.ENSP00000271636,9606.ENSP00000276198,9606.ENSP00000283547,9606.ENSP00000287	SLC10A1,CD79A,RABAC1,TMEM147,TSPAN12,CCDC47,SEC61A1,NCLN,CAPNS1,COX6B1,CHRM3,IER3IP1,RMDN3,SLC12A7,CGN,HTR2C,TEX29,NOMO1,SLC13A4,GPR101,PSCA,MTCH2,TACR1,FASN,TMEM42,SCAMP4,

						667,9606.ENSP00000297282,9606.ENSP00000298110,9606.ENSP00000301258,9606.ENSP00000303222,9606.ENSP00000303522,9606.ENSP00000304592,9606.ENSP00000306564,9606.ENSP00000316007,9606.ENSP00000316130,9606.ENSP00000318066,9606.ENSP00000319635,9606.ENSP00000320508,9606.ENSP00000326445,9606.ENSP00000327890,9606.ENSP00000328182,9606.ENSP00000329158,9606.ENSP00000339883,9606.ENSP00000340668,9606.ENSP00000340913,9606.ENSP00000347717,9606.ENSP00000348886,9606.ENSP00000351805,9606.ENSP00000353475,9606.ENSP00000355920,9606.ENSP00000355930,9606.ENSP00000356105,9606.ENSP00000356251,9606.ENSP00000357005,9606.ENSP00000357384,9606.ENSP00000358238,9606.ENSP00000360411,9606.ENSP00000361359,9606.ENSP00000362353,9606.ENSP00000364621,9606.ENSP00000366528,9606.ENSP00000369702,9606.ENSP00000371348,9606.ENSP00000373364,9606.ENSP00000379282,9606.ENSP00000380855,9606.ENSP00000386264,9606.ENSP00000388566,9606.ENSP00000392330,9606.ENSP00000402060,9606.ENSP00000404220,9606.ENSP00000414378,9606.ENSP00000417052,9606.ENSP00000417573,9606.ENSP00000420658,9606.ENSP00000432456,9606.ENSP00000438863,9606.ENSP00000468411,9606.ENSP00000473159,9606.ENSP00000473172,9606.ENSP00000473212,9606.ENSP00000480332,9606.ENSP00000480514,9606.ENSP00000481956,9606.ENSP00000484824	SYNE4,ENPP4,CXCR2,RNF185,SHISA3,IL3RA,CLN8,CLRN1,LBR,TMEM248,TRPC6,DHCR7,STOML2,AVPR2,CLDN7,SLC22A2,SLC22A1,SLC41A1,GPR37L1,F11R,DPM3,GJA8,LDLRAD1,CD40,GLP1R,SUSD3,TMEM252,LHFPL2,TMEM52B,GOLM1,ABHD16A,PDCD1LG2,TMEM237,CASP4,BCAP31,PVR,CCDC155,EFNA4,EBP,YIPF6,TMEM14B,GPR61,TMEM206,PSENEN,FFAR2,RUVBL2,GPR42,TRAPPC3,TMCO1,CREB3L1,MUC1
GO:0031226	intrinsic component of plasma membrane	26	1641	0.5	7.75E-06	9606.ENSP00000216540,9606.ENSP00000221972,9606.ENSP00000222747,9606.ENSP00000255380,9606.ENSP00000264930,9606.ENSP00000276198,9606.ENSP00000297282,9606.ENSP00000298110,9606.ENSP00000303522,9606.ENSP00000319635,9606.ENSP00000340913,9606.ENSP00000351805,9606.ENSP00000355920,9606.ENSP00000355930,9606.ENSP00000358238,9606.ENSP00000361359,9606.ENSP00000362353,9606.ENSP00000373364,9606.ENSP00000392330,9606.ENSP00000402060,9606.ENSP00000414378,9606.ENSP00000417052,9606.ENSP0000046841	SLC10A1,CD79A,TSPAN12,CHRM3,SLC12A7,HTR2C,SLC13A4,GPR101,TACR1,CXCR2,TRPC6,AVPR2,SLC22A2,SLC22A1,GJA8,CD40,GLP1R,GOLM1,BCAP31,PVR,EFNA4,EBP,PSENEN,FFAR2,GPR42,MUC1

						1,9606.ENSP00000473159,9606.ENSP00000473212,9606.ENSP00000484824	
GO:0005887	integral component of plasma membrane	25	1564	0.5	9.89E-06	9606.ENSP00000216540,9606.ENSP00000221972,9606.ENSP00000222747,9606.ENSP00000255380,9606.ENSP00000264930,9606.ENSP00000276198,9606.ENSP00000297282,9606.ENSP00000298110,9606.ENSP00000303522,9606.ENSP00000319635,9606.ENSP00000340913,9606.ENSP00000351805,9606.ENSP00000355920,9606.ENSP00000355930,9606.ENSP00000358238,9606.ENSP00000361359,9606.ENSP00000362353,9606.ENSP00000373364,9606.ENSP00000392330,9606.ENSP00000402060,9606.ENSP00000417052,9606.ENSP00000468411,9606.ENSP00000473159,9606.ENSP00000473212,9606.ENSP00000484824	SLC10A1,CD79A,TSPAN12,CHRM3,SLC12A7,HTR2C,SLC13A4,GPR101,TACR1,CXCR2,TRPC6,AVPR2,SLC22A2,SLC22A1,GJA8,CD40,GLP1R,GOLM1,BCAP31,PVR,EBP,PSENEN,FFAR2,GPR42,MUC1
GO:0042175	nuclear outer membrane-endoplasmic reticulum membrane network	17	1043	0.51	0.00086	9606.ENSP00000222284,9606.ENSP00000243253,9606.ENSP00000246117,9606.ENSP00000256433,9606.ENSP00000316130,9606.ENSP00000320508,9606.ENSP00000326445,9606.ENSP00000328182,9606.ENSP00000347717,9606.ENSP00000357384,9606.ENSP00000388566,9606.ENSP00000392330,9606.ENSP00000404220,9606.ENSP00000417052,9606.ENSP00000468411,9606.ENSP00000480514,9606.ENSP00000481956	TMEM147,SEC61A1,NCLN,IER3IP1,SYNE4,RNF185,SHISA3,CLN8,DHCR7,DPM3,CASP4,BCAP31,CCDC155,EBP,PSENEN,TMCO1,CREB3L1
GO:0071944	cell periphery	45	5254	0.23	0.0018	9606.ENSP00000216540,9606.ENSP00000221972,9606.ENSP00000222008,9606.ENSP00000222747,9606.ENSP00000246533,9606.ENSP00000255380,9606.ENSP00000264930,9606.ENSP00000271636,9606.ENSP00000276198,9606.ENSP00000297282,9606.ENSP00000298110,9606.ENSP00000301258,9606.ENSP00000303522,9606.ENSP00000304592,9606.ENSP00000318066,9606.ENSP00000319635,9606.ENSP00000327890,9606.ENSP00000329158,9606.ENSP00000340913,9606.ENSP00000348886,9606.ENSP00000351805,9606.ENSP00000353475,9606.ENSP00000355920,9606.ENSP00000355930,9606.ENSP00000356105,9606.ENSP00000356251,9606.ENSP00000357005,9606.ENSP00000358238,9606.ENSP00000361359,9606.ENSP00000362353,9606.ENSP00000364621,9606.ENSP00000369702,9606.ENSP00000373364,9606.ENSP00000380855,9606.ENSP00000388566,9606.ENSP00000392330,9606.ENSP00000402060,9606.ENSP00000405514,9606.	SLC10A1,CD79A,RABAC1,TSPAN12,CAPNS1,CHRM3,SLC12A7,CGN,HTR2C,SLC13A4,GPR101,PSCA,TACR1,FASN,ENPP4,CXCR2,IL3RA,CLRN1,TRPC6,STOML2,AVPR2,CLDN7,SLC22A2,SLC22A1,SLC41A1,GPR37L1,F11R,GJA8,CD40,GLP1R,SUSD3,LHFPL2,GOLM1,PDCD1LG2,CASP4,BCAP31,PVR,PPP1R9A,EFNA4,EBP,GPR61,PSENEN,FFAR2,GPR42,MUC1

						ENSP00000414378,9606.ENSP00000417052,9606.ENSP00000432456,9606.ENSP00000468411,9606.ENSP00000473159,9606.ENSP00000473212,9606.ENSP00000484824	
GO:0005886	plasma membrane	44	5159	0.23	0.0023	9606.ENSP00000216540,9606.ENSP00000221972,9606.ENSP00000222008,9606.ENSP00000222747,9606.ENSP00000246533,9606.ENSP00000255380,9606.ENSP00000264930,9606.ENSP00000271636,9606.ENSP00000276198,9606.ENSP00000297282,9606.ENSP00000298110,9606.ENSP00000301258,9606.ENSP00000303522,9606.ENSP00000304592,9606.ENSP00000318066,9606.ENSP00000319635,9606.ENSP00000327890,9606.ENSP00000329158,9606.ENSP00000340913,9606.ENSP00000348886,9606.ENSP00000351805,9606.ENSP00000353475,9606.ENSP00000355920,9606.ENSP00000355930,9606.ENSP00000356105,9606.ENSP00000356251,9606.ENSP00000357005,9606.ENSP00000358238,9606.ENSP00000361359,9606.ENSP00000362353,9606.ENSP00000364621,9606.ENSP00000369702,9606.ENSP00000373364,9606.ENSP00000380855,9606.ENSP00000388566,9606.ENSP00000392330,9606.ENSP00000402060,9606.ENSP00000414378,9606.ENSP00000417052,9606.ENSP00000432456,9606.ENSP00000468411,9606.ENSP00000473159,9606.ENSP00000473212,9606.ENSP00000484824	SLC10A1,CD79A,RABAC1,TSPAN12,CAPNS1,CHRM3,SLC12A7,CGN,HTR2C,SLC13A4,GPR101,PSCA,TACR1,FASN,ENPP4,CXCR2,IL3RA,CLRN1,TRPC6,STOML2,AVPR2,CLDN7,SLC22A2,SLC22A1,SLC41A1,GPR37L1,F11R,GJA8,CD40,GLP1R,SUSD3,LHFPL2,GOLM1,PDCD1LG2,CASP4,BCAP31,PVR,EFNA4,EBP,GPR61,PSENEN,FFAR2,GPR42,MUC1
GO:0005789	endoplasmic reticulum membrane	15	1022	0.47	0.006	9606.ENSP00000222284,9606.ENSP00000243253,9606.ENSP00000246117,9606.ENSP00000256433,9606.ENSP00000320508,9606.ENSP00000326445,9606.ENSP00000328182,9606.ENSP00000347717,9606.ENSP00000357384,9606.ENSP00000388566,9606.ENSP00000392330,9606.ENSP00000417052,9606.ENSP00000468411,9606.ENSP00000480514,9606.ENSP00000481956	TMEM147,SEC61A1,NCLN,IER3IP1,RNF185,SHISA3,CLN8,DHCR7,DPM3,CASP4,BCAP31,EBP,PSENEN,TMCO1,CREB3L1
GO:0031301	integral component of organelle membrane	8	310	0.71	0.006	9606.ENSP00000243253,9606.ENSP00000256433,9606.ENSP00000316130,9606.ENSP00000339883,9606.ENSP00000347717,9606.ENSP00000357384,9606.ENSP00000392330,9606.ENSP00000480514	SEC61A1,IER3IP1,SYNE4,LBR,DHCR7,DPM3,BCAP31,TMCO1
GO:0098827	endoplasmic reticulum subcompartment	15	1025	0.47	0.006	9606.ENSP00000222284,9606.ENSP00000243253,9606.ENSP00000246117,9606.ENSP00000256433,9606.ENSP00000320508,9606.ENSP00000326445,9606.ENSP00000328182,9606.ENSP0000	TMEM147,SEC61A1,NCLN,IER3IP1,RNF185,SHISA3,CLN8,DH

						0347717,9606.ENSP00000357384,9606.ENSP00000388566,9606.ENSP00000392330,9606.ENSP00000417052,9606.ENSP00000468411,9606.ENSP00000480514,9606.ENSP00000481956	CR7,DPM3,CASP4,BCAP31,EBP,PSENEN,TMCO1,CREB3L1
GO:0005640	nuclear outer membrane	3	25	1.38	0.0081	9606.ENSP00000316130,9606.ENSP00000347717,9606.ENSP00000404220	SYNE4,DHCR7,CCDC155
GO:0005783	endoplasmic reticulum	20	1796	0.35	0.0116	9606.ENSP00000222284,9606.ENSP00000225726,9606.ENSP00000243253,9606.ENSP00000246117,9606.ENSP00000256433,9606.ENSP00000320508,9606.ENSP00000326445,9606.ENSP00000328182,9606.ENSP00000347717,9606.ENSP00000351805,9606.ENSP00000357384,9606.ENSP00000373364,9606.ENSP00000388566,9606.ENSP00000392330,9606.ENSP00000417052,9606.ENSP00000417573,9606.ENSP00000468411,9606.ENSP00000480332,9606.ENSP00000480514,9606.ENSP00000481956	TMEM147,CCDC47,SEC61A1,NCLN,IER3IP1,RNF185,SHISA3,CLN8,DHCR7,AVPR2,DPM3,GOLM1,CASP4,BCAP31,EBP,YIPF6,PSENEN,TRAPPC3,TMCO1,CREB3L1
GO:0030176	integral component of endoplasmic reticulum membrane	5	147	0.83	0.0192	9606.ENSP00000243253,9606.ENSP00000347717,9606.ENSP00000357384,9606.ENSP00000392330,9606.ENSP00000480514	SEC61A1,DHCR7,DPM3,BCAP31,TMCO1
GO:0034993	meiotic nuclear membrane microtubule tethering complex	2	8	1.7	0.0197	9606.ENSP00000316130,9606.ENSP00000404220	SYNE4,CCDC155
GO:0036057	slit diaphragm	2	9	1.65	0.0197	9606.ENSP00000340913,9606.ENSP00000357005	TRPC6,F11R
GO:0031090	organelle membrane	29	3337	0.24	0.0199	9606.ENSP00000222284,9606.ENSP00000243253,9606.ENSP00000246117,9606.ENSP00000246554,9606.ENSP00000256433,9606.ENSP00000260385,9606.ENSP00000303222,9606.ENSP00000316130,9606.ENSP00000318066,9606.ENSP00000319635,9606.ENSP00000320508,9606.ENSP00000326445,9606.ENSP00000328182,9606.ENSP00000339883,9606.ENSP00000347717,9606.ENSP00000348886,9606.ENSP00000351805,9606.ENSP00000357384,9606.ENSP00000369702,9606.ENSP00000388566,9606.ENSP00000392330,9606.ENSP00000404220,9606.ENSP00000417052,9606.ENSP00000417573,9606.ENSP00000432456,9606.ENSP00000468411,9606.ENSP00000480332,9606.ENSP00000480514,9606.ENSP00000481956	TMEM147,SEC61A1,NCLN,COX6B1,IER3IP1,RMDN3,MTCH2,SYNE4,ENPP4,CXCR2,RNF185,SHISA3,CLN8,LBR,DHCR7,STOML2,AVPR2,DPM3,LHFPL2,CASP4,BCAP31,CCDC155,EBP,YIPF6,GPR61,PSENEN,TRAPPC3,TMCO1,CREB3L1

GO:0031984	organelle subcompartment	17	1616	0.32	0.0339	9606.ENSP00000222284,9606.ENSP00000243253,9606.ENSP00000246117,9606.ENSP00000256433,9606.ENSP00000320508,9606.ENSP00000326445,9606.ENSP00000328182,9606.ENSP00000347717,9606.ENSP00000357384,9606.ENSP00000388566,9606.ENSP00000392330,9606.ENSP00000417052,9606.ENSP00000417573,9606.ENSP00000468411,9606.ENSP00000480332,9606.ENSP00000480514,9606.ENSP00000481956	TMEM147,SEC61A1,NCLN,IER3IP1,RNF185,SHISA3,CLN8,DHCR7,DPM3,CASP4,BCAP31,EBP,YIPF6,PSENEN,TRAPPC3,TMCO1,CREB3L1
GO:0012505	endomembrane system	34	4347	0.19	0.0387	9606.ENSP00000215754,9606.ENSP00000221972,9606.ENSP00000222008,9606.ENSP00000222284,9606.ENSP00000225726,9606.ENSP00000226574,9606.ENSP00000243253,9606.ENSP00000246117,9606.ENSP00000256433,9606.ENSP00000304592,9606.ENSP00000316130,9606.ENSP00000318066,9606.ENSP00000319635,9606.ENSP00000320508,9606.ENSP00000326445,9606.ENSP00000328182,9606.ENSP00000339883,9606.ENSP00000347717,9606.ENSP00000351805,9606.ENSP00000357384,9606.ENSP00000369702,9606.ENSP00000373364,9606.ENSP00000380855,9606.ENSP00000388566,9606.ENSP00000392330,9606.ENSP00000404220,9606.ENSP00000417052,9606.ENSP00000417573,9606.ENSP00000432456,9606.ENSP00000468411,9606.ENSP00000480332,9606.ENSP00000480514,9606.ENSP00000481956,9606.ENSP00000484824	MIF,CD79A,RABAC1,TMEM147,CCDC47,NFKB1,SEC61A1,NCLN,IER3IP1,FASN,SYNE4,ENPP4,CXCR2,RNF185,SHISA3,CLN8,LBR,DHCR7,AVPR2,DPM3,LHFPL2,GOLM1,PDCD1LG2,CASP4,BCAP31,CCDC155,EBP,YIPF6,GPR61,PSENEN,TRAPPC3,TMCO1,CREB3L1,MUC1
GO:0031968	organelle outer membrane	5	203	0.69	0.0436	9606.ENSP00000260385,9606.ENSP00000316130,9606.ENSP00000320508,9606.ENSP00000347717,9606.ENSP00000404220	RMDN3,SYNE4,RNF185,DHCR7,CCDC155
GO:0016323	basolateral plasma membrane	5	213	0.67	0.0494	9606.ENSP00000216540,9606.ENSP00000255380,9606.ENSP00000353475,9606.ENSP00000355930,9606.ENSP00000356105	SLC10A1,CHRM3,CLDN7,SLC2A1,SLC41A1

Table 6.5: GO Biological Process terms

GO term ID	Term description	Observed gene count	Background gene count	Strength	False discovery rate	Matching proteins in your network (IDs)	Matching proteins in your network (labels)
GO:0072507	divalent inorganic cation homeostasis	12	429	0.75	0.0046	9606.ENSP00000225726,9606.ENSP00000260385,9606.ENSP00000276198,9606.ENSP00000303522,9606.ENSP00000319635,9606.ENSP00000340913,9606.ENSP00000348886,9606.ENSP00000356105,9606.ENSP00000361359,9606.ENSP00000362353,9606.ENSP00000392330,9606.ENSP00000480514	CCDC47,RMDN3,HTR2C,TACR1,CXCR2,TRPC6,STOML2,SLC41A1,CD40,GLP1R,BCAP31,TMCO1
GO:0055074	calcium ion homeostasis	11	402	0.74	0.0078	9606.ENSP00000225726,9606.ENSP00000260385,9606.ENSP00000276198,9606.ENSP00000303522,9606.ENSP00000319635,9606.ENSP00000340913,9606.ENSP00000348886,9606.ENSP00000361359,9606.ENSP00000362353,9606.ENSP00000392330,9606.ENSP00000480514	CCDC47,RMDN3,HTR2C,TACR1,CXCR2,TRPC6,STOML2,CD40,GLP1R,BCAP31,TMCO1
GO:0072503	cellular divalent inorganic cation homeostasis	11	407	0.73	0.0078	9606.ENSP00000260385,9606.ENSP00000276198,9606.ENSP00000303522,9606.ENSP00000319635,9606.ENSP00000340913,9606.ENSP00000348886,9606.ENSP00000356105,9606.ENSP00000361359,9606.ENSP00000362353,9606.ENSP00000392330,9606.ENSP00000480514	RMDN3,HTR2C,TACR1,CXCR2,TRPC6,STOML2,SLC41A1,CD40,GLP1R,BCAP31,TMCO1
GO:0006874	cellular calcium ion homeostasis	10	388	0.71	0.0145	9606.ENSP00000260385,9606.ENSP00000276198,9606.ENSP00000303522,9606.ENSP00000319635,9606.ENSP00000340913,9606.ENSP00000348886,9606.ENSP00000361359,9606.ENSP00000362353,9606.ENSP00000392330,9606.ENSP00000480514	RMDN3,HTR2C,TACR1,CXCR2,TRPC6,STOML2,CD40,GLP1R,BCAP31,TMCO1
GO:0055065	metal ion homeostasis	12	555	0.64	0.0145	9606.ENSP00000225726,9606.ENSP00000260385,9606.ENSP00000276198,9606.ENSP00000303522,9606.ENSP00000319635,9606.ENSP00000340913,9606.ENSP00000348886,9606.ENSP00000356105,9606.ENSP00000361359,9606.ENSP00000362353,9606.ENSP00000392330,9606.ENSP00000480514	CCDC47,RMDN3,HTR2C,TACR1,CXCR2,TRPC6,STOML2,SLC41A1,CD40,GLP1R,BCAP31,TMCO1
GO:0006875	cellular metal ion homeostasis	11	499	0.64	0.0182	9606.ENSP00000260385,9606.ENSP00000276198,9606.ENSP00000303522,9606.ENSP00000319635,9606.ENSP00000340913,9606.ENSP00000348886,9606.ENSP00000356105,9606.ENSP00000361359,9606.ENSP00000362353,9606.ENSP00000392330,9606.ENSP00000480514	RMDN3,HTR2C,TACR1,CXCR2,TRPC6,STOML2,SLC41A1,CD40,GLP1R,BCAP31,TMCO1

Table 6.6: UniProt Annotated Keyword terms

GO term ID	Term description	Observed gene count	Background gene count	Strength	False discovery rate	Matching proteins in your network (IDs)	Matching proteins in your network (labels)
KW-1133	Transmembrane helix	67	4950	0.43	1.07E-16	9606.ENSP00000216540,9606.ENSP00000221972,9606.ENSP00000222008,9606.ENSP00000222284,9606.ENSP00000222747,9606.ENSP00000225726,9606.ENSP00000243253,9606.ENSP00000246117,9606.ENSP00000255380,9606.ENSP00000256433,9606.ENSP00000260385,9606.ENSP00000264930,9606.ENSP00000276198,9606.ENSP00000283547,9606.ENSP00000287667,9606.ENSP00000297282,9606.ENSP00000298110,9606.ENSP00000303222,9606.ENSP00000303522,9606.ENSP00000306564,9606.ENSP00000316007,9606.ENSP00000316130,9606.ENSP00000318066,9606.ENSP00000319635,9606.ENSP00000320508,9606.ENSP00000326445,9606.ENSP00000327890,9606.ENSP00000328182,9606.ENSP00000329158,9606.ENSP00000339883,9606.ENSP00000340668,9606.ENSP00000340913,9606.ENSP00000347717,9606.ENSP00000351805,9606.ENSP00000353475,9606.ENSP00000355920,9606.ENSP00000355930,9606.ENSP00000356105,9606.ENSP00000356251,9606.ENSP00000357005,9606.ENSP00000357384,9606.ENSP00000358238,9606.ENSP00000360411,9606.ENSP00000361359,9606.ENSP00000362353,9606.ENSP00000364621,9606.ENSP00000366528,9606.ENSP00000369702,9606.ENSP00000371348,9606.ENSP00000373364,9606.ENSP00000379282,9606.ENSP00000380855,9606.ENSP00000386264,9606.ENSP00000392330,9606.ENSP00000402060,9606.ENSP00000404220,9606.ENSP00000417052,9606.ENSP00000417573,9606.ENSP00000420658,9606.ENSP00000432456,9606.ENSP00000438863,9606.ENSP00000468411,9606.ENSP00000473159,9606.ENSP00000473212,9606.ENSP00000480514,9606.ENSP00000481956,9606.ENSP00000484824	SLC10A1,CD79A,RABAC1,TMEM147,TSPAN12,CCDC47,SEC61A1,NCLN,CHRM3,IER3IP1,RMDN3,SLC12A7,HTR2C,TEX29,NOMO1,SLC13A4,GPR101,MTCH2,TACR1,TMEM42,SCAMP4,SYNE4,ENPP4,CXCR2,RNF185,SHISA3,IL3RA,CLN8,CLRN1,LBR,TMEM248,TRPC6,DHCR7,AVPR2,CLDN7,SLC22A2,SLC22A1,SLC41A1,GPR37L1,F11R,DPM3,GJA8,LDLRAD1,CD40,GLP1R,SUSD3,TMEM252,LHFPL2,TMEM52B,GOLM1,ABHD16A,PDCD1LG2,TMEM237,BCAP31,PVR,CCDC155,EBP,YIPF6,TMEM14B,GPR61,TMEM206,PSENEN,FFAR2,GPR42,TMCO1,CREB3L1,MUC1
KW-0472	Membrane	73	6985	0.32	4.37E-13	9606.ENSP00000216540,9606.ENSP00000221972,9606.ENSP00000222008,9606.ENSP00000222284,9606.ENSP00000222747,9606.ENSP00000225726,9606.ENSP00000243253,9606.ENSP00000246117,9606.ENSP00000246533,9606.ENSP00000255380,9606.ENSP000025643	SLC10A1,CD79A,RABAC1,TMEM147,TSPAN12,CCDC47,SEC61A1,NCLN,CAPNS1,CHRM3,IER3IP1,RMDN3,SLC12

						3,9606.ENSP00000260385,9606.ENSP00000264930,9606.ENSP00000276198,9606.ENSP00000283547,9606.ENSP00000287667,9606.ENSP00000297282,9606.ENSP00000298110,9606.ENSP00000301258,9606.ENSP00000303222,9606.ENSP00000303522,9606.ENSP00000306564,9606.ENSP00000316007,9606.ENSP00000316130,9606.ENSP00000318066,9606.ENSP00000319635,9606.ENSP00000320508,9606.ENSP00000326445,9606.ENSP00000327890,9606.ENSP00000328182,9606.ENSP00000329158,9606.ENSP00000339883,9606.ENSP00000340668,9606.ENSP00000340913,9606.ENSP00000347717,9606.ENSP00000348886,9606.ENSP00000351805,9606.ENSP00000353475,9606.ENSP00000355920,9606.ENSP00000355930,9606.ENSP00000356105,9606.ENSP00000356251,9606.ENSP00000357005,9606.ENSP00000357384,9606.ENSP00000358238,9606.ENSP00000360411,9606.ENSP00000361359,9606.ENSP00000362353,9606.ENSP00000364621,9606.ENSP00000366528,9606.ENSP00000369702,9606.ENSP00000371348,9606.ENSP00000373364,9606.ENSP00000379282,9606.ENSP00000380855,9606.ENSP00000386264,9606.ENSP00000388566,9606.ENSP00000392330,9606.ENSP00000402060,9606.ENSP00000404220,9606.ENSP00000414378,9606.ENSP00000417052,9606.ENSP00000417573,9606.ENSP00000420658,9606.ENSP00000432456,9606.ENSP00000438863,9606.ENSP00000468411,9606.ENSP00000473159,9606.ENSP00000473172,9606.ENSP00000473212,9606.ENSP00000480514,9606.ENSP00000481956,9606.ENSP00000484824	A7,HTR2C,TEX29,NOMO1,SLC13A4,GPR101,PSCA,MTCH2,TACR1,TMEM42,SCAMP4,SYNE4,ENPP4,CXCR2,RNF185,SHISA3,IL3RA,CLN8,CLRN1,LBR,TMEM248,TRPC6,DHCR7,STOML2,AVPR2,CLDN7,SLC22A2,SLC22A1,SLC41A1,GPR37L1,F11R,DPM3,GJA8,LDLRAD1,CD40,GLP1R,SUSD3,TMEM252,LHFPL2,TMEM52B,GOLM1,ABHD16A,PDCD1LG2,TMEM237,CASP4,BCAP31,PVR,CCDC155,EFNA4,EBP,YIPF6,TMEM14B,GPR61,TMEM206,PSENEN,FFAR2,RUVBL2,GPR42,TMCO1,CREB3L1,MUC1
KW-1003	Cell membrane	33	3214	0.31	0.0012	9606.ENSP00000221972,9606.ENSP00000222008,9606.ENSP00000222747,9606.ENSP00000246533,9606.ENSP00000255380,9606.ENSP00000264930,9606.ENSP00000276198,9606.ENSP00000298110,9606.ENSP00000301258,9606.ENSP00000303522,9606.ENSP00000318066,9606.ENSP00000319635,9606.ENSP00000329158,9606.ENSP00000340913,9606.ENSP00000348886,9606.ENSP00000351805,9606.ENSP00000353475,9606.ENSP00000355930,9606.ENSP00000356105,9606.ENSP00000356251,9606.ENSP00000357005,9606.ENSP00000358238,9606.ENSP00000361359,9606.ENSP00000362353,9606.ENSP00000364621,9606.ENSP00000380855,9606.ENSP00000402060,9606.ENSP00000414378,9606.ENSP00000432456,9606.ENSP00000468411,	CD79A,RABAC1,TSPAN12,CAPNS1,CHRM3,SLC12A7,HTR2C,GPR101,PSCA,TACR1,ENPP4,CXCR2,CLRN1,TRPC6,STOML2,AVPR2,CLDN7,SLC22A1,SLC41A1,GPR37L1,F11R,GJA8,CD40,GLP1R,SUSD3,PDCD1LG2,PVR,EFNA4,GPR61,PSENEN,FFAR2,GPR42,MUC1

						9606.ENSP00000473159,9606.ENSP00000473212,9606.ENSP00000484824	
KW-0256	Endoplasmic reticulum	17	1130	0.48	0.0018	9606.ENSP00000222284,9606.ENSP00000243253,9606.ENSP00000246117,9606.ENSP00000256433,9606.ENSP00000320508,9606.ENSP00000326445,9606.ENSP00000328182,9606.ENSP00000339883,9606.ENSP00000347717,9606.ENSP00000357384,9606.ENSP00000388566,9606.ENSP00000392330,9606.ENSP00000417052,9606.ENSP00000468411,9606.ENSP00000480332,9606.ENSP00000480514,9606.ENSP00000481956	TMEM147,SEC61A1,NCLN,IER3IP1,RNF185,SHISA3,CLN8,LBR,DHCR7,DPM3,CASP4,BCAP31,EBP,PSENEN,TRAPPC3,TMCO1,CREB3L1
KW-0675	Receptor	19	1423	0.43	0.0025	9606.ENSP00000216540,9606.ENSP00000255380,9606.ENSP00000276198,9606.ENSP00000298110,9606.ENSP00000303522,9606.ENSP00000319635,9606.ENSP00000327890,9606.ENSP00000339883,9606.ENSP00000351805,9606.ENSP00000356251,9606.ENSP00000357005,9606.ENSP00000360411,9606.ENSP00000361359,9606.ENSP00000362353,9606.ENSP00000380855,9606.ENSP00000402060,9606.ENSP00000432456,9606.ENSP00000473159,9606.ENSP00000473212	SLC10A1,CHRM3,HTR2C,GPR101,TACR1,CXCR2,IL3RA,LBR,AVPR2,GPR37L1,F11R,LDLRAD1,CD40,GLP1R,PDCD1LG2,PVR,GPR61,FFAR2,GPR42
KW-0152	Cholesterol biosynthesis	3	20	1.48	0.0053	9606.ENSP00000339883,9606.ENSP00000347717,9606.ENSP00000417052	LBR,DHCR7,EBP
KW-0297	G-protein coupled receptor	11	778	0.45	0.0356	9606.ENSP00000255380,9606.ENSP00000276198,9606.ENSP00000298110,9606.ENSP00000303522,9606.ENSP00000319635,9606.ENSP00000351805,9606.ENSP00000356251,9606.ENSP00000362353,9606.ENSP00000432456,9606.ENSP00000473159,9606.ENSP00000473212	CHRM3,HTR2C,GPR101,TACR1,CXCR2,AVPR2,GPR37L1,GLP1R,GPR61,FFAR2,GPR42

Table 6.7: PubMed Reference Publications

GO term ID	Term description	Observed gene count	Background gene count	Strength	False discovery rate	Matching proteins in your network (IDs)	Matching proteins in your network (labels)
PMID:23823179	(2013) Nature of SLC41A1 complexes: report on the split-ubiquitin yeast two hybrid assay.	7	17	1.91	2.28E-06	9606.ENSP00000222284,9606.ENSP00000256433,9606.ENSP00000303222,9606.ENSP00000356105,9606.ENSP00000392330,9606.ENSP00000417052,9606.ENSP00000417573	TMEM147,IER3IP1,MTCH2,SLC41A1,BCAP31,EBP,YIPF6
PMID:24340240	(2013) Solute Carrier Family SLC41, what do we really know about it?	7	27	1.71	1.70E-05	9606.ENSP00000222284,9606.ENSP00000256433,9606.ENSP00000303222,9606.ENSP00000356105,9606.ENSP00000392330,9606.ENSP00000417052,9606.ENSP00000417573	TMEM147,IER3IP1,MTCH2,SLC41A1,BCAP31,EBP,YIPF6
PMID:32820719	(2020) An ER translocon for multi-pass membrane protein biogenesis.	5	6	2.22	4.79E-05	9606.ENSP00000222284,9606.ENSP00000225726,9606.ENSP00000243253,9606.ENSP00000246117,9606.ENSP00000480514	TMEM147,CCDC47,SEC61A1,NCLN,TMCO1

Table 6.8: Reactome pathways

GO term ID	Term description	Observed gene count	Background gene count	Strength	False discovery rate	Matching proteins in your network (IDs)	Matching proteins in your network (labels)
HSA-157579	Telomere Maintenance	2	7	1.76	0.026	9606.ENSP00000274606,9606.ENSP00000473172	NHP2,RUVBL2

Table 6.9: Pfam Protein Domain

GO term ID	Term description	Observed gene count	Background gene count	Strength	False discovery rate	Matching proteins in your network (IDs)	Matching proteins in your network (labels)
PF01222	Ergosterol biosynthesis ERG4/ERG24 family	2	3	2.12	0.0351	9606.ENSP00000339883,9606.ENSP00000347717	LBR,DHCR7

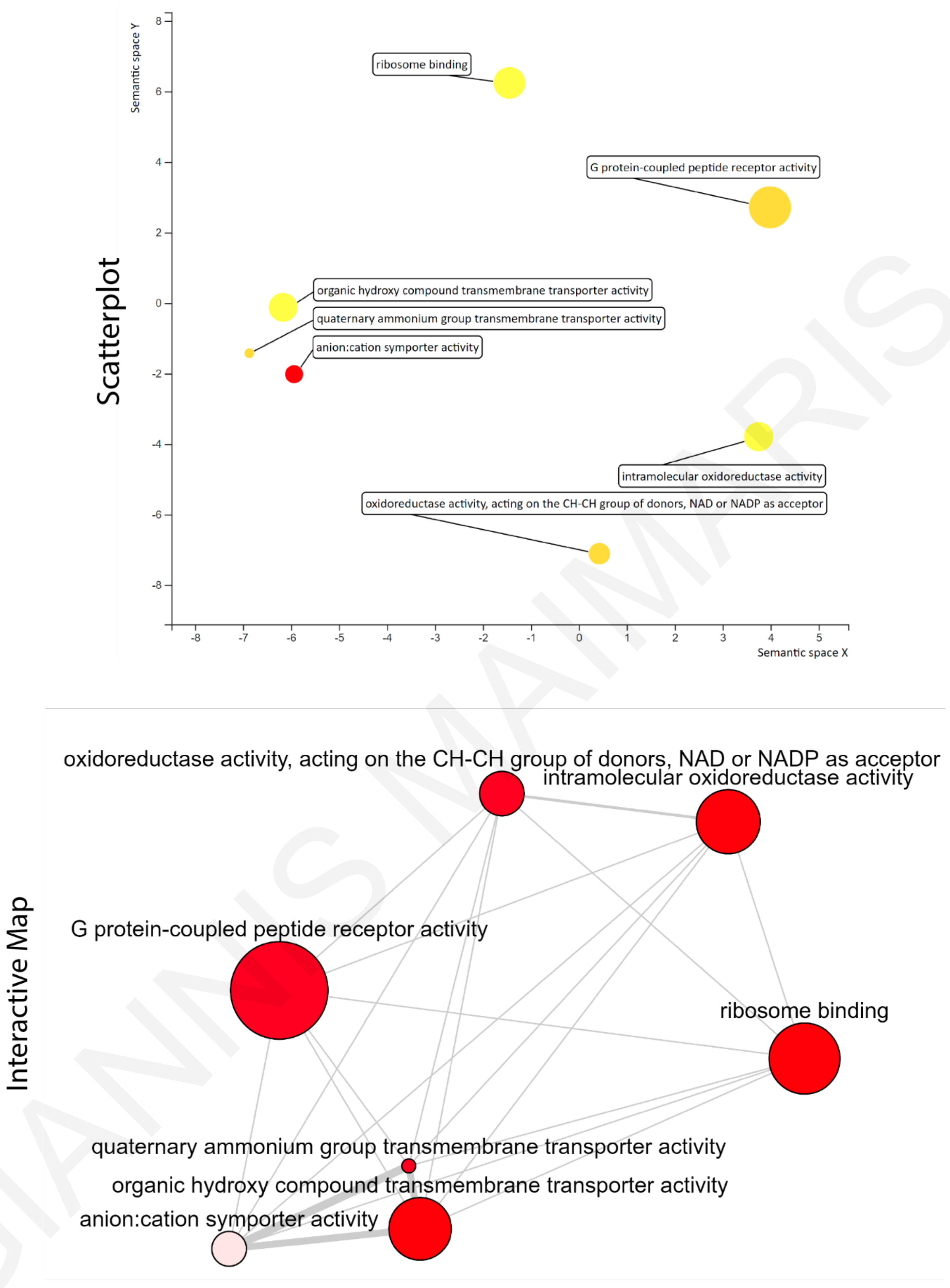

Figure 6.1: REVIGO analysis Scatterplot and Interactive Map.
Scatterplot (Top panel): *Alternative simplified display of TMEM147-associated GO terms. Arrangement of the terms corresponds to the legibility and the proximity of the related terms. Semantically similar GO terms are in close proximity and correspond to the color code of the TreeMap (Axes have no intrinsic meaning).*
Interactive Map (lower panel): *Another alternative simplified display of TMEM147-associated GO terms Bubble size indicates the frequency of the GO term in the underlying database. Highly similar GO terms are linked by edges in the graph, where the line width indicates the degree of similarity. Bubble color indicates the user-provided p-value (red color: bigger p-value, pink color: smaller p-value).*

6.1 Publication 1

© 2020. Published by The Company of Biologists Ltd | Journal of Cell Science (2020) 133, jcs245357. doi:10.1242/jcs.245357

RESEARCH ARTICLE

TMEM147 interacts with lamin B receptor, regulates its localization and levels, and affects cholesterol homeostasis

Andri Christodoulou[1,‡], Giannis Maimaris[1], Andri Makrigiorgi[1], Evelina Charidemou[1], Christian Lüchtenborg[2], Antonis Ververis[1,*], Renos Georgiou[1], Carsten W. Lederer[3], Christof Haffner[4], Britta Brügger[2] and Niovi Santama[1,‡]

ABSTRACT

The structurally and functionally complex endoplasmic reticulum (ER) hosts critical processes including lipid synthesis. Here, we focus on the functional characterization of transmembrane protein TMEM147, and report that it localizes at the ER and nuclear envelope in HeLa cells. Silencing of *TMEM147* drastically reduces the level of lamin B receptor (LBR) at the inner nuclear membrane and results in mistargeting of LBR to the ER. LBR possesses a modular structure and corresponding bifunctionality, acting in heterochromatin organization via its N-terminus and in cholesterol biosynthesis via its sterol-reductase C-terminal domain. We show that TMEM147 physically interacts with LBR, and that the C-terminus of LBR is essential for their functional interaction. We find that TMEM147 also physically interacts with the key sterol reductase DHCR7, which is involved in cholesterol biosynthesis. Similar to what was seen for LBR, *TMEM147* downregulation results in a sharp decline of DHCR protein levels and co-ordinate transcriptional decreases of *LBR* and *DHCR7* expression. Consistent with this, lipidomic analysis upon *TMEM147* silencing identified changes in cellular cholesterol levels, cholesteryl ester levels and profile, and in cellular cholesterol uptake, raising the possibility that TMEM147 is an important new regulator of cholesterol homeostasis in cells.

This article has an associated First Person interview with the first author of the paper.

KEY WORDS: ER transmembrane proteins, LBR, Cholesterol, Sterol reductases

INTRODUCTION

The endoplasmic reticulum (ER) is the most extensive intracellular membranous compartment, consisting of a network of interconnected flat sheets and tubules, and the contiguous nuclear envelope (NE) (Baumann and Walz, 2001; Lynes and Simmen, 2011). The ER, as the site of protein synthesis, processing and assembly and membrane and lipid supplier of the cell, exhibits not only morphological but also functional compartmentalization (Baumann and Walz, 2001; Chen et al., 2013; Hu et al., 2011; Goyal and Blackstone, 2013; Lin et al., 2012; Shibata et al., 2006). Understanding how structural and functional specificity is formed and maintained is an ongoing challenge.

In our work on ER membrane morphogenesis (Santama et al., 2004; Christodoulou et al., 2016), we recently focused on transmembrane protein TMEM147, a 25 kDa protein that localizes to ER membranes (Dettmer et al., 2010; Rosemond et al., 2011) and possesses seven transmembrane domains with its N-terminus residing in the ER lumen and its C-terminus facing the cytosolic side of the membrane. The amino acid sequence of TMEM147 is highly conserved among mammalian species (human, rat, bovine and mouse sequences are 99% identical) and it is expressed at constant levels across many human tissues (Rosemond et al., 2011). TMEM147 was found to exhibit intricate reciprocal interactions with the ER proteins nicalin and NOMO (NOMO1,-2 and -3) and be a core component of a complex involving all three proteins that is important for early embryonic Nodal signaling in vertebrates (Dettmer et al., 2010). Furthermore, TMEM147 has been shown to influence forward trafficking, via the ER, of the muscarinic acetylcholine receptor M3R (CHRM3) (Rosemond et al., 2011). Both studies indicate important protein interactions of TMEM147 within the ER; its function, however, is still unknown.

At the onset of our experiments, we detected interactions between TMEM147 and lamin B receptor (LBR), which we fully characterize in this work (see Results). LBR is an extensively studied cellular protein that localizes to the inner nuclear membrane (INM). Its nucleoplasmic, hydrophilic N-terminus [amino acids (aa) 1–208 in human, including a chromatin-binding Tudor domain] was found to interact with lamin B (hence its name) and heterochromatin-associated proteins (HP1 and MeCP2) (Makatsori et al., 2004; Pyrpasopoulou et al., 1996; Worman et al., 1988). Through these interactions, LBR is assumed to provide a platform for internal nuclear organization by mediating the deposition of repressed and transcriptionally inactive heterochromatin to the NE periphery. The C-terminus of LBR (aa 208–615) is proposed to contain 8–10 transmembrane domains, whose topological organization within the INM is not settled in literature, and a short C-terminal 'tail' whose localization can be either nucleoplasmic or within the lumen between the outer and inner NE sheets (Olins et al., 2010).

A fascinating aspect of LBR structure is that, while the N-terminal part has a distinct nuclear function, unexpectedly, its C-terminus resembles C-14 sterol reductase enzymes (Li et al., 2015; Silve et al., 1998; Worman et al., 1990). In fact, the intron between exons 4 and 5 in the LBR gene is 10 kb long, raising the possibility that the gene may have evolved from a recombination event between two primordial genes, giving rise to a chimeric protein (Schuler et al., 1994; Olins et al., 2010). Specifically, LBR displays significant

---

[1]Department of Biological Sciences, University of Cyprus, 1678 Nicosia, Cyprus. [2]Biochemistry Center (BZH), University of Heidelberg, 69120 Heidelberg, Germany. [3]Department of Molecular Genetics Thalassaemia and Cyprus School of Molecular Medicine, The Cyprus Institute of Neurology and Genetics, 1683 Nicosia, Cyprus. [4]Institute of Stroke and Dementia Research, University of Munich, 81377 Munich, Germany.
*Present address: Neurogenetics Department and Cyprus School of Molecular Medicine, The Cyprus Institute of Neurology and Genetics, Cyprus.

‡Authors for correspondence (santama@ucy.ac.cy; christodoulou.c.andri@ucy.ac.cy)

A.C., 0000-0001-7151-6408; E.C., 0000-0002-2299-9471; A.V., 0000-0003-1798-6550; R.G., 0000-0002-2415-9230; C.W.L., 0000-0003-3920-9584; N.S., 0000-0002-8370-8674

Handling Editor: Arnoud Sonnenberg
Received 18 February 2020; Accepted 2 July 2020

sequence similarity over its C-terminus with two key sterol reductases involved in late, post-squalene and smooth ER-localized steps of cholesterol biosynthesis; the C-terminus of LBR is 37% identical and 62% conserved with the 7-dehydrocholesterol reductase DHCR7, and 58% identical or 75% conserved with the 3 β-hydroxysterol Δ-14 reductase TM7SF2. Additionally, LBR harbors two 'sterol reductase family signatures 1 and 2' within its C-terminus, short motifs with similarities to many sterol reductases, including TM7SF2 and DHCR7 (Olins et al., 2010).

Functionally, human LBR complements the TM7SF2-like C14 sterol reductase ERG24 in *Saccharomyces cerevisiae* (Silve et al., 1998), and both LBR and TM7SF2 complement ERG3 reductase in *Neurospora crassa* (Prakash et al., 1999). Furthermore, it has been demonstrated that LBR is required for viability under cholesterol starvation conditions, and is constitutively expressed and essential for cholesterol synthesis, despite the presence of sterol-inducible TM7SF2 in human *LBR*-knockout cell lines (Tsai et al., 2016). The same study documented that the C-terminal sterol reductase domain of LBR alone is both necessary and sufficient for cholesterol production in HeLa cells and, importantly, nonsense LBR mutations, associated with Greenberg skeletal dysplasia or Pelger–Huët human congenital disorders of cholesterol metabolism, fail to rescue the cholesterol auxotrophy of an LBR-deficient human cell line (Tsai et al., 2016). Although LBR and TM7SF2 catalyze the same biosynthetic step and it appears that they provide some compensatory redundancy, their functional interactions are far from clear. Deletion of mouse *Tm7sf2* does not impair cholesterol biosynthesis (Bennati et al., 2008) and, interestingly, a small-molecule inhibitor of TM7SF2 drives oligodendrocyte differentiation from progenitor cells and induces oligodendrocyte remyelination via the concomitant accumulation of the intermediate 8,9-unsaturated sterol (Hubler et al., 2018).

Mutations in DHCR7, characterized by a cholesterol deficit and 7DHC precursor accumulation, are the cause of Lemli–Optiz syndrome (SLOS), the most common cholesterol metabolic disorder (Fitzky et al., 1998; Wassif et al., 1998; Waterham et al., 1998; Tint et al., 1994). Reduced cholesterol levels in SLOS impair hedgehog signaling by inhibiting the appropriate ciliary localization and activation of the smoothened receptor (Blassberg et al., 2016). The understanding of the molecular interactions between DHCR7 and LBR in cholesterol synthesis, pursued in mouse double knockout studies, remains incomplete (Wassif et al., 2007).

Thus, the overall functional interrelationships between LBR, TM7SF2 and DHCR7 in cholesterol biosynthesis require further elucidation. The role of LBR as a multitasking protein at the INM, the possible co-ordination between its dual role and its regulation also remain focal points of interest. In this work, we present new findings showing that the ER transmembrane protein TMEM147 drastically influences LBR levels and LBR targeting to the INM and impacts on cellular cholesterol levels by regulating both LBR and DHCR7.

RESULTS

TMEM147 localizes at the ER and NE in HeLa cells

Extending our interest in the role of ER-transmembrane proteins on ER morphogenesis and function (Christodoulou et al., 2016), we focused in this work on the characterization of TMEM147 (also known as NIFIE14; NM_032635.4) in human cells. Because of lack of an antibody suitable for immunofluorescence, we pursued transient transfections with an N-terminally FLAG-tagged full length *TMEM147* cDNA in HeLa cells; this revealed labeling of both the ER (Fig. 1A1,A2), consistent with previous findings (Dettmer et al., 2010; Rosemond et al., 2011), and also of the nuclear rim (Fig. 1A1; this is also visible with COS-7 cells in fig. 5A of Rosemond et al., 2011). We subsequently constructed a stable cell line, HeLa-TMEM147-GFP, constitutively expressing C-terminally GFP-tagged TMEM147. In these cells, TMEM147–GFP displayed the same distribution as the FLAG-tagged version (Fig. 1B1,B2) and confirmed colocalization at the ER upon double labeling with the ER marker protein calnexin (Fig. 1C1–C3) and overlap at the NE upon double labeling with the INM marker Lap2β (Fig. 1D1–D3).

Silencing of TMEM147 downregulates protein levels of LBR

To probe the function of TMEM147, we used RNAi as a tool. We established conditions for reliable siRNA-mediated silencing of *TMEM147*: typically, *TMEM147* mRNA levels were reduced down to 2.10±1.87% (mean±s.e.m.) or by a factor of 47.42 (P<0.0001) compared to what was detected with negative control silencing (mock silencing without siRNAs), as assessed with RT-qPCR (Fig. 2A). In silenced HeLa cells, TMEM147 protein levels, as assessed by quantitative western blot (WB) analysis, represented only 13.36±2.27% (mean±s.d.; P=0.0011) of negative control levels (Fig. 2B,C). When silencing was repeated in the stable HeLa-TMEM147-GFP cell line, it was accompanied by loss of GFP signal in immunofluorescence experiments (as a proxy for TMEM147–GFP expression) in silenced cells only, and not in negative control cells (Fig. 2D, compare D2 and D4), and by a marked reduction of signals for both native TMEM147 and TMEM147–GFP proteins as determined by WB analysis (Fig. 2E).

One consistent observation with *TMEM147* silencing was decreased cell viability compared with negative control cells, specifically affecting growth at late stages post-transfection (48–72 h) (Fig. 3A). In addition, the most striking result upon *TMEM147* silencing was our observation of a concomitant drastic reduction of levels of INM LBR, which could be detected at earlier time points (already by 48 h). As shown by representative WB experiments in Fig. 3B, LBR is consistently and significantly downregulated. Quantification showed LBR protein levels reaching only 9.93±6.23% (P=0.0065; mean±s.d.) of negative control levels (Fig. 3C), a reduction closely resembling that typically obtained for the TMEM147 protein itself (Fig. 2C). By comparison, the relative levels of emerin, another INM integral protein, and those of the protein-folding chaperone and ER integral protein calnexin, were not detectably altered (Fig. 3B).

The defining reduction of LBR protein was also visualized by confocal microscopy, revealing that specifically in *TMEM147*-silenced cells, LBR is hardly detectable at the INM (Fig. 3, compare panels D3 and D6), while lamin A, a nuclear lamina constituent demarcating the INM, is essentially unaffected (Fig. 3D2 and D5). The loss of immunofluorescence signal for LBR upon *TMEM147* silencing in HeLa cells (also seen by wide-field microscopy; Fig. S1A1–B3) was recapitulated in the stable HeLa-TMEM147-GFP cell line, in which loss of GFP signal (Fig. S1C1,D1) was accompanied by corresponding disappearance of LBR label in the same cells (see Fig. S1C2,D2, and C3 and D3 for overlays).

We sought to further examine the specificity of the observed effect of *TMEM147* silencing on LBR protein by utilizing an alternative siRNA (oligo#2), targeting a more downstream exon sequence than that used in the previous experiments (oligo#1) (#oligo1 and oligo#2 are shown in Fig. S2A, displaying part of the gene sequence and a TMEM147 protein membrane topology model). Silencing of *TMEM147* with oligo#2 not only effectively reduced TMEM147 protein levels but, again, also decreased LBR

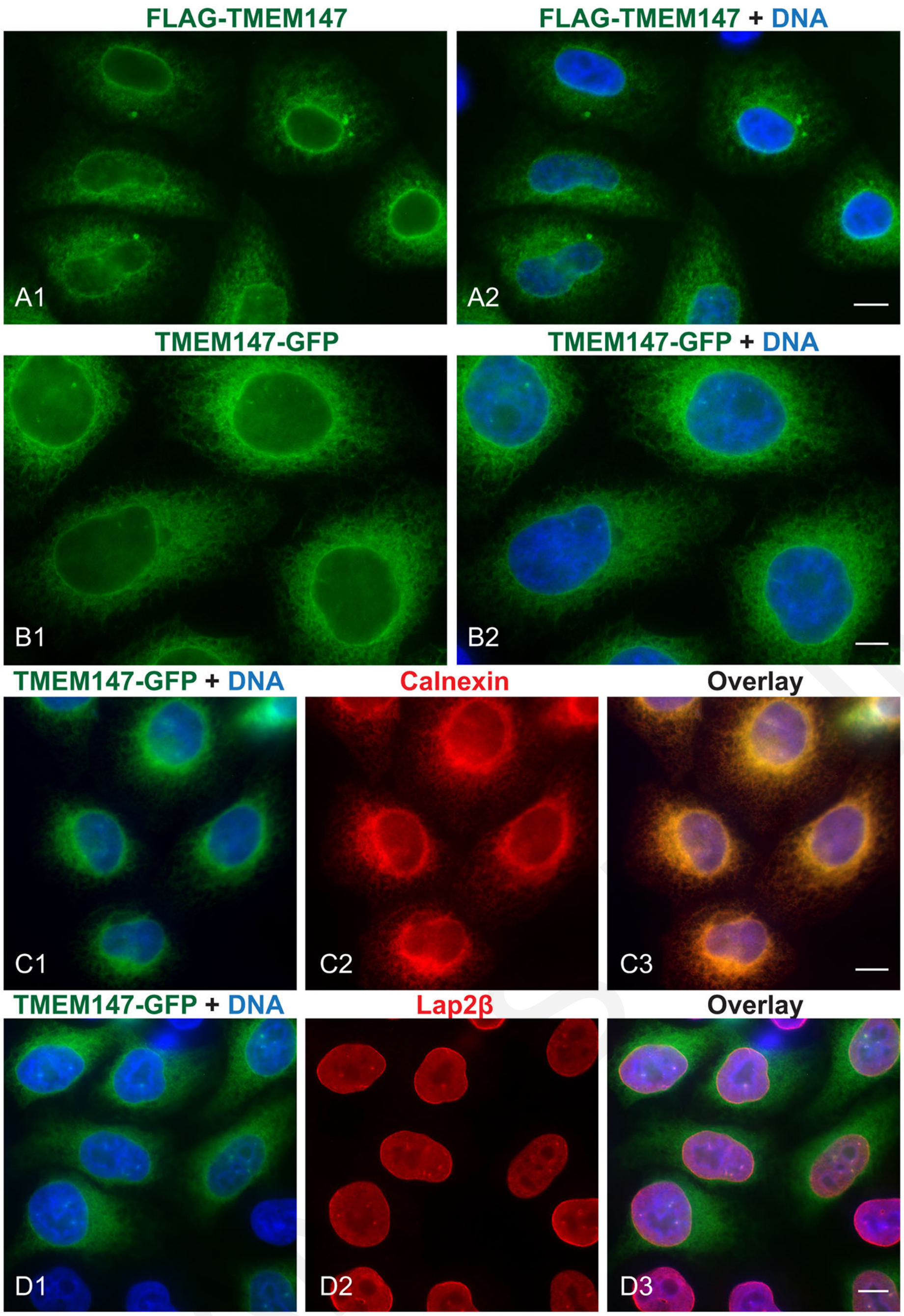

Fig. 1. Localization of TMEM147 at the ER and NE. (A1,A2) Immunofluorescence images of HeLa cells transiently transfected with plasmid expressing FLAG–TMEM147 reveal labeling of the ER and NE. FLAG immunoreactivity corresponds to green fluorescence (A1) and nuclear counterstain by Hoechst to blue fluorescence in overlay image (A2). (B1,B2) Immunofluorescence images of the TMEM147–GFP stable HeLa cell line, similarly, exhibit GFP fluorescence at the ER and nuclear rim (B1). Nuclei in blue in overlay image (B2). (C1–C3) Confirmation of ER labeling of TMEM147–GFP. Overlay of GFP (green) and nuclear staining (blue) is shown in C1. Concurrent immunolabeling for ER marker calnexin (red; C2) reveals a signal that overlaps with GFP signal in overlay image of all colors (C3). (D1–D3) Confirmation of NE labeling of TMEM147–GFP. GFP fluorescence (green; D1) and INM marker protein Lap2β immunofluorescence (red; D2) displays a yellow rim of overlap around the nucleus in overlay image D3. Scale bars: 10 µm (A,C,D); 5 µm (B).

levels, as observed by WB analysis (Fig. S2B), and visibly reduced LBR immunofluorescence signal, compared to negative control cells (Fig. S2, compare panels C2 and D2).

These data, therefore, show that reduction of TMEM147 results in a concomitant reduction of LBR protein at the INM.

Silencing of TMEM147 causes mislocalization of LBR to the ER

To analyze the cellular phenotype resulting from *TMEM147* silencing and its specific effect on LBR in more depth, we conducted a quantitative morphometric comparison in four independent experiments of *TMEM147*-silenced cells (n=48 cells) and negative control cells (n=55) labeled with anti-LBR antibody and Hoechst stain and optically sectioned by confocal microscopy (Fig. 4A1 and A2). Quantification of LBR mean fluorescence intensity in all cells was in line with our quantification of LBR protein levels by WB analysis, and again confirmed the significantly reduced signals in *TMEM147*-silenced vs control cells (P<0.0001) (Fig. 4B1). Interestingly, quantitation of Hoechst fluorescence in the same cells also revealed a clear reduction of Hoechst incorporation, indicative of loss of chromatin compaction specifically in *TMEM147*-silenced cells (P<0.0001) (Fig. 4A3,A4 and B2) and, consistent with this, a clear reduction of histone H3K9 methylation, serving as a heterochromatin marker and anchor of chromatin to the nuclear lamina (reviewed by Mattout et al., 2015) (Fig. 4A5,A6). Additionally, *TMEM147* silencing appeared to introduce changes in nuclear shape (altered sphericity, P<0.0001), presumably due to changes in the shape of the INM, where LBR resides (Fig. 4B3).

Using the stacks of optical sections for all 103 cells analyzed above, we produced 3D-rendered images which revealed a striking

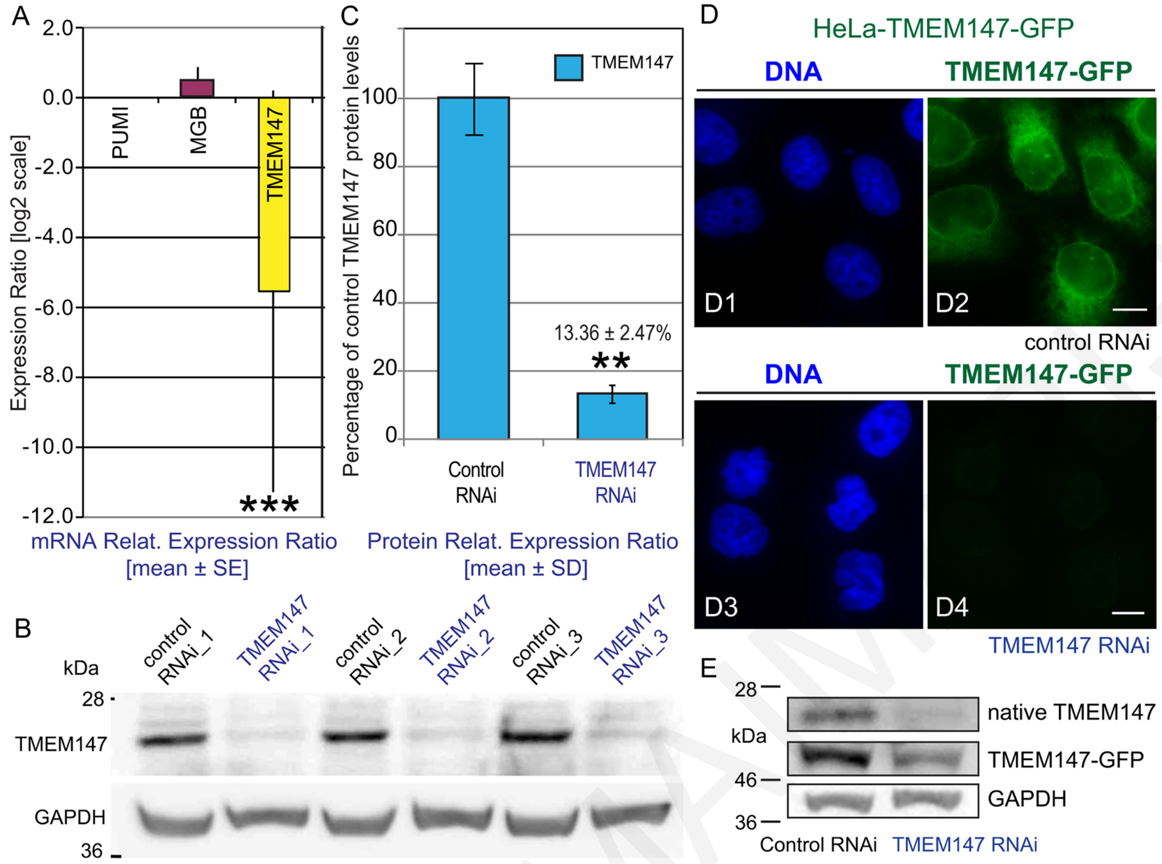

Fig. 2. Confirmation and quantification of silencing of *TMEM147*. (A) Efficiency of *TMEM147*-specific silencing, assessed by RT-qPCR in three independent experiments, depicts an extremely significant (***P<0.0001) normalized *TMEM147* knockdown in silenced cells down to 2.10±1.87% (mean±s.e.m.), expressed as a ratio to the normalized mean negative control value. *PUM1* housekeeping gene mRNA levels were used for sample normalization and *MGB* as an unrelated control. (B) WB analysis of three sets of independent *TMEM147* silencing experiments in HeLa cells showing drastic reduction of the band corresponding to TMEM147, relative to the corresponding negative control silencing reactions. GAPDH immunoreactivity was used as loading control. (C) Quantification of results in B reveals effective reduction of TMEM147 protein levels (normalized to GAPDH) down to 13.36±2.47% (mean±s.d.) of negative control (100±10.35%), with high statistical significance (**P=0.0011) as assessed by a one-tailed heteroscedastic *t*-test. (D) Loss of GFP signal in the TMEM147–GFP stable cell line, as a proxy for TMEM147–GFP protein levels, upon repetition of *TMEM147* silencing, comparing the negative control silencing regime (D1,D2) and *TMEM147*-specific oligonucleotide (D3,D4). Nuclei were counterstained for DNA with Hoechst (blue; D1,D3), and corresponding GFP fluorescence in the same cells is shown in green (D2,D4). Scale bars: 10 µm. (E) Confirmation by WB analysis of effective silencing in TMEM147–GFP HeLa cell line of both native TMEM147 (top panel) and TMEM147-GFP (middle panel). GADPH served as loading control.

mislocalization of LBR, with partitioning of LBR signal to both INM and ER membranes specifically in *TMEM147*-silenced cells (*TMEM147* silencing led to 6.0-fold increased frequency of cells with LBR-positive staining in the ER compared to negative control cells, P<0.0001) (see Fig. 4C,D for representative images; Movie 1 for animation; Table S1 for quantification). Taken together, our analyses suggest that not only does loss of TMEM147 negatively impact LBR production, but it also results in the loss of correct targeting of the residual LBR to the INM and its enhanced mislocalization to the ER. Furthermore, the diminution of LBR levels at the INM is accompanied by chromatin decondensation and a change in nuclear shape.

TMEM147 and LBR proteins physically interact and the C-terminus of LBR is essential for this interaction

Prompted by the observed impact of TMEM147 on LBR protein levels and intracellular targeting, we next investigated, by performing co-immunoprecipitation (co-IP) experiments, whether the two proteins also physically interact. First, conducting IP with an anti-GFP antibody in extracts from the HeLa-TMEM147-GFP or a HeLa-GFP-only stable cell line resulted in the co-selection and detection of endogenous LBR specifically from HeLa-TMEM147-GFP cells, excluding unspecific binding of antibody or GFP to LBR (Fig. 5A, compare lanes c and d). Second, additional IP analyses in HeLa-TMEM147-GFP or HeLa-GFP-only cells that were concurrently transiently transfected with FLAG-tagged full-length LBR detected FLAG–LBR specifically in the bound fraction of TMEM147–GFP samples (Fig. 5B, compare lanes c and f). Thus, these experiments confirm a protein–protein interaction between TMEM147 and LBR and, together with the silencing results, imply a functional interaction between the two proteins.

As mentioned in the Introduction, LBR protein displays a modular organization with involvement of its nucleoplasmic N-terminal domain in chromatin binding and organization at the nuclear periphery, and implication of its membrane-spanning C-terminus in cellular cholesterol biosynthesis. This modular structure thus reflects distinct cellular functions of LBR. To probe the functional association between TMEM147 and LBR, we conducted *TMEM147*-silencing experiments using, in parallel, both wild-type HeLa cells and a stable cell line expressing a GFP-tagged truncated version of LBR, consisting of its full N-terminus plus its first transmembrane domain, HeLa-LBR$_{238}$-GFP (Fig. 6A1; cell line

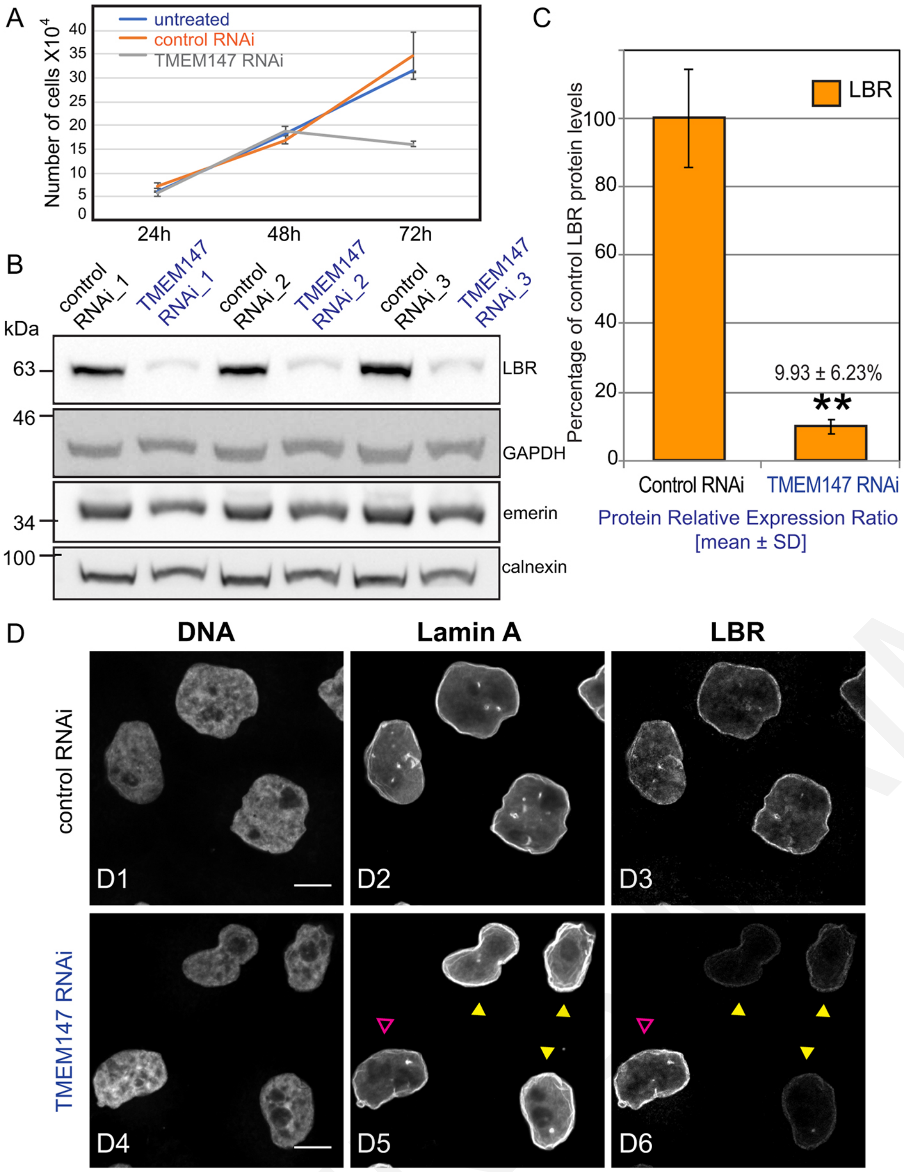

Fig. 3. *TMEM147* silencing results in concurrent significant reduction of LBR protein levels. (A) Growth curves comparing cultures of untreated, control-silenced and *TMEM147*-silenced HeLa cells, seeded in a 24-well plate from an identical number of starting cells (7600) and monitored for 72 h. Cultures were seeded in triplicate, and duplicate measurements were taken from each culture at each time point. Values represent means and bars denote standard deviation of the three experiments, showing a sharp decline in cell numbers in *TMEM147*-silenced cells over time. (B) WB analysis of three sets of independent *TMEM147* silencing experiments in HeLa cells (the same as in Fig. 2A) showing a very large reduction of the band representing LBR, relative to the corresponding negative control silencing reactions. For comparison and as specificity controls, immunoreactivity to INM protein emerin is shown (no change), and to ER integral folding chaperone calnexin (no change). GAPDH immunoreactivity is shown as a loading control. (C) Quantification of results in B determines a reduction of LBR protein levels (normalized to GAPDH) down to 9.93±6.23% (mean±s.d.) of negative control (100±14.35%). The difference is very significant (***P*=0.0065), as assessed by two-tailed unpaired *t*-test with Welch's correction. (D1–D6) Representative examples of maximum intensity projection images by confocal microscopy of nuclei of control-silenced cells labeled for DNA (Hoechst; D1), lamin A as a marker of INM (D2) and LBR (D3), compared with equivalent *TMEM147*-silenced cells (D4,D5,D6). In *TMEM147*-silenced cells, LBR is hardly detectable in the INM (yellow arrowheads in panels D5,D6) (notice one non-silenced cell, indicated with a magenta arrowhead), while lamin A is essentially unaffected. Imaging of different panels was conducted using the same acquisition parameters to allow direct comparison. Scale bars: 10 µm. See also Fig. S1.

by Ellenberg et al., 1997). In these experiments, we assessed and compared the fate of both the endogenous, full-length LBR and the N-terminal LBR$_{238}$–GFP construct, upon *TMEM147* silencing. Owing to their difference in mass, the two forms of LBR can be distinguished in WB analysis with the anti-LBR antibody, while the truncated form is moreover uniquely detectable with anti-GFP antibody (Fig. S3A,B). As expected, *TMEM147* silencing (22.60±6.81% of negative control levels, *P*=0.0025; mean±s.d.) produced a robust reduction of endogenous LBR protein (12.77±11.58% of negative control levels, *P*=0.045) (Fig. 6A2,A3). In contrast, the signal detected for LBR$_{238}$–GFP either with anti-LBR or anti-GFP antibodies upon *TMEM147* silencing exhibited modest reductions relative to control levels (96.39±41.78% and 77.12±18.10%, respectively) that were not statistically significant (Fig. 6A2,A3). This indicated that the observed stability and persistence of the N-terminal truncated LBR, which contrasted with the drastic reduction of the full-length LBR, likely stemmed from a requirement of the LBR C-terminus for the effect of TMEM147 on LBR protein levels to be manifested. We note, however, the lack of LBR promoter elements driving the expression of LBR238–GFP in the stable cell line, which would explain the lack of effect if regulation was only at the transcriptional level.

We, therefore, next directly addressed the interaction between the two proteins. We designed two overlapping truncated, tagged versions of LBR: LBR$_{372}$–GFP (the 'N-terminal construct' encompassing the first 372 amino acids of LBR) and LBR$_{209\text{-}615}$–GFP (the 'C-terminal construct" containing amino acids 209–615) and also employed full-length LBR–GFP as a positive control for TMEM147–LBR interaction (Fig. 6B1). Upon transient transfection in HeLa cells, all three constructs localized appropriately to the nuclear rim, with some partitioning to the ER, likely due to overexpression (Fig. 6B2–B4). We conducted IP experiments with anti-GFP beads, immobilizing the GFP-tagged N-terminal, C-terminal or full-length LBR as bait and screened for the presence of endogenous TMEM147 in the bound fractions. We found that, compared to binding of TMEM147 to the full-length LBR–GFP, the binding to the C-terminal construct appeared equally strong, whereas binding to the N-terminal construct was very markedly reduced (Fig. 6B5, compare bound TMEM147 signals in lanes c, f and i). In agreement, the LBR$_{238}$–GFP N-terminal

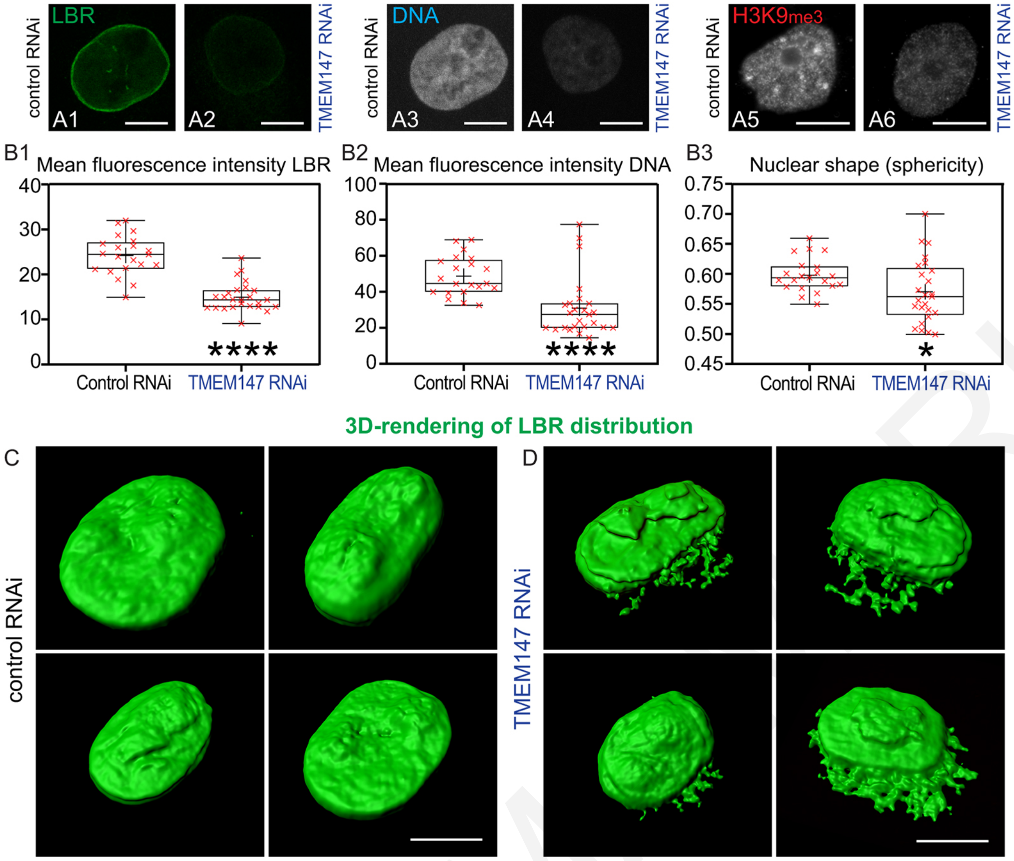

Fig. 4. Further morphometric analysis of LBR changes upon *TMEM147* silencing. (A1,A2) Representative single confocal image of LBR labeling of INM from control-silenced HeLa cell (A1) and loss of LBR labeling in *TMEM147*-silenced HeLa cell (A2). (A3,A4) Maximal projection imaging of stacks of optical sections of the same cells as in A1,A2, respectively, showing drastic reduction of Hoechst labeling of chromatin upon *TMEM147* silencing. (A5,A6) Representative images by widefield microcopy showing clear reduction of H3K9me3 heterochromatin upon *TMEM147*-silencing. Scale bars: 10 µm. (B1) Box-and-whisker plot analysis showing the distribution of all green mean fluorescence intensity (MFI) values for LBR labeling of confocal stacks from four independent silencing experiments for a total of 103 cells (*n*=55 control silencing, *n*=48 *TMEM147* siRNA). Mean value marked with a cross (+). Median value of fluorescence intensity of LBR in *TMEM147* siRNA was 14.34 compared to 24.44 units for negative control. MANOVA revealed significant overall difference between silencing and control treatment in LBR signal intensity (****P<0.0001), additionally Mann–Whitney *U*-test with FDR correction (Q=5%) reported the difference in LBR MFI as an extremely significant discovery (q=0.0002). (B2) Corresponding box-and-whisker plot analysis of the same cells as in B1, exhibiting drastic reduction of Hoechst incorporation, indicative of loss of chromatin compaction in *TMEM147*-silenced cells. Median value of MFI for Hoechst in *TMEM147* siRNA was 27.45 vs 44.66 units for negative control. MANOVA revealed significant overall difference between silencing and control treatment in Hoechst signal intensity (****P<0.0001), additionally Mann–Whitney *U*-test with FDR correction (Q=5%) reported the difference in Hoechst MFI as extremely significant (q=0.0002). (B3) Box-and-whisker plot analysis of the same cells as in B1 and B2, presenting a small but statistically significant difference in nuclear shape (sphericity quantified in arbitrary units in the whisker plot, as defined by the Imaris algorithm) between control- and *TMEM147*-silenced treatments. Median value of *TMEM147* siRNA was 0.5621 units compared to 0.5937 for negative control [MANOVA *P<0.05 and Mann–Whitney *U*-test with FDR correction (Q=5%, q=0.0218)]. In all box-and-whisker plots, whiskers indicate minimum to maximum, boxes indicate 25th to 75th percentile, and the central line indicates the median. (C,D) Collections of images of 3D-rendering (Imaris software) of optical section stacks from representative control-silenced (C) and *TMEM147*-silenced cells (D), displaying a clear change in the distribution of LBR signal. Pronounced decoration of additional, ER-bound LBR is detected in *TMEM147*-silenced cells in comparison with control cells displaying the more typical targeting of LBR to the NE. For illustrative purposes, the displays were generated with the same color intensity, not reflecting the profound changes in fluorescence intensity of LBR labeling, as quantified in B1. See also Movie 1. Scale bars: 10 µm.

construct, used in Fig. 6A1–A3, was also unable to bind the native TMEM147, as was the GFP-only bait, used as a negative control (Fig. S3C). These results seem consistent with a protein interaction of TMEM147 with the C-terminus of LBR, and in agreement with the likely topology and orientation of LBR in the INM. Taken together, the results suggest that this interaction at the C-terminus of LBR is the basis of the functional interaction between the two proteins.

Silencing of TMEM147 impacts cellular cholesterol homeostasis

On the basis of our findings that there is a physical and functional interaction between TMEM147 and the C-terminus of LBR, known to exhibit essential C14-sterol reducing activity in cellular cholesterol synthesis, we then investigated whether knockdown of TMEM147 may also impact other key sterol reductases in the same pathway.

Interestingly, quantitative WB analysis of protein levels of 7-dehydrocholesterol reductase DHCR7, the sterol reductase catalyzing the ultimate step in cholesterol biosynthesis and localized, similar to TMEM147, at both ER and the INM (Koczok et al., 2019), revealed that it, too, showed significant reduction to only 32.78±7.98% (mean±s.d.) of control levels specifically upon *TMEM147* silencing in HeLa cells (P=0.026) (Fig. 7A,B). Repetition of these experiments with the stable HeLa TMEM147-GFP cells confirmed similar reductions (Fig. 7A and see legend).

This finding was supported by our additional discovery that DHCR7 was one of the proteins identified as interacting with

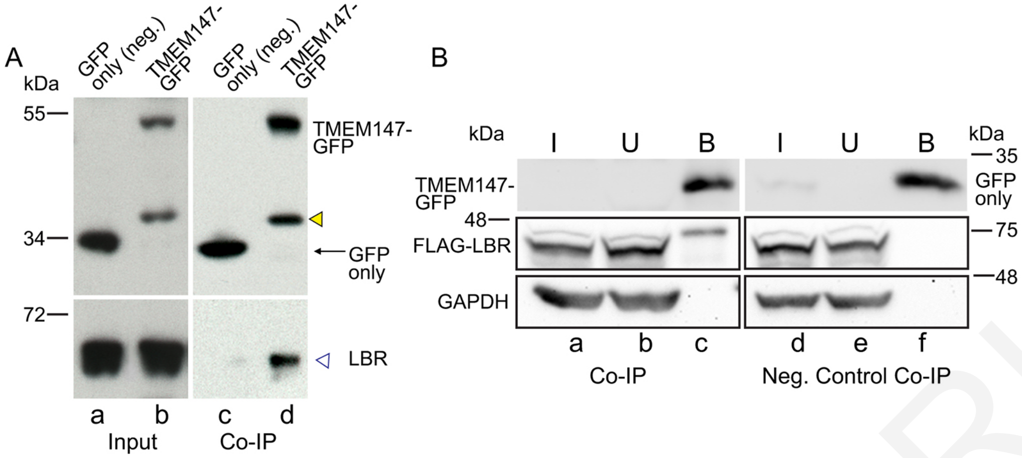

Fig. 5. TMEM147 and LBR proteins interact. (A) The TMEM147–GFP HeLa stable cell line (lanes a,c) or a GFP–only stable line (lanes b,d) were subjected to IP, using anti-GFP beads. Input and GFP-bound fractions were analyzed by WB. Only TMEM147–GFP co-immunoprecipitated the native LBR protein (lane d), while GFP-only, used as a negative control, did not give a signal (lane c). A GFP-containing additional band (lanes b, d), corresponding to an internal translation initiation product, is indicated by a yellow arrowhead. (B) The TMEM147–GFP HeLa stable cell line (left panel) or a GFP-only stable line (right panel) were transiently transfected with a plasmid expressing FLAG–LBR and subjected to IP, using anti-GFP beads. Input, unbound and bound fractions were analyzed by WB. The presence of FLAG–LBR was detected uniquely in the GFP-bound fraction of TMEM147–GFP cells (lane c) but not of GFP-only expressing cells (lane f). I, input; U, unbound fraction/supernatant; B, bound fraction.

TMEM147–GFP by anti-GFP IP, followed by liquid chromatography coupled with tandem mass spectrometry (Fig. S4). In this proteomic analysis, LBR came up as another enriched hit, consistent with our other results, as did the known TMEM147-interacting proteins nicalin and NOMO (Dettmer et al., 2010), validating the analysis (Fig. S4). Thus, TMEM147 and DHCR7 physically interact, and, similar to what is seen for LBR, DHCR7 protein levels are significantly reduced in the absence of TMEM147. TM7SF2, a second key C14 sterol reductase catalyzing the NADPH-dependent reduction earlier in the cholesterol biosynthetic pathway, was also identified as an interacting protein but, in the absence of a reliable antibody, we were unable to validate this further.

We extended our analysis by assessing whether *TMEM147* silencing affected transcription levels of *LBR*, *DHCR7* and *TM7SF2*. Quantification by RT-qPCR indicated that, upon *TMEM147* silencing, there was a clear concurrent reduction of gene expression for both *LBR* and *DHCR7* (Fig. 7C; *P*<0.001 for both *LBR* and *DCHR7*), consistent with the reductions already identified at protein level and the corresponding protein–protein interactions between TMEM147 and these key reductases. In contrast, the level of mRNA for the reductase *TM7SF2* remained essentially unchanged (Fig. 7C). We repeated a quantitative analysis of *TMEM147*, *LBR*, *DHCR7* and *TM7SF2* expression levels, this time from cells grown in parallel in either complete or lipid-restrictive medium (no serum) (Fig. S5). We found *LBR* to be constitutively expressed and unresponsive to lipid starvation (Fig. S5B), in agreement with previous reports (Tsai et al., 2016) and the same applied to the expression of *TMEM147* (Fig. S5A). Furthermore, we observed that negative control cells (as previously reported by Bennati et al., 2008 and Tsai et al., 2016) but also *TMEM147*-silenced (thus *LBR*-downregulated) cells upregulated *TM7SF2* under lipid restriction (Fig. S5C). Interestingly, we detected an even stronger upregulation of *DHCR7* under lipid restriction, and this response was also directly correlated with *TMEM147*/*LBR* expression (Fig. S5D).

Overall, the interconnection found between TMEM147 and both LBR and DHCR7 was remarkable and raised the possibility of a resulting impact of TMEM147 depletion on cellular cholesterol biosynthesis. We thus next employed a full lipidomic analysis to directly measure lipids, including total cellular cholesterol and cholesteryl esters and also quantify the cholesteryl ester species profile (Table S2). We conducted a multivariate analysis of the lipidomics data; a principal component analysis (PCA) of the cellular lipidome (Fig. S6A) indicated that *TMEM147*-silenced cells separated from the control-silenced and untreated cells along the first principal component. Using the loadings plot, we identified that cholesterol and cholesteryl esters (CE) were among the most significant features that drive this separation (Fig. S6B). Surprisingly, total free cholesterol cellular levels in *TMEM147*-silenced cells exhibited a small but significant increase (by 13.4%) when compared with negative control cells (Fig. 7D). Specifically, free cholesterol represented 16.36±0.45 mol% in *TMEM147*-silenced cells vs 14.43±0.16 in negative control (*P*<0.05; mean±s.d.) (Fig. 7D). At the same time, total levels of cholesteryl esters (CEs) were greatly reduced, by 40.5% (5.80±1.68 mol% in *TMEM147*-silenced cells versus 9.74±1.83 compared to negative control cells; *P*=0.05) (Fig. 7D). In addition, quantitation of the full spectrum of lipid species in CEs displayed *TMEM147* silencing-specific alterations (both decreases and increases) in several lipid species (Fig. S6C) with decreases in saturated and short lipid species and increases in several polyunsaturated long fatty-acyl chains of the esterified cholesterol (Fig. S6C).

CEs, as the intracellular storage forms of excess cholesterol, are of central importance to cholesterol homeostasis, and their formation is a measure of the availability of cellular free cholesterol (Luo et al., 2020); reduced CE levels would be consistent with downregulation of sterol reductase activity in *TMEM147*-silenced cells. At the same time, levels of total free cellular cholesterol in *TMEM147*-silenced cells, which were found to be modestly increased in our experiments, represent the contribution of both cellular synthesis as well as that of cholesterol uptake from the growth medium. To specifically determine the contribution of cholesterol uptake in the different cell groups, we therefore conducted cholesterol uptake assays using fluorescently labeled cholesterol, comparing negative control and *TMEM147*-silenced cells under different growth conditions. Cells were grown, in parallel, in complete or lipid-

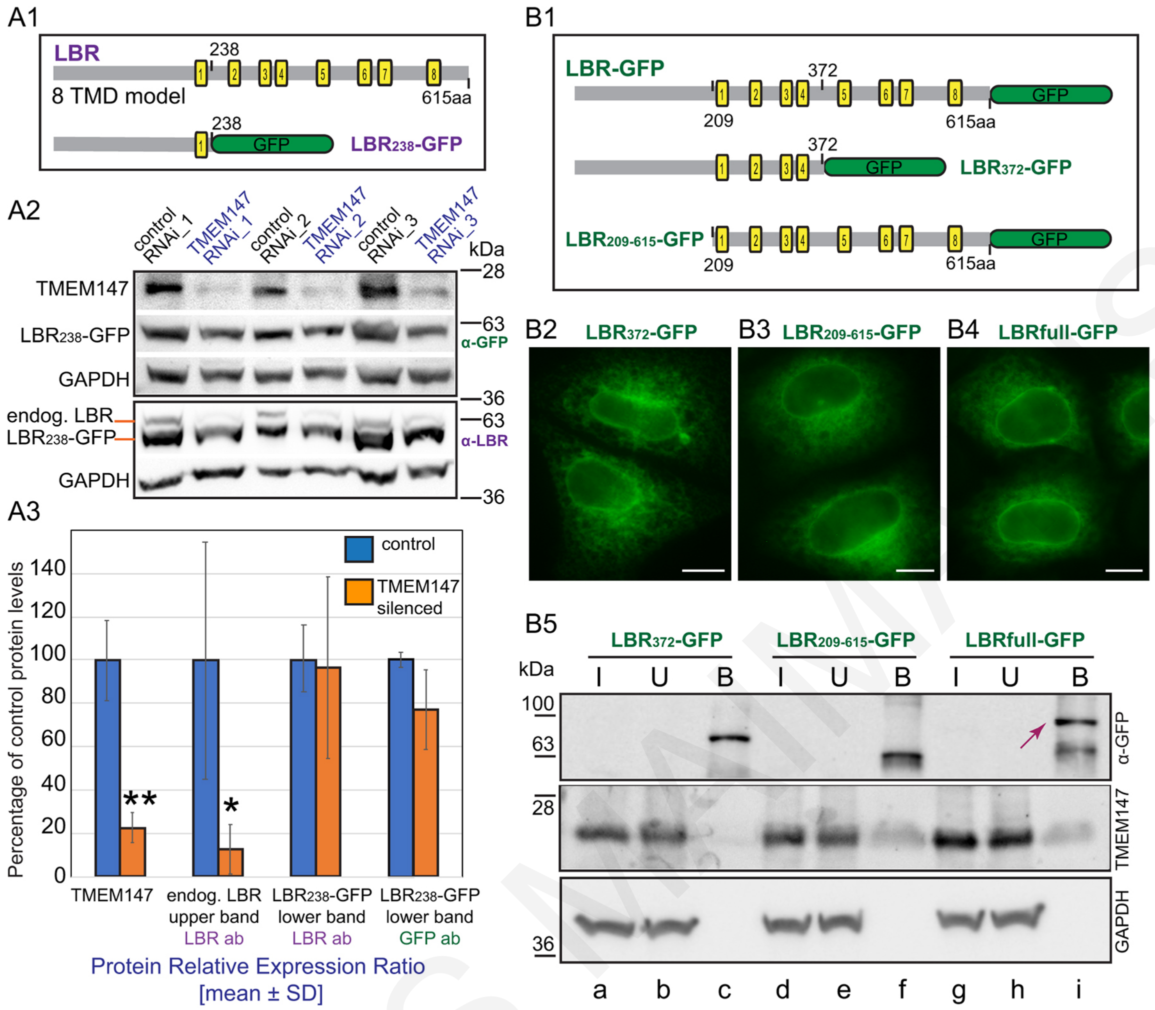

Fig. 6. The C-terminus of LBR is essential for its interaction with TMEM147. (A1) Model of an eight transmembrane domain (TMD) organization of LBR protein; yellow blocks correspond to predicted TMDs (based on LBR transmembrane helix prediction at Uniprot). Below, the structure of a C-terminally truncated construct of LBR containing the first 238 aa fused C-terminally with GFP, as expressed in a stable LBR238-GFP HeLa cell line used in the experiments presented in panels A2 and A3. (A2) WB analysis of three sets of independent *TMEM147* silencing experiments in the LBR$_{238}$–GFP stable HeLa cell line with the top panel confirming efficient depletion of native TMEM147 protein. Probing with anti-GFP antibody, specifically detecting the GFP-tagged N-terminal truncated version of LBR$_{238}$-GFP protein, reveals a modest reduction of the band corresponding to LBR$_{238}$–GFP relative to the equivalent negative control silencing reactions. GAPDH immunoreactivity in the same blots (third panel) was used as loading control. Application of anti-LBR antibody in parallel (fourth panel) allows the detection of both the endogenous full-length LBR (upper band, orange position mark) and LBR$_{238}$–GFP (lower band, orange mark) (see also Fig. S3A); knockdown of full-length LBR appears more pronounced than reduction of LBR$_{238}$–GFP signal. GAPDH immunoreactivity in the same blot (bottom) is shown as a loading control. (A3) Quantification of results in A2 confirming effective reduction of TMEM147 protein levels (normalized to GAPDH) down to 22.60±6.81% (mean±s.d.) of negative control (***P*=0.002). Furthermore, comparison of endogenous LBR levels (upper band in bottom panel in A2) shows a drastic reduction in *TMEM147*-silenced cells, consistent with our other findings (Fig. 3, Figs S1 and S2), to 12.77±11.58% of negative control (**P*=0.04). In contrast, the truncated construct LBR238-GFP (lower band in bottom panel in A2) shows small and statistically non-significant reduction upon *TMEM147* silencing, as revealed both by LBR and GFP immunoreactivity [96.39±41.78% (*P*=0.7) and 77.12±18.10% (*P*=0.06), respectively]. The impact of *TMEM147* silencing on protein levels was assessed without assuming a consistent s.d. and using individual two-tailed unpaired *t*-tests for TMEM147, the upper and lower LBR bands and GFP values, normalized to GAPDH. (B1) Schematic summarizing the 'N-terminal' (LBR$_{372}$–GFP) and 'C-terminal' constructs (LBR$_{209\text{-}615}$–GFP), both fused C-terminally with GFP, as compared to full-length LBR. These three constructs were used for transient transfections in the experiments shown in B2–B5. (B2–B4) Representative images of the expression of LBR$_{372}$–GFP, LBR$_{209\text{-}615}$–GFP and full-length LBR–GFP in HeLa cells (green GFP fluorescence), displaying appropriate localization at the NE and extending to the ER (possibly due to overexpression). Scale bars: 10 µm. (B5) HeLa cells transiently transfected in parallel with plasmids expressing LBR$_{372}$–GFP, or LBR$_{209\text{-}615}$–GFP or full-length LBR–GFP, were subjected to IP using anti-GFP beads. Input (I), unbound (U) and bound (B) fractions were analyzed by WB to compare the presence of native TMEM147 in each case. Top panel confirms binding of GFP-tagged versions of LBR in the bound fractions as bait (full-length LBR-GFP indicated by red arrow). Middle panel indicates co-selection of native TMEM147 in the bound fractions of full-length LBR–GFP (lane f) and of the bound fraction of C-terminal construct LBR$_{209\text{-}615}$–GFP (lane i) but only a barely detectable signal in the bound fraction of N-terminal construct LBR$_{372}$–GFP (lane c). Bottom panel displays GAPDH immunoreactivity as a loading control. This result was representative of multiple repetitions of the experiment. See also Fig. S3C for extra results and negative controls.

restrictive medium (no serum) or in the presence of cholesterol transport inhibitor U-18666A (as a positive control of increased uptake) (Fig. 7E). In all conditions tested, normalized cholesterol uptake was markedly and significantly increased in *TMEM147*-silenced cells in comparison with negative controls. In particular, uptake was doubled in restrictive medium conditions relative to negative control, and in complete medium it increased by 2.3-fold (Fig. 7E). Increased uptake, to counteract impaired cellular

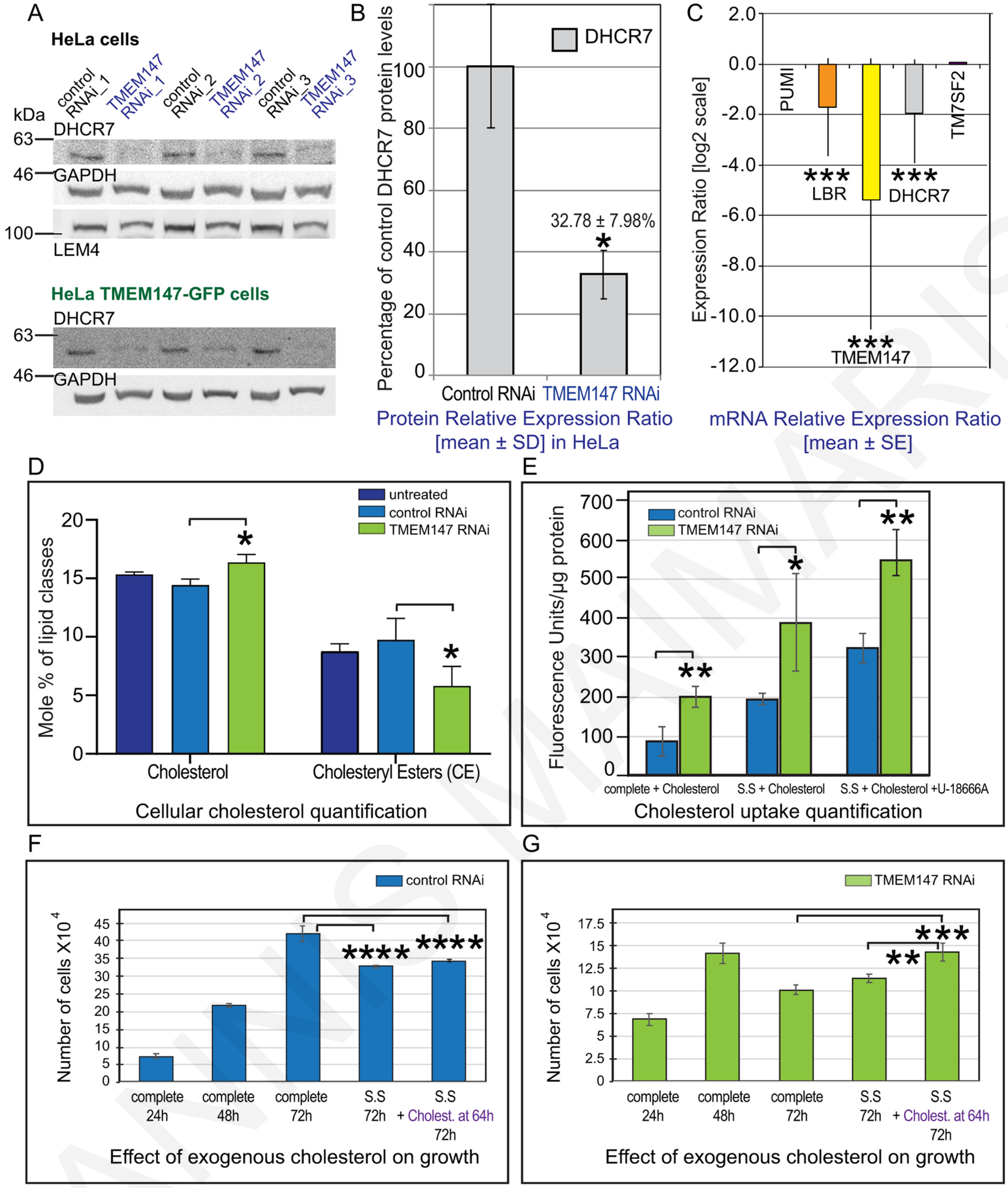

Fig. 7. See next page for legend.

biosynthesis due to the reduction of both LBR and DHCR7, would explain the maintenance of free cholesterol levels in *TMEM147*-silenced cells grown in non-restrictive media (Fig. 7D).

Consistent with these findings was the effect of cholesterol rescue in growth assays. Control and *TMEM147*-silenced cells were grown either in complete medium or in complete medium followed by a 24-h lipid restriction (no serum) either on its own or in combination with exogenous cholesterol, and cell viability was monitored at different time points (Fig. 7F,G). Addition of exogenous cholesterol for the last 8 h during the 24-h lipid restriction rescued growth and restored it by 72 h to the same levels [$(14.27{\pm}0.95){\times}10^4$ cells] as those observed for cells at 48 h in complete medium [$(14.06{\pm}1.13){\times}10^4$ cells], specifically in *TMEM147* silencing (Fig. 7G); in comparison, equivalent *TMEM147*-silenced cells at 72 h without cholesterol showed the typical drastic reduction in viability [$(11.35{\pm}0.48){\times}10^4$ *TMEM147*-silenced cells with serum starvation at 72 h versus $(14.3{\pm}0.95){\times}10^4$ cells with serum starvation plus cholesterol at 72 h (P=0.0046), or $(10.10{\pm}0.48){\times}10^4$ *TMEM147*-silenced cells in complete medium at 72 h compared again with cells in the presence of cholesterol (P=0.0003)] (Fig. 7G). Cholesterol addition had only a very modest positive effect on lipid-restricted negative control cells (Fig. 7F). Interestingly, we observed that in *TMEM147*-silenced cells that were already growth affected at 48 h, subsequent lipid depletion at 48 h had essentially no additional aggravating impact compared to the rapid growth decline manifested by 72 h in complete medium, in contrast to control

Fig. 7. Silencing of *TMEM147* impacts cholesterol metabolism in HeLa cells. (A) WB analysis of three sets of independent *TMEM147* silencing experiments in HeLa cells (top set) or TMEM147–GFP HeLa cells (bottom set) showing a large decrease of the band corresponding to C14-sterol reductase DHCR7, relative to the corresponding negative control samples. Immunoreactivity to the ER integral protein LEM4 was used as negative control and GAPDH immunoreactivity as loading control. (B) Quantification of results in A showing a reduction of DHCR7 protein levels (normalized to GAPDH) in *TMEM147*-silenced cells down to 32.78±7.98% (mean±s.d.) of negative control (100±20.01%), with statistical significance (*P=0.026), as assessed by a two-tailed heteroscedastic *t*-test (Microsoft Excel). The corresponding value for TMEM147–GFP HeLa cells in A was down to 36.80±19.25% of negative control value (*P=0.04). (C) Assessment by RT-qPCR in three independent experiments of *LBR*, *DHCR7* and *TM7SF2* mRNA levels in *TMEM147*-silenced cells showing that there is a highly statistically significant co-ordinated downregulation of *LBR* and *DHCR7* (***P<0.0001), but no change of *TM7SF2*, expressed as a ratio to the normalized mean control value. Specifically, *LBR* mRNA levels are down by 3.29 times or to 30.40±26.08% (mean±s.e.m.) and *DHCR7* by 3.84 times or to 26.0±24.04% of negative control levels. *TM7SF2* is essentially unchanged compared to negative control (increase by a factor of 1.058 and non-significant P=0.09). *L19* and *PUM1* were used as reference genes for normalization. Error bars correspond to the s.e.m. of triplicate analysis. (D) Total free cellular cholesterol levels and total cholesteryl ester (CE) levels, as determined by LC/MS analysis, comparing untreated cells, negative control silenced and *TMEM147*-silenced cells in three independent experiments. Changes in cholesterol or CE, for a comparison of *TMEM147*-silenced to control-silenced cells, were significant as assessed by multiple *t*-test with multiple testing correction based on FDR correction (Q=5%). Specifically, free cholesterol in *TMEM147*-silenced cells was increased to 16.36±0.45 mol% vs 14.43±0.16 in negative control cells (q=0.017). Total CE were reduced in *TMEM147*-silenced cells to 5.80±1.68 mol% vs 9.74±1.83 in negative control cells (q=0.0267). Results are mean±s.d. (E) Cholesterol uptake assay comparing negative control silenced and *TMEM147*-silenced cells in three independent experiments with cells grown in complete medium, or serum-free medium or serum-free medium in the presence of 1 µM cholesterol transport inhibitor U-18666A. Emission of fluorescently labeled cholesterol was normalized to protein content in each well and background fluorescence was subtracted from equivalent measurements per condition without cholesterol. Changes in all cases were significant, as assessed by multiple *t*-test with multiple testing correction and FDR correction (Q=5%). In particular, cholesterol uptake in *TMEM147*-silenced cells in complete medium was increased to 199.39±26.14 emission units/µg protein vs 86.58±35.65 (mean±s.d.) in negative control cells (**q=0.006); in *TMEM147*-silenced cells in restrictive, serum-starvation (S.S) medium, it was increased to 388.43 ±123.93 vs 193.50±14.17 (*q=0.019); in restrictive medium plus transport inhibitor to 548.80±56.17 vs 324.22±36.85 (**q=0.005). (F,G) Assessment of growth in three independent experiments, comparing cultures of control-silenced (F) and *TMEM147*-silenced cells (G), seeded in identical numbers and monitored for 72 h (triplicate measurements/time point). Cells were grown in complete medium for 72 h, or in complete medium for 48 h and then with serum starvation (S.S) until 72 h, or in complete medium for 48 h and with serum starvation until 72 h with addition of cholesterol at 64 h. Values represent means±s.d. Addition of cholesterol in lipid restricted *TMEM147*-silenced cells (G) restores growth at 72 h to values similar to those in cells at 48 h in complete medium and this does not happen in the absence of cholesterol [$(11.35\pm0.48)\times10^4$ *TMEM147*-silenced cells with S.S at 72 h vs $(14.3\pm0.95)\times10^4$ with S.S plus cholesterol at 72 h (**P=0.0046), or $(10.10\pm0.48)\times10^4$ *TMEM147*-silenced cells in complete medium at 72 h vs, again, cells with S.S and cholesterol addition (***P=0.0003)]. In F, differences between cell numbers at 72 h in complete medium vs S.S without cholesterol or vs S.S with cholesterol addition remain significantly reduced (****P<0.0001 for both comparisons), indicating that addition of cholesterol does not improve cell viability.

cells (Fig. 7F,G), suggesting that the detrimental impact of *TMEM147* silencing on growth was severe and already developing in complete medium (see also Fig. 3A). This is different to the observations of Tsai et al. (2016), where decreased viability of LBR-knockout cells occurred under lipid restriction only, and likely underlines the more severe phenotypes resulting from TMEM147-induced depletion of both LBR and DHCR7.

In conclusion, our work provides evidence to indicate a role for TMEM147 as a novel functional modulator of cholesterol homeostasis in cells.

DISCUSSION

Previously described roles for TMEM147 included membrane complex stabilization (Dettmer et al., 2010), acetylcholine receptor trafficking (Rosemond et al., 2011) and NF-κB activation (Ota et al., 2019). In this work, we present evidence for physical and functional interactions between the ER and INM transmembrane protein TMEM147 and the well-characterized LBR protein, which, through its modular structure, serves both as a heterochromatin organizer at the nuclear lamina and a sterol reductase in the late steps of cholesterol biosynthesis. We discovered that downregulation of *TMEM147* in human cells induces a sharp reduction in LBR protein levels and mislocalization of the remaining LBR to the ER at the expense of its typical localization at the INM. Furthermore, we discovered that TMEM147 physically interacts with DHCR7, another key sterol reductase in cholesterol biosynthesis in cells. Interestingly, *LBR* and *DHCR7* exhibit co-ordinated reductions in gene expression upon *TMEM147* knockdown, in contrast with what was seen with the sterol reductase TM7SF2, the gene expression of which appeared to be unaffected by downregulation of *TMEM147*. Consistent with these data on interactions and gene expression, we identified changes in cellular cholesterol and cholesteryl ester levels as well as in cellular cholesterol uptake in *TMEM147*-silenced cells, supporting the idea that TMEM147 functions as an important regulator of cholesterol homeostasis in cells.

Cholesterol is the major sterol in terrestrial vertebrates and critical for normal growth, development and hedgehog signaling in mammals. It is a regulator of membrane fluidity and organization, a key component of lipid rafts in the plasma membrane, and important in myelin formation in nerves (reviewed by Platt et al., 2014). Most mammalian cell types modulate the cholesterol content of their membranes by finely balancing cellular cholesterol biosynthesis, uptake by receptor-mediated endocytosis and export of esterified cholesterol via ABC transporters. Our findings reveal that in the absence of TMEM147 (and consequent depletion in the levels of both LBR and DHCR7), uptake of cholesterol is increased, presumably to counteract the reduction of endogenously produced cholesterol and its cholesteryl esters. Despite increased uptake, changes in cholesterol metabolism may account for the observed cell death at late stages of *TMEM147* silencing, compared to negative control cells, even in the presence of complete medium. Addition of exogenous cholesterol increased cell viability, but we cannot formally exclude additive detrimental effects of TMEM147 silencing contributing to increased cell death rates.

Our finding that *TMEM147* downregulation in HeLa cells, resulting in concomitant downregulation of *LBR* (and *DHCR7*), does not seem to affect gene expression of the reductase TM7SF2, indicates that there are distinct forms of transcriptional regulation for LBR and TM7SF2, even though both proteins are thought to catalyze the same enzymatic step in cholesterol biosynthesis. These results appear in agreement with both the study by Bennati et al., 2008, in which *Tm7sf2*$^{-/-}$ mice had normal LBR protein levels, and the more recent analysis by Tsai et al., 2016, in which primary human cells or cell lines (including HeLa cells) did not show co-ordination of gene expression between *LBR* (constitutively expressed) and *TM7SF2* (sterol-inducible), either under standard conditions or under prolonged lipid starvation. During mouse liver regeneration, TM7SF2 and LBR are again differently modulated and absence of TM7SF2 does not impair cholesterol biosynthesis

(Bartoli et al., 2016). TM7SF2 and LBR were also found to undergo differential post-translational regulation, with TM7SF2 manisfesting sterol-dependent turnover while LBR remained stable (Capell-Hattam et al., 2020). The unresponsiveness of *TM7SF2* to changes in *LBR* expression, revealed in all of these studies and by our experiments, is somewhat counterintuitive and would challenge the notion that TM7SF2 can compensate for cholesterol biosynthesis in the absence of functional LBR in order to sustain cholesterol levels (Wassif et al., 2007).

We report here both a novel protein–protein interaction between TMEM147 and DHCR7, a co-ordinate gene expression between *LBR* and *DHCR7* in response to *TMEM147* depletion in normal conditions, and an induction of *DHCR7* under lipid restriction that is modulated by *TMEM147*/*LBR* expression. Despite the wealth of studies on DHCR7 as the cause of SLOS, its functional relationship and molecular interactions with LBR have remained relatively obscure. It would appear that TMEM147 as an upstream positive regulator impacts both LBR and DHCR7, affecting their gene expression and protein levels in a molecular mechanism that remains to be investigated. Interestingly, protein interaction data (https://www.ebi.ac.uk/intact/interactors/id:Q9BVK8), include experimental evidence for physical interaction between TMEM147 and the emopamil-binding protein EBP (or D8D7I), a 3-β-hydroxysteroid-δ(8),δ(7) isomerase catalyzing the conversion of δ(8) sterols to their corresponding δ(7) isomers in cholesterol biosynthesis, upstream of DHCR7 (Silve et al., 1996). EBP (also known as D8D78I), like TMEM147 and LBR, localizes to both the ER and the NE, and its mutations impair cholesterol synthesis and cause X-dominant chondrodysplasia punctata with ichthyosis (Braverman et al., 1999; Liu et al., 1999). EBP displays co-ordinate transcription with DHCR7, with which it also forms a bifunctional complex (ChEH, cholesterol-5-6-epoxide hydrolase) (Kedjouar et al., 2004; de Medina et al., 2010), raising the possibility that the pattern of common gene expression of LBR and DHCR7 influenced by TMEM147 may include further enzymes of late cholesterol synthesis steps, like EBP.

Our observation of LBR mislocalization to the ER in the absence of TMEM147 is intriguing and reminiscent of its similar partitioning when the nucleoporin ELYS (also known as AHCTF1) is downregulated (Clever et al., 2012; Mimura et al., 2016). Following its synthesis, LBR diffuses laterally through the ER and the nuclear pore membrane domains, via lateral peripheral channels of the complexes, before becoming anchored at the INM by binding, via its N-terminus, to the nuclear lamina, heterochromatin or other proteins (Ellenberg et al., 1997; Makatsori et al., 2004; Ungricht et al., 2015; Boni et al., 2015; Giannios et al., 2017). The vast majority of steady-state LBR is at the INM, as opposed to the ER (Nikolakaki et al., 2017). Not only does the number of nuclear pore complexes thus appear important, but also INM localization of LBR was found to be inhibited by SR phosphorylation of the N-terminal domain, involving kinases CDK, SRPKs or ELYS protein acting on protein phosphatases (Nikolakaki et al., 1996; Tseng and Chen, 2011; Fukuhara et al., 2006; Mimura et al., 2016). An interesting point of discussion has been whether the ability of LBR to contribute to cholesterol synthesis *in vivo* is conditional on its presence at the NE or the ER (Hoffmann et al., 2007). If LBR localization is indeed critical for its enzymatic activity, then it would appear that interaction between LBR and TMEM147 is essential for INM targeting of LBR. We found that absence of TMEM147 not only caused a drastic decline of LBR protein levels but also an altered diffusional mobility of LBR and its relocation to the ER. This mislocalization of LBR may further contribute to the impact of LBR reduction on cholesterol synthesis.

Other phenotypic effects that we report, upon *TMEM147* silencing and the associated LBR depletion from the NE, were a change in nuclear shape (but not size or surface area) as well as evidence of loss of chromatin compaction. Both of these features (1) are highly consistent with observed effects upon loss of LBR expression in many studies, and (2) were shown to be tightly entwined in cellular physiology. Specifically, in Pelger–Huët syndrome in humans, mutations resulting in truncated and unstable forms of LBR are accompanied by hypolobulated nuclei in granulocytes (Hoffmann et al., 2002), while in ichtyosis in mice, nuclei are ovoid and with ‘inverted nuclear organization’, that is with heterochromatin masses accumulating internally and non-compacted chromatin at the nuclear periphery (Hoffmann et al., 2007; Shultz et al., 2003). Additionally, it is well documented that in healthy blood granulocyte differentiation in the bone marrow, wild-type LBR is developmentally upregulated as granulopoiesis progresses, relating to both increased nuclear indentation (shaping the characteristic polylobular nuclei) and heterochromatin tethering to the nuclear periphery in mature neutrophils, the main granulocyte cell type (Olins et al., 2008). In myeloid cell line models (human HL-60 and mouse EPRO promyelocytes), correspondingly, the absence of LBR produces profound effects in both nuclear shape and heterochromatin distribution in a dose-dependent manner (Zwerger et al., 2008; Hoffmann et al., 2007; Olins et al., 2010). In the same vein, it was demonstrated that *LBR* knockdown in HeLa cells resulted in redistribution and unfolding of heterochromatin from the INM towards the nucleoplasm (Lukášová et al., 2017). LBR has additionally been proposed as a stimulator of NE growth on the basis of overexpression experiments resulting in NE overproduction, inducing NE invagination and membrane stack formation (Ma et al., 2007).

The evidence linking the generation of nuclear shape with the function of LBR as organizer of underlying heterochromatin is compelling; however, one thought-provoking novel hypothesis, also taking into consideration the question of why there should be a need for cholesterol production specifically at the INM (in addition to the ER), is the idea that cholesterol, becoming readily accessible to the nucleus, may participate in the assembly of nuclear lipid microdomains (‘nuclear lipid rafts’, in analogy to plasma membrane lipid rafts) that may provide specialized chromatin-anchoring platforms, nucleosome-binding domains, or scaffolds for protein organization or oligomerization (Cascianelli et al., 2008; Codini et al., 2016; Silva et al., 2017; Nikolakaki et al., 2017). This possibility was proposed as an explanation of the unique role of LBR in cholesterol biosynthesis, which cannot be compensated for by the ER sterol reductase TM7SF2, even though both proteins catalyze the same reaction (Nikolakaki et al., 2017). If this were indeed the case, it would provide an intriguing and meaningful framework to reconcile and understand the dual and diverging modular structure and functional role of LBR in both nuclear organization/gene expression and cholesterol biosynthesis. And it would illuminate TMEM147 as a putative upstream functional integrator, via its modulation of LBR, of gene expression and cholesterol homeostasis. Dissecting the molecular mechanism through which the novel physical and functional interaction of TMEM147 with LBR impacts both processes is now essential in order to fully understand their cellular interplay.

MATERIALS AND METHODS

Cell culture and generation of the HeLa-TMEM147-GFP stable cell line

HeLa (Kyoto; K; EMBL) cells were cultured in DMEM containing 10% (v/v) fetal bovine serum (FBS), 2 mM glutamine and 50 U/ml of penicillin/

streptomycin (complete medium) and maintained at 37°C in 5% CO_2. For some experiments, cells were grown in lipid restrictive medium (complete medium without FBS). Cells were regularly tested by PCR and Hoechst 33342 staining to ascertain lack of mycoplasma infection.

The stable HeLa K TMEM147-GFP cell line was generated by transient transfection of pEGFPN1-TMEM147 into HeLa K cells. Expressing cells were selected in the complete medium supplemented with 0.5 mg/ml G418 (Invitrogen) and further enriched by FACS.

The HeLa LBR_{238}–GFP stable cell line, expressing a fusion between the first 238 N-terminal amino acids (aa) of human LBR and a C-terminal in-frame GFP sequence, was a gift from Jan Ellenberg (EMBL Heidelberg, Germany).

RT-qPCR for analysis of gene expression

For relative quantification of mRNA in silencing experiments, RT-qPCR was conducted on the CFX96 Real-Time PCR system (Bio-Rad) in 96-well plates and primers specific for either human *TMEM147* (for, 5′-GTACAACGCCTTCTGGAAATG-3′; rev, 5′-ATGCTGTTCTTGGCCACTTT-3′), *LBR* (for, 5′-GGTCGACCACCTAAAAGTGC-3′; rev, 5′-CCCCATTATATCTGCTGATGC-3′), *DHCR7* (for, 5′-CCCAGCTCTATACCTTGTGG-3′; rev, 5′-CCAGAGCAGGTGCGTGAGGAG-3′) or *TM7SF2* (for, 5′-AACTCAGGCAATCCGATTTACG-3′; rev, 5′-GGGTCGCAGTTCACAGAAATA-3′). Melting curve analysis was performed to determine the amplification specificity. Three independent experiments were conducted, and each included two no-template controls; all samples were repeated in triplicate reactions. For data normalization, expression of ribosomal protein L19 (*RPL19*) and pumilio homolog 1 transcript variant 2 (*PUM1*) were used as reference genes and mammaglobin B-2 (*MGB2*) as an unrelated marker (all sequences of PCR primers as per Pantelidou et al., 2007). For statistical analysis of RT-qPCR data, the REST-384© software was used to calculate the relative expression ratio of the different groups and determine the significance of results (Pfaffl et al., 2002; Pantelidou et al., 2007). For the RT-qPCR analysis in Fig. S5, negative control or *TMEM147*-silenced cells were grown in parallel either in complete medium (72 h) or lipid restrictive medium (48 h in complete medium+24 h under serum starvation). The Common Base method was used to allow direct quantitative comparisons across samples (Ganger et al., 2017), combined with statistical evaluation by two-way ANOVA followed by Tukey's post hoc test for multiple comparisons (GraphPad Prism 8.0).

siRNA-mediated silencing

Transfections for RNAi experiments were performed using INTERFERin (Polyplus Transfection) and siRNA oligonucleotides specific for *TMEM147* (oligo#1, 5′-GGCGGCAUCUAUGACUUCATT-3′; oligo#2, 5′-CGCUAUGAUCUGUACCACATT-3′) (Ambion Inc.), at a final concentration of 40 nM and according to the manufacturer's specifications. Negative control was a mock, no-oligo, transfection reaction. Cells were harvested 72 h after addition of siRNAs (96 h for oligo#2) for immunofluorescence (IF), RT-qPCR and western blot (WB) analysis.

SDS-PAGE, quantitative WB and statistical analysis

Protein samples were heated only to 60°C for 10 min to avoid aggregation of TMEM147 (Dettmer et al., 2010). SDS-PAGE was performed on a Mini-Protean II Electrophoresis Cell, WB on a Mini Trans-Blot Transfer Cell (Bio-Rad), using 48 mM Tris-HCl pH 9.2, 39 mM glycine and 20% (v/v) methanol for transfer, and the ECL System (GE Healthcare) with G:BOX (SYNGENE) for visualization. For quantification of protein levels, intensity volumes (area×height) of signals were extracted with ImageJ 1.49n and normalized using same-sample and same-membrane band intensities for the housekeeping protein GAPDH (in triplicate reactions for each independent experiment). GAPDH-normalized protein expression values were subjected to normality tests (GraphPad Prism 8.0) and significance of knockdown for individual protein bands was assessed by corresponding parametric or non-parametric statistical comparisons (Microsoft Excel and GraphPad Prism 8.0) (see figure legends for further details).

Antibodies

A mouse monoclonal antibody against human TMEM147 (NM_001242598.1) had previously been generated and characterized (Dettmer et al., 2010) and was used here at 1:8 dilution for WB. Additional commercial primary antibodies used were as follows: rabbit anti-LBR (E398L) (Abcam ab32535; 1:300 for IF and WB), mouse anti-LAP2β (BD Transduction Laboratories 611000; 1:500 for IF), mouse anti-GAPDH (Santa Cruz Biotechnology sc-32233; 1:500 for WB), mouse anti-FLAG (Sigma-Aldrich F4042; 1:500 for IF and WB), mouse anti-EGFP (Roche 11814460001; 1:1000 for IF and WB), rabbit anti-calnexin (Santa Cruz Biotechnology sc-11397; 1:100 for IF and 1:200 for WB), rabbit anti-emerin (Abcam ab14208; 1:400 for WB), rabbit anti-LEM4 (Asencio et al., 2012; 1:100 for WB), mouse anti-lamin A (Abcam ab8980; 1:500 for IF), rabbit anti-DHCR7 (Origene TA349889; 1:300 for IF), anti-histone H3K9-me3 (Millipore 17-625; 1:500 for IF). Primary antibodies were used in conjunction with appropriate fluorescently labeled Alexa-Fluor secondary antibodies (Thermo Fisher Scientific) for immunofluorescence, or HRP-labeled secondary antibodies (Santa Cruz Biotechnology) for WB. Nuclei were counterstained with Hoechst 33342 (0.5 µg/ml).

Expression plasmid constructs

For expression in HeLa cells, the full length ORF of *TMEM147* was amplified from HeLa K with primer set TMEM147F, 5′-CGCTCGAGATGACCCTGTTTCACTTCGGGAACTG-3′ and TMEM147R, 5′-GCGAATTCCGGAGTGCACATTGACAACGGCGACAT-3′, transferred as an XhoI/*Eco*RI fragment into pEGFP-N1 (Clontech) and transferred as a BglII/KpnI fragment into pFLAG-CMV-2 (Sigma-Aldrich).

An equivalent cloning strategy was followed for generating full-length GFP- and FLAG-tagged LBR constructs for expression in HeLa cells with primer set LBR1-615F, 5′-CGCGCTCGAGATGCCAAGTAGGAAATTTG-3′ and LBR1-615R: 5′-CGCGGAATTCGGTAGATGTATGGAAATA-3′. To clone truncated version LBR_{372}–GFP into pEGFP-N1, oligo LBR1-615F was used in conjunction with LBR1-372R, 5′-CGCGGAATTCGACGGCCAATGAAGAAATCATA-3′. Finally, to generate truncated version $LBR_{209-615}$–GFP, oligo LBR209-615F, 5′-CGCGCTCGAGTTTGGAGGAGTACCTGGTG-3′ was used in conjunction with LBR1-615R.

Co-IP analysis of protein interactions and LC-MS/MS analysis

HeLa K TMEM147-GFP cell line and HeLa K GFP cell line (negative control), either alone or transiently transfected with FLAG–LBR constructs, were lysed in lysis buffer [20 mM Tris-HCl pH 7.5, 150 mM NaCl, 1% v/v NP40 and 1× Complete™ (a protease inhibitor cocktail by Roche)]. Each of the extracts was incubated with a 10 µl slurry of GFP-Trap_A beads (Chromotek) for 2 h at room temperature. After binding, beads were extensively washed in lysis buffer and bound proteins were eluted from beads using 30 µl SDS-PAGE sample buffer. Samples were heated to 60°C for 10 min and then analyzed by SDS-PAGE, followed by WB.

For the co-IP experiment shown in Fig. S4, proteomic analysis was carried out at the EMBL Heidelberg Proteomics Facility. IP samples (TMEM147-GFP IP as test sample, TMEM129-GFP IP for comparison, and GFP-only IP as negative control) from two independent experiments in parallel (six samples in total) were prepared for MS analysis using the SP3 protocol (Hughes et al., 2019). Peptides were labeled with TMT6plex Isobaric Label Reagent (ThermoFisher), according the manufacturer's instructions, pooled and cleaned up further with an OASIS® HLB µElution Plate (Waters). Offline high pH reversed phase fractionation was carried out on an Agilent 1200 Infinity high-performance liquid chromatography system, equipped with a Gemini C18 column (Phenomenex). MS data acquisition was performed with an UltiMate 3000 RSLC nano LC system (Dionex), fitted with a trapping cartridge (µ-Precolumn C18 PepMap 100) and an analytical column (nanoEase™ M/Z HSS T3 column Waters), directly coupled to an Orbitrap Fusion Lumos (ThermoFisher) mass spectrometer, using the proxeon nanoflow source in positive ion mode. Peptides were introduced via a Pico-Tip Emitter 360 µm OD×20 µm ID; 10 µm tip (New Objective) and an applied spray voltage of 2.4 kV at capillary temperature at 275°C. Full mass scan was acquired with mass range 375–1500 *m*/*z* in profile mode with Orbitrap resolution of 60,000 and fill time at maximum of 50 ms. Data-dependent acquisition was performed with Orbitrap resolution at 15,000, fill time of 54 ms and a limitation of 10^5 ions. A normalized collision energy of 36 was applied and MS^2 data acquired in profile mode. For MS data analysis, IsobarQuant (Franken et al., 2015) and

Mascot (v2.2.07) were used to process the acquired data, which were searched against Uniprot *H. sapiens* UP000005640 proteome database, containing common contaminants and reversed sequences. Raw output files (protein.txt) of IsobarQuant were processed using the R programming language (ISBN 3-900051-07-0). Only proteins quantified with at least two unique peptides were used for data analysis. Raw signal-sums (signal_sum columns) were cleaned with the 'removeBatchEffect' function from the limma package (Ritchie et al., 2015) and further normalized using the variance stabilization normalization package (Huber et al., 2002). All experimental conditions were normalized separately to keep differences in protein abundance. Proteins were tested for differential expression using limma, based on false discovery rate (FDR) correction (Q=5%) and scoring a fold-change of at least 100% as a hit. The mass spectrometry proteomics data have been deposited to the ProteomeXchange Consortium via the PRIDE partner repository (EMBL-EBI) with the dataset identifier PXD019598.

Immunofluorescence and microscopy

For immunofluorescence, cells were grown on coverslips, fixed with 3.7% (w/v) paraformaldehyde in PHEM (30 mM HEPES, 65 mM PIPES, pH 6.9, 10 mM EGTA and 2 mM $MgCl_2$) for 10 min, permeabilized for 15 min with 0.5% v/v Triton X-100 in PHEM and immunolabeled with appropriate primary and secondary antibodies. Samples were analyzed with a Zeiss Apochromat 63×1.4 NA oil lens on a Zeiss Axiovert 200M inverted microscope with an AxioCam MRm camera.

Confocal imaging in Fig. 3D was carried out with a Zeiss LSM710 Axiovert confocal microscope using a 63× Plan-Neofluar 1.4 NA oil immersion objective lens, and in Fig. 4 with a Leica TCS SP2 DMIRE2 confocal microscope using 63×1.4 NA oil immersion objective lens.

Images were acquired with Zeiss Axiovision 4.2 software or LSM Zen or Leica LAS (v.4.1.0), processed using Adobe Photoshop CS6 and assembled into figures with Adobe Illustrator CS6.

Morphometric analysis and statistical evaluation

Fluorescence and morphology parameters [area, volume, oblate ellipticity, prolate ellipticity, sphericity and LBR (green)/Hoechst (blue) mean fluorescence intensity], as determined by Imaris (Bitplane AG, v 9.2.1), were compared in four independent experiments for a total of 103 cells (*n*=55 negative control treatment, *n*=48 *TMEM147* siRNA treatment) in stacks acquired on a Leica TCS SP2 DMIRE2 confocal microscope, using identical acquisition settings across samples. MANOVA using Pillai's test and α=0.05 (Addinsoft XLSTAT) was used to calculate the statistical difference between treatments (negative control and *TMEM147*-silencing), across all parameters. To assess statistical significance, individual parameters were analyzed by Mann–Whitney *U*-test (GraphPad Prism 8.0) with *P*-value adjustment using the FDR approach by the two-stage linear step-up procedure of Benjamini, Krieger and Yekutieli (Q=5%).

3D rendering of serial confocal *z*-stacks of HeLa nuclei (from the same control and *TMEM147*-silenced cells as above) was also performed with Imaris. 3D reconstruction of each nucleus was rendered using the 'new surface' algorithm with surface detail magnitude set at 0.250 µm and manual thresholding until voxels covered the entire surface of the nucleus according to LBR staining. Snapshots of 3D images were acquired to compare the localization of LBR in control and *TMEM147*-silenced cells. Elevated occurrence of ER localization for LBR labeling was tested by two-sided Fisher's exact test in Prism 8.0 (GraphPad) for the total of four independent experiments.

Lipidomics, cholesterol uptake analysis and statistical evaluation

For lipid analysis, 3×10^4–5×10^4 cells were used per condition. Acidic extractions were performed as previously described (Özbalci et al., 2013), in the presence of an internal lipid standard mix containing 50 pmol phosphatidylcholine (13:0/13:0, 14:0/14:0, 20:0/20:0; 21:0/21:0; Avanti Polar Lipids), 50 pmol sphingomyelin (d18:1 with N-acylated 13:0, 17:0, 25:0), 100 pmol D6-cholesterol (Cambridge Isotope Laboratory), 25 pmol phosphatidylinositol (16:0/16:0; Avanti Polar Lipids), 25 pmol phosphatidylethanolamine and 25 pmol phosphatidylserine (both 14:1/14:1, 20:1/20:1, 22:1/22:1), 25 pmol diacylglycerol (17:0/17:0; Larodan), 25 pmol cholesteryl ester (9:0, 19:0; Sigma), 24 pmol triacylglycerol (D5-Mix, LM-6000/D5-17:0/17:1/17:1; Avanti Polar Lipids), 5 pmol ceramide and 5 pmol glucosylceramide (both d18:1 with N-acylated 15:0, 17:0, 25:0), 5 pmol lactosylceramide (d18:1 with N-acylated C12 fatty acid), 10 pmol phosphatidic acid (21:0/22:6; Avanti Polar Lipids), 10 pmol phosphatidylglycerol (14:1/14:1, 20:1/20:1, 22:1/22:1) and 5 pmol lyso-phosphatidylcholine (17:1; Avanti Polar Lipids). Neutral extractions were performed in the presence of a phosphatidylethanolamine plasmalogen (PE P-)-containing standard mix, supplemented with 22 pmol PE P-Mix 1 (16:0p/15:0, 16:0p/19:0, 16:0p/25:0), 31 pmol PE P-Mix 2 (18:0p/15:0, 18:0p/19:0, 18:0p/25:0) and 43 pmol PE P-Mix 3 (18:1p/15:0, 18:1p/19:0, 18:1p/25:0). Lipid extracts were resuspended in 60 µl methanol, 2 µl-aliquots were diluted 1:10 in 96-well plates in methanol, and ammonium acetate was added to a final concentration of 10 mM. Samples were analyzed on a SCIEX QTRAP 6500+ mass spectrometer (Sciex, Canada) with chip-based (HD-D ESI Chip, Advion Biosciences, USA) nano-electrospray infusion and ionization via a Triversa Nanomate (Advion Biosciences, Ithaca, USA), employing precursor ion or neutral loss scanning as described (Özbalci et al., 2013). The remaining sample was evaporated and free cholesterol was subjected to acetylation and MS analysis as described previously (Özbalci et al., 2013). Data evaluation was undertaken using LipidView (ABSciex) and an in-house-developed software (ShinyLipids). Statistical evaluation of comparisons was assessed by multiple *t*-test with multiple testing correction, based on an FDR of <0.05 (Fig. 7).

For lipidomics, multivariate statistics analyses were performed in MetaboAnalyst version 4.0. All variables were log transformed and scaled by performing mean-centering and division by the standard deviation of each sample. All variables were then subjected to an unsupervised principal component analysis (PCA), generating a scores plot showing the variance in the dataset. The loadings plot for the generated model was used to determine which variables drive the separation between classes. The most discriminant variables were visualized using univariate statistics (Fig. S6).

For univariate statistics, GraphPad Prism 8.0 software was used. All data were expressed as mean±s.e.m. In GraphPad, one- or two-way ANOVA was performed where appropriate. For one-way ANOVA, Dunnett's post hoc multiple-comparisons test was performed, while for two-way ANOVA, Šidák's post hoc multiple-comparisons test was used (Fig. S6).

Cellular uptake of fluorescently tagged cholestrol was measured in three independent experiments using the Cholesterol Uptake Assay Kit (ab236212; Abcam) in a 96-well format, following the manufacturer's specifications. Briefly, cells were silenced for 48 h, subsequently incubated for a further 24 h with fluorescently tagged NBD-cholesterol at 20 µg/ml in either complete or serum-free medium or in the presence of cholesterol transport inhibitor U-18666A at 1 µM (as a positive control of increased retained cholesterol). NBD-cholesterol is an established probe for examining lipoprotein-mediated cholesterol uptake *in vivo* and in cultured cells (Frolov et al., 2000; Huang et al., 2015). Fluorescence emission readings with an FITC/GFP filter set were normalized to protein concentrations, determined for the same wells with bicinchonic acid (BCA) assays, followed by subtraction of background fluorescence. To assess statistical significance in uptake assays, multiple *t*-tests with multiple testing correction were performed (GraphPad Prism 8.0), using one unpaired *t*-test per row without assuming a consistent s.d. and applying the two-stage linear step-up procedure of Benjamini, Krieger and Yekutieli (Q=5%) to determine discovery (Fig. 7).

Cell growth assays

For the experiments shown in Fig. 7F,G, cells were seeded in multiple 24-well plates (15×10^3/well), grown in parallel either with control or *TMEM147* silencing and sampled by trypsination and counting in triplicate at time points 24 h, 48 h and 72 h post silencing. For each silencing regime, cells were either grown in complete medium for 72 h, or in complete medium for 48 h and under serum starvation until 72 h, or in complete medium for 48 h and under serum starvation until 72 h with the addition of exogenous cholesterol (20 µg/ml) at 64 h (i.e. for the last 8 h before sampling). Three independent experiments were performed and statistical evaluation was assessed for parametric (medium) comparisons after confirming normality with the Shapiro–Wilk test, with one-way ANOVA based on the two-stage linear step-up procedure of Benjamini, Krieger and Yekutieli (Q=5%) to determine discovery (GraphPad Prism 8.0).

Acknowledgements

We are indebted to Prof. Iain W. Mattaj, in whose lab at the EMBL (Heidelberg) this project was initiated, for his kind and sustained support. We are grateful to Dr Chrysoula Pitsouli (University of Cyprus) for granting us access to a Leica confocal microscope SP2 and to Dr Jan Ellenberg (EMBL, Heidelberg) for providing the HeLa-LBR238-GFP cell line. We are thankful to Drs Mandy Rettel and Frank Stein for their expert assistance at the EMBL Proteomic Facility and Ms Anastasia Raoukka (University of Cyprus) for background work on TMEM147.

Competing interests

The authors declare no competing or financial interests.

Author contributions

Conceptualization: A.C., B.B., N.S.; Methodology: A.C., B.B., N.S.; Formal analysis: A.C., E.C., C.W.L., B.B.; Investigation: A.C., G.M., A.M., C.L., A.V., R.G.; Resources: A.C., C.H., N.S.; Writing - original draft: N.S.; Writing - review & editing: A.C., G.M., A.V., R.G., C.W.L., C.H., B.B., N.S.; Visualization: N.S.; Supervision: A.C., N.S.; Project administration: N.S.; Funding acquisition: N.S.

Funding

This work was supported by the University of Cyprus internal research funds (N.S.).

Data availability

The mass spectrometry proteomics data have been deposited to the ProteomeXchange Consortium via the PRIDE partner repository (EMBL-EBI) with the dataset identifier PXD019598.

Supplementary information

Supplementary information available online at
https://jcs.biologists.org/lookup/doi/10.1242/jcs.245357.supplemental

Peer review history

The peer review history is available online at
https://jcs.biologists.org/lookup/doi/10.1242/jcs.245357.reviewer-comments.pdf

References

Asencio, C., Davidson, I. F., Santarella-Mellwig, R., Ly-Hartig, T. B. N., Mall, M., Wallenfang, M. R., Mattaj, I. W. and Gorjánácz, M. (2012). Coordination of kinase and phosphatase activities by Lem4 enables nuclear envelope reassembly during mitosis. *Cell* **150**, 122-135. doi:10.1016/j.cell.2012.04.043

Bartoli, D., Piobbico, D., Bellet, M. M., Bennati, A. M., Roberti, R., Della Fazia, M. A. and Servillo, G. (2016). Impaired cell proliferation in regenerating liver of 3 β-hydroxysterol Δ14-reductase (TM7SF2) knock-out mice. *Cell Cycle* **15**, 2164-2173. doi:10.1080/15384101.2016.1195939

Baumann, O. and Walz, B. (2001). Endoplasmic reticulum of animal cells and its organization into structural and functional domains. *Int. Rev. Cytol.* **205**, 149-214. doi:10.1016/S0074-7696(01)05004-5

Bennati, A. M., Schiavoni, G., Franken, S., Piobbico, D., Della Fazia, M. A., Caruso, D., De Fabiani, E., Benedetti, L., Cusella De Angelis, M. G., Gieselmann, V. et al. (2008). Disruption of the gene encoding 3β-hydroxysterol Δ14-reductase (Tm7sf2) in mice does not impair cholesterol biosynthesis. *FEBS J.* **275**, 5034-5047. doi:10.1111/j.1742-4658.2008.06637.x

Blassberg, R., Macrae, J. I., Briscoe, J. and Jacob, J. (2016). Reduced cholesterol levels impair Smoothened activation in Smith-Lemli-Opitz syndrome. *Hum. Mol. Genet.* **25**, 693-705. doi:10.1093/hmg/ddv507

Boni, A., Politi, A. Z., Strnad, P., Xiang, W., Hossain, M. J. and Ellenberg, J. (2015). Live imaging and modeling of inner nuclear membrane targeting reveals its molecular requirements in mammalian cells. *J. Cell Biol.* **209**, 705-720. doi:10.1083/jcb.201409133

Braverman, N., Lin, P., Moebius, F. F., Obie, C., Moser, A., Glossmann, H., Wilcox, W. R., Rimoin, D. L., Smith, M., Kratz, L. et al. (1999). Mutations in the gene encoding 3β-hydroxysteroid-Δ8,Δ7-isomerase cause X-linked dominant Conradi-Hünermann syndrome. *Nat. Genet.* **22**, 291-294. doi:10.1038/10357

Capell-Hattam, I. M., Sharpe, L. J., Qian, L., Hart-Smith, G., Prabhu, A. V. and Brown, A. J. (2020). The cholesterogenic enzymes DHCR14 and LBR are differentially regulated transcriptionally and post-translationally. *J. Biol. Chem* **295**, 2850-2865. doi:10.1074/jbc.RA119.011323

Cascianelli, G., Villani, M., Tosti, M., Marini, F., Bartoccini, E., Magni, M. V. and Albi, E. (2008). Lipid microdomains in cell nucleus. *Mol. Biol. Cell* **19**, 5289-5295. doi:10.1091/mbc.e08-05-0517

Chen, S., Novick, P. and Ferro-Novick, S. (2013). ER structure and function. *Curr. Opin. Cell Biol.* **25**, 428-433. doi:10.1016/j.ceb.2013.02.006

Christodoulou, A., Santarella-Mellwig, R., Santama, N. and Mattaj, I. W. (2016). Transmembrane protein TMEM170A is a newly discovered regulator of ER and nuclear envelope morphogenesis in human cells. *J. Cell Sci.* **129**, 1552-1565. doi:10.1242/jcs.175273

Clever, M., Funakoshi, T., Mimura, Y., Takagi, M. and Imamoto, N. (2012). The nucleoporin ELYS/Mel28 regulates nuclear envelope subdomain formation in HeLa cells. *Nucleus* **3**, 187-199. doi:10.4161/nucl.19595

Codini, M., Cataldi, S., Lazzarini, A., Tasegian, A., Ceccarini, M. R., Floridi, A., Lazzarini, R., Ambesi-Impiombato, F. S., Curcio, F., Beccari, T. et al. (2016). Why high cholesterol levels help hematological malignancies: role of nuclear lipid microdomains. *Lipids Health Dis.* **15**, 4. doi:10.1186/s12944-015-0175-2

de Medina, P., Paillasse, M. R., Segala, G., Poirot, M. and Silvente-Poirot, S. (2010). Identification and pharmacological characterization of cholesterol-5,6-epoxide hydrolase as a target for tamoxifen and AEBS ligands. *Proc. Natl. Acad. Sci. USA* **107**, 13520-13525. doi:10.1073/pnas.1002922107

Dettmer, U., Kuhn, P.-H., Abou-Ajram, C., Lichtenthaler, S. F., Krüger, M., Kremmer, E., Haass, C. and Haffner, C. (2010). Transmembrane protein 147 (TMEM147) is a novel component of the Nicalin-NOMO protein complex. *J. Biol. Chem.* **285**, 26174-26181. doi:10.1074/jbc.M110.132548

Ellenberg, J., Siggia, E. D., Moreira, J. E., Smith, C. L., Presley, J. F., Worman, H. J. and Lippincott-Schwartz, J. (1997). Nuclear membrane dynamics and reassembly in living cells: targeting of an inner nuclear membrane protein in interphase and mitosis. *J. Cell Biol.* **138**, 1193-1206. doi:10.1083/jcb.138.6.1193

Fitzky, B. U., Witsch-Baumgartner, M., Erdel, M., Lee, J. N., Paik, Y.-K., Glossmann, H., Utermann, G. and Moebius, F. F. (1998). Mutations in the Delta7-sterol reductase gene in patients with the Smith-Lemli-Opitz syndrome. *Proc. Natl. Acad. Sci. USA* **95**, 8181-8186. doi:10.1073/pnas.95.14.8181

Franken, H., Mathieson, T., Childs, D., Sweetman, G. M., Werner, T., Tögel, I., Doce, C., Gade, S., Bantscheff, M., Drewes, G. et al. (2015). Thermal proteome profiling for unbiased identification of direct and indirect drug targets using multiplexed quantitative mass spectrometry. *Nat. Protoc.* **10**, 1567-1593. doi:10.1038/nprot.2015.101

Frolov, A., Petrescu, A., Atshaves, B. P., So, P. T. C., Gratton, E., Serrero, G. and Schroeder, F. (2000). High density lipoprotein mediated cholesterol uptake and targeting to lipid droplets in intact L-cell fibroblasts. *J. Biol. Chem.* **275**, 12769-12780. doi:10.1074/jbc.275.17.12769

Fukuhara, T., Hosoya, T., Shimizu, S., Sumi, K., Oshiro, T., Yoshinaka, Y., Suzuki, M., Yamamoto, N., Herzenberg, L. A., Herzenberg, L. A. et al. (2006). Utilization of host SR protein kinases and RNA-splicing machinery during viral replication. *Proc. Natl. Acad. Sci. USA* **103**, 11329-11333. doi:10.1073/pnas.0604616103

Ganger, M. T., Dietz, G. D. and Ewing, S. J. (2017). A common base method for analysis of qPCR data and the application of simple blocking in qPCR experiments. *BMC Bioinf.* **18**, 534. doi:10.1186/s12859-017-1949-5

Giannios, I., Chatzantonaki, E. and Georgatos, S. (2017). Dynamics and structure-function relationships of the Lamin B Receptor (LBR). *PLoS ONE* **12**, e0169626. doi:10.1371/journal.pone.0169626

Goyal, U. and Blackstone, C. (2013). Untangling the web: mechanisms underlying ER network formation. *Biochim. Biophys. Acta* **1833**, 2492-2498. doi:10.1016/j.bbamcr.2013.04.009

Hoffmann, K., Dreger, C. K., Olins, A. L., Olins, D. E., Shultz, L. D., Lucke, B., Karl, H., Kaps, R., Müller, D., Vayá, A. et al. (2002). Mutations in the gene encoding the lamin B receptor produce an altered nuclear morphology in granulocytes (Pelger-Huët anomaly). *Nat. Genet.* **31**, 410-414. doi:10.1038/ng925

Hoffmann, K., Sperling, K., Olins, A. L. and Olins, D. E. (2007). The granulocyte nucleus and lamin B receptor: avoiding the ovoid. *Chromosoma* **116**, 227-235. doi:10.1007/s00412-007-0094-8

Hu, J., Prinz, W. A. and Rapoport, T. A. (2011). Weaving the web of ER tubules. *Cell* **147**, 1226-1231. doi:10.1016/j.cell.2011.11.022

Huang, H., McIntosh, A. L., Landrock, K. K., Landrock, D., Storey, S. M., Martin, G. G., Gupta, S., Atshaves, B. P., Kier, A. B. and Schroeder, F. (2015). Human FABP1 T94A variant enhances cholesterol uptake. *Biochim. Biophys. Acta Mol. Cell Biol. Lipids* **1851**, 946-955. doi:10.1016/j.bbalip.2015.02.015

Huber, W., von Heydebreck, A., Sültmann, H., Poustka, A. and Vingron, M. (2002). Variance stabilization applied to microarray data calibration and to the quantification of differential expression. *Bioinformatics* **18** Suppl. 1r, S96-S104. doi:10.1093/bioinformatics/18.suppl_1.S96

Hubler, Z., Allimuthu, D., Bederman, I., Elitt, M. S., Madhavan, M., Allan, K. C., Shick, H. E., Garrison, E., Karl, M. T., Factor, D. C. et al. (2018). Accumulation of 8,9-unsaturated sterols drives oligodendrocyte formation and remyelination. *Nature* **560**, 372-376. doi:10.1038/s41586-018-0360-3

Hughes, C. S., Moggridge, S., Müller, T., Sorensen, P. H., Morin, G. B. and Krijgsveld, J. (2019). Single-pot, solid-phase-enhanced sample preparation for proteomics experiments. *Nat. Protoc.* **14**, 68-85. doi:10.1038/s41596-018-0082-x

Kedjouar, B., de Médina, P., Oulad-Abdelghani, M., Payré, B., Silvente-Poirot, S., Favre, G., Faye, J.-C. and Poirot, M. (2004). Molecular characterization of the microsomal tamoxifen binding site. *J. Biol. Chem.* **279**, 34048-34061. doi:10.1074/jbc.M405230200

Koczok, K., Gurumurthy, C. B., Balogh, I., Korade, Z. and Mirnics, K. (2019). Subcellular localization of sterol biosynthesis enzymes. *J. Mol. Histol.* **50**, 63-73. doi:10.1007/s10735-018-9807-y

Li, X., Roberti, R. and Blobel, G. (2015). Structure of an integral membrane sterol reductase from Methylomicrobium alcaliphilum. *Nature* **517**, 104-107. doi:10.1038/nature13797

Lin, S., Sun, S. and Hu, J. (2012). Molecular basis for sculpting the endoplasmic reticulum membrane. *Int. J. Biochem. Cell Biol.* **44**, 1436-1443. doi:10.1016/j.biocel.2012.05.013

Liu, X. Y., Dangel, A. W., Kelley, R. I., Zhao, W., Denny, P., Botcherby, M., Cattanach, B., Peters, J., Hunsicker, P. R., Mallon, A.-M. et al. (1999). The gene mutated in bare patches and striated mice encodes a novel 3β-hydroxysteroid dehydrogenase. *Nat. Genet.* **22**, 182-187. doi:10.1038/9700

Lukášová, E., Kovařík, A., Bačíková, A., Falk, M. and Kozubek, S. (2017). Loss of lamin B receptor is necessary to induce cellular senescence. *Biochem. J.* **474**, 281-300. doi:10.1042/BCJ20160459

Luo, J., Yang, H. and Song, B.-L. (2020). Mechanisms and regulation of cholesterol homeostasis. *Nat. Rev. Mol. Cell Biol.* **21**, 225-245. doi:10.1038/s41580-019-0190-7

Lynes, E. M. and Simmen, T. (2011). Urban planning of the endoplasmic reticulum (ER): how diverse mechanisms segregate the many functions of the ER. *Biochim. Biophys. Acta* **1813**, 1893-1905. doi:10.1016/j.bbamcr.2011.06.011

Ma, Y., Cai, S., Lv, Q., Jiang, Q., Zhang, Q., Sodmergen, Zhai, Z. and Zhang, C. (2007). Lamin B receptor plays a role in stimulating nuclear envelope production and targeting membrane vesicles to chromatin during nuclear envelope assembly through direct interaction with importin beta. *J. Cell Sci.* **120**, 520-530. doi:10.1242/jcs.03355

Makatsori, D., Kourmouli, N., Polioudaki, H., Shultz, L. D., Mclean, K., Theodoropoulos, P. A., Singh, P. B. and Georgatos, S. D. (2004). The inner nuclear membrane protein lamin B receptor forms distinct microdomains and links epigenetically marked chromatin to the nuclear envelope. *J. Biol. Chem.* **279**, 25567-25573. doi:10.1074/jbc.M313606200

Mattout, A., Cabianca, D. S. and Gasser, S. M. (2015). Chromatin states and nuclear organization in development-a view from the nuclear lamina. *Genome Biol.* **16**, 174. doi:10.1186/s13059-015-0747-5

Mimura, Y., Takagi, M., Clever, M. and Imamoto, N. (2016). ELYS regulates the localization of LBR by modulating its phosphorylation state. *J. Cell Sci.* **129**, 4200-4212. doi:10.1242/jcs.190678

Nikolakaki, E., Simos, G., Georgatos, S. D. and Giannakouros, T. (1996). A nuclear envelope-associated kinase phosphorylates arginine-serine motifs and modulates interactions between the lamin B receptor and other nuclear proteins. *J. Biol. Chem.* **271**, 8365-8372. doi:10.1074/jbc.271.14.8365

Nikolakaki, E., Mylonis, I. and Giannakouros, T. (2017). Lamin B receptor: interplay between structure, function and localization. *Cells* **6**, 28. doi:10.3390/cells6030028

Olins, A. L., Zwerger, M., Herrmann, H., Zentgraf, H., Simon, A. J., Monestier, M. and Olins, D. E. (2008). The human granulocyte nucleus: Unusual nuclear envelope and heterochromatin composition. *Eur. J. Cell Biol.* **87**, 279-290. doi:10.1016/j.ejcb.2008.02.007

Olins, A. L., Rhodes, G., Welch, D. B. M., Zwerger, M. and Olins, D. E. (2010). Lamin B receptor: multi-tasking at the nuclear envelope. *Nucleus* **1**, 53-70. doi:10.4161/nucl.1.1.10515

Ota, M., Tanaka, Y., Nakagawa, I., Jiang, J. J., Arima, Y., Kamimura, D., Onodera, T., Iwasaki, N. and Murakami, M. (2019). Chondrocytes play a role in the development of rheumatoid arthritis via TMEM147-mediated NF-kappaB activation. *Arthritis Rheumatol.* **72**, 931-942. doi:10.1002/art.41182

Özbalci, C., Sachsenheimer, T. and Brügger, B. (2013). Quantitative analysis of cellular lipids by nano-electrospray ionization mass spectrometry. *Methods Mol. Biol.* **1033**, 3-20. doi:10.1007/978-1-62703-487-6_1

Pantelidou, M., Zographos, S. E., Lederer, C. W., Kyriakides, T., Pfaffl, M. W. and Santama, N. (2007). Differential expression of molecular motors in the motor cortex of sporadic ALS. *Neurobiol. Dis.* **26**, 577-589. doi:10.1016/j.nbd.2007.02.005

Pfaffl, M. W., Horgan, G. W. and Dempfle, L. (2002). Relative expression software tool (REST(C)) for group-wise comparison and statistical analysis of relative expression results in real-time PCR. *Nucleic Acids Res.* **30**, e36. doi:10.1093/nar/30.9.e36

Platt, F. M., Wassif, C., Colaco, A., Dardis, A., Lloyd-Evans, E., Bembi, B. and Porter, F. D. (2014). Disorders of cholesterol metabolism and their unanticipated convergent mechanisms of disease. *Annu. Rev. Genomics Hum. Genet.* **15**, 173-194. doi:10.1146/annurev-genom-091212-153412

Prakash, A., Sengupta, S., Aparna, K. and Kasbekar, D. P. (1999). The erg-3 (sterol Δ14,15-reductase) gene of Neurospora crassa: generation of null mutants by repeat-induced point mutation and complementation by proteins chimeric for human lamin B receptor sequences. *Microbiology* **145**, 1443-1451. doi:10.1099/13500872-145-6-1443

Pyrpasopoulou, A., Meier, J., Maison, C., Simos, G. and Georgatos, S. D. (1996). The lamin B receptor (LBR) provides essential chromatin docking sites at the nuclear envelope. *EMBO J.* **15**, 7108-7119. doi:10.1002/j.1460-2075.1996.tb01102.x

Ritchie, M. E., Phipson, B., Wu, D., Hu, Y., Law, C. W., Shi, W. and Smyth, G. K. (2015). limma powers differential expression analyses for RNA-sequencing and microarray studies. *Nucleic Acids Res.* **43**, e47. doi:10.1093/nar/gkv007

Rosemond, E., Rossi, M., Mcmillin, S. M., Scarselli, M., Donaldson, J. G. and Wess, J. (2011). Regulation of M(3) muscarinic receptor expression and function by transmembrane protein 147. *Mol. Pharmacol.* **79**, 251-261. doi:10.1124/mol.110.067363

Santama, N., Er, C. P., Ong, L. L. and Yu, H. (2004). Distribution and functions of kinectin isoforms. *J. Cell Sci.* **117**, 4537-4549. doi:10.1242/jcs.01326

Schuler, E., Lin, F. and Worman, H. J. (1994). Characterization of the human gene encoding LBR, an integral protein of the nuclear envelope inner membrane. *J. Biol. Chem.* **269**, 11312-11317.

Shibata, Y., Voeltz, G. K. and Rapoport, T. A. (2006). Rough sheets and smooth tubules. *Cell* **126**, 435-439. doi:10.1016/j.cell.2006.07.019

Shultz, L. D., Lyons, B. L., Burzenski, L. M., Gott, B., Samuels, R., Schweitzer, P. A., Dreger, C., Herrmann, H., Kalscheuer, V., Olins, A. L. et al. (2003). Mutations at the mouse ichthyosis locus are within the lamin B receptor gene: a single gene model for human Pelger-Huet anomaly. *Hum. Mol. Genet.* **12**, 61-69. doi:10.1093/hmg/ddg003

Silva, I. T. G., Fernandes, V., Souza, C., Treptow, W. and Santos, G. M. (2017). Biophysical studies of cholesterol effects on chromatin. *J. Lipid Res.* **58**, 934-940. doi:10.1194/jlr.M074997

Silve, S., Dupuy, P. H., Labit-Lebouteiller, C., Kaghad, M., Chalon, P., Rahier, A., Taton, M., Lupker, J., Shire, D. and Loison, G. (1996). Emopamil-binding protein, a mammalian protein that binds a series of structurally diverse neuroprotective agents, exhibits Δ8-Δ7 sterol isomerase activity in yeast. *J. Biol. Chem.* **271**, 22434-22440. doi:10.1074/jbc.271.37.22434

Silve, S., Dupuy, P.-H., Ferrara, P. and Loison, G. (1998). Human lamin B receptor exhibits sterol C14-reductase activity in Saccharomyces cerevisiae. *Biochim. Biophys. Acta* **1392**, 233-244. doi:10.1016/S0005-2760(98)00041-1

Tint, G. S., Irons, M., Elias, E. R., Batta, A. K., Frieden, R., Chen, T. S. and Salen, G. (1994). Defective cholesterol biosynthesis associated with the Smith-Lemli-Opitz syndrome. *N. Engl. J. Med.* **330**, 107-113. doi:10.1056/NEJM199401133300205

Tsai, P.-L., Zhao, C., Turner, E. and Schlieker, C. (2016). The Lamin B receptor is essential for cholesterol synthesis and perturbed by disease-causing mutations. *eLife* **5**, e16011. doi:10.7554/eLife.16011

Tseng, L.-C. and Chen, R.-H. (2011). Temporal control of nuclear envelope assembly by phosphorylation of lamin B receptor. *Mol. Biol. Cell* **22**, 3306-3317. doi:10.1091/mbc.e11-03-0199

Ungricht, R., Klann, M., Horvath, P. and Kutay, U. (2015). Diffusion and retention are major determinants of protein targeting to the inner nuclear membrane. *J. Cell Biol.* **209**, 687-703. doi:10.1083/jcb.201409127

Wassif, C. A., Maslen, C., Kachilele-Linjewile, S., Lin, D., Linck, L. M., Connor, W. E., Steiner, R. D. and Porter, F. D. (1998). Mutations in the human sterol Δ7-reductase gene at 11q12-13 cause Smith-Lemli-Opitz syndrome. *Am. J. Hum. Genet.* **63**, 55-62. doi:10.1086/301936

Wassif, C. A., Brownson, K. E., Sterner, A. L., Forlino, A., Zerfas, P. M., Wilson, W. K., Starost, M. F. and Porter, F. D. (2007). HEM dysplasia and ichthyosis are likely laminopathies and not due to 3β-hydroxysterol Δ14-reductase deficiency. *Hum. Mol. Genet.* **16**, 1176-1187. doi:10.1093/hmg/ddm065

Waterham, H. R., Wijburg, F. A., Hennekam, R. C. M., Vreken, P., Poll-The, B. T., Dorland, L., Duran, M., Jira, P. E., Smeitink, J. A., Wevers, R. A. et al. (1998). Smith-Lemli-Opitz syndrome is caused by mutations in the 7-dehydrocholesterol reductase gene. *Am. J. Hum. Genet.* **63**, 329-338. doi:10.1086/301982

Worman, H. J., Yuan, J., Blobel, G. and Georgatos, S. D. (1988). A lamin B receptor in the nuclear envelope. *Proc. Natl. Acad. Sci. USA* **85**, 8531-8534. doi:10.1073/pnas.85.22.8531

Worman, H. J., Evans, C. D. and Blobel, G. (1990). The lamin B receptor of the nuclear envelope inner membrane: a polytopic protein with eight potential transmembrane domains. *J. Cell Biol.* **111**, 1535-1542. doi:10.1083/jcb.111.4.1535

Zwerger, M., Herrmann, H., Gaines, P., Olins, A. L. and Olins, D. E. (2008). Granulocytic nuclear differentiation of lamin B receptor-deficient mouse EPRO cells. *Exp. Hematol.* **36**, 977-987. doi:10.1016/j.exphem.2008.03.003

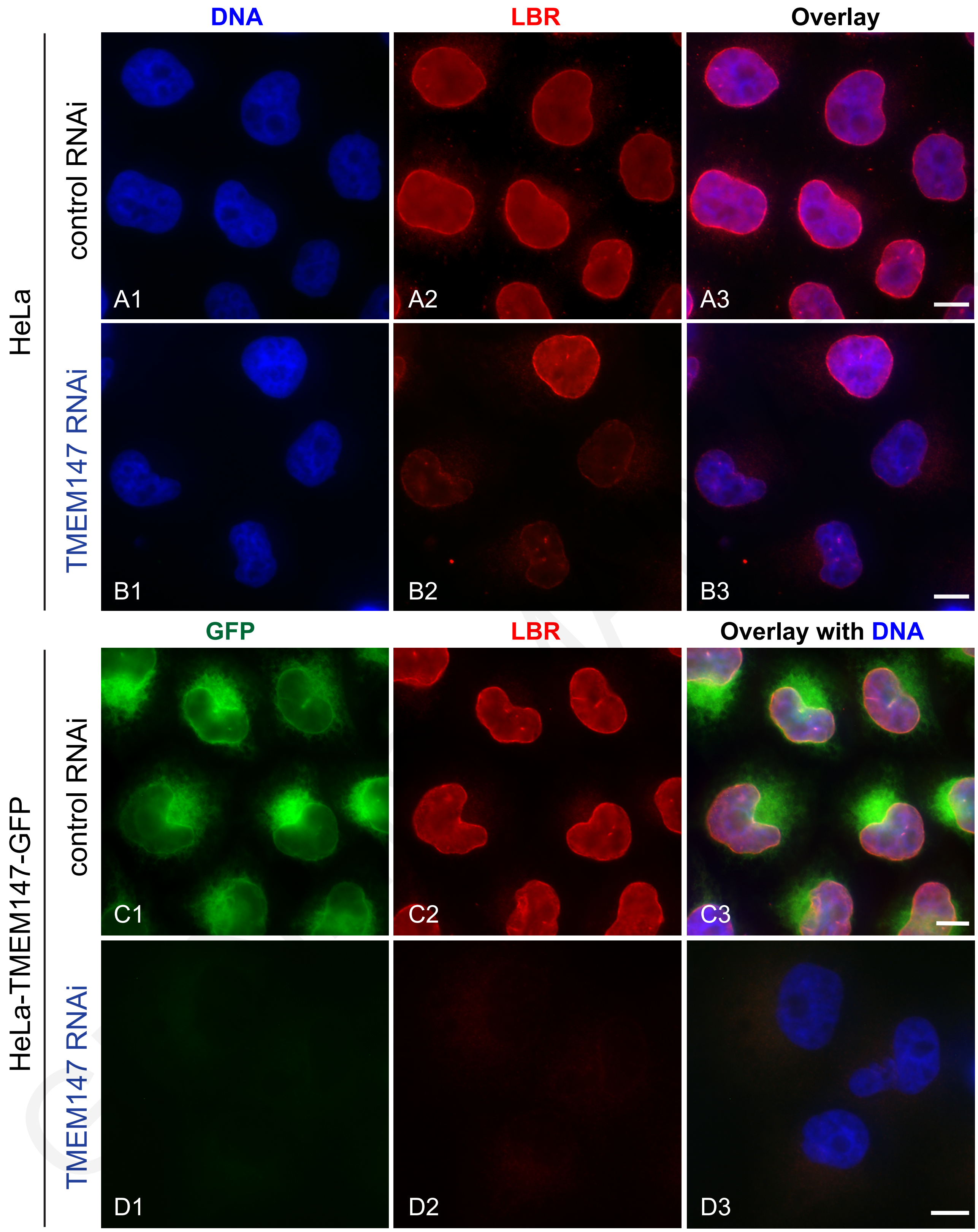

SUPPLEMENTARY FIGURE 1

FIGURE S1

Effect of *TMEM147* silencing on LBR

(A, B series) Representative examples of loss of immunofluorescence for LBR (red) during silencing of *TMEM147* in HeLa cells (compare control silencing in panels A with *TMEM147* silencing in panels B). Nuclei were counterstained for DNA (blue), and overlay images display blue and red fluorescence concurrently.

(C, D series) Equivalent analysis as for A+B, but using the stably transfected TMEM147-GFP cell line, where GFP fluorescence serves as a marker for the expression of TMEM147-GFP (green). Again, LBR expression (red) is extremely reduced upon *TMEM147* silencing. Overlay images display GFP, LBR labeling together with blue Hoechst counterstaining for nuclei. Scale bars 10 µm.

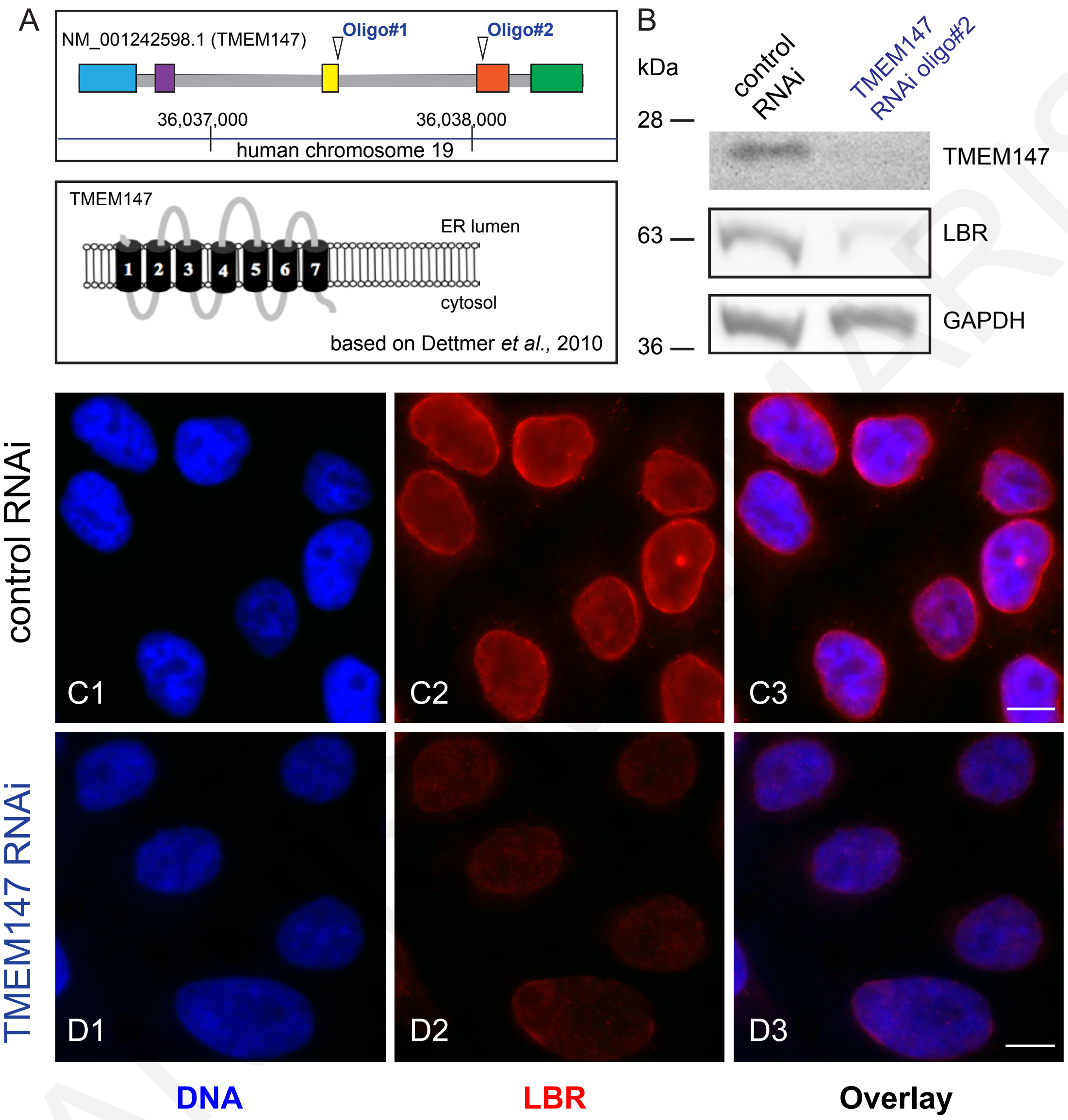

SUPPLEMENTARY FIGURE 2

FIGURE S2

Confirmation of effect of *TMEM147* silencing on LBR using an alternative siRNA silencing oligo

(A) (Top panel) Sketch of the multi-exon mRNA organization of human *TMEM147*, highlighting the targeting positions of the siRNA oligonucleotide 1 (oligo#1), used for silencing experiments in Figs. 2, 3, 4, 6 and 7, and siRNA oligonucleotide 2 (oligo#2) used in the current figure for confirmation of the specificity of the silencing phenotypes and in particular the effect on LBR.

(Bottom panel) Sketch of the model, based on Dettmer et al., 2010, of the multidomain topology of TMEM147 in the ER membranes.

(B) Similar to oligo#1 (Fig. 1 and 2), siRNA-silencing with oligo#2, is efficient in knocking down *TMEM147* (top panel), as assessed by WB analysis, and in drastically reducing LBR protein levels (middle panel). GAPDH serves as loading control.

(C, D series) Immunofluorescence analysis of HeLa cells silenced with oligo#2 (panels D1-D3), replicates significant loss of LBR labeling (red in D2), as compared with control-silenced cells (panels C1-C3, red in C2). Nuclei are labeled by Hoechst (blue) and overlay images combine LBR and DNA signals. Scale bars 10 µm.

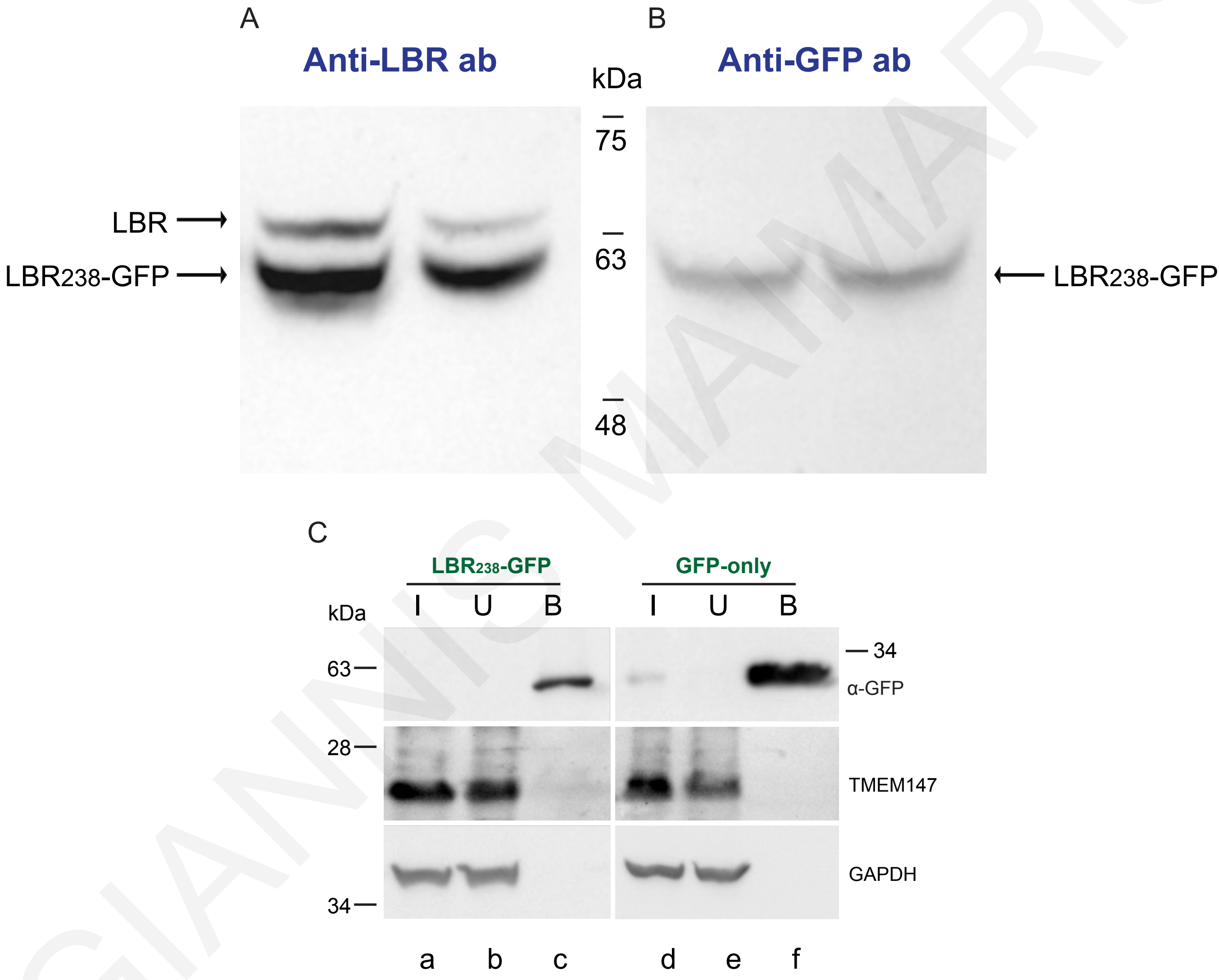

SUPPLEMENTARY FIGURE 3

FIGURE S3

Expression and detection of LBR238-GFP in the stable LBR238-GFP HeLa cell line

(A) Application of anti-LBR antibody in a total protein extract from the stable LBR238-GFP HeLa cell line results in the detection of an upper band of molecular mass close to 63kDa, that corresponds to endogenous full-length LBR, and a faster-migrating lower band, corresponding to LBR238-GFP.

(B) Use of anti-GFP antibody with the same samples appropriately only detects the lower band with the GFP-tagged protein.

(C) Test and negative control experiments, in parallel to the analysis shown in Fig.6 B5. Samples shown here were from HeLa cells transfected with N-terminal construct LBR238-GFP or with GFP-only construct. Top panels confirm binding of GFP-tagged versions of LBR or GFP-only in the bound fractions as bait; middle panels indicate absence of co-selection of native TMEM147 in the bound fractions; bottom panel displays GAPDH immunoreactivity as loading control. Abbreviations: (I) input, (U)"unbound, and (B) bound fractions.

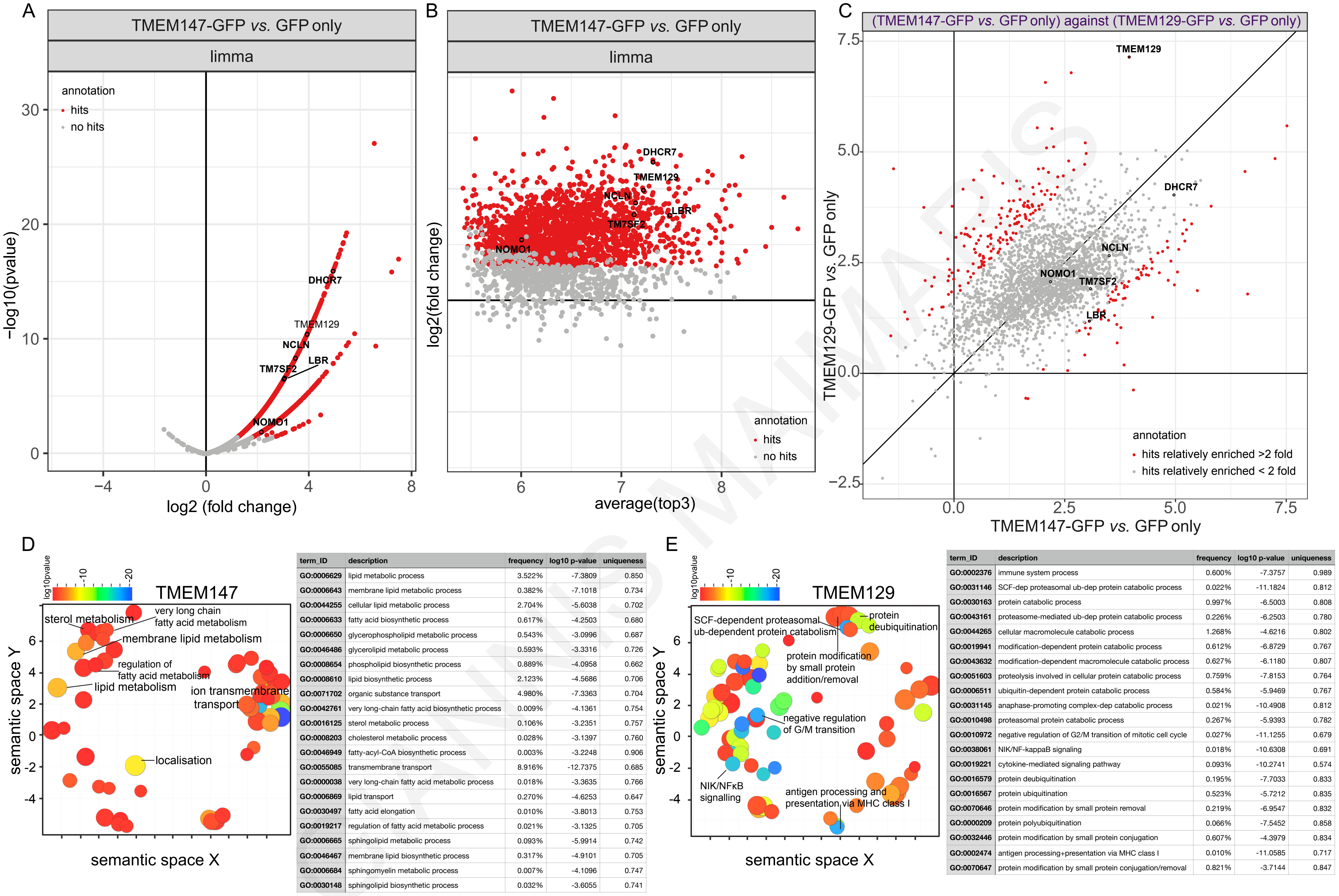

term_ID	description	frequency	log10 p-value	uniqueness
GO:0006629	lipid metabolic process	3.522%	-7.3809	0.850
GO:0006643	membrane lipid metabolic process	0.382%	-7.1018	0.734
GO:0044255	cellular lipid metabolic process	2.704%	-5.6038	0.702
GO:0006633	fatty acid biosynthetic process	0.617%	-4.2503	0.680
GO:0006650	glycerophospholipid metabolic process	0.543%	-3.0996	0.687
GO:0046486	glycerolipid metabolic process	0.593%	-3.3316	0.726
GO:0008654	phospholipid biosynthetic process	0.889%	-4.0958	0.662
GO:0008610	lipid biosynthetic process	2.123%	-4.5686	0.706
GO:0071702	organic substance transport	4.980%	-7.3363	0.704
GO:0042761	very long-chain fatty acid biosynthetic process	0.009%	-4.1361	0.754
GO:0016125	sterol metabolic process	0.106%	-3.2351	0.757
GO:0008203	cholesterol metabolic process	0.028%	-3.1397	0.760
GO:0046949	fatty-acyl-CoA biosynthetic process	0.003%	-3.2248	0.906
GO:0055085	transmembrane transport	8.916%	-12.7375	0.685
GO:0000038	very long-chain fatty acid metabolic process	0.018%	-3.3635	0.766
GO:0006869	lipid transport	0.270%	-4.6253	0.647
GO:0030497	fatty acid elongation	0.010%	-3.8013	0.753
GO:0019217	regulation of fatty acid metabolic process	0.021%	-3.1325	0.705
GO:0006665	sphingolipid metabolic process	0.093%	-5.9914	0.742
GO:0046467	membrane lipid biosynthetic process	0.317%	-4.9101	0.705
GO:0006684	sphingomyelin metabolic process	0.007%	-4.1096	0.747
GO:0030148	sphingolipid biosynthetic process	0.032%	-3.6055	0.741

term_ID	description	frequency	log10 p-value	uniqueness
GO:0002376	immune system process	0.600%	-7.3757	0.989
GO:0031146	SCF-dep proteasomal ub-dep protein catabolic process	0.022%	-11.1824	0.812
GO:0030163	protein catabolic process	0.997%	-6.5003	0.808
GO:0043161	proteasome-mediated ub-dep protein catabolic process	0.226%	-6.2503	0.780
GO:0044265	cellular macromolecule catabolic process	1.268%	-4.6216	0.802
GO:0019941	modification-dependent protein catabolic process	0.612%	-6.8729	0.767
GO:0043632	modification-dependent macromolecule catabolic process	0.627%	-6.1180	0.807
GO:0051603	proteolysis involved in cellular protein catabolic process	0.759%	-7.8153	0.764
GO:0006511	ubiquitin-dependent protein catabolic process	0.584%	-5.9469	0.767
GO:0031145	anaphase-promoting complex-dep catabolic process	0.021%	-10.4908	0.812
GO:0010498	proteasomal protein catabolic process	0.267%	-5.9393	0.782
GO:0010972	negative regulation of G2/M transition of mitotic cell cycle	0.027%	-11.1255	0.679
GO:0038061	NIK/NF-kappaB signaling	0.018%	-10.6308	0.691
GO:0019221	cytokine-mediated signaling pathway	0.093%	-10.2741	0.574
GO:0016579	protein deubiquitination	0.195%	-7.7033	0.833
GO:0016567	protein ubiquitination	0.523%	-5.7212	0.835
GO:0070646	protein modification by small protein removal	0.219%	-6.9547	0.832
GO:0000209	protein polyubiquitination	0.066%	-7.5452	0.858
GO:0032446	protein modification by small protein conjugation	0.607%	-4.3979	0.834
GO:0002474	antigen processing+presentation via MHC class I	0.010%	-11.0585	0.717
GO:0070647	protein modification by small protein conjugation/removal	0.821%	-3.7144	0.847

SUPPLEMENTARY FIGURE 4

FIGURE S4

TMEM147 interacts with DHCR7

Bound proteins from IP experiments using as baits TMEM147-GFP, TMEM129-GFP (for comparison) and GFP-only (negative control) were processed and extracted peptides subjected to liquid chromatography coupled with tandem mass spectrometry for protein identification.

(A) Volcano plot with identified hit proteins for TMEM147 (using GFP-only as negative control), in which some proteins of interest (POIs) are indicated (DHCR7, LBR, TM7SF2 and, known TMEM147 interactors, NOMA and Nicalin, NCLN).

(B) Corresponding TOP3 plot with the same proteins highlighted.

(C) Comparison of enrichment between the TMEM147 and TMEM129 hits (using in both cases GFP-only as negative control).

(D, E) Gene Ontology (GO) analysis of top biological processes identified from the ranked hits for TMEM147 (D) and TMEM129 (E), using *GOrilla* (Gene Ontology enRIchment anaLysis and visuaLizAtion tool; http://cbl-gorilla.cs.technion.ac.il/) and REVIGO (REduce and VIsualize Gene Ontology; http://revigo.irb.hr/). "*Lipid metabolism*", "*membrane lipid biosynthesis*" and "*sterol metabolism*" were among the top GO terms (statistical significance, frequency and uniqueness) associated with TMEM147, consistent with our findings. For TMEM129 (an ERAD E3 ubiquitin ligase, essential for virus-induced degradation of MCH-I; van den Boomen et al., 2014 van de Weijer et al., 2014), top GO terms included "*SCF-dependent proteasomal ubiquitin-dependent protein catabolic process*" and "*antigen processing and presentation of peptide antigen via MHC class I*", again consistent with its characterised function. The associated tables display some examples of top GO terms, selected for their relevance.

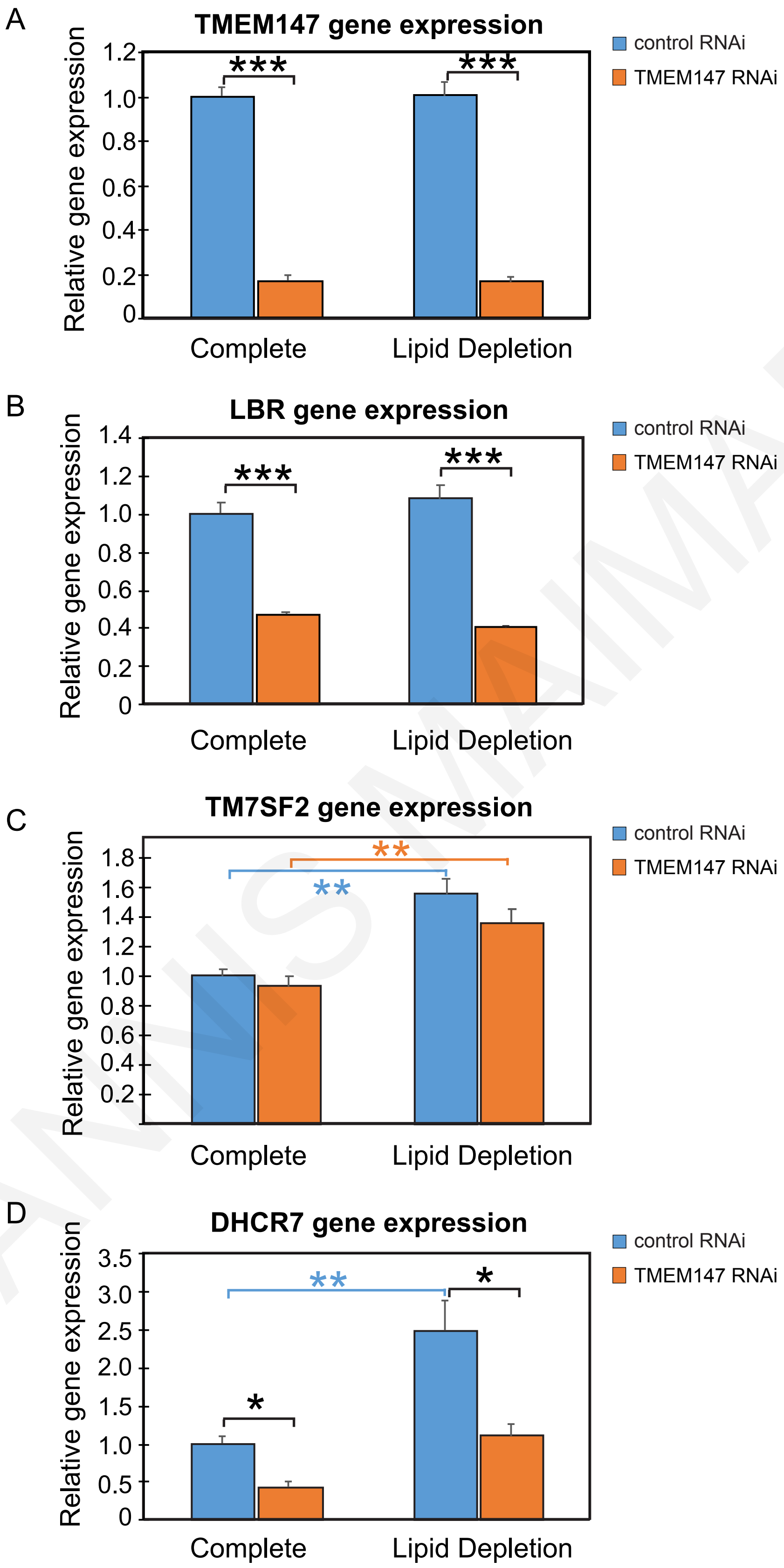

SUPPLEMENTARY FIGURE 5

FIGURE S5

Assessment by RT-qPCR in three independent experiments of *TMEM147, LBR*, *DHCR7* and *TM7SF2* mRNA levels in negative control and *TMEM147*-silenced cells grown in parallel, either in full media (72 h) or in lipid restrictive media (48 h in complete media and serum starved for 24 h). To be directly comparable, values are calculated using the common base method (Ganger et al., 2017) and expressed as a ratio to the normalized mean control value with error bars corresponding to SE of triplicate analysis. The results show that both *TMEM147* and *LBR* are constitutively expressed, irrespective of lipid restriction and their co-ordinate downregulation upon *TMEM147* silencing remains unchanged (A and B). Lipid restriction induces statistically significant and almost identical *TM7SF2* upregulation both in the presence and absence of *TMEM147* (C). *DHCR7* expression is even more markedly induced upon lipid restriction, specifically 2.5-fold in the presence of *TMEM147* (from 1.00±0.10 relative expression in complete medium to 2.49±0.40 upon lipid restriction, p=0.007). The absence of *TMEM147* induces downregulation of *DHCR7*, as also seen in Fig. 7C, both in normal conditions and in lipid restriction, but although the absolute values of *DHCR7* expression are reduced, the 2.5-fold induction ratio of *DHCR7* expression is maintained upon lipid restriction (from 0.44±0.07 in complete medium to 1.11±0.15 upon lipid restriction, p=0.01).

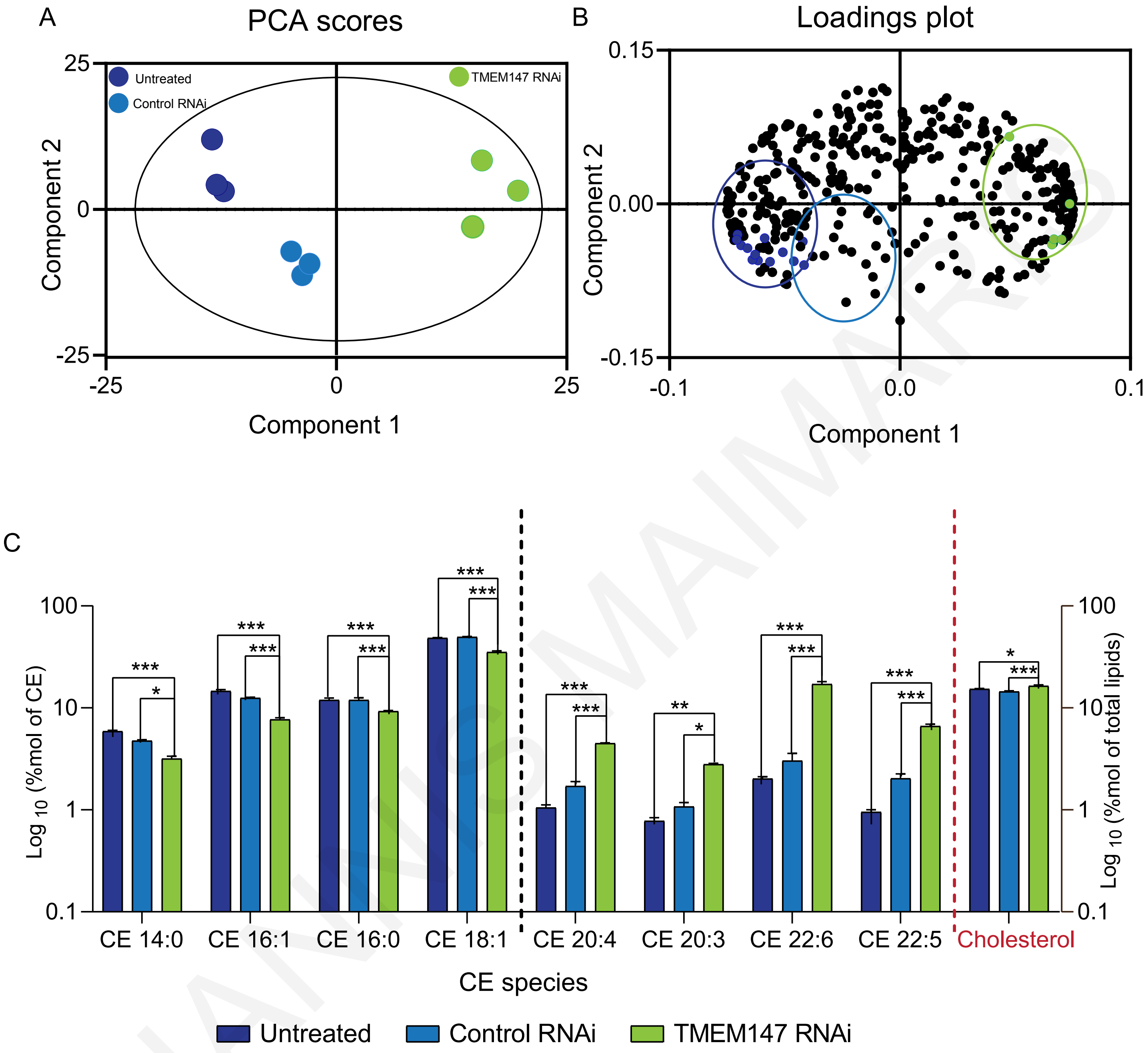

SUPPLEMENTARY FIGURE 6

FIGURE S6

Lipidomic rewiring in TMEM147 silenced HeLa cells.

(A) PCA (principal component analysis) scores plot of the total lipid profiles in untreated, control and" TMEM147 silenced cells. **(B)** PCA loadings plot showing the lipid species influence on the separation" between untreated, control and *TMEM147* silenced cells**(C)** Most important CE species and" cholesterol in untreated, control- and *TMEM147*-silenced cells. Data are presented as mean±SEM and" analysed by 2-way ANOVA with post hoc Tukey's multiple-comparisons test; *$p \leq 0.05$, ** $p \leq 0.01$," *** $p \leq 0.001$ $n = 3$/group.

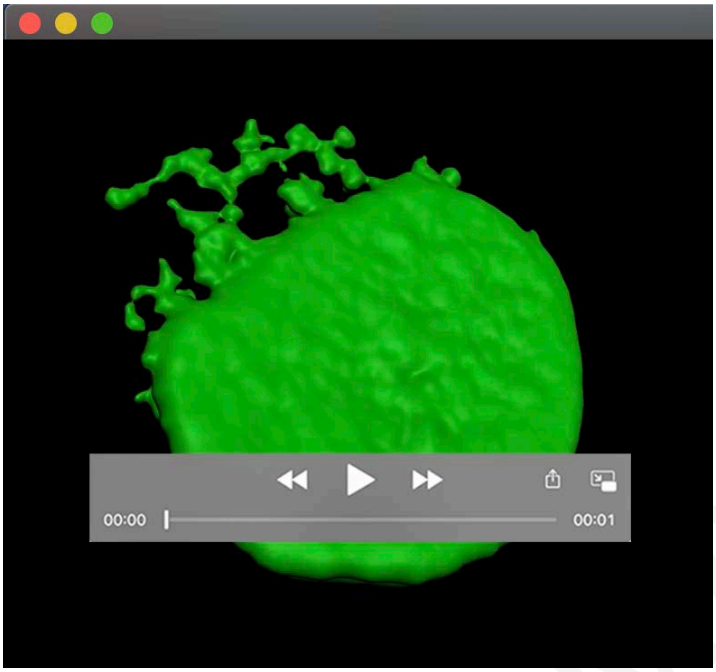

Movie 1

Animation of 3D rendering of one of the silenced cells in Fig. 6D, to illustrate enhanced LBR mislocalization at the ER upon *TMEM147* silencing.

TABLE S1

Percentages of cells exhibiting LBR labeling at the NE only or partitioning between the NE+ER.

	No. cells with NE-localized LBR (% of population)	No. cells with ER-localized LBR (% of population)	No. cells with unclear localization	Total number of cells
Control RNAi	47 (**85.5%**)	6 (**10.9%**)	2	55
TMEM147 RNAi	15 (**31.3%**)	31 (**64.6%**)	2	48

TABLE S2

Click here to Download Table S2

6.2 Publication 2

International Journal of
Molecular Sciences

Article

Regulation of ER Composition and Extent, and Putative Action in Protein Networks by ER/NE Protein TMEM147

Giannis Maimaris [1], Andri Christodoulou [1], Niovi Santama [1] and Carsten Werner Lederer [2,*]

[1] Department of Biological Sciences, University of Cyprus, Nicosia 1678, Cyprus; maimaris.giannis@ucy.ac.cy (G.M.); christodoulou.c.andri@ucy.ac.cy (A.C.); santama@ucy.ac.cy (N.S.)
[2] Department of Molecular Genetics Thalassaemia, The Cyprus Institute of Neurology and Genetics, Nicosia 2371, Cyprus
* Correspondence: Lederer@cing.ac.cy; Tel.: +357-22-392764

Abstract: Nuclear envelope (NE) and endoplasmic reticulum (ER) collaborate to control a multitude of nuclear and cytoplasmic actions. In this context, the transmembrane protein TMEM147 localizes to both NE and ER, and through direct and indirect interactions regulates processes as varied as production and transport of multipass membrane proteins, neuronal signaling, nuclear-shape, lamina and chromatin dynamics and cholesterol synthesis. Aiming to delineate the emerging multifunctionality of TMEM147 more comprehensively, we set as objectives, first, to assess potentially more fundamental effects of TMEM147 on the ER and, second, to identify significantly TMEM147-associated cell-wide protein networks and pathways. Quantifying curved and flat ER markers RTN4 and CLIMP63/CKAP4, respectively, we found that TMEM147 silencing causes area and intensity increases for both RTN4 and CLIMP63, and the ER in general, with a profound shift toward flat areas, concurrent with reduction in DNA condensation. Protein network and pathway analyses based on comprehensive compilation of TMEM147 interactors, targets and co-factors then served to manifest novel and established roles for TMEM147. Thus, algorithmically simplified significant pathways reflect TMEM147 function in ribosome binding, oxidoreductase activity, G protein-coupled receptor activity and transmembrane transport, while analysis of protein factors and networks identifies hub proteins and corresponding pathways as potential targets of TMEM147 action and of future functional studies.

Keywords: nuclear envelope; endoplasmic reticulum; network analysis; gene ontology; RNA interference

check for updates

Citation: Maimaris, G.; Christodoulou, A.; Santama, N.; Lederer, C.W. Regulation of ER Composition and Extent, and Putative Action in Protein Networks by ER/NE Protein TMEM147. *Int. J. Mol. Sci.* **2021**, *22*, 10231. https://doi.org/10.3390/ijms221910231

Academic Editor: James M. Holaska

Received: 31 August 2021
Accepted: 19 September 2021
Published: 23 September 2021

1. Introduction

Transmembrane Protein 147 (TMEM147), also known as NIFIE14, is a small, fairly recently discovered protein that localizes to the endoplasmic reticulum (ER) [1,2]. Encoded on the large arm of chromosome 19 (19q13.12) in *Homo sapiens*, it consists of seven exons, which through alternative splicing give rise to multiple isoforms [3], three of which have been validated as variants for the NCBI Gene database (Gene ID: 10430) [4]. The most abundant of the latter three in-frame variants is also the largest and translates to a 224-amino-acid (aa) protein of 26.2 kDa (see Table 1 and Supplementary Figures S1–S3).

TMEM147 has seven transmembrane domains, each of which fully span the ER membrane, with the N-terminus facing the ER lumen and the C-terminus facing the cytosol [5]. Its expression in many tissues [6] (see Supplementary Figure S4) suggests its general and wide-ranging physiological role, as does the high level of conservation of the *TMEM147* gene across mammals, with sequence similarity in human, mouse, rat and bovine species of up to 99% [1,2]. However, *TMEM147* is phylogenetically older than the class of mammals and was originally isolated in zebrafish. There, early embryonic development is controlled by the NODAL signal transduction pathway, which Haffner and co-workers found to be modulated by a protein complex containing Nicalin and NOMO [7]. Differences in molecular weight between the native protein complex (200–220 kDa) and its known denatured components, Nicalin (60 kDa) and NOMO (130 kDa), three years later prompted purification of the 26-kDa TMEM147 as an additional, smaller ER-localized core component [1].

Table 1. TMEM147 variants in *H. sapiens*. Range information for Variants 2 and 3 indicates corresponding amino acids for Variant 1; nt—nucleotides; aa—amino acids.

Variant	mRNA Length	Protein Length	Accession No.	Note
1	868 nt	224 aa	NP_116024.1NM_032635.4	Main isoform
2	939 nt	175 aa (aa 50–224)	NP_001229526.4NM_001242597.2	Compared to Variant 1 with truncated N terminus and identical C terminus, by inclusion of an additional exon in its extended 5′ UTR and initiating translation at a downstream, in-frame start codon
3	646 nt	150 aa (aa 1–70, aa 144–224)	NP_001229527.1NM_001242598.2	Compared to Variant 1 with identical N and C terminus, but lacking two consecutive exons in the coding region; shortest variant

Beyond action in the Nicalin-NOMO-TMEM147 complex, which in addition to NODAL signaling also has a critical role in translocon function and thus ER-localized translation [5], TMEM147 interacts with the M3 muscarinic acetylcholine receptor (M3R), as has been shown with membrane-based yeast-2-hybrid detection systems, as well as with other class-I G-protein-coupled receptors, such as vasopressin-2 receptor and M1 muscarinic acetylcholine receptor (M1R). In this context, expression of TMEM147 in COS-7 cells inhibits trafficking of the receptor to the cell surface and additionally impairs receptor function, resulting in reduced levels of Ca^{2+} compared to control cells upon induction with the muscarinic agonist carbachol. Silencing of TMEM147 in H508 colon cancer cells, where TMEM147 and the M3R are normally co-expressed, causes an increase in the receptor molecules on the cell surface along with an overall increase in the properly folded receptors, implicating TMEM147 in both trafficking and folding of M3R [2].

Although *TMEM147* sequence conservation among organisms, its presence in a three-protein complex modulating the NODAL pathway and its interaction with M3R all point to the importance of TMEM147 and its interactions, details of TMEM147 function were until most recently largely unknown. To address this issue, our team has proven that TMEM147 not only localizes to ER membranes but also to the nuclear envelope (NE) of HeLa cells, as independently shown in immunofluorescence images labeled for either N-terminally FLAG-tagged and C-terminally GFP-tagged TMEM147 constructs [8], in line with incidental earlier observations in COS-7 cells [2]. Additionally, we have shown that depletion of TMEM147 causes transcriptional reduction of two ER-associated cholesterol biosynthesis pathway constituents. The first component is Lamin B receptor (LBR); a bifunctional protein best characterized for its N-terminal interaction with Lamin B and heterochromatin-related-proteins (HP1 and MeCR2) [9–11] and for its consequent role in tethering the transcriptionally inactive heterochromatin at the periphery of the NE [12]. However, in tandem to a chromatin-associated region extending throughout its C-terminus, LBR also contains a C-14 sterol reductase activity domain [13–16], showing extensive sequence similarity with evolutionary diversification for two other C-14 sterol reductases of the post-squalene biosynthetic pathway TM7SF2 and DHCR7 [12,17–19]. TMEM147 has been shown to physically interact with the C-terminal domain of LBR, which gave a first indication of a potential indirect regulatory role for TMEM147 in cholesterol synthesis. This notion was vindicated by our subsequent discovery of additional TMEM147 interaction with DHCR7 and of reduced transcript and protein levels for DHCR7 upon TMEM147 silencing [8].

Interactions of TMEM147 with NE components, such as with LBR, have implications beyond effects on cholesterol biosynthesis, including the localization of membrane components and NE structure. Specifically, in addition to transcriptional silencing of LBR, TMEM147 also effects a change in distribution for the remaining LBR protein, allowing detection of LBR in the proximal ER, in addition to the NE [8]. Additionally, TMEM147-silenced cells show significant changes in sphericity as a key parameter of nuclear shape, which is regulated by a complex network of pathways and factors [20]. These observations raise the question whether TMEM147, similar to its role in the NE, may also affect ER structure or abundance and position of ER integral membrane components. In this context, it is of interest that some components, such as TMEM147, may be shared between NE and ER, while others, such as LBR under normal conditions, are exclusively located in one of the compartments, despite the contiguity of ER and NE membranes and lumen.

A key example of shared ER and NE components is the reticulon (Rtn) family of highly conserved integral ER-membrane proteins with a characteristic wedge-shaped topological domain [21–24]. Rtn marks regions with high membrane curvature in both compartments, such as tubules in the smooth ER (sER) and the elongated highly bent membrane edges of rough ER (rER) sheets or matrices, as well as the developing nuclear pore complex of the NE [25]. The role of Rtn is well established in the ER, where its overexpression increases sER tubule length but reduces rER sheets [26], whereas Rtn depletion results in the expansion of peripheral sheets and the reduction in sER tubules and tubule branching [27,28]. Moreover, purified reticulons support membrane tubule generation from proteoliposomes in vitro [29]. Taken together, these data indicate that reticulons are both necessary and sufficient to induce tubule formation and to control the ratio of ER sheets to tubules [22,23].

A key example of components exclusive to the ER membrane is cytoskeleton linking membrane protein 63 (CLIMP63, formerly known as p63, official HGNC gene symbol *CKAP4*), which as a single-transmembrane ER protein binds microtubules with its N-terminus [30] and stabilizes ER luminal distance with its C terminus [22]. CLIMP63 overexpression results in sheet proliferation at the expense of tubules, whereas depletion of CLIMP63 unexpectedly does not affect the number of ER sheets, but instead decreases the rER luminal distance from $\approx$50 nm to $\approx$30 nm, comparable to that observed in lower organisms that lack CLIMP63 [31]. Furthermore, CLIMP63 overexpression diffuses sheets and the position of rER-ribosome-associated translocons throughout the cytoplasm [22], which is conversely not affected by CLIMP63 depletion [32] and which, moreover, establishes a tentative functional link to TMEM147 [5]. Highly expressed in the perinuclear rER, CLIMP63 is also detectable by advanced imaging in dynamic subdomains in peripheral ER tubules [24], where its expression and presence is associated with luminal elongation, while Rtn is associated with luminal branching, as Gao and co-workers revealed [28]. In either part of the ER, Rtn and CLIMP63 are therefore functional and topological opposites. Whereas Rtn is a marker of and essential for ER tubule, branch and edge formation as a major determinant of tubule:sheet ratio, CLIMP63 is a marker and facilitator of sheet formation and of unbranched ER areas [33]. Akin to LBR for the NE and regarding their role in the ER, CLIMP63 is both marker and structural determinant for the rER, while Rtn is both marker and structural determinant of the sER.

With our aim the comprehensive delineation of TMEM147 functions in the ER and cell-wide, we thus pursued two objectives. First, we set out to exploit our insights into CLIMP63 and Rtn function for an assessment of TMEM147 function in the ER. To this end, and in analogy to our previous analyses of TMEM147 and LBR concerning the NE, we investigated the effect of TMEM147 silencing on CLIMP63 and Rtn as markers and potential facilitators of TMEM147 ER action. Second, we set out to identify and summarize significantly TMEM147-associated protein networks and pathways as targets for future investigations and to address our currently limited understanding of TMEM147 multifunctionality, for which we employed comprehensive data mining and in silico analyses for reported TMEM147 upstream and downstream actors and interactors.

2. Results

2.1. Establishment of TMEM147 Silencing

For evaluation of TMEM147-dependent action we employed RNA interference (RNAi) to deplete *TMEM147* transcripts and protein, as previously reported [8]. Upon silencing of TMEM147, LBR is dramatically downregulated and its protein levels reduced by $\approx$90% [8], which allowed us to employ detection of LBR expression as a proxy for the confirmation of TMEM147 protein depletion (Figure 1a).

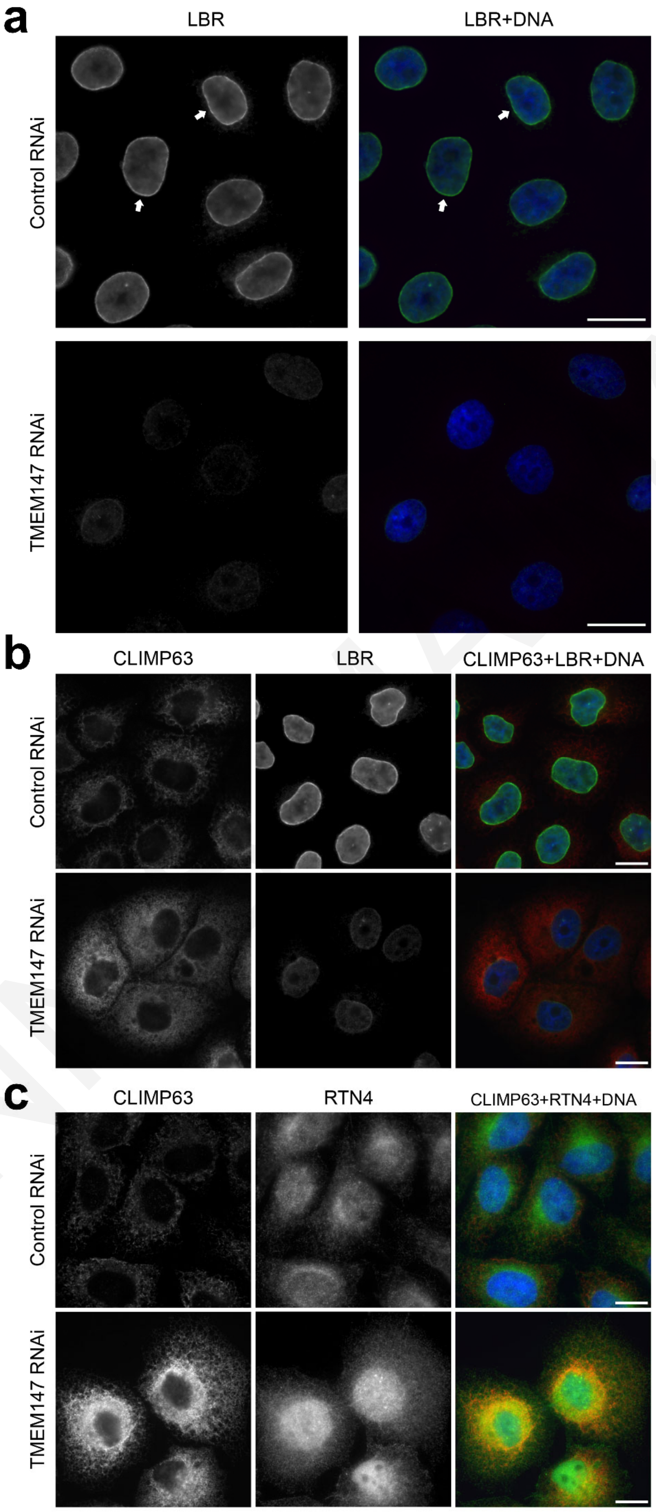

Figure 1. Immunofluorescence imaging of TMEM147 silencing in HeLa cells. (**a**) Cells stained for LBR and DNA show downregulation of LBR expression in response to TMEM147 silencing, in line with [8]; arrows indicate the nuclear rim on the inner nuclear membrane; (**b**) cells stained for CLIMP63, LBR and DNA; (**c**) Cells stained for CLIMP63, RTN4 and DNA. For (**b**,**c**), TMEM147-silenced cells show elevated fluorescence intensity and area for the respective ER marker. Size markers indicate 20 µm.

2.2. Silencing of TMEM147 Alters CLIMP63/RTN4 ER Labeling

To investigate the effect of TMEM147 silencing on ER area and composition, RNAi- and control-treated HeLa cells were stained with α-CLIMP63 and α-RTN4 antibodies to label the flattened and curved areas of the ER, respectively [22], LBR as a positive control for TMEM147 silencing in imaged cells and Hoechst 33342 as an LBR-independent nuclear size and DNA marker (Figure 1b,c). Upon TMEM147 silencing, ER labeling for both markers underwent pronounced elevation and expansion. CLIMP63 labeling expanded and increased, suggesting an increase in the flattened surface area and network density of ER (Figure 1b). In agreement with a denser ER network is also the observation of brighter RTN4 labeling (Figure 1c), suggesting an increase in the curved edges of the flat cisternae and tubular area, mainly at the periphery of the ER. The increase in both RTN4 and CLIMP63 labeling intensity and area additionally suggested an overall expansion of the ER density and surface area.

2.3. Statistical Analysis of ER Morphological Alterations in TMEM147-Silenced Cells

To quantify these observations concerning CLIMP63 and RTN4 and thus of ER composition and area after TMEM147-silencing, we conducted quantitative morphometric microscopy analyses for three independent silencing experiments and based on images acquired with identical, non-saturating-exposure settings (Figure 2a). Area analyses for a total of 457 cells ($n = 232$ silenced, $n = 225$ negative control) were performed for three independent fluorescence channels after labeling with α-CLIMP63 and α-RTN4 antibodies and Hoechst 33342 staining (Figure 2b).

Mean Fluorescence Intensity (MFI). Analysis of MFI for DNA staining confirmed our previous finding that silencing of TMEM147 promotes a loss of chromatin compaction, with a significant decrease in the DNA signal after silencing (Figure 2c, $p < 0.0001$) [8]. By contrast, MFI for both ER markers, CLIMP63 and RTN4, significantly increased compared to that of untreated cells by 122.9% ($p < 0.0001$) and 60.3% ($p < 0.0001$), respectively, suggesting an increased density of the ER network and/or increased retention of both markers in ER membranes after TMEM147 silencing.

Surface area analysis. Corresponding analysis of nuclear surface area, ER surface area and ER flat and tubular domain surface areas revealed differential effects of TMEM147 silencing. While treatment had no effect on the surface area of the cell nucleus, it increased total ER surface area by 46.97% compared to control cells ($p < 0.0001$) (Figure 2d). Based on the universally fixed ratio of nuclear area to cell size [34,35], these MFI measurements indicated that TMEM147 silencing resulted in an almost 50% expansion of labeled ER area and a likely increase in ER density at unchanged cell size, with clear implications for the intracellular organization and transport of non-ER organelles. Moreover, the increase in ER area was not contributed in equal measure by both ER domains, with an area increase in flat ER cisternae of 100.13% ($p < 0.0001$) and with a more moderate increase in the tubular ER area of 41.39% ($p < 0.0001$) (Figure 2d).

ER Domains Surface Area Ratios. Differential area increases for flat and curved areas predictably resulted in a change in the area ratio for both ER domains compared to untreated cells (Figure 2e). While there was no difference in the ratio of curved area compared to the total ER area for treated vs. control-treated cells, the cisternal area increased by 34.22% ($p < 0.0001$) more than the total ER area and by 39.76% ($p < 0.0001$) more than the curved areas, clearly indicating a disproportionate expansion of flat areas upon silencing of TMEM147, in addition to an overall increase in ER area and density.

2.4. Data Mining to Compile TMEM147 Interactors

Taken together with our own previous observations for TMEM147 effects on LBR and cholesterol homeostasis, our present findings for its apparent inhibitory effect on ER size and density suggested a wide array of additional research targets for future investigation. In order to identify the most promising targets and experimental strategies for future investigations and to allow deeper insight into potential functional roles of TMEM147, we performed comprehensive datamining of interaction and association databases and of the literature, to identify all known TMEM147 interactions and associations. This revealed 98 interactors (Table 2; for full annotations see Supplementary Table S1), as input for subsequent network and pathway analysis.

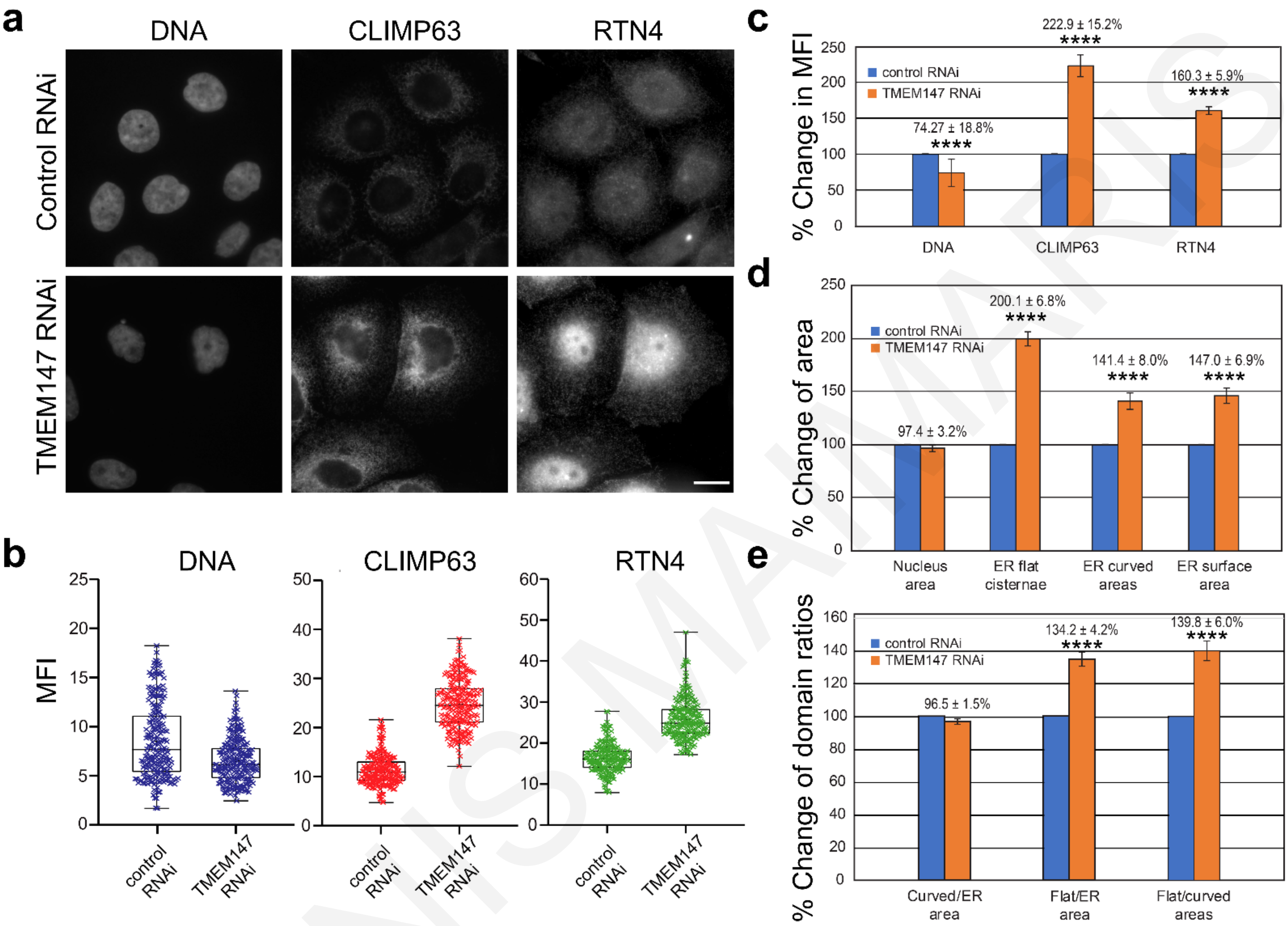

Figure 2. Statistical evaluation of immunofluorescence imaging after RNAi treatment. (**a**) Representative images employed for fluorescence and area quantifications; (**b**) box-and-whisker diagrams of mean fluorescence intensities for DNA, CLIMP63 and RTN4, as indicated; (**c**) bar chart of mean fluorescence intensity (MFI) percentage changes in DNA, CLIMP63 and RTN4 signals for TMEM147 vs. control silencing; (**d**) Bar chart of organelle surface area percentage changes of nucleus (measured as DNA), ER flat cisternae (measured as CLIMP63), ER curved areas (measured as RTN4) and total ER surface area (measured as the overlap-corrected union of CLIMP63 and RTN4 areas) for TMEM147 vs. control silencing; (**e**) bar chart of percentage changes in ER domain ratios, corresponding to (**d**). Error bars indicate the standard deviation of the population. Size markers indicate 20 µm. **** indicates $p < 0.0001$.

Table 2. Reported TMEM147 associations and interaction. This manually curated, non-redundant list of proteins as retrieved from twelve different repositories is the basis for network and pathway enrichment analyses. The input list of identifiers for String-db and an annotated version of this table are provided as Supplementary Table S1.

Gene Symbol [a] [String-db ID] [b]	Uniprot ID [c]	Interaction Type [d]	GO IDs [e]	GO Group/ Context [f]	Protein [g]	Source Db [h]
ABHD16A	O95870	A			Phosphatidylserine lipase ABHD16A	A,B,C,D,E,G,F,J
ABI3	Q9P2A4	A			ABI gene family member 3	A,B,D,E,G,F,I,J
AVPR2	P30518	B	4888, 8528, 38023, 4930	A	Vasopressin V2 receptor	C
BCAP31	P51572	F			B-cell receptor-associated protein 31	C
BRF2	Q9HAW0	B			Transcription factor IIIB 50 kDa subunit	A,D,F,I,J
CAPNS1	P04632	F			Calpain small subunit 1	C
CASP4	P49662	B			Caspase-4	A,D,F,J

Table 2. *Cont.*

Gene Symbol [a] [String-db ID] [b]	Uniprot ID [c]	Interaction Type [d]	GO IDs [e]	GO Group/ Context [f]	Protein [g]	Source Db [h]
CCDC47	Q96A33	A			PAT complex subunit CCDC47	H
CD40	P25942	A	4888, 38023	A	Tumor necrosis factor receptor superfamily member 5	A,B,G,F,I,J
CD79A	P11912	A	4888, 38023	A	B-cell antigen receptor complex-associated protein alpha chain	A,B,G,F,I,J
CGN	Q9P2M7	B			Cingulin	A
CHRM3	P20309	A	4888, 38023, 8227, 4930	A	Muscarinic acetylcholine receptor M3	C,H
CLDN7	O95471	A			Claudin-7	A,B,G,F,I,J
CLN8	Q9UBY8	A			Protein CLN8	A,B,D,H,J
CLRN1	P58418	A			Clarin-1	A,B,D,H,J
COX6B1	P14854	F	22890, 15077	B	Cytochrome c oxidase subunit 6B1	C
CREB3L1	Q96BA8	A			Cyclic AMP-responsive element-binding protein 3-like protein 1	A,B,D,G,F,I,J,K
CXCR2	P25025	A	4888, 8528, 38023, 4930	A	C-X-C chemokine receptor type 2	A,B,G,F,I,J,K
DHCR7	Q9UBM7	A	16628	C	7-dehydrocholesterol reductase	H
DPM3	Q9P2X0	A			Dolichol-phosphate mannosyltransferase subunit 3	A,B,G,F,I,J
EBP	Q15125	A	4888, 38023, 16860, 16863	A,C	3-beta-hydroxysteroid-Delta(8),Delta(7)-isomerase	A,B,G,F,I,J,K
EFNA4	P52798	A	4888, 38023	A	Ephrin-A4	A,B,G,F,I,J
EIF3K	Q9UBQ5	F	43022	D	Eukaryotic translation initiation factor 3 subunit K	C
ENPP4	Q9Y6X5	A			Bis(5′-adenosyl)-triphosphatase ENPP4	A,B,G,F,J
F11R	Q9Y624	A			Junctional adhesion molecule A	A,B,G,F,J,K
FASN	P49327	G	16628	C	Fatty acid synthase	B
FFAR2	O15552	A	4888, 38023, 4930	A	Free fatty acid receptor 2	A,B,G,F,J,K
FOXF2	Q12947	E			Forkhead box protein F2	I
GJA8	P48165	A			Gap junction alpha-8 protein	A,B,G,F,J
GLP1R	P43220	A	4888, 8528, 38023, 4930	A	Glucagon-like peptide 1 receptor	A,B,D,G,H,J
GOLM1	Q8NBJ4	A			Golgi membrane protein 1	A,B,G,F,J
GPR101	Q96P66	A	4888, 38023, 8227, 4930	A	Probable G-protein coupled receptor 101	A,B,G,F,J
GPR37L1	O60883	A	4888, 8528, 38023, 4930	A	G-protein coupled receptor 37-like 1	A,B,G,F,J,K
GPR42	O15529	A	4888, 38023, 4930	A	G-protein coupled receptor 42	B,G,F,I,J
GPR61	Q9BZJ8	A	4888, 38023, 4930	A	G-protein coupled receptor 61	A,B,G,F,J
HTR2C	P28335	A	4888, 38023, 8227, 4930	A	5-hydroxytryptamine receptor 2C	A,B,D,G,F,J
IER3IP1	Q9Y5U9	C			Immediate early response 3-interacting protein 1	L
IL3RA	P26951	A	4888, 38023	A	Interleukin-3 receptor subunit alpha	A,B,G,F,J,K
KASH5 [*CCDC155*]	Q8N6L0	A			Protein KASH5	A,B,G,F,I,J
LBR	Q14739	A	16628	C	Delta (14)—Sterol Reductase LBR	H
LDLRAD1	Q5T700	A			Low-density lipoprotein receptor class A domain-containing protein 1	A,B,D,G,F,J
LEF1	Q9UJU2	E	38023	A	Lymphoid enhancer-binding factor 1	I
LEUTX	A8MZ59	A			Paired-like homeodomain transcription factor LEUTX	A,B,G,F,I,J
LHFPL2	Q6ZUX7	A			LHFPL tetraspan subfamily member 2 protein	A,B,G,F,J
LRRFIP2	Q9Y608	B			Leucine-rich repeat flightless-interacting protein 2	A
MIF	P14174	F	16860, 16863	C	Macrophage migration inhibitory factor	C
MPRIP	Q6WCQ1	B			Myosin phosphatase Rho-interacting protein	A
MTCH2	Q9Y6C9	C			Mitochondrial carrier homolog 2	L
MTIF3	Q9H2K0	A	43022	D	Translation initiation factor IF-3, mitochondrial	A,B,G,F,I,J,K
MUC1	P15941	A			Mucin-1	A,B,G,F,I,J
NCLN	Q969V3	A			Nicalin	C,H,L
NFKB1	P19838	A			Nuclear factor NF-kappa-B p105 subunit	H
NHP2	Q9NX24	F			H/ACA ribonucleoprotein complex subunit 2	C
NOMO		A			NODAL modulator	H
PACC1 [*TMEM206*]	Q9H813	A			Proton-activated chloride channel	A,B,D,G,F,J
PDCD1LG2	Q9BQ51	A			Programmed cell death 1 ligand 2	A,B,G,F,I,J
PHPT1	Q9NRX4	F			14 kDa phosphohistidine phosphatase	L
PLEKHG3	A1L390	B			Pleckstrin homology domain-containing family G member 3	A
POLE4	Q9NR33	F			DNA polymerase epsilon subunit 4	C
POLR2I	P36954	F			DNA-directed RNA polymerase II subunit RPB9	C
PPP1R9A	Q9ULJ8	B			Neurabin-1	A
PSCA	O43653	A			Prostate stem cell antigen	A,B,G
PSENEN	Q9NZ42	F			Gamma-secretase subunit PEN-2	L
PVR	P15151	A	38023	A	Poliovirus receptor	A,B,G,F,J,K
RABAC1	Q9UI14	F			Prenylated Rab acceptor protein 1	C
RBM42	Q9BTD8	F			RNA-binding protein 42	C
RMDN3	Q96TC7	A			Regulator of microtubule dynamics protein 3	A,B,G,F,J
RNF185	Q96GF1	A			E3 ubiquitin-protein ligase RNF185	A,B,G,F,J
RTKN	Q9BST9	B			Rhotekin	A
RUVBL2	Q9Y230	F			RuvB-like 2	C
SCAMP4	Q969E2	A			Secretory carrier-associated membrane protein 4	A,B,G,J
SEC61A1	P61619	A	43022	D	Protein transport protein Sec61 subunit alpha isoform 1	H

Table 2. *Cont.*

Gene Symbol [a] [String-db ID] [b]	Uniprot ID [c]	Interaction Type [d]	GO IDs [e]	GO Group/ Context [f]	Protein [g]	Source Db [h]
SHISA3	A0PJX4	A			Protein shisa-3 homolog	A,B,G,F,J
SLC10A1	Q14973	A	15294, 15370, 15291, 15081, 46873, 1901618, 22890, 15077	B	Sodium/bile acid cotransporter	A,B,G,F,J,K
SLC12A7	Q9Y666	A	15296, 15377, 15294, 15291, 46873, 22890, 15077	B	Solute carrier family 12 member 7	A,B,G,F,J
SLC13A4	Q9UKG4	A	15296, 15373, 15294, 15370, 15291, 15081, 46873, 22890, 15077	B	Solute carrier family 13 member 4	A,B,G,F,I,J,K
SLC22A1	O15245	A	15296, 15373, 15377, 5277, 5330, 5334, 8513, 15294, 15370, 15651, 15291, 15081, 46873, 1901618, 22890, 15077	B	Solute carrier family 22 member 1	A,B
SLC22A2	O15244	A	15296, 15373, 15377, 5277, 5330, 5334, 8513, 15294, 15370, 15651, 15291, 15081, 46873, 1901618, 22890, 15077	B	Solute carrier family 22 member 2	A,B
SLC41A1	Q8IVJ1	A	15291, 15081, 46873, 22890, 15077	B	Solute carrier family 41 member 1	H
STOML2	Q9UJZ1	F			Stomatin-like protein 2, mitochondrial	C
SUSD3	Q96L08	A			Sushi domain-containing protein 3	A,B,G,F,I,J
SYNE4	Q8N205	A			Nesprin-4	A,B,D,G,F,I,J
TACR1	P25103	A	4888, 8528, 38023, 4930	A	Substance-P receptor	A,B,G,F,I,J,K
TBCB	Q99426	F			Tubulin-folding cofactor B	C
TEX29	Q8N6K0	A			Testis-expressed protein 29	A,B,G,F,J
TMCO1	Q9UM00	A	46873, 22890	B,D	Calcium load-activated calcium channel	H
TMEM14B	Q9NUH8	A			Transmembrane protein 14B	A,B,G,F,J
TMEM237	Q96Q45	A			Transmembrane protein 237	A,B,G,F,J
TMEM248	Q9NWD8	A			Transmembrane protein 248	A,B,G,F,I,J
TMEM252	Q8N6L7	A			Transmembrane protein 252	A,B,G,F,I,J
TMEM42	Q69YG0	A			Transmembrane protein 42	A,B,G,F,J
TMEM52B	Q4KMG9	A			Transmembrane protein 52B	A,B,G,F,I,J
TPI1	P60174	F	16860	C	Triosephosphate isomerase	C
TRAPPC3	O43617	F			Trafficking protein particle complex subunit 3	C
TRPC6	Q9Y210	H	46873, 22890	B	Short transient receptor potential channel 6	B,H,J
TSPAN12	O95859	A			Tetraspanin-12	A,B,G,F,J
YIPF6	Q96EC8	C			Protein YIPF6	L

[a] Official gene symbol according to the HUGO Gene Nomenclature Committee (HGNC); [b] the associated STRING ID used in STRING analysis, if different from the official gene symbol; [c] protein UniProt ID; [d] nature of discovered TMEM147 interactions: [A] direct physical interaction: the interaction is at the protein–protein level; [B] physical interaction: co-existence in a stable complex; [C] indirect physical interaction: both proteins have a common direct physical interactor; [D] functional association: the combined function with TMEM147 affects the corresponding phenotype; [E] expression regulation: the interactor controls the expression of TMEM147; [F] genetic: significant co-regulation, protein expression dependency or intercellular co-localization with TMEM147; [G] positive modifier: the phenotype is more severe when both are defective; [H] negative modifier: the phenotype is milder when both are defective. [e] Gene Ontology ID with format GO:###### after removal of "GO:" and leading zeros for the sake of compactness; [f] representative non-redundant Gene Ontology category according to REVIGO: [A] G-protein coupled receptor activity; [B] Transmembrane transport; [C] Oxidoreductase activity; [D] Ribosome binding; [g] protein name as found in UniProt; [h] query sources: [A] APID; [B] BioGRID; [C] GeneMania; [D] GPS-Prot; [E] Human Protein Reference Database; [F] IntAct EMBL-EBI; [G] HuRi; [H] PubMed; [I] Pathwaycommons; [J] PINA3; [K] Reactome; [L] STRING.

2.5. Network Analyses of Reported TMEM147-Associated Proteins

We then used this input list of TMEM147 interactors, co-actors, targets and effectors for network analysis using String-db [36], in order to produce a comprehensive network of TMEM147-associated factors and pathways (Figure 3a). While identified from other repositories as interconnected, twelve of our list components were not associated by connections with any of the other 87 components. Likewise, comparison of our list-based analysis with identical analysis of TMEM147 as single input protein gave a network of only ten interactors (Figure 3b), excluding, e.g., LBR. Both observations indicated that while constantly updated and exceptionally powerful and versatile, String-db as an analysis tool cannot be a complete repository of interactions, e.g., for TMEM147, and benefits from the provision of manually curated input lists.

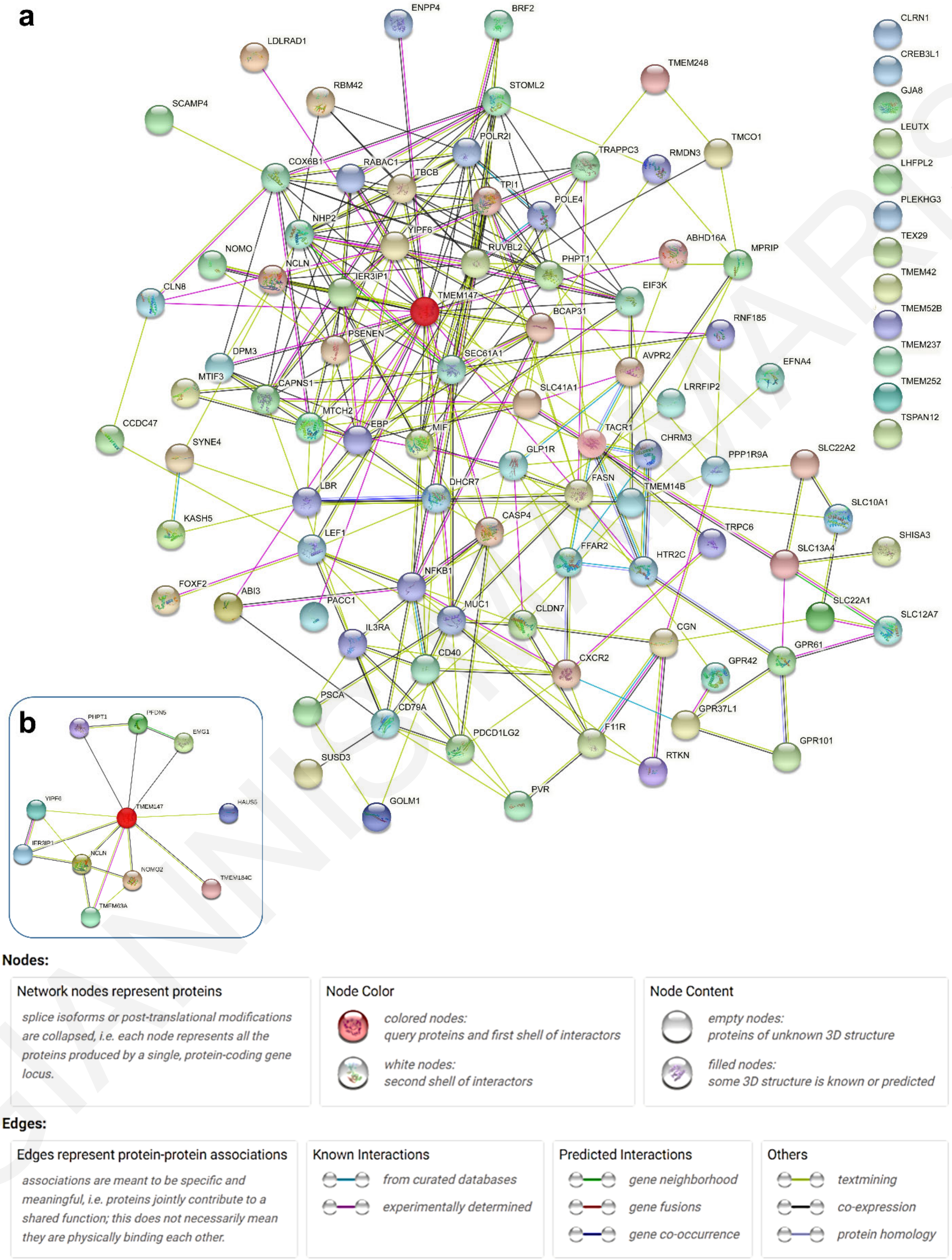

Figure 3. Network analysis for TMEM147-associated proteins. (**a**) Primary network of proteins based on our manually curated list of known interactions and reports for TMEM147 (indicated by transparent red overlay) as analyzed in String-db 11.0b. Proteins without interaction in the String-db 11.0b database are aligned at the top right. (**b**) Primary network of TMEM147-associated proteins as held in String-d 11.0b, based on TMEM147 as input. The color code for underlying database information used by String-db is given in the in-figure legend. Of note, no white nodes are present, because network analysis was restricted to query proteins (**a**) or the first shell of interactors (**b**).

Pathway-based analyses in String-db then revealed several pathway categories with statistically significant enrichment in the supplied list of TMEM147-associated proteins, including 25 GO Molecular Function terms, 21 GO Cellular Component terms, 7 UniProt Annotated Keyword terms, 6 GO Biological Process terms, 3 PubMed Reference Publications, 1 Reactome pathway, 1 Pfam Protein Domain (see Supplementary Table S1). As particularly informative for further analysis, the significantly enriched GO Molecular Function nodes were then exported to REVIGO [37] for content simplification.

2.6. Pathway Analysis for the TMEM147 Gene Network

Removal of redundant GO terms in REVIGO gave four functional groups of GO terms as a summary of a pathway-based analysis for all currently known TMEM147-associated proteins (Figure 4). The resulting non-redundant GO terms can be further summarized based on color coding provided by REVIGO, into our GO summary terms [A] *G-protein coupled receptor activity*; [B] *Transmembrane transport*; [C] *Oxidoreductase activity* and [D] *Ribosome binding* as given in Table 1, in back-annotation of corresponding GO terms, and thus GO summary terms, to each original protein identifier.

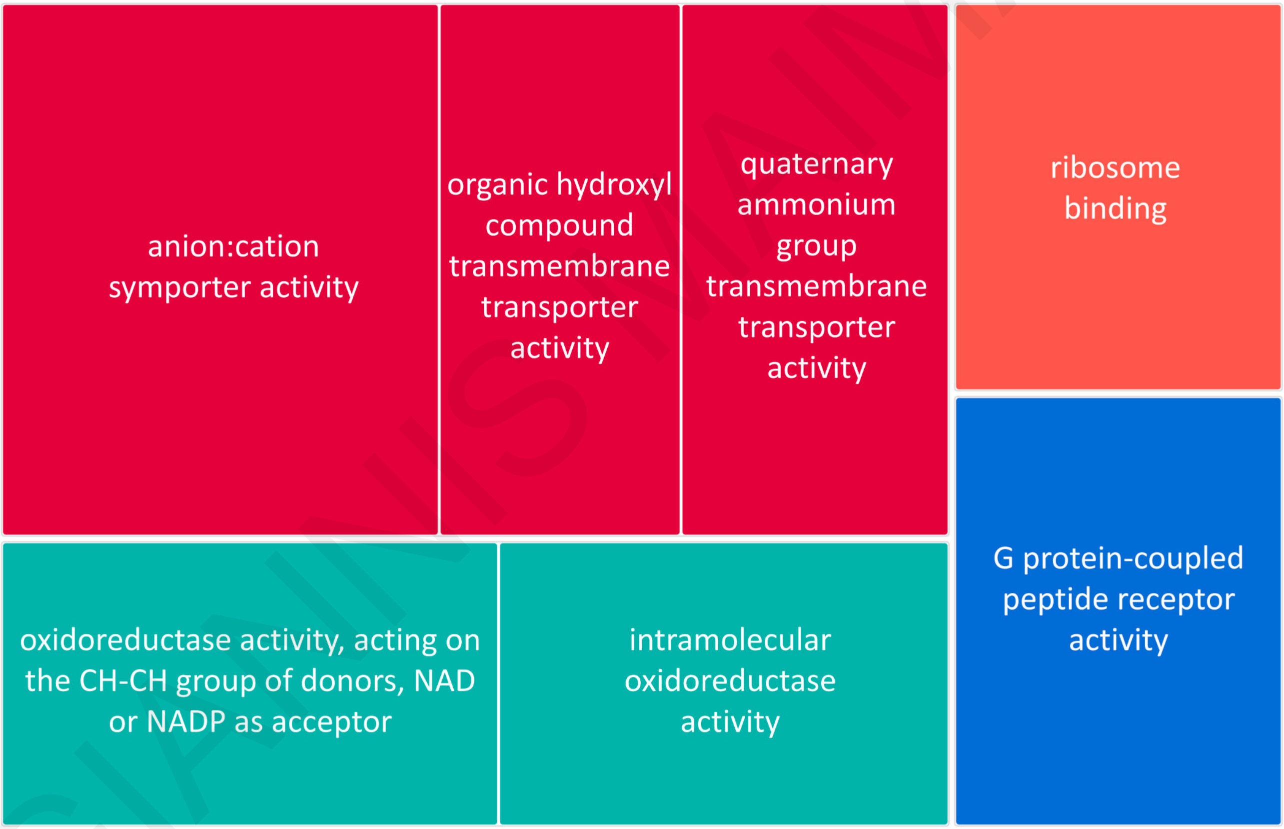

Term ID	Name	Frequency	Value	Uniqueness	Dispensability
GO:0015296	anion:cation symporter activity	0.121%	−2.6576	0.38	0.00
GO:0016628	oxidoreductase activity, acting on the CH-CH group of donors, NAD or NADP as acceptor	0.160%	−1.6271	0.98	0.00
GO:0043022	ribosome binding	0.364%	−1.4685	1.00	0.00
GO:0008528	G protein-coupled peptide receptor activity	0.817%	−1.6271	0.80	0.00
GO:0016860	intramolecular oxidoreductase activity	0.298%	−1.4750	0.93	0.13
GO:1901618	organic hydroxy compound transmembrane transporter activity	0.287%	−1.4685	0.54	0.41
GO:0015651	quaternary ammonium group transmembrane transporter activity	0.061%	−1.6271	0.47	0.45

Figure 4. Reduction in pathway complexity for TMEM147. Reduction in Gene Ontology Molecular Function terms for TMEM147 interactors based on enriched Gene Ontology Molecular Function terms identified by String-db 11.0b, with target being a "Small" output list in REVIGO. Alternatively, non-redundant GO terms are provided by REVIGO in Scatterplots and Interactive Maps, as shown in Supplementary Figure S5. For clarity, fonts for TreeMap and table outputs have been enhanced compared to the original REVIGO display.

3. Discussion

3.1. Effect of TMEM147 Silencing on Rtn, CLIMP63 and ER Structure

In this study, we show that TMEM147 fundamentally affects the composition, the size and likely the structure and the density of the ER. While lowering DNA staining, silencing of TMEM147 significantly enhances labeling intensity and area of flat and curved ER areas, as measured by CLIMP63/CKAP4 and RTN4, respectively, as ER subdomain markers. TMEM147 silencing more substantially increases CLIMP63 labeling and thus additionally raises the ratio between flat and curved areas of the ER.

Importantly, both CLIMP63 and RTN4 are not inert markers of ER subdomains, but are dynamically regulated in their expression and distribution, with evidence of mutual exclusion in dynamic ER nanodomains [28]. Additional markers and, ideally, ultrastructural imaging will therefore be required to discern how far differences in brightness and extent of ER staining reported here reflect a difference in the ER membrane network or differential expression and/or retention in ER membranes of CLIMP63 and RTN4. Exclusion of both proteins from ER membranes as direct action by TMEM147 and conversely, their increased inclusion upon depletion of TMEM147 would be consistent with our observations here. In this context, marker-independent ultrastructural imaging would indicate the state of ER reorganization, while not revealing if any such change would be caused by or in turn causative of CLIMP63 and RTN4 enrichment in the ER for lowered TMEM147 levels. Whatever the causative mechanisms, increased ER area, and likely density, at identical cell size puts constraints on intracellular organization and transport of non-ER organelles, while facilitating ER luminal transport. This might be noticeable in transport defects, as could be evaluated in models, e.g., for secretory pathways or for in vitro neurogenesis, where transport represents a readily detectable bottleneck [38,39].

The differential effect of TMEM147 silencing on the expansion of tubular and cisternal compartments and, more immediately, on CLIMP63 and RTN4 abundance in the ER membrane, might be mirrored by corresponding TMEM147 effects in the NE. While based on our previous analyses we may exclude TMEM147 action on area, volume and ellipticity of the nucleus as key morphological parameters, TMEM147 silencing induced changes in nuclear sphericity and in LBR expression as nuclear effects [8]. It remains to be investigated whether in analogy to its action in the ER, TMEM147 depletion would also lead to an increase in structural NE membrane components. In the complex interplay of factors controlling nuclear size and shape [40], an increase in transient RTN4 in nascent nuclear pore complexes or, with exclusion of CLIMP63 from the NE [41], of functionally CLIMP63-analogous structural proteins, such as Nvj1 [42], might affect architecture and composition of the NE. Moreover, Rtn-dependent formation of ER tubules and formation of the NE are interlinked processes, in that NE assembly is dependent on ER tubules [43], but is encouraged by depletion of Rtn molecules [44]. In addition to interaction with LBR [8], putative interference with integral NE membrane components and with NE/ER membrane dynamics would therefore be an additional mechanism by which TMEM147 may effect changes in the nucleus.

3.2. Network Analysis for Additional TMEM147 Action

Despite a still limited number of studies, TMEM147 has already been implicated in an array of diverse nuclear and cytoplasmic actions and interactions, in line with other integral nuclear membrane proteins, such as the nesprin, emerin and SUN components of the LINC complex [45–50]. Manual curation of reported TMEM147 interactors, regulators and mediators thus revealed a wealth of protein factors in a multitude of pathways that show functional relationships with TMEM147. Statistical evaluation and simplification of the corresponding gene networks and pathways in turn highlighted specific highly connected proteins and prominent pathways that are informative for our growing understanding of TMEM147-related processes.

Pathway enrichment analysis, and in particular removal of redundant pathways post-analysis, crystallized key points of our current understanding of TMEM147 function.

REVIGO-based simplification of findings confirmed *G-protein coupled receptor function* as one of four key clusters of pathways highlighted for TMEM147, tying in with TMEM147 regulation of muscarinic receptors [2]. Likewise, *Ribosome binding* fits the role of TMEM147 in the Nicalin-NOMO-TMEM147 complex and in the establishment of co-translational translocation in the ribosome associated translocon complex [5], whereas *Oxidoreductase activity* with the numerous protein components prompting its detection largely reflects the role of TMEM147 in sterol synthesis [8]. The identification of *Transmembrane transport*, with its associated factors mediating also ion transport across membranes, highlights an emerging aspect of TMEM147 biology, which has come into focus through the recent structural resolution of the Nicalin-NOMO-TMEM147 complex [5], specifically that beyond action in the rER translocon, the complex might dynamically interact with and facilitate transmembrane transport by hundreds of transmembrane channels. Besides its general implications for TMEM147 function, this insight is intriguing also with regard to the role of TMEM147 in the ER and suggests investigation of potential effects on Ca^{2+} uptake and release by the sER.

Creation of gene networks with our shortlist of factors in String-db expectedly established TMEM147 as the major hub protein of the overall network. More importantly, though possibly biased through the specific focus of a limited number of formally published or database-only studies, the resulting networks also gave indication of additional protein factors as possible key mediators of TMEM147 function. Accordingly, a high level of connectedness within the network indicated among others EBP, CD40, COX6B1, NFKB1, NHP2, STOML2 and YIPF6 as hub proteins. From these, the sterol reductase EBP fits into our understanding of TMEM147 as a regulator of sterol homeostasis [51]. Likewise, inclusion of the immune-related CD40 and NFKB1, with CD40 as a mediator of immune responses [52] and NFKB1 as a regulator of innate immunity [53], fits into our understanding of TMEM147 as an activator of proinflammatory NF-κB action [54]. However, other highly connected components are less expected, such as COX6B1and STOML2 with their roles in mitochondria. COX6B1 is a critical component of the cytochrome c oxidase complex and thus of mitochondrial function [55], whereas STOML2 is a facilitator of mitochondrial membranes and biogenesis [56]. Additional less expected highly connected protein factors are YIPF6, with a role in glycan synthesis and assembly of the Golgi apparatus [57], and NHP2, one of four protein factors required for telomere maintenance and ribosome biogenesis by association with nucleolar and telomerase RNAs [58].

3.3. Pointers for Future Investigation

Only eleven years after its discovery, TMEM147 has already been implicated in a wide array of physiological processes, many of which might be interconnected by common components or shared pathways. It is therefore difficult to discern primary from secondary or more distant downstream effects. For instance, analysis of protein networks and pathways has drawn new links to regulatory RNAs, the Golgi apparatus, glycans and mitochondria, which could be tested for their biological significance by knockout, knockdown or overexpression of TMEM147 and measurement of corresponding effects on ribosome, telomerase, Golgi, matrix and mitochondrial functions, respectively. However, TMEM147 is already linked to ribosome function through its action in the Nicalin-NOMO-TMEM147 complex [5], and effects on mitochondria and Golgi could also stem from our newly established TMEM147 action on the ER and from widely reported ER association with these organelles through membrane contact sites [38]. Once a TMEM147-associated phenotype has been established, discernment of corresponding primary and secondary effects will thus rely on further analyses, including the isolation of additional and possibly highly transient membrane-associated protein complexes. As for network analyses, the quandary of determining primary causality for a multifunctional protein also affects follow-up for our in vitro findings. If TMEM147 is inhibitory to density and expansion of smooth ER tubules, how much of its effect on sterol synthesis is mediated through interaction with LBR and how much through interference with the sER as a major intracellular compartment responsible for sterol synthesis? Indeed, TMEM147 effects on the ER alone touch on many biological phenomena and research fields with medical relevance. For instance, it is tantalizing to speculate in how far TMEM147 expression may be therapeutic in cancer by limiting RTN4 action [59]. Likewise, and given its profound effect on ER structure and size, TMEM147 expression might also limit the capacity for regular rER protein processing [60] and intracellular calcium signaling [61] (beyond its action on muscarinic acetylcholine receptors [2]), prevent useful or curb excessive ER expansion during ER stress situations [62], facilitate ER luminal transport or interfere with ongoing axonal dynamics in neurons [38,39,59]. Our analyses here indicate an expanding network of pathways and protein factors as a functional context for an array of future investigations.

4. Conclusions

Here we revealed through in silico analysis of protein networks that known TMEM147 activities affect four areas of molecular function and, based on established roles of highly interconnected proteins, propose additional, testable TMEM147 activities that extend beyond the function of already established direct interactors. Moreover, we showed experimentally that TMEM147 depletion increases ER area overall and flat areas in particular. Whether this occurs through a direct effect on ER domain markers and structural determinants CLIMP63 and RTN4 or through other interactions, the observation suggests wider action by TMEM147 on transmembrane proteins in both the ER and the NE, and turns TMEM147 into a putative regulator of many additional processes and into a potential therapeutic target for a range of diseases.

5. Materials and Methods

5.1. Cell Culture

HeLa (Kyoto; K) cells were used for all experimentation, cultured in complete medium (DMEM-GlutaMAX, 10% v/v heat-inactivated fetal bovine serum, penicillin/streptomycin at 100 U/mL and Sodium Pyruvate at 1 mM; all GIBCO/ThermoFisher, Waltham, MA, USA) and treated as previously reported [8].

5.2. RNA Interference

Cells were passaged in 60 mm culture dishes (Corning Inc., Corning, NY, USA), covered with sterile coverslips, to a cell density of 50–60%. 24 h later, cells were washed with DPBS (GIBCO/Thermo Fisher Scientific, Waltham, MA, USA) and the medium replaced with 4 mL of fresh complete medium. The siRNA oligonucleotide mixture were prepared by adding 8 µL of 40 nM siRNA oligonucleotides (#109789 Silencer® Pre-designed siRNA, 5′-GGCGGCAUCUAUGACUUCATT-3′, Thermo Fisher Scientific/Ambion Inc., Austin, TX, USA), or 8 µL water for negative controls, and 12 µL INTERFERin transfection agent (Polyplus Transfection, Vectura, Illkirch-Graffenstaden, France) to 400 µL OptiMEM (GIBCO/Thermo Fisher Scientific, Waltham, MA, USA) before vortexing and 10 min incubation at room temperature, according to the transfection reagent manufacturer's recommendations. At t = 0 h, the mixture was added dropwise to the cells with gentle agitation. At t = 24 h, the medium was changed as required and at t = 72 h coverslips were harvested for immunofluorescence (IF) analysis.

5.3. Immunofluorescence

All incubation and handling steps were at room temperature, unless indicated otherwise.

5.3.1. Antibodies Used

Antibodies and dilutions for immunofluorescence were, as primary antibodies, mouse αCLIMP63 (dilution 1:1000G1/296, ABS669-0100 Enzo Life Sciences, Farmingdale, NY, USA), rabbit αRTN4 (dilution 1:300, ab47085, Abcam, Cambridge, UK), rabbit αLBR (dilution 1:300, ab32535, Abcam, Cambridge, UK), and as secondary antibodies goat αRabbit AlexaFluor488 (1:1000, IgG/A-11034, Molecular Probes/Invitrogen/Thermo Fisher Scientific, Waltham, MA, USA) and donkey αMouse AlexaFluor555 (1:1000, IgG/A-31570, Molecular Probes/Invitrogen/Thermo Fisher Scientific, Waltham, MA, USA). Hoechst 33342 was used as a DNA counterstain at 0.5 µg/mL (B2261, Sigma-Aldrich, St. Louis, MO, USA).

5.3.2. Cell Fixation

Fixation solution was prepared as paraformaldehyde (PFA) 4% (*w*/*v*) in PHEM pH 8.0 (30 mM HEPES, 60 mM Pipes pH 6.9, 10 mM EGTA, 2 mM $MgCl_2$) and permeabilization solution as 0.5% (*v*/*v*) triton-X in PHEM (all Sigma-Aldrich, St. Louis, MO, USA). Coverslips were placed in a 12-well plate containing fixation solution, followed by 10 min of incubation, replacement of the fixation solution with permeabilization solution for 5 min of incubation, and three 3 min washes of coverslips with PHEM. After application of 50 mM NH_4Cl in DPBS as quenching solution and 10 min incubation, coverslips were stored in DPBS until immunofluorescence staining.

5.3.3. Immunofluorescence Staining and Mounting

Coverslips bearing fixed cells were placed on PARAFILM® (Sigma-Aldrich, St. Louis, MO, USA) and incubated with blocking solution (2% (*w*/*v*) FBS, 2% (*w*/*v*) BSA, 0.2% (*w*/*v*) fish skin gelatin, in DPBS) for 1 h, before its replacement by the appropriate dilution of primary antibody or a mixture of primary antibodies in 5% blocking solution in DPBS and incubation for 16–18 h at 4 °C. After three 3 min washes with washing solution (0.1% (*v*/*v*) Tween® 20 in PHEM), the appropriate secondary antibody or antibody mixture in 5% blocking solution in DPBS was applied and left to incubate at room temperature for 1 h, followed by two 3 min washes in washing solution and one 3 min wash in DPBS, before mounting of the dry coverslip using Dako Fluorescence Mounting Medium (Agilent/Dako, Santa Clara, CA, USA)

5.4. Microscopy

Microscopy was performed on a Carl Zeiss Axiovert 200 M with a Plan-Apochromat 63×/1.4NA oil lens and wavelength filter sets for detection of Hoechst 33342 (450 nm), Alexa Fluor 488 (520 nm) and Alex Fluor 555 (568 nm) The images were acquired using the high sensitivity digital camera AxioCam HRc for multicolor fluorescent images along with the Zeiss software Axiovision, v4.8.2.SP2. All same-figure images were taken at identical exposure and filter settings for comparability of intensities. Images were processed with uniform and unbiased application of contrast and brightness settings in Photoshop and Illustrator (Adobe Inc., San Jose, CA, USA).

5.5. Morphometric Analysis

Using the standard microscopy setup, ER alterations after TMEM147 silencing were measured after staining for CLIMP63 and RTN4 for a total of 457 HeLa cell images, including 225 control-silenced and 232 TMEM147-silenced cells, from three independent experiments and with identical acquisition settings across control and corresponding silenced samples. The pixel area of staining for CLIMP63 (corresponding to flattened ER cisternae) and RTN4 (corresponding to ER tubules) was measured in ImageJ v1.52p by manually selecting the boundaries of each cell as a region of interest (ROI). For each cell and fluorescence channel, thresholding algorithms were applied to determine the corresponding area, and the total ER area was calculated as the union of both channels without double-counting areas of overlap.

5.6. Statistical and Bioinformatics Evaluation

5.6.1. Network Analyses

Reported TMEM147 targets, direct, indirect and same-complex interactors, co-regulated and co-expressed proteins were identified and manually curated for redundancy and spurious or erroneous database entries based on the following repositories: APID [63], BioGRID, GeneMania [64], GPS-Prot [65], Human Protein Reference Database [66,67], IntAct

EMBL-EBI [68], HuRi [69], PubMed, Pathway Commons [70], PINA [71,72], Reactome [73], STRING [36], with identifiers and annotations from UniProt [74].

The resulting list of 98 protein factors plus TMEM147 was used as a list of input proteins in String-db.org 11.0b (STRING, Available online: https://version-11-0b.string-db.org (accessed on 28 July 2021)) [36], applying as settings full network analysis, network edges representing evidence, using all active interaction sources, applying 0.150 as the required interaction score and displaying only the query proteins and no additional layers of secondary interactors (for Figure 3b, including the first shell of interactors for illustration). The network output images were manually curated to align unlinked protein factors outside the network, to apply the official HUGO gene symbol where String-db applied alternative protein names and to include the legend.

5.6.2. Pathway Reduction

Significant Gene Ontology Molecular Function nodes derived from String-db were imported with their corresponding false discovery rate (FDR) values to the Reduce and Visualize Gene Ontology (REVIGO, Available online: http://revigo.irb.hr (accessed on 14 August 2021)) tool [37], in order to remove redundant GO terms and interpret more readily the underlying enrichment analysis. The settings applied were the choice of Small (0.5) for the resulting list, the provision of P value (as the most suitable choice) for associated values, the removal of obsolete GO terms, the choice of *Homo sapiens* as target species and the choice of the default SimRel semantic similarity measure. Of the resulting output, TreeMap and the table of non-redundant GO terms were included in Figure 3, whereas corresponding Scatterplot and Interactive Function graphs are available as Supplementary Figure S5.

5.6.3. Summary Statistics and Groupwise Comparisons

Summary statistics and groupwise comparisons for image analyses based on DNA, CLIMP63 and RTN4 fluorescence measurements after TMEM147 silencing were based on composite images for a total of 457 HeLa cells. Box-and-whisker diagrams displaying all values were based on raw data for all cells, whereas bar charts and groupwise comparisons were based on data after outlier removal using the 1.5x IQR rule [75], resulting in evaluable data for 362 HeLa cells (n = 177 control, n = 185 silenced). These data were tested for statistical significance between untreated and treated cells by MANOVA analysis using Pillai's test at a statistical significance $\alpha = 5\%$ in Excel (Microsoft Office, 2016, Redmond, WA, USA) and XLSTAT (Addinsoft, Paris, France).

Supplementary Materials: The following are available online at https://www.mdpi.com/article/10.3390/ijms221910231/s1, Supplementary Figure S1. The three main splice variants and isoforms of human TMEM147. Supplememtary Figure S2. Alignment of RefSeq cDNA sequences for the three main TMEM splice variants. Supplementary Figure S3. Alignment of RefSeq protein sequences for the three main TMEM147 protein isoforms. Supplementary Figure S4. Transcript and protein expression of TMEM147 across all isoforms. Supplementary Figure S5. Alternative simplified display of TMEM147-associated GO terms. Supplementary Table S1. Known TMEM147 associations and interaction.

Author Contributions: Conceptualization, G.M., N.S. and C.W.L.; methodology, G.M., A.C., N.S. and C.W.L.; validation, G.M. and C.W.L.; formal analysis, G.M., A.C. and C.W.L.; investigation, G.M., N.S. and C.W.L.; resources, N.S. and C.W.L.; data curation, G.M. and C.W.L.; writing—original draft preparation, G.M. and C.W.L.; writing—review and editing, G.M., A.C., N.S. and C.W.L.; visualization, G.M. and C.W.L.; supervision, N.S. and C.W.L.; project administration, N.S. and C.W.L.; funding acquisition, N.S. and C.W.L. All authors have read and agreed to the published version of the manuscript.

Funding: This work was supported by the University of Cyprus internal research funds (N.S.) and co-financed by the Republic of Cyprus through the Research and Innovation Foundation (EXCELLENCE/1216/0092) (C.W.L.).

Institutional Review Board Statement: Not applicable.

Informed Consent Statement: Not applicable.

Data Availability Statement: Not applicable.

Conflicts of Interest: The authors declare no conflict of interest. The funders had no role in the design of the study; in the collection, analyses or interpretation of data; in the writing of the manuscript or in the decision to publish the results.

References

1. Dettmer, U.; Kuhn, P.H.; Abou-Ajram, C.; Lichtenthaler, S.F.; Kruger, M.; Kremmer, E.; Haass, C.; Haffner, C. Transmembrane protein 147 (TMEM147) is a novel component of the Nicalin-NOMO protein complex. *J. Biol. Chem.* **2010**, *285*, 26174–26181. [CrossRef] [PubMed]
2. Rosemond, E.; Rossi, M.; McMillin, S.M.; Scarselli, M.; Donaldson, J.G.; Wess, J. Regulation of M (3) muscarinic receptor expression and function by transmembrane protein 147. *Mol. Pharm.* **2011**, *79*, 251–261. [CrossRef] [PubMed]
3. NCBI-AceView. TMEM147 Isoforms. Available online: https://www.ncbi.nlm.nih.gov/ieb/research/acembly/av.cgi?db=human&term=tmem147 (accessed on 10 February 2021).
4. NCBI. TMEM147 Variants. Available online: https://www.ncbi.nlm.nih.gov/nuccore/NM_032635.4,NM_001242597.2,NM_001242598.2 (accessed on 9 June 2020).
5. McGilvray, P.T.; Anghel, S.A.; Sundaram, A.; Zhong, F.; Trnka, M.J.; Fuller, J.R.; Hu, H.; Burlingame, A.L.; Keenan, R.J. An ER translocon for multi-pass membrane protein biogenesis. *Elife* **2020**, *9*, e56889. [CrossRef] [PubMed]
6. Ensembl. TMEM147 Gene Expression. Available online: https://asia.ensembl.org/Homo_sapiens/Gene/ExpressionAtlas?db=core;g=ENSG00000105677;r=19:35545600-35547526 (accessed on 11 June 2020).
7. Haffner, C.; Dettmer, U.; Weiler, T.; Haass, C. The Nicastrin-like protein Nicalin regulates assembly and stability of the Nicalin-nodal modulator (NOMO) membrane protein complex. *J. Biol. Chem.* **2007**, *282*, 10632–10638. [CrossRef]
8. Christodoulou, A.; Maimaris, G.; Makrigiorgi, A.; Charidemou, E.; Lüchtenborg, C.; Ververis, A.; Georgiou, R.; Lederer, C.W.; Haffner, C.; Brügger, B.; et al. TMEM147 interacts with Lamin B Receptor, regulates its localization and levels, and affects cholesterol homeostasis. *J. Cell Sci.* **2020**, *133*, jcs245357. [CrossRef]
9. Makatsori, D.; Kourmouli, N.; Polioudaki, H.; Shultz, L.D.; McLean, K.; Theodoropoulos, P.A.; Singh, P.B.; Georgatos, S.D. The inner nuclear membrane protein lamin B receptor forms distinct microdomains and links epigenetically marked chromatin to the nuclear envelope. *J. Biol. Chem.* **2004**, *279*, 25567–25573. [CrossRef]
10. Pyrpasopoulou, A.; Meier, J.; Maison, C.; Simos, G.; Georgatos, S.D. The lamin B receptor (LBR) provides essential chromatin docking sites at the nuclear envelope. *EMBO J.* **1996**, *15*, 7108–7119. [CrossRef]
11. Worman, H.J.; Yuan, J.; Blobel, G.; Georgatos, S.D. A lamin B receptor in the nuclear envelope. *Proc. Natl. Acad. Sci. USA* **1988**, *85*, 8531–8534. [CrossRef]
12. Olins, A.L.; Rhodes, G.; Welch, D.B.; Zwerger, M.; Olins, D.E. Lamin B receptor: Multi-tasking at the nuclear envelope. *Nucleus* **2010**, *1*, 53–70. [CrossRef]
13. Papavinasasundaram, K.G.; Kasbekar, D.P. TheNeurospora crassa erg3 gene encodes a protein with sequence homology to both yeast sterol C-14 reductase and chicken lamin B receptor. *J. Genet.* **1994**, *73*, 33. [CrossRef]
14. Li, X.; Roberti, R.; Blobel, G. Structure of an integral membrane sterol reductase from Methylomicrobium alcaliphilum. *Nature* **2015**, *517*, 104–107. [CrossRef]
15. Silve, S.; Dupuy, P.H.; Ferrara, P.; Loison, G. Human lamin B receptor exhibits sterol C14-reductase activity in Saccharomyces cerevisiae. *Biochim. Biophys. Acta* **1998**, *1392*, 233–244. [CrossRef]
16. Worman, H.J.; Evans, C.D.; Blobel, G. The lamin B receptor of the nuclear envelope inner membrane: A polytopic protein with eight potential transmembrane domains. *J. Cell Biol.* **1990**, *111*, 1535–1542. [CrossRef]
17. Holmer, L.; Pezhman, A.; Worman, H.J. The Human Lamin B Receptor/Sterol Reductase Multigene Family. *Genomics* **1998**, *54*, 469–476. [CrossRef]
18. Prakash, A.; Kasbekar, D.P. Genes encoding chimeras of Neurospora crassa erg-3 and human TM7SF2 proteins fail to complement Neurospora and yeast sterol C-14 reductase mutants. *J. Biosci.* **2002**, *27*, 105–112. [CrossRef]
19. Capell-Hattam, I.M.; Sharpe, L.J.; Qian, L.; Hart-Smith, G.; Prabhu, A.V.; Brown, A.J. Twin enzymes, divergent control: The cholesterogenic enzymes DHCR14 and LBR are differentially regulated transcriptionally and post-translationally. *J. Biol. Chem.* **2020**, *295*, 2850–2865. [CrossRef]
20. Deolal, P.; Mishra, K. Regulation of diverse nuclear shapes: Pathways working independently, together. *Commun. Integr. Biol.* **2021**, *14*, 158–175. [CrossRef]
21. Van de Velde, H.J.; Roebroek, A.J.; Senden, N.H.; Ramaekers, F.C.; Van de Ven, W.J. NSP-encoded reticulons, neuroendocrine proteins of a novel gene family associated with membranes of the endoplasmic reticulum. *J. Cell Sci.* **1994**, *107*, 2403–2416. [CrossRef]
22. Shibata, Y.; Shemesh, T.; Prinz, W.A.; Palazzo, A.F.; Kozlov, M.M.; Rapoport, T.A. Mechanisms determining the morphology of the peripheral ER. *Cell* **2010**, *143*, 774–788. [CrossRef]
23. Westrate, L.M.; Lee, J.E.; Prinz, W.A.; Voeltz, G.K. Form follows function: The importance of endoplasmic reticulum shape. *Annu. Rev. Biochem.* **2015**, *84*, 791–811. [CrossRef]

24. Nixon-Abell, J.; Obara, C.J.; Weigel, A.V.; Li, D.; Legant, W.R.; Xu, C.S.; Pasolli, H.A.; Harvey, K.; Hess, H.F.; Betzig, E.; et al. Increased spatiotemporal resolution reveals highly dynamic dense tubular matrices in the peripheral ER. *Science* **2016**, *354*, aaf3928. [CrossRef]
25. Dawson, T.R.; Lazarus, M.D.; Hetzer, M.W.; Wente, S.R. ER membrane-bending proteins are necessary for de novo nuclear pore formation. *J. Cell Biol.* **2009**, *184*, 659–675. [CrossRef]
26. Shibata, Y.; Voss, C.; Rist, J.M.; Hu, J.; Rapoport, T.A.; Prinz, W.A.; Voeltz, G.K. The reticulon and DP1/Yop1p proteins form immobile oligomers in the tubular endoplasmic reticulum. *J. Biol. Chem.* **2008**, *283*, 18892–18904. [CrossRef]
27. Voeltz, G.K.; Prinz, W.A.; Shibata, Y.; Rist, J.M.; Rapoport, T.A. A class of membrane proteins shaping the tubular endoplasmic reticulum. *Cell* **2006**, *124*, 573–586. [CrossRef]
28. Gao, G.; Zhu, C.; Liu, E.; Nabi, I.R. Reticulon and CLIMP-63 regulate nanodomain organization of peripheral ER tubules. *PLoS Biol.* **2019**, *17*, e3000355. [CrossRef]
29. Hu, J.; Shibata, Y.; Voss, C.; Shemesh, T.; Li, Z.; Coughlin, M.; Kozlov, M.M.; Rapoport, T.A.; Prinz, W.A. Membrane proteins of the endoplasmic reticulum induce high-curvature tubules. *Science* **2008**, *319*, 1247–1250. [CrossRef]
30. Klopfenstein, D.R.; Kappeler, F.; Hauri, H.P. A novel direct interaction of endoplasmic reticulum with microtubules. *EMBO J.* **1998**, *17*, 6168–6177. [CrossRef]
31. Bernales, S.; McDonald, K.L.; Walter, P. Autophagy counterbalances endoplasmic reticulum expansion during the unfolded protein response. *PLoS Biol.* **2006**, *4*, e423. [CrossRef]
32. Nikonov, A.V.; Hauri, H.P.; Lauring, B.; Kreibich, G. Climp-63-mediated binding of microtubules to the ER affects the lateral mobility of translocon complexes. *J. Cell Sci.* **2007**, *120*, 2248–2258. [CrossRef]
33. Schwarz, D.S.; Blower, M.D. The endoplasmic reticulum: Structure, function and response to cellular signaling. *Cell Mol. Life Sci.* **2016**, *73*, 79–94. [CrossRef]
34. Cantwell, H.; Nurse, P. Unravelling nuclear size control. *Curr. Genet.* **2019**, *65*, 1281–1285. [CrossRef] [PubMed]
35. Hara, Y. Specialization of nuclear membrane in eukaryotes. *J. Cell Sci.* **2020**, *133*, jcs241869. [CrossRef] [PubMed]
36. Szklarczyk, D.; Gable, A.L.; Lyon, D.; Junge, A.; Wyder, S.; Huerta-Cepas, J.; Simonovic, M.; Doncheva, N.T.; Morris, J.H.; Bork, P.; et al. STRING v11: Protein-protein association networks with increased coverage, supporting functional discovery in genome-wide experimental datasets. *Nucleic Acids Res.* **2019**, *47*, D607–D613. [CrossRef]
37. Supek, F.; Bosnjak, M.; Skunca, N.; Smuc, T. REVIGO summarizes and visualizes long lists of gene ontology terms. *PLoS ONE* **2011**, *6*, e21800. [CrossRef]
38. Öztürk, Z.; O'Kane, C.J.; Pérez-Moreno, J.J. Axonal Endoplasmic Reticulum Dynamics and Its Roles in Neurodegeneration. *Front. Neurosci.* **2020**, *14*, 48. [CrossRef] [PubMed]
39. Konno, T.; Parutto, P.; Bailey, D.M.D.; Davì, V.; Crapart, C.; Awadelkareem, M.A.; Hockings, C.; Brown, A.; Xiang, K.M.; Agrawal, A.; et al. Endoplasmic Reticulum morphological regulation by RTN4/NOGO modulates neuronal regeneration by curbing luminal transport. *bioRxiv* **2021**. [CrossRef]
40. Mukherjee, R.N.; Chen, P.; Levy, D.L. Recent advances in understanding nuclear size and shape. *Nucleus* **2016**, *7*, 167–186. [CrossRef]
41. Klopfenstein, D.R.; Klumperman, J.; Lustig, A.; Kammerer, R.A.; Oorschot, V.; Hauri, H.P. Subdomain-specific localization of CLIMP-63 (p63) in the endoplasmic reticulum is mediated by its luminal alpha-helical segment. *J. Cell Biol.* **2001**, *153*, 1287–1300. [CrossRef]
42. Millen, J.I.; Pierson, J.; Kvam, E.; Olsen, L.J.; Goldfarb, D.S. The luminal N-terminus of yeast Nvj1 is an inner nuclear membrane anchor. *Traffic* **2008**, *9*, 1653–1664. [CrossRef]
43. Anderson, D.J.; Hetzer, M.W. Nuclear envelope formation by chromatin-mediated reorganization of the endoplasmic reticulum. *Nat. Cell Biol.* **2007**, *9*, 1160–1166. [CrossRef]
44. Anderson, D.J.; Hetzer, M.W. Reshaping of the endoplasmic reticulum limits the rate for nuclear envelope formation. *J. Cell Biol.* **2008**, *182*, 911–924. [CrossRef]
45. Demmerle, J.; Koch, A.J.; Holaska, J.M. The nuclear envelope protein emerin binds directly to histone deacetylase 3 (HDAC3) and activates HDAC3 activity. *J. Biol. Chem.* **2012**, *287*, 22080–22088. [CrossRef]
46. Holaska, J.M.; Wilson, K.L. An emerin "proteome": Purification of distinct emerin-containing complexes from HeLa cells suggests molecular basis for diverse roles including gene regulation, mRNA splicing, signaling, mechanosensing, and nuclear architecture. *Biochemistry* **2007**, *46*, 8897–8908. [CrossRef]
47. Burger, M.; Schmitt-Koopmann, C.; Leroux, J.C. DNA unchained: Two assays to discover and study inhibitors of the DNA clustering function of barrier-to-autointegration factor. *Sci. Rep.* **2020**, *10*, 12301. [CrossRef]
48. Noegel, A.A.; Neumann, S. The role of nesprins as multifunctional organizers in the nucleus and the cytoskeleton. *Biochem. Soc. Trans.* **2011**, *39*, 1725–1728. [CrossRef]
49. May, C.K.; Carroll, C.W. Differential incorporation of SUN-domain proteins into LINC complexes is coupled to gene expression. *PLoS ONE* **2018**, *13*, e0197621. [CrossRef]
50. Hieda, M.; Matsumoto, T.; Isobe, M.; Kurono, S.; Yuka, K.; Kametaka, S.; Wang, J.Y.; Chi, Y.H.; Kameda, K.; Kimura, H.; et al. The SUN2-nesprin-2 LINC complex and KIF20A function in the Golgi dispersal. *Sci. Rep.* **2021**, *11*, 5358. [CrossRef]
51. Silve, S.; Dupuy, P.H.; Labit-Lebouteiller, C.; Kaghad, M.; Chalon, P.; Rahier, A.; Taton, M.; Lupker, J.; Shire, D.; Loison, G. Emopamil-binding protein, a mammalian protein that binds a series of structurally diverse neuroprotective agents, exhibits delta8-delta7 sterol isomerase activity in yeast. *J. Biol. Chem.* **1996**, *271*, 22434–22440. [CrossRef]

52. Takada, Y.K.; Yu, J.; Shimoda, M.; Takada, Y. Integrin Binding to the Trimeric Interface of CD40L Plays a Critical Role in CD40/CD40L Signaling. *J. Immunol.* **2019**, *203*, 1383–1391. [CrossRef]
53. Beinke, S.; Robinson, M.J.; Hugunin, M.; Ley, S.C. Lipopolysaccharide activation of the TPL-2/MEK/extracellular signal-regulated kinase mitogen-activated protein kinase cascade is regulated by IkappaB kinase-induced proteolysis of NF-kappaB1 p105. *Mol. Cell Biol.* **2004**, *24*, 9658–9667. [CrossRef]
54. Ota, M.; Tanaka, Y.; Nakagawa, I.; Jiang, J.J.; Arima, Y.; Kamimura, D.; Onodera, T.; Iwasaki, N.; Murakami, M. Role of Chondrocytes in the Development of Rheumatoid Arthritis Via Transmembrane Protein 147-Mediated NF-kappaB Activation. *Arthritis Rheumatol.* **2020**, *72*, 931–942. [CrossRef]
55. Abdulhag, U.N.; Soiferman, D.; Schueler-Furman, O.; Miller, C.; Shaag, A.; Elpeleg, O.; Edvardson, S.; Saada, A. Mitochondrial complex IV deficiency, caused by mutated COX6B1, is associated with encephalomyopathy, hydrocephalus and cardiomyopathy. *Eur. J. Hum. Genet.* **2015**, *23*, 159–164. [CrossRef] [PubMed]
56. Christie, D.A.; Lemke, C.D.; Elias, I.M.; Chau, L.A.; Kirchhof, M.G.; Li, B.; Ball, E.H.; Dunn, S.D.; Hatch, G.M.; Madrenas, J. Stomatin-like protein 2 binds cardiolipin and regulates mitochondrial biogenesis and function. *Mol. Cell Biol.* **2011**, *31*, 3845–3856. [CrossRef] [PubMed]
57. Soonthornsit, J.; Sakai, N.; Sasaki, Y.; Watanabe, R.; Osako, S.; Nakamura, N. YIPF1, YIPF2, and YIPF6 are medial-/trans-Golgi and trans-Golgi network-localized Yip domain family proteins, which play a role in the Golgi reassembly and glycan synthesis. *Exp. Cell Res.* **2017**, *353*, 100–108. [CrossRef]
58. Wang, C.; Meier, U.T. Architecture and assembly of mammalian H/ACA small nucleolar and telomerase ribonucleoproteins. *EMBO J.* **2004**, *23*, 1857–1867. [CrossRef] [PubMed]
59. Pathak, G.P.; Shah, R.; Kennedy, B.E.; Murphy, J.P.; Clements, D.; Konda, P.; Giacomantonio, M.; Xu, Z.; Schlaepfer, I.R.; Gujar, S. RTN4 Knockdown Dysregulates the AKT Pathway, Destabilizes the Cytoskeleton, and Enhances Paclitaxel-Induced Cytotoxicity in Cancers. *Mol. Ther.* **2018**, *26*, 2019–2033. [CrossRef] [PubMed]
60. Benyair, R.; Ron, E.; Lederkremer, G.Z. Protein quality control, retention, and degradation at the endoplasmic reticulum. *Int Rev. Cell Mol. Biol.* **2011**, *292*, 197–280. [PubMed]
61. Stutzmann, G.E.; Mattson, M.P. Endoplasmic reticulum Ca (2+) handling in excitable cells in health and disease. *Pharm. Rev.* **2011**, *63*, 700–727. [CrossRef]
62. Ferro-Novick, S.; Reggiori, F.; Brodsky, J.L. ER-Phagy, ER Homeostasis, and ER Quality Control: Implications for Disease. *Trends Biochem. Sci.* **2021**, *46*, 630–639. [CrossRef]
63. Alonso-Lopez, D.; Campos-Laborie, F.J.; Gutierrez, M.A.; Lambourne, L.; Calderwood, M.A.; Vidal, M.; De Las Rivas, J. APID database: Redefining protein-protein interaction experimental evidences and binary interactomes. *Database Oxf.* **2019**, *2019*, baz005. [CrossRef]
64. Warde-Farley, D.; Donaldson, S.L.; Comes, O.; Zuberi, K.; Badrawi, R.; Chao, P.; Franz, M.; Grouios, C.; Kazi, F.; Lopes, C.T.; et al. The GeneMANIA prediction server: Biological network integration for gene prioritization and predicting gene function. *Nucleic Acids Res.* **2010**, *38*, W214–W220. [CrossRef]
65. Fahey, M.E.; Bennett, M.J.; Mahon, C.; Jäger, S.; Pache, L.; Kumar, D.; Shapiro, A.; Rao, K.; Chanda, S.K.; Craik, C.S.; et al. GPS-Prot: A web-based visualization platform for integrating host-pathogen interaction data. *BMC Bioinform.* **2011**, *12*, 298. [CrossRef]
66. Keshava Prasad, T.S.; Goel, R.; Kandasamy, K.; Keerthikumar, S.; Kumar, S.; Mathivanan, S.; Telikicherla, D.; Raju, R.; Shafreen, B.; Venugopal, A.; et al. Human Protein Reference Database-2009 update. *Nucleic Acids Res.* **2009**, *37*, D767–D772. [CrossRef]
67. Peri, S.; Navarro, J.D.; Amanchy, R.; Kristiansen, T.Z.; Jonnalagadda, C.K.; Surendranath, V.; Niranjan, V.; Muthusamy, B.; Gandhi, T.K.; Gronborg, M.; et al. Development of human protein reference database as an initial platform for approaching systems biology in humans. *Genome Res.* **2003**, *13*, 2363–2371. [CrossRef]
68. Orchard, S.; Ammari, M.; Aranda, B.; Breuza, L.; Briganti, L.; Broackes-Carter, F.; Campbell, N.H.; Chavali, G.; Chen, C.; del-Toro, N.; et al. The MIntAct project–IntAct as a common curation platform for 11 molecular interaction databases. *Nucleic Acids Res.* **2014**, *42*, D358–D363. [CrossRef]
69. Luck, K.; Kim, D.-K.; Lambourne, L.; Spirohn, K.; Begg, B.E.; Bian, W.; Brignall, R.; Cafarelli, T.; Campos-Laborie, F.J.; Charloteaux, B.; et al. A reference map of the human binary protein interactome. *Nature* **2020**, *580*, 402–408. [CrossRef]
70. Cerami, E.G.; Gross, B.E.; Demir, E.; Rodchenkov, I.; Babur, O.; Anwar, N.; Schultz, N.; Bader, G.D.; Sander, C. Pathway Commons, a web resource for biological pathway data. *Nucleic Acids Res.* **2011**, *39*, D685–D690. [CrossRef]
71. Wu, J.; Vallenius, T.; Ovaska, K.; Westermarck, J.; Makela, T.P.; Hautaniemi, S. Integrated network analysis platform for protein-protein interactions. *Nat. Methods* **2009**, *6*, 75–77. [CrossRef]
72. Cowley, M.J.; Pinese, M.; Kassahn, K.S.; Waddell, N.; Pearson, J.V.; Grimmond, S.M.; Biankin, A.V.; Hautaniemi, S.; Wu, J. PINA v2.0: Mining interactome modules. *Nucleic Acids Res.* **2012**, *40*, D862–D865. [CrossRef]
73. Jassal, B.; Matthews, L.; Viteri, G.; Gong, C.; Lorente, P.; Fabregat, A.; Sidiropoulos, K.; Cook, J.; Gillespie, M.; Haw, R.; et al. The reactome pathway knowledgebase. *Nucleic Acids Res.* **2020**, *48*, D498–D503. [CrossRef]
74. UniProt, C. The universal protein resource (UniProt). *Nucleic Acids Res.* **2008**, *36*, D190–D195.
75. Tukey, J.W. *Exploratory Data Analysis*; Addison-Wesley Pub. Co.: Reading, MA, USA, 1977.